

CRANFIELD UNIVERSITY

Aver Hemben

**Metallic Nanocarrier Complex Targeting Neuroendocrine
Prostate Cancer Cells**

School of Aerospace, Transport and Manufacturing
PhD

PhD in Manufacturing
Academic Years: 2018 - 2022

Supervisor: Dr Iva Chianella
Associate Supervisor: Dr Glenn Leighton
September 2022

CRANFIELD UNIVERSITY

School of Aerospace, Transport and Manufacturing

PhD

Academic Years: 2018 - 2022

Aver Hemben

**Metallic Nanocarrier Complex Targeting Neuroendocrine
Prostate Cancer Cells**

Supervisor: Dr Iva Chianella

Associate Supervisor: Dr Glenn Leighton

September 2022

This thesis is submitted in partial fulfilment of the requirements for
the degree of PhD

© Cranfield University 2022. All rights reserved. No part of this
publication may be reproduced without the written permission of the
copyright owner.

ABSTRACT

Iron oxide nanoparticles were successfully produced by inert gas condensation using the Mantis NanoGen Trio system. The nanoparticles were produced *via* a novel approach using the Physical Vapour Deposition (PVD) method to condense iron oxide nanoparticles of small size and small size distribution of 1-6 nm diameter. The sputtered nanoparticles were soft-landed on a polyethylene glycol-coated silicon wafer, then dispersed in RNase free water (PEG-IONPs) to functionalise them for biocompatibility and use in nanocarrier synthesis. The sputtered iron oxide nanoparticles were characterised by transmission electron microscopy, atomic force microscopy, nanoparticle tracking analysis, dynamic light scattering and magnetic resonance imaging. The different techniques demonstrated that whereas the IONPs themselves were less than 10 nm (seen by TEM) the PEG-IONPs demonstrated a size range slightly different according to the technique used for its evaluation (e.g. 47 ± 22.75 nm by DLS and 143 ± 100 nm by NTA) with the variation most likely due to the high concentration of PEG present in solution. In parallel to sputtering IONPs, commercial iron oxide nanoparticles (CIONPs) were used to demonstrate and optimise the attachment of a therapeutic drug (siRNA) to the nanoparticles in 1:1 polyethylene glycol and polyethyleneimine. Then the release profile of the attached siRNA from CIONPs in PBS buffer pH 6.4 and 7.4 was studied. While using a sample of PBS/PEG/PEI, approximately 75% of siRNA was attached to CIONPs and approximately 86% siRNA was released in PBS after 300 minutes of incubation at 37°C. The research findings demonstrate the potential use of the synthesised nanoparticles and nanocarrier complex in targeted drug deliver to neuroendocrine prostate cells.

Keywords:

Iron oxide nanoparticles, inert gas condensation sputtering, drug delivery, prostate cancer metallic nanoparticles, metallic nanocarrier.

ACKNOWLEDGEMENTS

I would like to thank Dr Iva Chianella and Dr Glenn Leighton for providing guidance and support throughout the course of the research. I would also like to thank Professor Jose Luis Endrino, Dr Greg Bizarri, Dr Quentin Lonné, Dr Chris Shaw, Andrew Stallard and other staff for technical support with the research. I thank Dr Francesco Crea, Dr Igor Kraev (Open University, Milton Keynes, UK) for TEM analysis and Professor Galina Pavlovskaya, University of Nottingham, UK for help with MRI characterisation of the sputtered IONPs. I would also like to thank all my colleagues and friends, many of whom were on the same journey. I appreciate my family for very kind, unflinching support.

TABLE OF CONTENTS

ABSTRACT	i
ACKNOWLEDGEMENTS.....	iii
LIST OF FIGURES.....	viii
LIST OF TABLES	xii
LIST OF EQUATIONS.....	xiii
LIST OF ABBREVIATIONS.....	xiv
1 INTRODUCTION AND LITERATURE REVIEW	1
1.1 INTRODUCTION	1
1.2 PROSTATE CANCER	3
1.2.1 Prostate cancer diagnosis	5
1.2.2 Treatment of prostate cancer	5
1.2.3 Neuroendocrine prostate cancer (NEPC).....	8
1.2.4 Detection of neuroendocrine prostate cancer.....	9
1.2.5 Treatment of neuroendocrine prostate cancer	11
1.3 SMALL INTERFERING RNA AS A THERANOSTIC AGENT	11
1.3.1 Drug delivery by nanoparticles	14
1.4 NANOPARTICLES IN BIOMEDICINE	20
1.4.1 Iron oxide nanoparticles in biomedicine	21
1.4.2 Functionalisation of Nanoparticles	23
1.5 NANOPARTICLES SYNTHESIS METHODS	25
1.5.1 Production of Nanoparticles using Mantis NanoGen Trio.....	28
1.6 AIMS AND OBJECTIVES	31
2 PRODUCTION AND CHARACTERISATION OF IRON OXIDE NANOPARTICLES	35
2.1 INTRODUCTION	35
2.2 MATERIALS	39
2.2.1 General chemicals and instrumentation	39
2.3 METHODS.....	39
2.3.1 Preparation of silicon wafer with copper TEM grid	40
2.3.2 Preparation of PEG in acetone.....	40
2.3.3 Coating of the silicon wafer with PEG in acetone.....	41
2.3.4 Plasma cleaning of the silicon wafer	41
2.3.5 Spin coating of the silicon wafer with PEG in acetone.....	42
2.3.6 Contact angle measurements for plain and PEG coated silicon wafer	43
2.3.7 DektakXT stylus profile of the PEG – coated silicon wafer.....	44
2.3.8 Mantis NanoGenTrio	46
2.3.9 Optimisation of sputtering process parameters	54
2.3.10 Characterisation of IONPs by TEM	57

2.3.11 AFM characterisation of sputtered IONPs on bare silicon wafer	60
2.3.12 DLS characterisation of sputtered IONPs.....	60
2.3.13 NTA characterisation of sputtered IONPs	62
2.3.14 MRI characterisation of water relaxation in the presence of sputtered IONPs.....	63
2.4 RESULTS AND DISCUSSION	64
2.4.1 Preparation of the silicon wafer substrate	64
2.4.2 Production of IONPs by Inert gas condensation technique	67
2.4.3 Transmission Electron Microscopy (TEM).....	78
2.4.4 Atomic Force Microscopy (AFM)	83
2.4.5 Dynamic light scattering (DLS).....	85
2.4.6 Nanoparticle Tracking Analysis (NTA).....	89
2.4.7 Magnetic resonance imaging	97
2.5 CONCLUSIONS.....	101
3 BOVINE SERUM ALBUMIN (BSA)TEXAS RED™	104
3.1 INTRODUCTION	104
3.2 MATERIALS	109
3.2.1 General chemicals and instrumentation	109
3.3 METHODS.....	110
3.3.1 Reconstitution of BSA Texas Red™ conjugate in RNase free water.	110
3.3.2 Phosphate buffered saline pH 7.4	110
3.3.3 Preparation of PEG in PBS	110
3.3.4 Preparation of PBS/PEG/PEI	110
3.3.5 Preparation of BSA Texas Red™ conjugate in PBS	111
3.3.6 Commercial IONPs in PBS/PEG/PEI	112
3.3.7 Fluorescence of pre-suspended and powdered CIONPs	112
3.3.8 Powdered commercial IONPs in PBS/PEG/PEI	113
3.4 RESULTS AND DISCUSSION	114
3.4.1 Fluorescence of BSA Texas Red™ in PBS solution	114
3.4.2 BSA Texas Red™ conjugate in PBS.....	118
3.4.3 Fluorescence of BSA Texas Red™ in PBS/PEG solution.....	124
3.4.4 Effect of pre-suspended CIONPs on fluorescence of BSA Texas Red™ conjugate in PBS/PEG/PEI solution.....	128
3.4.5 Powdered CIONPs effect on fluorescence	129
3.5 CONCLUSIONS.....	132
4 ENCAPSULATION OF TEX 615-siRNA TO CIONPs IN PBS/PEG/PEI AND RELEASE IN PBS	135
4.1 INTRODUCTION	135
4.2 MATERIALS	140
4.2.1 General chemical and instrumentation	140

4.3 METHODS.....	141
4.3.1 Optimisation of loading of TEX 615-siRNA to CIONPs.....	141
4.3.2 Release of TEX 615-siRNA from CIONPs.....	143
4.4 RESULTS AND DISCUSSION	146
4.4.1 Attachment of TEX 615-siRNA to CIONPs.....	146
4.4.2 Release of TEX 615-siRNA from CIONPs.....	153
4.5 CONCLUSIONS.....	159
5 FINAL CONCLUSIONS AND RECOMMENDATIONS FOR FURTHER WORK.....	162
5.1 FINAL CONCLUSIONS	162
5.2 LIMITATIONS	163
5.3 FURTHER WORK.....	164
REFERENCES.....	167
APPENDICES	209
Appendix A : Poster presentations 2019.....	209
Appendix B : Presentation at University of Columbia 2019.....	212
Appendix C : DektakXT measurements	213
Appendix D : Cranfield Doctoral Network Conference 2020	216
Appendix E : Published paper 2021	218

LIST OF FIGURES

Figure 1-1: Cancer cases (World Health Organisation Factsheet, 2018).	1
Figure 1-2: Prostate glands (https://www.Menshormonalhealth.Com/Pictures-of-Prostate-Cancer (Accessed December, 2018)	4
Figure 1-3: Theranostic nanoparticle (Gobbo et al., 2015).	13
Figure 1-4: Gene silencing mechanism in siRNA (Wang et al., 2010).	14
Figure 1-5: Polyethylene glycol	17
Figure 1-6: Polyethyleneimine- Linear (A), branched (B) and dendrimeric (C). ..	18
Figure 1-7: Adapted from NanoGen Trio (www.mantisdeposition.com , 2019)..	29
Figure 1-8: The two main sections of the experimental work and Chapters	33
Figure 2-1: Mantis (mantisdeposition.com/nanoparticlegenerators , 2019).	36
Figure 2-2: Plasma Cleaner prior to loading silicon wafer (Diener, 2022).	42
Figure 2-3: The spin coater used for coating the silicon wafer with PEG	42
Figure 2-4: Drying PEG-coated wafers on a hot plate	43
Figure 2-5: Contact angle measurements set up.....	44
Figure 2-6: Scratch depth of PEG on silicon wafer.....	45
Figure 2-7: Three magnetron heads on Mantis NanoGen Trio	46
Figure 2-8: Agglomeration chamber	47
Figure 2-9: Mantis NanoGen Trio coupled to SVS main chamber.....	48
Figure 2-10: Generation of IONPs by inert gas condensation	50
Figure 2-11: MesoQ Controller display panel	51
Figure 2-12: Nanoparticle filtration (www.mantisdeposition.com , 2019).....	52
Figure 2-13: Scientific Vacuum Systems display panel.....	53
Figure 2-14: PEG-IONPs in RNase free water stored in a labelled container .	56
Figure 2-15: Plasma removal of TEM grids from the lining.....	57
Figure 2-16: Glo plasma discharge to clean in-house TEM grids.....	58
Figure 2-17: The drop of sputtered IONPs on the TEM grid.....	58
Figure 2-18: Transmission electron microscope.....	59
Figure 2-19: Dynamic light scattering (Malvern Panalytical Ltd., 2022).....	61

Figure 2-20: NanoSight LM20 (Nanoparticle Tracking Analysis, 2021).	62
Figure 2-21: Contact angle measurements	65
Figure 2-22: DektakXT profiler measurements.....	66
Figure 2-23: Spectral evolution graphs from IONPs sputtering	68
Figure 2-24: Spectral evolution graphs from low power sputtering (A) and high- power sputtering (B).	70
Figure 2-25: Effect of argon flow (30-100 sccm) on spectra evolution graph ...	72
Figure 2-26: Worn vacuum seal	75
Figure 2-27: Broken iron oxide target.....	75
Figure 2-28: Target holders before (A) cleaned after sputtering (B).	76
Figure 2-29: Bare TEM grid.....	79
Figure 2-30: PEG coated IONPs dried on the TEM grid.....	80
Figure 2-31: Sputtered IONPs directly on the TEM grid.	81
Figure 2-32: Soft-landed sputtered IONPs on a PEG-coated TEM grid.	81
Figure 2-33: AFM of bare silicon wafer (A) and PEG-IONPs on the substrate (B).	84
Figure 2-34: Dynamic light scattering of free standing IONPs in PEG Vs PEG alone (A), concentrated PEG-IONPs solution (B) and concentrated PEG solution (C), as control. Averaged signal as well as individual runs are depicted (Hemben et al., 2021).	87
Figure 2-35: DLS correlograms and cumulative fits (insets) for PEG-IONP(A) and PEG only (B) samples	89
Figure 2-36: NTA analysis of sputtered IONPs (Hemben et al., 2021).	90
Figure 2-37: Nanoparticle Tracking Analysis CIONP 0.001 mg/mL (A), CIONP 0.01 mg/mL (B), CIONP 0.1 mg/mL (C) and average measurements (D). 93	
Figure 2-38: Regression curve depicting CIONPs concentration	95
Figure 2-39: MRI plot of sputtered IONPs (A, B).	98
Figure 3-1: Texas Red dye chemical structure A) Texas Red B) Sulforhodamine 101 (Aldrich, 2021).	106
Figure 3-2: Fluorescence spectra (excitation in blue and emission in red) for BSA Texas Red™ conjugate (Thermofisher.com, 2019).	107
Figure 3-3: Varioskan plate reader used to read fluorescence of solution of BSA Texas Red™ conjugate at different concentrations and incubation time. 112	

Figure 3-4: Branson ultrasonication of CIONPs in PBS/PEG/PEI	113
Figure 3-5: Fluorescence values for 1.5 µg/mL of BSA Texas Red™ conjugate when varying the testing conditions.....	115
Figure 3-6: Calibration curve for BSA Texas Red™ conjugate obtained with excitation fixed at 590 nm and emission at 615 nm.	116
Figure 3-7: BSA Texas Red™ conjugate excitation and emission scans for 10 µg/mL BSA Texas Red prepared in PBS.....	117
Figure 3-8: Effect of pH signals on BSA Texas Red™ conjugate (10 µg/mL).	118
Figure 3-9: Fluorescence emission of BSA Texas Red™ conjugate in PBS at 0 minutes and 60 minutes of incubation.	121
Figure 3-10: Fluorescence emission of Lower concentrations of BSA Texas Red™ conjugate (0.5-2.5 µg/mL).	123
Figure 3-11: Fluorescence emission of BSA Texas Red™ conjugate in the presence PBS/PEG at 0 minutes and 60 minutes.	126
Figure 3-12: Fluorescence emission of BSA Texas Red™ conjugate (2.5 µg/mL) in PBS/PEG 5.5, 6.2, 7, 7.4 and 7.6.	127
Figure 3-13: Fluorescence signal of Pre-suspended CIONPs (1 mg/mL) in BSA Texas Red™ conjugate in PBS/PEG/PEI.....	128
Figure 3-14: Pre-suspended CIONPs (A) powdered CIONPs (B) magnetic behaviour when extracted on an Eppendorf magnetic sample holder.	129
Figure 3-15: Fluorescence emissions obtained for PBS, PBS/PEG/PEI, PBS/PEG/PEI/IONP and PBS/PEG/PEI/IONPTEX 615 at pH 5.5 and 7.4	130
Figure 3-16: Fluorescence signal of BSA Texas Red™ conjugate in the presence of CIONPs (1 mg/mL) prepared in PBS/PEG/PEI (pH 5.5 and 7.4).....	132
Figure 4-1: Types of RNA (Inamura, 2017).	139
Figure 4-2: Extracted CIONPs from PBS/PEG/PEI/CIONPs/siRNA samples (A) Supernatant removed revealing only CIONPs out of solution (B) PBS added to resuspend CIONPs for siRNA release experiments (C).	144
Figure 4-3: Fluorescence emission of TEX 615-siRNA at pH 5.5 (A) and 7.4 (B) in presence of CIONPs up to 60 minutes incubation.	147
Figure 4-4: Example of relative fluorescence values obtained when testing the attachment of TEX 615-siRNA to CIONPs in nanocarrier complex.	149
Figure 4-5: Attachment of TEX 615-siRNA to CIONPs.....	151
Figure 4-6: Percentage of TEX 615-siRNA attached to CIONPs.....	152

Figure 4-7: Release of siRNA (%) from CIONPs in PBS pH 6.4.....	153
Figure 4-8: Release of siRNA (%) from CIONPs in PBS pH 7.4.....	154
Figure 4-9: Release (%) of TEX 615-siRNA in PBS with pH 7.4 and 6.4.	155

LIST OF TABLES

Table 1-1: Some nanoparticles production methods	27
Table 2-1: Sputtering parameters.....	54
Table 2-2: Process parameters	55
Table 2-3: Optimisation of sputtering process parameters	71
Table 2-4: Points to derive regression curve of concentration of CIONPs.....	94
Table 3-1: BSA conjugates (Adapted from Molecular Probes, 2005)	105
Table 3-2: Excitation and Emission wavelengths of BSA Texas Red in PBS .	114
Table 4-1: Powdered commercial IONP (CIONP) nanocarrier complex	142
Table 4-2: Conditions tested for the optimisation of PEG/PEI ratio using 0.1 mg/mL CIONP and 2 μ M TEX 615 -siRNA	143

LIST OF EQUATIONS

Equation 2-1: Stoke-Einstein equation	96
---	----

LIST OF ABBREVIATIONS

AFM	Atomic Force Microscopy
BSA	Bovine Serum Albumin
CIONPs	Commercial Iron Oxide Nanoparticles
DC	Direct Current
DLS	Dynamic Light Scattering
DNA	Deoxyribo Nucleic Acid
DOX	Doxorubicin
DRE	Direct Rectal Examination
ELISA	Enzyme Linked Immunosorbent Assay
EE	Encapsulation Efficiency
EPR	Enhanced Permeability Receptor
ENI	Epigenetic Non / Coding Interactive
FDA	Food And Drug Administration
HEPA	High Efficiency Particulate Air
HNK-1	Human Natural Killer
HPLC	High Power Liquid Chromatography
HV	High Voltage
lncRNA	Long Coding Ribo Nucleic Acid
IGC	Inert Gas Condensation
IONP	Iron Oxide Nanoparticle
LE	Loading Efficiency
LEU	Leucine
LNRNA	Long Non-Coding Ribo Nucleic Acid
MIAT	Myocardial Infarction Associated Transcript
MiRNA	Micro Ribo Nucleic Acid
MNP	Magnetic Nanoparticle
MPI	Magnetic Particle Imaging
MRI	Magnetic Resonance Imaging
MRNA	Messenger Ribo Nucleic Acid
NCAM	Neural Adhesion Molecules
NCRNA	Non-Coding Ribonucleic Acid
NDD	Nanoparticle Drug Delivery
NEC	Neuroendocrine Cell
NEPC	Neuroendocrine Prostate Cancer

NMR	Nuclear Magnetic Resonance
NPs	Nanoparticles
NSE	Neuron Specific Enolase
NTA	Nanoparticle Tracking Analysis
PCa	Prostate Cancer
PEG	Polyethylene Glycol
PEI	Polyethyleneimine
PHI	Prostate Health Index
PIRNA	Piwi-Interacting Ribo Nucleic Acid
PLA	Poly Lactic Co-Glycolic Acid
PSA	Prostate Specific Antigen
PVD	Physical Vapour Deposition
RAB 3	Ras Related Protein 3
RF	Radio Frequency
RISC	Ribo Nuclei Acid Induced Silencing Complex
RLT	Radioligand Therapy
RRNA	Ribosomal Ribo Nucleic Acid
SNARE 25	Snap Receptor 25
SNAP	Synaptosomal Associated Protein
QDOTS	Quantum Dots
shRNA	Short Hairpin Ribo Nucleic Acid
SiRNA	Small Interfering Ribo Nucleic Acid
SNRNA	Small Nuclear Ribo Nucleic Acid
SPION	Super Paramagnetic Iron Oxide Nanoparticles
SVS	Scientific Vacuum Systems
SV2	Synaptic Vesicle
TEM	Transmission Electron Microscope
TRNA	Transfer Ribonucleic Acid
TRUS	Transrectal Ultrasound
USPIONP	Ultra-Super Paramagnetic Iron Oxide Nanoparticles
VAMP	Vesicle Associated Membrane Proteins
VMAT	Vesicular Monoamine Transporters
WD	Working Distance
WHO	World Health Organisation

1 INTRODUCTION AND LITERATURE REVIEW

1.1 INTRODUCTION

Cancer is commonly used nomenclature referring to a vast number of ailments in most areas of the body. They can also be said to be aggressive or non-aggressive, disease-causing agents (Hanahan & Weinberg, 2011). There are six biological phenomena during growth of human neoplasms: proliferative signalling, evading growth suppressor resisting cell death, enabling replicative immortality, inducing angiogenesis and activation, invasion and metastasis (Hanahan and Weinberg, 2011). These cancers are known to be quick-generating entities, spreading profusely to other parts of the body which may or may not be in close proximity to the disease origin.

Metastases are the primary cause of death from cancer (Ferlay et al., 2020). After cardiovascular diseases cancers are globally the main cause of mortality; and in 2021 were responsible for approximately 9.6 million deaths. These are comparable to figures reported by the World Health Organisation (WHO) for cancer cases worldwide (Figure 1-1).

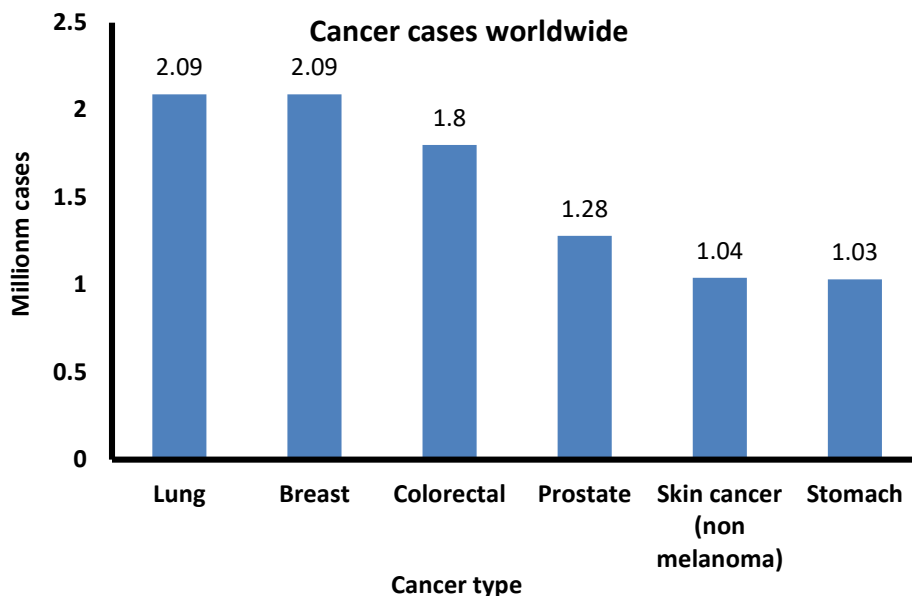


Figure 1-1: Cancer cases (World Health Organisation Factsheet, 2018).

Further reports state that the leading cause of global mortality is cancer, which accounts for approximately 10 million deaths in 2020 or nearly one in six deaths (WHO, 2022). Recent data show the most common cancers are breast, lung, colon and rectum and prostate cancers (WHO, 2022). It is reported that nearly one-third of deaths due to cancer are related to tobacco use, elevated body mass index, alcohol consumption, low fruit and vegetable dietary intake and the lack of adequate physical activity.

Over the past few decades, progress in cancer research has enriched areas in medicine related to nanotechnology. Many of the common treatments and management strategies for cancer, namely surgery, radiation therapy, and chemotherapy have not evolved significantly (DeVita and Chu, 2008). One of the most challenging aspects for these treatments is the tendency for tumours to metastasise after recording tumour shrinkage. Malignant tumours are complex (Hanahan and Weinberg, 2011). This phenotypic diversity leads to potential for sub-populations of cancer cells to resist a single mode of therapy and give rise to a drug-resistant tumour (Sumer and Gao, 2008). Thus, more specific and potent classes of treatment or combinations of treatments capable of destroying patient cancerous cells are required (Marusyk and Polyak, 2010).

Nano pharmacology and nano diagnostics are the main avenues for designing disease treatments. These treatments combine selective drug delivery and release to the diseased cells and also monitor patient's response to treatment (Akhtar et al., 2011). Multifunctional drug carriers (nanocarriers) used for theranostics (a combination of therapy and diagnostic) can be prepared by functionalising iron oxide nanoparticles (IONPs) (Li et al., 2017). Drug therapy used commonly for cancer is associated with severe secondary effects on healthy tissues, which could be minimised with more efficient and targeted drug delivery. Recently, gene therapy has gained attention as being a powerful treatment for certain types of cancer. Nucleic acids are equipped to target specific genes and can change pathological protein expression, slowing down or stopping altogether

the proliferation of cancer cells. The symptoms of the disease thereby diminish (Moghimi et al., 2005). The main advantage of nanocarriers is their potential for multi-functionality, which can enable payloading of therapeutic drugs as well as affinity ligands, to guide the nanocarrier to the cancer site, and imaging moieties within a single nanoparticle (NP) vehicle, permitting an enhanced targeted and tagged drug delivery (Probst et al., 2013). Therefore, nanomedicine could help in addressing the challenges linked to tumour heterogeneity and could help in reducing the adaptive resistance to therapy (Probst et al., 2013). This work focuses on the production of free-standing, soft-landed iron oxide nanoparticles (IONPs) by inert gas condensation technique, to develop a nanocarrier with potential for targeted drug delivery of a therapeutic agent silencer RNA (siRNA) to neuroendocrine prostate cancer cells. The anti-cancer agent will be attached to IONPs within a polymer to prevent destruction by the body's enzymes before the drug is delivered to the cancer cells. The targeted drug delivery of siRNA to cancer cells will help side-step the unfavourable response to side effects to healthy tissues from the more commonly used cancer treatment methods of chemotherapy and radiotherapy. siRNA has been used in combination with radiotherapy to investigate treatment of cancer (Qizhen et al., 2006).

1.2 PROSTATE CANCER

The prostate gland located in the pelvis in males is not normally a large structure, surrounding the urethra (Sikora, 1998). A healthy prostate gland secretes a thick mucoid substance.

The normal human prostate is known to be a tubular-alveolar gland made of distinct, glandular regions. The glandular region is composed of ducts and acini or cells. The non-glandular region comprises pre-prostatic sphincter, fibromuscular stroma, capsules and supplying blood vessels and nerves. The stromal compartment contains cells, nerves, fibroblasts, infiltrating lymphocytes and macrophages, endothelial and smooth muscle cells.

Prostate cancer is the second most common cancer found in males and has been known to be a slowly developing ailment that progresses for several years

unnoticed. Images of normal and cancerous prostate tissue are presented in Figure 1-2.

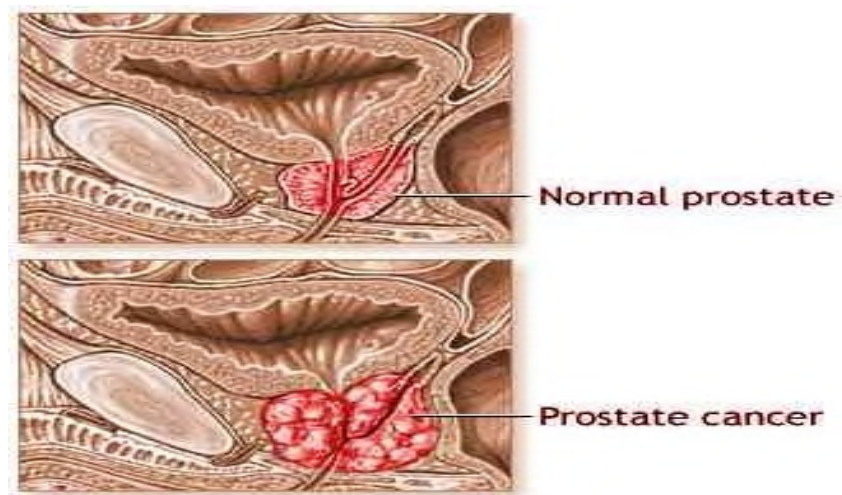


Figure 1-2: Prostate glands (<https://www.Menshormonalhealth.Com/Pictures-of-Prostate-Cancer> (Accessed December, 2018))

Prostate cancer is so stealthy, and may be the reason ‘new’ tumours are discovered in as many as 30% of men between the ages of 30 and 60 years and as many as 45–75% of men between 60 and 80 years (Powell et al., 2010; Zlotta et al., 2013). According to research, cigarette smoking, particularly heavy smoking, increases the risk of prostate cancer (Moreira et al., 2014). Drugs and chemoprevention in addition to dietary changes have not recorded much success, despite smoking cessation. Dietary supplements, especially vegetable and soy extracts have limited preventive effect (Bosland et al., 2015).

20 countries well known for high incidence rates of fatal prostate cancer are Guadeloupe (France), Martinique (France), Ireland, Barbados, Estonia, Norway, Sweden, Puerto Rico, France (Metropolitan), New Caledonia (Guiana), New Zealand, Czech Republic, Bahamas, Australia, UK, Latvia, Slovenia, Luxembourg and Switzerland (Bray et al., 2018). Mmetastatic PCa remains fatal (Wu et al., 2014).

1.2.1 Prostate cancer diagnosis

Current methods for diagnosis of prostate cancer include magnetic resonance imaging (MRI) scan following raised prostate specific antigen (PSA) levels detected via a blood test (Sikora, 1998). PSA above 4 ng/mL may indicate increased risk of prostate cancer, however, most men with elevated PSA do not have prostate cancer. The main diagnostic tools to diagnose PCa include direct rectal examination (DRE), serum concentration of PSA, and transrectal ultrasound (TRUS)–guided biopsies. In about 18% of all patients, PCa is detected by a suspect DRE alone, irrespective of the PSA level (Gustavo et al., 1999). A suspect DRE in patients with a PSA level of up to 2 ng/mL has a positive predictive value of 5–30% (Loeb and Catalona, 2009).

The Prostate Health Index (*phi*) is commercialised by Beckman Coulter Inc. and is a U.S. Food & Drug Administration (FDA) approved blood test used as an aid in distinguishing prostate cancer from benign prostatic conditions (Loeb et al., 2015; Beckman Coulter Inc., 2021). Studies report a relationship between pro PSA and prostate cancer (PCa) (Song et al., 2021).

The prostate health index (*phi*) test outperforms PSA alone (Tosoian et al., 2017) and has 90% clinical sensitivity and 31% specificity at a *phi* value of 27.0 allowing for a reduction of nearly 1/3 of all biopsies while detecting 90% of cancers (Beckman Coulter Inc., 2021).

1.2.2 Treatment of prostate cancer

Treatments for metastatic prostate cancer include androgen-ablation therapy which was used at the start of a new era of prostate cancer therapy. Hormone treatment with oral estrogens has been used in medical castration, the first systemic treatment of any cancer. Regarding prostate cancer, however, androgen ablation is currently the most generally useful therapeutic approach (Corbett et al., 2021).

In 1941, Huggins and Clarence Hodges measured serum acid-phosphatase levels to assess prostate size and therapeutic efficacy and determined that

prostatic cancer is affected by the presence of androgen. The removal of androgens prevents the spread of prostate carcinoma by castration or neutralisation of their activity by oestrogen injection (Corbett et al., 2021).

More recently, progress has been made in the surgical and radiological techniques used in treating localised prostate cancer. Surgical removal of the prostate was initially performed to alleviate the signs and symptoms due to retention of urine. Reports using radiation to treat localised prostate cancer were on the introduction of radium sources into the urethra and rectum as a palliative option, replacing surgery. Later, growth of the tumour was controlled by insertion of radium via needles into the prostate gland through the perineum, the rectum, or the open bladder.

In the 1970s, Willet Whitmore described Brachytherapy, a form of radiotherapy and an open implant technique using the ^{125}I radioisotope of iodine (Corbett et al., 2021). The isotope was sealed in small titanium cylinders and introduced into the prostate. No imaging instruments were used for this procedure and very often there were instances of uneven dose distributions with some areas receiving excessive amounts of radiation while others received less than optimal amounts. This led to serious complications and a high rate of local failure thus there was reduced use of Brachytherapy until 1983. Brachytherapy is now commonly used for treating localised prostate cancer, in which a therapeutic radioisotope is administered directly into the body in the region of the cancer, in order to destroy the cancer cells. Studies have shown the beneficial effects of combining androgen-ablation therapy with radiation, improving times of relapse-free and overall survival.

Some patients seem to benefit from androgen ablative therapy though eventually develop fatal androgen-independent malaise. This led to research on cytotoxic chemotherapy as a treatment for hormone refractory prostate cancer, involving interactions between diet (Imir et al., 2021), environmental exposure (Vigneswaran et al., 2021), inherited susceptibility (Maxwell et al., 2021), and ageing (Lim, 2021). As a result, different methods have been developed for

preventing the progression of life-changing or otherwise fatal prostate cancer. These include dietary and chemoprevention approaches to lower the risk of clinical prostate cancer development. Furthermore, due to serum PSA screening and improved biopsy techniques, most cases of prostate cancer will be detected early and therefore will be treatable by commonly used surgical or radiological techniques. Results from recent trials show significant progress is still needed in non-androgen-ablative approaches, especially for use in the treatment of androgen-independent prostate cancer. Several being trialled are PSA-activated prodrugs (Pereira et al., 2022), which after administration, is converted or metabolised within the body, into a pharmacologically active drug. Instead of administering a drug directly, a corresponding prodrug can be used to improve how the drug is absorbed, distributed, metabolised and excreted. Anti-angiogenic agents (Ioannidou et al., 2021) are also used in targeted therapy by preventing the formation of new blood vessels. Prevention of the formation of new blood vessels arising from pre-existing blood vessels helps reduce the spread of cancer cells, especially in the immediate environment of the cancer cells where angiogenic agents are known to be high. Targeted gene-therapy (Gregg and Thompson, 2021) approach has also been developed to activate the immune system to recognise prostate cancer cells. Targeted therapy or molecularly targeted therapy in addition to hormonal therapy and cytotoxic chemotherapy forms a family of modern medical cancer treatments. Targeted therapy disrupts cancer cell development by interfering with specific targeted molecules which are required for the formation of new cancer cells and their proliferation. The blocking of cancer cell development is utilised rather than simply interfering with all rapidly dividing cells.

Surgical removal of the tumour is the treatment of choice for low- and intermediate-risk localised prostate cancer; also for some patients with high-risk localised disease (Heidenreich et al., 2011). However, surgical removal of cancer tissue remains challenging (Ferlay et al., 2010) and can lead to complications like nerve damage that may cause debilitating, functional side effects of urinary incontinence and erectile dysfunction. With surgical removal of the tumour there

is the risk that all the tumour may not be removed and the chances of recurrence may increase (Alberts et al., 2021). Hormone and radiotherapeutic methods are used to treat cancers in the locality (Sine et al., 2021).

1.2.3 Neuroendocrine prostate cancer (NEPC)

Neuroendocrine prostate cancer is a rare (less than 2% of prostate cancers) form of cancer that has been known to arise following previous treatment of prostate cancer (Neuroendocrine Prostate Cancer, 2022). It is also linked to nutrition and smoking habits and has been known to linger for years in a patient, unnoticed. The actual cause of NEPC is not known, though healthy lifestyle is advised such as taking regular exercise and consuming alcohol in moderation. These may help prevent occurrence. As most endocrine cancers do not run in families, it is recommended that personal medical history be examined as some rare conditions may predispose the individual to NEPC (Neuroendocrine Prostate Cancer, 2022). Neuroendocrine cells (NEC) are cells that receive neuronal information and relay these neuronal messages into the circulatory system. The neuroendocrine cells thereby team up the nervous and endocrine systems in a process termed neuroendocrine integration. Neuroendocrine cells occur throughout the body and work as a network, transmitting messages across various organs and systems, while helping to regulate the secretion of chemical substances such as hormones or peptides to keep the body systems functioning optimally (Corbett et al., 2021). Depending on the location in the body, the neuroendocrine cells can regulate sleep, digestion, breathing or heart rate and as such cancer of the neuroendocrine system can present with some or no symptoms of disease.

In terms of the prostate, neuroendocrine cells are found spread out in the epithelial compartment of the prostate gland. The cell membrane is composed of multiple stem cell units (Isaacs and Coffey, 1989; Bonkhoff et al., 1994; Ung, 1998; Van Leenders et al., 2000; Hudson et al., 2000) where the stem cell is unlimited in its self-renewal capacity but only rarely proliferates to provide progeny that differentiate to become either transit-amplifying or neuroendocrine

cells (Bonkhoff et al., 1994). Epigenetic / non-coding interactome (ENI) plays a crucial role in NEPC development and progression. It was postulated that some long non-coding RNAs (lncRNAs) are implicated in NEPC initiation (onco-suppressor gene silencing) and progression (acquisition of metastatic and drug resistance potential). It was however found that myocardial infarction associated transcript (MIAT) expression, (responsible for heart attack) is restricted to a small percentage of prostate cancers (PCas), with high metastatic potential, poor prognosis and frequent mutations. Altered expression of this gene locus has been associated with heart attack. All these are descriptive of NEPC (Tan et al., 2014; Lugnani et al., 2015) and there are strong indications that MIAT transcripts in NEPC occur mainly in the tumour cell nucleus. NEPC show histological similarities to other neuroendocrine tumours throughout the body depending on histological subtype (Schron et al., 1984; Ro et al., 1987; Nadal et al., 2014). NEPC is incurable, and identification of viable therapeutic targets is of paramount importance (Crea et al., 2016).

1.2.4 Detection of neuroendocrine prostate cancer

Neuroendocrine prostate cancer is detectable by extensive staining of NEC biomarker (e.g. chromogranin and synaptophysin) and microscopic examination of the affected tissue (Parimi et al., 2014). Neuroendocrine carcinoma may not be detected as accurately by prostate specific antigen (PSA) as adenocarcinoma of the prostate, because some forms do not secrete PSA. In prostate cancer for example, PSA may not be highly expressed in a patient who has a malignant tumour. Also, some PSA may be found in cases where no tumour exists.

In clinical practice or research, markers are used to determine neuroendocrine differentiation. Typical neuroendocrine markers used in clinical practice to elucidate neuroendocrine (NE) cells are chromogranin, synaptophysin, neuron specific enolase (NSE), and CD56. Neuron specific enolase (NSE) is considered a generic marker for both neurons and NE cells (Schmechel, 1978) and although it has high sensitivity, its specificity is low (Seshi et al., 1988). Chromogranin is a

specific NEC marker as it is one of the common constituents of NEC secretory granules.

Other NEC markers have been reported, although they are not typically used in clinical practice. They include the SNARE (SNAP-Receptor) family of proteins involved in vesicle fusion; SNARE Cytochrome b561 (Winkler and Westhead, 1980), (Chromomembrin B) and synaptic vesicle elements include synaptophysin (Wiedenmann et al., 1986 ; Gould et al., 1986), synaptic vesicle protein 2 (SV2) (Portela-gomes et al., 2000; Nilsson et al., 2004), vesicular monoamine transporters (VMAT) (Rindi et al., 2000), SNARE complex (Elfennk and Scheller,1993), (synaptobrevin, syntaxin and SNAP-25), Rab3 (Tahara et al., 1999) and vesicle associated membrane proteins (VAMP) (Regazzi et al., 1995; Braun et al., 1994). SNARE proteins are involved in the regulation of cancer cell invasion (Gorshtein et al., 2021), chemo-resistance (Qian et al., 2021), the transportation of autocrine and paracrine factors (Qian et al., 2021), autophagy (Kimura et al., 2017), apoptosis and the phosphorylation of kinases essential for cancer cell biogenesis (Meng and Wang, 2015). Furthermore, some unique lympho-reticular antigens expressed by NEC such as CD57 (Seeger et al., 1982; Lipinski et al., 1983; Tischler et al., 1986; (Leu 7 HNK-1) and neural cell adhesion molecules (NCAM) are known for their role in cell to cell recognition, migration, differentiation and proliferation of prostatic adenocarcinoma cells through paracrine effect (Qian et al., 2021).

Neuroendocrine markers commonly used in clinical practice include Chromogranin, Synaptophysin Neuron specific enolase CD56. Cytochrome b561, Synaptic vesicle, protein 2 (SV2), Vesicular monoamine transporters (VMAT), Synaptobrevin, Syntaxin, SNAP-25, Rab3 Vesicle associated membrane proteins are not used for clinical detection. The biomarkers for different cancers differ in their expression.

Magnetic nanoparticles (MNPs) have been found highly applicable and versatile in lithium ion batteries (Koo, et al., 2012) supercapacitors (Xuan et al., 2009) catalysis, (Lin et al., 2013) labelling and sorting of cells (Chemla et al., 2000), the

separation of biochemical products (Ugelstad et al., 1987) also as diagnostic magnetic resonance imaging (MRI) (Kim et al., 2008) thermal therapy (Cheng et al., 2005 ; Kim et al., 2006) and drug delivery (Ankerhold, 2013) by conjugating iron oxide nanoparticles to contrast agents (Li et al., 2013; Khaleghi et al., 2016), and several methods for enhancing picture quality (Chen et al., 2015).

1.2.5 Treatment of neuroendocrine prostate cancer

Over the years, chemotherapy, radiotherapy and surgical removal of the tumour have been NEPC treatment options, though not all the treatment options have been suitable for every single NEPC tumour presentation. Different cases have different levels of success as factors including individual response to treatment type and stage of the cancer are taken into consideration. Some cases are inoperable while others opt for management as far as possible without direct treatment. NEPC can be treated, however, with careful patient selection in relation to response to treatment type, Radioligand (RLT) therapy is a promising treatment option. With RLT, alpha, beta or electron ray emitting radiopharmaceuticals attach to specific receptors or antigen on the tumour cell surface and impose a well-placed inhibitory effect on the tumour cells with a limited amount of negative impact on the patient (Puranik et al., 2021).

The success rate for NEPC treatments varies with individuals, as NEPC cases seem to form a heterogeneous group requiring tailored approaches to specific, individual responses and needs. Hence there is a growing need for the treatment and management of NEPC.

1.3 SMALL INTERFERING RNA AS A THERANOSTIC AGENT

Small interfering RNA (siRNA) also called short interfering RNA or silencer RNA (Grimm, 2009), is a class of double-stranded RNA (DsRNA) molecules, 20-25 base pairs in length. siRNA transfection is a powerful tool used to understand the mechanisms of gene regulation and molecular pathways when a fluorescent molecule is attached to siRNA. siRNA known for its property of inhibiting protein synthesis has the potential to destroy cancer cells (Cao et al., 2021). siRNA is

introduced to tumour cells when encapsulated in a polymer like polyethylene glycol (PEG). The chemistry of siRNA-based targeted gene silencing may allow for development of gene-specific drugs against certain genes that are otherwise difficult to manipulate (Jiang et al., 2021). Furthermore, siRNA suppresses oncogene factors in prostate cancer (Ashrafizadeh et al., 2020) though it has been known to elicit non target immune response (Oh & Gwan, 2009).

Very recently, molecular agents like DNA and short-interfering RNA (siRNA) have been used for investigating gene function and have made remarkable breakthrough in the area of cancer research (Oh and Gwan, 2009). Rapid clearance from the body has however been a major challenge in the use of gene therapies (Davis, 2002; McCaffrey et al., 2002 ; Lewis et al., 2002 ; Song et al., 2003). Small interfering RNAs (siRNAs) have also been shown to be more potent than conventional antisense strategies (Miyagishi, 2004; Beale et al., 2008; Khan et al., 2008). Earlier research has demonstrated use of antisense oligonucleotides, beneficial in chemical modification of siRNA (Layzer et al., 2004; Allerson et al., 2005; Antonin et al., 2005; Choung et al., 2006; Derfus et al., 2007).

Common nanomaterials explored for biomedical applications include cyclodextrin nanoparticles (Krauland and Alonso, 2007), liposomes (Bozzuto and Molinari, 2015), polymeric micelles (Wang et al., 2014), quantum dots (Wagner et al., 2019), silica (Vallet-Regí et al., 2018), gold nanoparticles (Sztandera et al., 2019) and ferric oxide nanoparticles (Ma et al., 2012).

Magnetic nanoparticles are affected by magnetic fields producing an energy relay effect called magnetic hysteresis; known as the lag in properties of a material in relation to its history (Huang and Hainfeld, 2013). Theranostic particles which are defined as particles with both diagnostic and therapeutic properties have potential for molecular drug delivery to carcinomas (Figure 1-3).

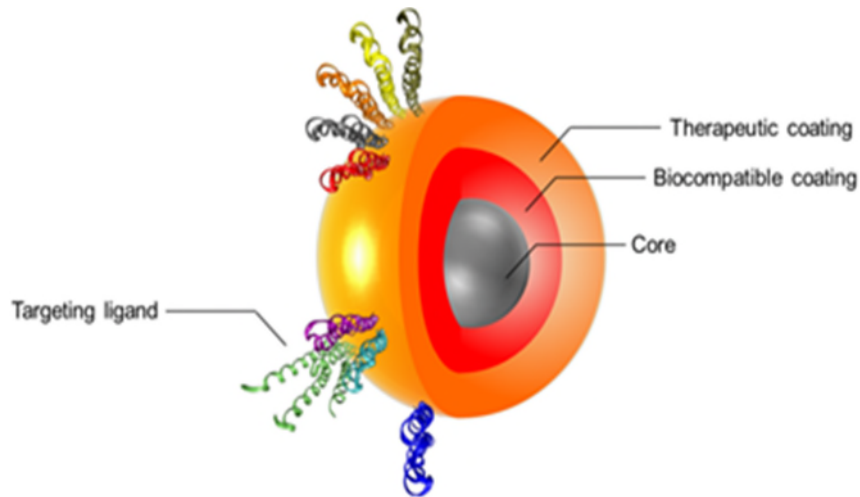


Figure 1-3: Theranostic nanoparticle (Gobbo et al., 2015).

The theranostic particle is a much-desired outcome of nano technological application in biomedical science. It is hoped that a particle will be produced, upon which medication can be applied for conveyance to a target tumour. Theranostic agents involving siRNA are being investigated for potential use in drug delivery to cancer cells (Sioud, 2003; Sørensen et al., 2003; Seton-Rogers, 2012; Jiang et al., 2021) in which the synthesis of proteins is inhibited. Disruption of the process of protein synthesis has been used to block gene expression in infectious diseases and cancers. siRNA has been investigated as a cancer fighting agent via vehicular delivery to cancer cells., involving the gene silencing mechanism (Figure 1-4).

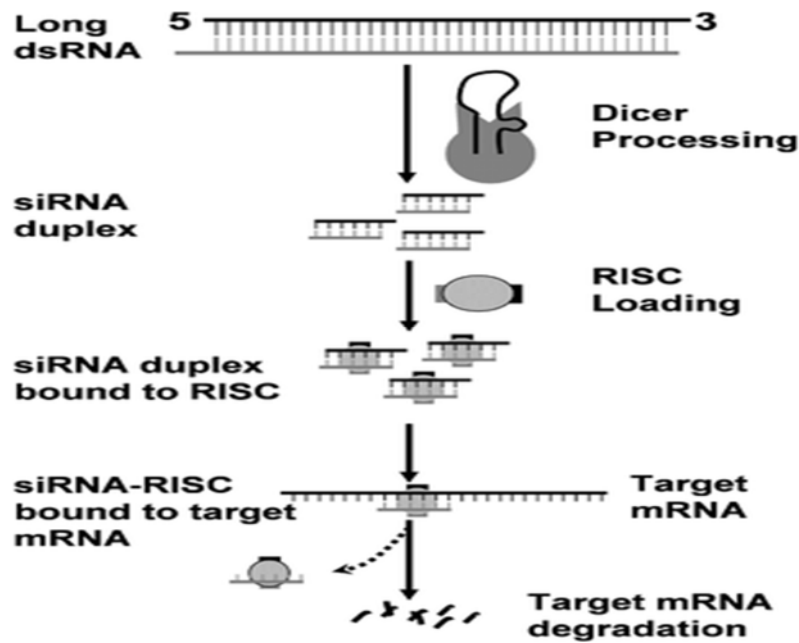


Figure 1-4: Gene silencing mechanism in siRNA (Wang et al., 2010).

In the process of gene silencing the dicer cleaves the long double stranded RNA into shorter lengths. The siRNA is then bound to RNA-induced silencing complex (RISC). RISC is made up of one strand of siRNA which cleaves to complementary messenger RNA (mRNA). Finally, the siRNA – RISC bound to target mRNA undergoes degradation to release RISC.

1.3.1 Drug delivery by nanoparticles

Nanoparticles for drug delivery is an emerging method to overcome therapeutic challenges and trace the biochemical pathway (Probst et al., 2013; Akhter et al., 2013). Recently, the use of targeted drug delivery for the treatment of cancers reduced the exposure of patients to harmful irradiation and limited the negative side effects. The small size of the nanoparticles used as carriers enabled them for inter-cellular diffusion (Vauthier and Labarre, 2008). It has been shown that PEGylated nanoparticles are higher in uptake in the size of 10 nm. Super-paramagnetic and magnetic nanoparticles have recognised advantages in targeted drug delivery and other biomedical utilisation (Allen and Cullis, 2004; Prabakaran and Mano, 2008). Iron oxide nanoparticles are regularly surface

engineered to suit the framework of biomedical application (Long et al., 2013; Qiu et al., 2017). Superparamagnetic iron oxide nanoparticles (SPIONs) <100 nm, with high magnetisation and appropriate surface chemistry are constantly being researched because of their suitability for many *in-vivo* investigations (Gupta and Gupta, 2005; Lee et al., 2007).

Nanoparticles serve to sheath the siRNAs for prolonged blood circulation. Nanoparticles are adept at utilising ligand–receptor binding relationships to interact with biological entities via the enhanced permeability and retention (EPR) effect (Shi et al., 2017). EPR is understood to be the characteristic by which different sized molecules preferentially aggregate in healthy tissues. The abnormal molecular and fluid transport dynamics of EPR assist the cancer cells to proliferate, as some molecules tend to accumulate more in tumour tissues than in normal cell tissues (Davis et al., 2010; Pecot et al., 2011; Shi et al., 2017). There are therefore still some challenges (Torchilin, 2014).

Suitable drug delivery mechanisms support payload loading extracellularly and successful release of the drug in a response-elicited environment. Internal stimuli such as enzymes (Yingyuad et al., 2014) and pH (Hong et al., 2013), or external triggers like thermal and magnetic field (Yang et al., 2016), ultrasound (Argenziano et al., 2022) and light (Sun et al., 2021) trigger release at the targeted cells. On stimulation, nanocarriers show change in physical and chemical properties (Lai and He., 2016).

Quantum dots (Qdots) have been shown to facilitate NP intracellular and systemic distribution (Derfus et al., 2007; Qi and Gao, 2008; Jung et al., 2010; Bagalkot and Gao, 2011; Zhao et al., 2011). Semiconductor quantum dots (Qdots) form a group of inorganic nanoparticles with potential for use in siRNA-based cancer gene therapy. Small, bright, Qdots can be functionalised by hydrophobic organic molecules to conjugate nucleic acid molecules to the surface through electrostatic and disulphide bonds. Qdots can act as a payloaded, drug delivery system to provide both siRNA-based gene silencing and diagnostic imaging (Kaaki et al., 2011; Chen et al., 2013). Cytotoxicity of the

Qdots has like other nanoparticles, been known to be a limitation to the extent to which they are used in targeted drug research (Winnik and Maysinger, 2013).

Targeted delivery of drugs by nanoparticles can overcome difficulties associated with insolubility, non-specificity to human tissues (leading to harmful effects in healthy tissue) and bio-distribution (Martino et al., 2017). Nanodrug technology has the added advantage of increased bio availability, extended drug half-life and reduced off-target toxicities (Gupta and Gupta, 2005; Shapira et al., 2011).

The reaction of delivery of drugs to the environmental conditions makes for specificity of drug release in the presence of light, magnetic field, enzymes, redox state, and pH (Mellati et al., 2016). The loaded nanocarrier is therefore required to have specific characteristics to avoid wrong-time release of the pay loaded oligo, and to limit non target interaction with healthy tissue. New methods to produce iron oxide nanoparticles to produce theranostics are still heavily explored, as commercial iron oxide nanoparticles are expensive and not available in the suitable size for development of a nanocarrier to cross the membrane of the tumour. Some water-soluble, anti-cancer drugs like Doxorubicin (Dox) are used for the treatment of many cancers (Weigert et al., 2007; Sun et al., 2008; Munnier et al., 2008; Tacar et al., 2013 ; Kumar et al., 2016).

Polyethylene glycol (PEG) is a common polymer used in several biomedical applications, for example to house the siRNA, as siRNA is highly labile and prone to destruction by proteolytic enzymes. The use of PEG therefore improves delivery and enhances biocompatibility of nanocarriers or therapeutic drugs. When this nanocarrier complex is in the body, siRNA can be delivered to the tumour site. PEG is a widely used polymer in industry, research, pharmaceutical, and cosmetics and even forms the base for some toothpastes (Okpalugo et al., 2009). PEG has been widely investigated for intra and intercellular introduction of nanocarrier to the site of cancerous tumours. PEG is usually a solid at room temperature, depending on the molecular weight and is hydrophilic, low melting with a loose structure (Figure 1-5). PEG is extremely soluble in water and most organic solvents.

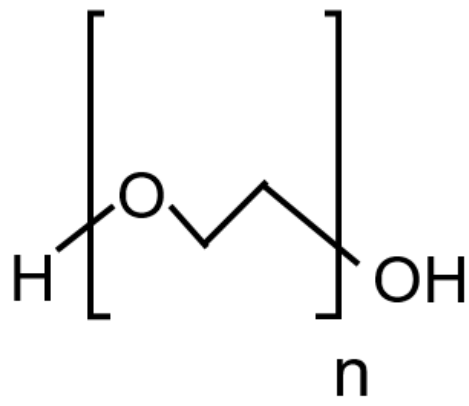


Figure 1-5: Polyethylene glycol

PEG (a solid at room temperature) is used in this study in combination with polyethyleneimine (PEI). Polyethyleneimine (PEI) is a clear, viscous liquid with linear (Weyts and Goethals, 1988), branched (Kurzer and Douraghi-Zadeh, 1967) and dendrimeric structures (Yemul and Imae, 2008) (Figure 1-6).

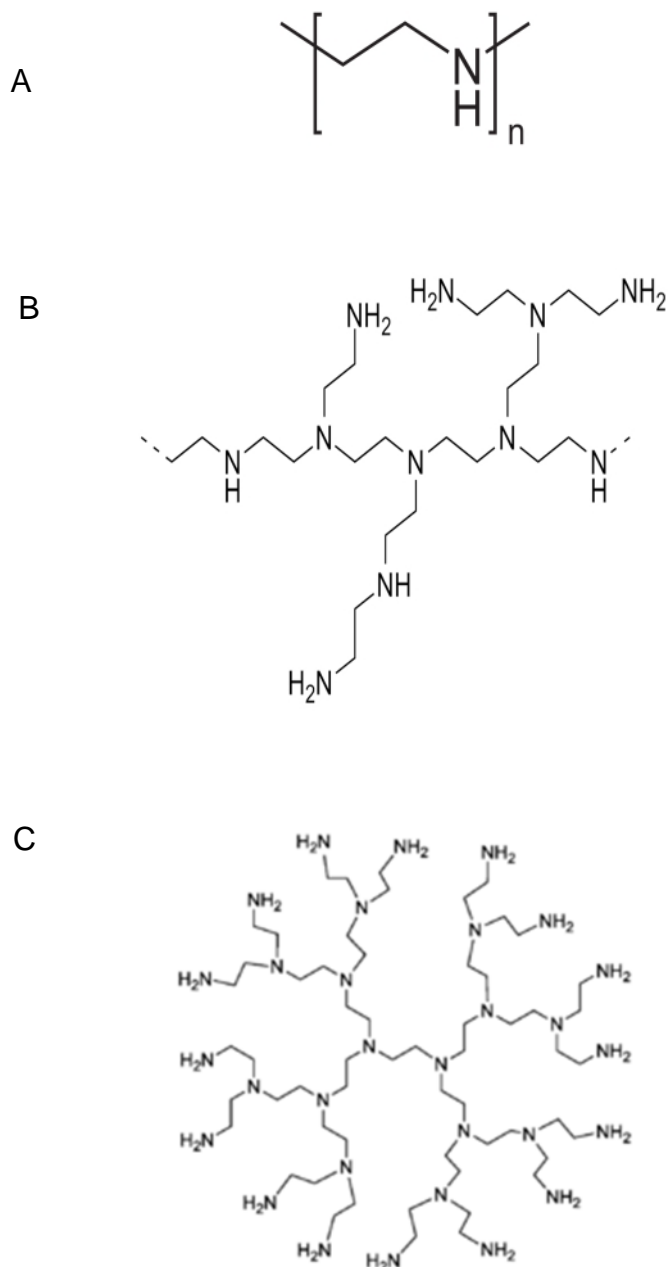


Figure 1-6: Polyethylenimine- Linear (A), branched (B) and dendrimeric (C)

The linear PEI is solid at room temperature while branched PEI is a liquid at room temperature, regardless of their molecular weights. PEI is known to be intracellularly toxic (Von Harpe et al., 2000), and its toxicity increases with its molecular weight. Long chain PEI is therefore not very popular as a coating for delivery of therapeutic drugs (Beyerle et al., 2010). The short chain PEI molecule is known to be less toxic (Lin et al., 2008) and is used in combination with PEG as a coating for iron oxide nanoparticles (IONPs) and other materials. The surface

charge of a nanoparticle plays an important role in regulation of blood circulation, nanoparticle-cell association and affects activities within the cell. It is disadvantageous for a nanoparticle surface to be positively charged before reaching the tumour site, as the positive charge on the nanoparticles interact strongly with blood, leading to rapid clearance from the blood (due to aggregation), and by implication, reduced accumulation of nanoparticles at the tumour site. The negative charge of PEG (brought about by induction effect in which oxygen atoms obtain partial negative charge from near-by carbon atoms in the polymeric chain) repels the cell membranes which are often also negatively charged (An et al., 2014). On reaching the tumour site however, the positive charge on the nanoparticle enhances the assimilation of nanoparticles by the tumour cells and aids the release of the payload moiety within the cells. Ideally, a suitable nanocarrier system for drug delivery should therefore possess a neutral or negatively charged surface while in the circulatory system and later develop a positively charged surface when the nanocarrier arrives at the tumour site, or within the cancer cells (An et al., 2014).

PEI comprises repeating units composed of amino groups and has adhesive properties (Lee et al., 2010; Rios et al., 2019). The high positive charge density of PEI encourages electrostatic interaction to negatively charged molecules and facilitates cellular internalisation (Godbey et al., 1999) which results in biocompatible, stable dispersions for modification and conjugation in a range of biomedical applications (Sangeetha et al., 2013; Borny et al., 2015). The polymer is therefore suitable for use in cancer therapy, as patients with hepatocellular carcinoma have less severe liver dysfunction than counterparts with alcoholic liver disease (Reddy et al., 2012). For the application used in this research, the short chain PEI (Lin et al., 2008) is used in combination with polyethylene glycol (PEG).

PEI-coated superparamagnetic iron oxide nanoparticles have been studied for biomedical applications including drug delivery (Steitz et al., 2007), and has been used in co-delivery mechanisms targeting cancerous tumours. As mentioned above, PEI with higher molecular weight exhibits higher toxicity.

Several studies have used PEI in drug delivery (Pham et al., 2016; Sohrabijam, et al., 2017), gene therapy (Bhattacharya et al., 2011; Unsoy et al., 2012), imaging (Tsai et al., 2010) and bio sensing (Tan et al., 2009; Yang et al., 2017).

1.4 NANOPARTICLES IN BIOMEDICINE

Nanomedicine is a research area that is advancing cancer diagnosis and therapy. Nanoparticles (NPs) have unique biological properties. They are small sized (diameter within 1–100 nm) with large surface area to volume ratio, for payloading anticancer moieties, drugs, DNA, RNA, proteins, and imaging agents. Various NPs are used in drug-related techniques (Schroeder et al., 2012; Mazzotta et al., 2016).

Nanoparticles and other nanomaterials impact our everyday existence. In industrial applications, they have become indispensable components of catalysts (Astruc, 2007), sensors (Saha et al., 2012) or photovoltaic devices (Stratakis and Kymakis, 2013). Biomedically, they have found wide-spread use as nano vaccines (Saroja et al., 2011), nano drugs (Meng et al., 2012) and diagnostic imaging tools (Yoo et al., 2011). Despite this, knowledge of ill effect and potential risk is limited (Stark, 2011; Cheng et al., 2013).

Some types of magnetic nanoparticles show peculiar properties when compared to bulk materials (Laconte et al., 2005), including super paramagnetism, high coercivity, low Curie temperature and high magnetic susceptibility. Very commonly, it is difficult to fashion nanoparticles according to a chosen set of characteristics such as size, shape, stability, and dispersion of NPs in solvents. The surface-to-volume ratio of magnetic NPs is large. The particles therefore possess high surface energies. As a result of this they form aggregates that minimise the surface energies. Bare iron oxide NPs however have high chemical activity and are readily oxidised in air (especially magnetite). By implication, proper surface modification or coating, and development of other methods to maintain magnetic iron oxide NPs stability is paramount. Protective shells stabilise magnetic iron oxide NPs, and have the added advantage of further chemical functionalisation (Wu et al., 2008).

According to (Jiang et al., 2000 ; Barick et al., 2009) magnetite nanoparticles are not toxic to humans, while Hong and co-workers, 2008 state that nanoparticles are recommended for use in biomedical applications. It is widely accepted, however, that toxicity of nanoparticles depends on the preparation method and intended application. Furthermore, nanoparticles have been known to aggregate in the body and this is still under investigation (Sangnier et al., 2019). Therefore appropriate synthesis methods need to be developed such that nanoparticles such as SPIONPs are capable of performing biocompatible roles, while maintaining superparamagnetic and biofunctionalised properties (Cinti et al., 2011).

1.4.1 Iron oxide nanoparticles in biomedicine

Magnetic NPs may be of various materials including iron, cobalt, or nickel oxides, all showing large surface area and magnetic moment affected by an external magnetic field (Caroso et al., 2018). IONPs comprising magnetite (Fe_3O_4) and maghemite ($\gamma\text{-Fe}_2\text{O}_3$) both possess ideal biocompatibility and superparamagnetic properties to enhance widespread biomedical uses (Khanna et al., 2018; Xie et al., 2018). Iron oxide commonly known as rust, has other names such as maghemite, magnetite, depending on the number of atoms of iron in the compound (magnetite has three iron atoms while maghemite has two), and the oxidation state of the metal: Iron (II) or Fe^{2+} and Iron (III) or Fe^{3+} and differ in their valence electrons Fe^{3+} having one electron less than Fe^{2+} . Generally, two broad categories rank the production of nanoparticles such as the breakdown of larger material to nano sized particles (top down approach) or the aggregation of miniscule material to compose the nanoparticle (bottom up approach) (Ghafelehbashy et al, 2020). The synthesis method is important in developing effective nanocarriers (Ghafelehbashy et al., 2020).

One of the first clinical applications of interstitial hyperthermia using magnetic nanoparticles to treat prostate cancer involved interstitial hyperthermia generated by the magnetic nanoparticles (Johannsen et al., 2009). From the study it became clear that there were several important factors to consider including type

of material, geometry, anisotropy constant, size, number of MNPs and configuration of the cluster of MNPs in the development of nanorobotics agents for specific targets (Cheheltani et al., 2018).

Due to their similar dimensions when compared to cells, viruses, proteins, and genes, they demonstrate potential to interact with biological processes (McNamara and Tofail, 2015).

Metallic nanoparticles are frequently used as magnetic resonance imaging contrast agents (Kim et al., 2009 ; Cao et al., 2020). They are also used as gene-carriers in molecular therapeutics against hyperthermia-based cancer treatment, magnetic sensitive probes for *in-vivo* diagnostics and for target – specific drug delivery (Corot et al., 2006 ; Neuwelt, et al., 2007; Figuerola et al., 2010; Daldrup-Link et al., 2011; Ansari et al., 2014; Klenk et al., 2014; Mohammed et al., 2017). After being delivered to the target area, the drug is then released by cytolysis, involving rupture of the cell wall (Roger et al., 1999).

Among the methods used for the characterisation of sputtered IONPs in this work, MRI (Li et al., 2013) was used to determine the effect of IONPs sputtered from an iron oxide target via inert gas condensation technique on water relaxation. Particularly, tests were done to assess the potential of the sputtered nanoparticles for use as negative contrast agents for MRI, with potential for *in-vivo* translation. As mentioned earlier, MRI is one of the many methods used in biomedical investigations, particularly in cell culture studies, in which tracking of nanoparticles within biological environments by MRI has been reported (Khaleghi et al., 2016).

Among the wide range of iron oxide-based nanoparticles are magnetite (Fe_3O_4), maghemite ($\gamma\text{-Fe}_2\text{O}_3$) and mixed ferrites (MFe_2O_4 where $\text{M} = \text{Co}, \text{Mn}, \text{Ni}$ or Zn) (Wu et al., 2015). Once surface modified, the resulting superparamagnetic iron oxide nanoparticles (SPION) find application in MRI (Cheng et al., 2005; McCarthy and Weissleder, 2008; Xu et al., 2011; Caruso et al., 2012; Jin et al., 2014) magnetic particle imaging (MPI) (Weizenecker et al., 2009; Khandhar et al., 2013; Du et al., 2013; Furguson et al., 2015; targeted delivery of drugs,

proteins, antibodies, and nucleic acids (Xu et al., 2011; McCarthy and Weissleder, 2008; Mahmoudi et al., 2011). hyperthermia (Laurent et al., 2011; Schleich et al., 2015; Périgo et al., 2015), biosensing (Huan et al., 2010), tissue repair (Siddiqi et al., 2016; Hedayatnasab et al., 2017); and separation of biomolecules (Tan and Yiap, 2009). To this end, magnetic iron oxide NPs became strong candidates, and the application of small iron oxide NPs in *in-vitro* diagnostics has been practiced for nearly half a century (Gupta and Gupta, 2005; Stevens et al., 2005 ; Mornet et al., 2006 ; Patel et al., 2008). In this study, the iron oxide nanoparticles will be sputtered by inert gas condensation technique and functionalised for potential use in targeted drug delivery.

1.4.2 Functionalisation of Nanoparticles

Functionalisation involves changing the surface of NPs, by conjugation to chemicals (Herranz et al., 2012), making the NPs biocompatible, stable, and suitable for use in the desired application (Aravind et al., 2012). Studies on functionalised NPs show that the NPs have desirable characteristics such as anti-corrosion and anti-agglomeration (Subbiah et al., 2010). When functionalising magnetic or superparamagnetic nanoparticles, the external magnetic field can readily induce the nanoparticles towards magnetic resonance. Behaviour of MNPs however depends on crystallisation method, size, and shape. These intrinsic properties of NPs must be taken into consideration, to make them more compatible in bio-systems (Lantada and Endrino, 2016).

By applying MNPs modified with synthetic silencer RNA (siRNA) molecules, through ionic interactions, researchers have identified greatly reduced gene expression rates in *in-vitro* drug delivery (Duguet et al., 2006; Sinha et al., 2006; (Lee et al., 2011). This property of siRNA is an advantage. Some modifications impose additional chemical and/or physical properties to the NPs (Sheng-Nan et al., 2014), while improving the biological and biochemical response of several biomedical devices.

Enhanced permeability retention (EPR) effect which brings about aggregation of molecules of certain sizes (typically liposomes, nanoparticles, and

macromolecular drugs) inside tumour tissues rather than normal tissues, can be a major challenge (Maeda, 2012). Polyethylene glycol has been used to diminish the EPR effect in the past thirty years. However, PEG has its limitations and, as a result, the interaction of PEG with the target cells did not occur effectively and the loaded drugs were degraded in lysosomes (Amoozgar and Yeo, 2012 ; Mishra et al., 2016). In response to this dilemma, this research has incorporated PEI with PEG (Hemben et al., 2021). The nonbonding interactions due to spatial arrangement of molecules bring about a steric effect which may influence the shape (conformation) and reactivity of ions and molecules (Choi et al., 2007; Hatekayama et al., 2013; Ahmadzada et al., 2018 Liang and Lam, 2021). Superparamagnetic nanoparticles have been investigated as functionalised nanoparticles using mouse models (Xie et al., 2015). PEG with general chemical formula $C_{2n}H_{4n+2}O_{n+1}$ and a molecular mass 18.02 g/mol has found extensive use in biomedical applications. PEG is a derivative of ethylene glycol which is a diol, an alcohol with a molecular structure that contains two hydroxyl (OH) groups.

PEG is non-hazardous, soluble in water and has found application in many areas including industrial manufacturing, pharmaceutical and biomedical applications (Mohammadi and Babaei., 2022). Very often it is used in conjunction with peptides, proteins, or oligonucleotides which are investigated as drugs for a wide range of illnesses. Interestingly, PEG can conjugate itself to a target molecule by attaching itself to the target for optimisation of the pharmacokinetic properties of drug therapy. The polymer can also be used as a passive chemical for transport of a therapeutic agent. PEG can also be used as a coating layer on the surface of iron oxide nanoparticles (Hemben et al., 2021).

PEG has been used in tissue engineering, protein analysis and to control the clearance of engineered proteins from the circulatory system (Shchapova et al., 2019). The PEG hydrogels possess polymer networks made by crosslinking reactive PEG end groups, to produce gels that can withstand proteolysis and adhesion. These are useful characteristics in tissue engineering and drug delivery. *In-vitro* assays have also become dependent on PEG, as PEG is a

biomimetic compound that aids the investigation of intracellular environments 'created' outside the body (Derfus et al., 2007). It is also used as precipitant for DNA isolation (Ganji et al., 2016) and cell crystallisation, supporting the study of protein structure. PEG utilised in gene therapy can be used for coating vectors. Vectors such as plasmids and viruses serve as a vehicle for the delivery of genetic material into recipient cells. The PEG coating of vectors therefore guards against their being neutralised by the body's immune system (Tortajada et al., 2022) and can play a vital role in blood banks by enhancing salience of antibodies and antigens (Zhang et al., 2014). Potential use for PEG in neurological research (Fan et al., 2018) may emerge in the application of PEG for the treatment and management of spinal cord injury and peripheral nerves. In chemistry, PEG is known to be a binding and dispersing agent (Pitek et al., 2016) as it enhances disaggregation of particles reducing for example, immunogenicity of virus nanoparticles (Pitek et al., 2016). The hydrophilic characteristics of PEG (Kadanyo et al., 2022) fashions a role in preventing the non-specific adhesion of proteins in studies using single-molecule fluorescence; in addition, PEG is an FDA approved lubricant (Li et al., 2022) and wood preservative (Jiang et al., 2021) with possibilities for increased use in other areas including gene therapy (Kean, 2019). An ideal vector, or vehicle for transporting genetic material to recipient cells, must be (i) biocompatible, biodegradable, and immunologically inert, (ii) tissue-targeted, (iii) not size-limited, (iv) stable, easy to produce, and scalable, and (v) suited for accommodating site-specific moieties for the delivery of genetic material to the target cell (Zhou et al., 2017). PEG meets most of the requirements listed above making it a promising candidate as a vector.

1.5 NANOPARTICLES SYNTHESIS METHODS

In the current application of nanoparticles there are two broad categories described as bottom up methods and top down techniques (physical, chemical or biological methods) which depend on the source material (Jamkhande et al., 2019). Nanoparticle preparations are useful in surface coatings and include spin coating (Xu et al., 2012), dip coating (Xu et al., 2012), thin film, sol-gel, spray

zinc coating and vapour coating. In vapour coating, fluid composition is atomised and allowed to interact with a carrier gas. Conditions in the chamber are suitable to atomise fluid composition to coat a substrate. The surface temperature of the material to be coated is maintained lower than the condensation temperature of the vapour. The vapour then condenses on and coats the surface (Naghdi and Mišković-Stanković, 2022).

Nanoparticles may be synthesised by a range of wet or dry methods, yielding nanoparticles with a range of sizes (Table 1-1). In this study, the iron oxide nanoparticles of size (1-6 nm), such as can pass through the cell membrane of a cancer cell are generated on a substrate by the dry NPs production method of inert gas condensation. The coated substrate is then washed to suspend the deposited nanoparticles.

Table 1-1: Some nanoparticles production methods

Chemical / wet synthesis	Nanoparticles Size (nm)	References
Aqueous phase green synthesis: <i>Platanus orientalis</i> .; <i>Sargassum muticum</i> .	18± 4	(Mahdavi et al., 2013; Devi et al., 2019)
Chemical reaction of iron filings	30	(Arenas-Alatorre et al., 2019)
Chemical reduction <i>Ficus carica</i> (common Fig) Plant extract <i>Lagenaria siceraria</i> .	9 ± 4; 30-100	(Demirezen et al., 2019; Kanagasubbulakshmi and Kadirvelu, 2017)
Co precipitation	30	(Vergés et al., 2008)
Hydrothermal preparation	15-31	(Ge et al., 2009 ; Takami et al., 2007)
Thermal decomposition.	18-21 ± 2	(Unni et al., 2017)
Microemulsion	4-9	(Chin and Yaacob, 2007)
Aqueous hydrolysis	24-40	(Adimoolam et al., 2018)
Reactive sputtering / physical deposition methods in which energised gas strikes a target and sputters atoms from the target to coat a substrate.	1-20	(Safi, 2000; Hemen et al., 2021)

1.5.1 Production of Nanoparticles using Mantis NanoGen Trio

In recent years, the production of nanomaterial thin films and nanostructures has been investigated for use in various applications as a result of their desirable structural, electrical, optical and magnetic properties (Williams et al., 2018). Iron oxide films were synthesised by sputtering Fe metallic target in Ar and O₂ gas mixtures (Aubry et al., 2019).

Mantis NanoGen Trio is one of the reactive sputtering systems used in the production of a variable, pre-selectable size of nanoparticles from high purity (~99%) commercial, solid targets attached to a magnetron and suspended in the agglomeration chamber. Sputtering of the targets takes place in the agglomeration chamber using a voltage-energised inert gas to excite and elicit release of particles from the surface of the target into the gas-filled agglomeration chamber. In response and due to energy transfer the gas and target particles interact continuously, and more and more target particles are released in the pressurised chamber. The NanoGen Trio source designed for synthesis of complex alloy nanoparticles, generates nanoparticles by a "terminated gas condensation" method. In this method, three magnetron targets may be sputtered independently (Figure 1-7).

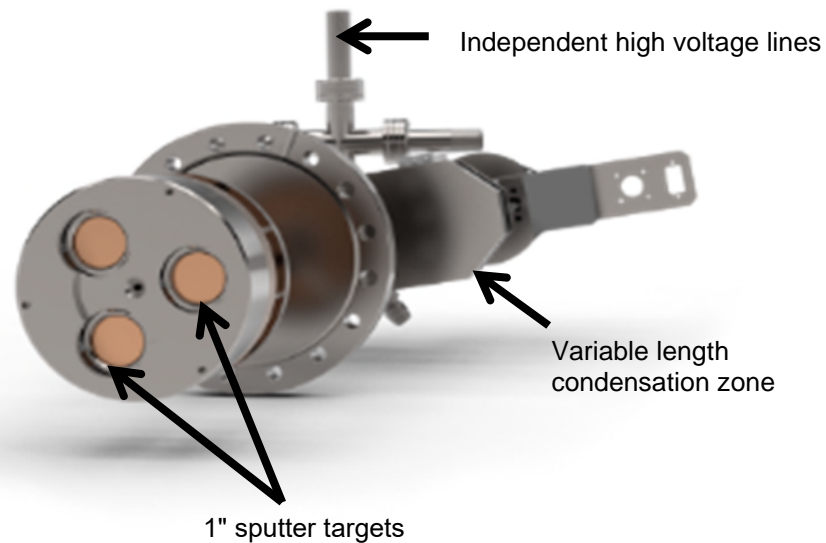


Figure 1-7: Adapted from NanoGen Trio (www.mantisdeposition.com, 2019).

Three targets are attached to the magnetron heads which are in turn attached to an extensible, flexi tube portion with a handle for adjusting the working distance for sputtering and deposition of nanoparticles. The independent voltage lines transmit power to the system, which transmits through the magnetron heads and targets. One or more magnetrons may be used in the sputtering of nanoparticles.

Composition of the resulting nanoparticles depends on the material of the targets (www.mantisdeposition.com, 2019), while the ability to control the size, density and in some cases the morphology of the deposited particles allows for flexible use of NanoGen sources in the creation of new types of nanostructure (Grammatikopoulos et al., 2016). Physical vapour deposition (PVD) techniques are some of the surface coating methods. Sputtering is a PVD technique which produces charged nanoparticles freely interacting with other nanoparticles and noble gas to transfer energies within the system, for example inert gas

condensation (IGC) technique used in this work utilised Argon gas. Magnetron sputtering is used to produce hard, wear-resistant coatings, low friction coatings, decorative coatings and coatings with specific optical or electrical properties (Rossnagel, 1999). The advantage of control of nanoparticles size, shape and structure over other chemical methods of nanoparticle production provide for predictability and repeatability, and for assessing superparamagnetism. The control of size of sputtered nanoparticles using IGC technique is also possible with the alteration of temperature within the agglomeration chamber. Generally, the cooler the environment within the agglomeration chamber, the larger the sputtered nanoparticles size will be. With the Mantis NanoGen Trio, a chiller can be used to control (lower) the temperature in the agglomeration chamber. In addition, two or all three of the magnetrons can be used simultaneously to sputter the targets of different metals to produce hybrid nanoparticles (www.mantisdeposition.com, 2019).

The physical vapour deposition coating method used in producing coatings for various items in manufacturing industry (Pinto, 2018; Aubry et al., 2019) has been applied in a novel approach for soft-landing iron oxide nanoparticles. These nanoparticles have been used in the synthesis of a nanocarrier complex coated with the biocompatible polyethylene glycol, which forms the broad aim of this research.

Furthermore, the nanoparticles produced in this work do not require chemical precursors and therefore do not require further purification steps before they can be used in nanocarrier synthesis.

The significant research gap involves nanoparticle production by a facile method which yields small-sized, free-standing nanoparticles with narrow size distribution. Although other sputtering methods have demonstrated some of these requirements, the nanoparticles produced are usually deposited for the purpose of coating a surface, and not for obtaining free-standing IONPs.

The novelty of this work is in the use of a nanoparticles coating method, physical vapour deposition *via* inert gas condensation to produce a nanocarrier complex.

This is the first time that inert gas condensation has been used to produce nanoparticles with potential for use in targeted drug delivery. In a pilot study conducted during a brief (3 months) MSc research project, the synthesis of free-standing IONPs via inert gas condensation was demonstrated (Serfimowicz, 2018), although the production method was not fully investigated or optimized. In the pilot study, commercial iron oxide nanoparticles were also used to develop the attachment of a therapeutic drug (siRNA) to the nanoparticles. However, the dye (Texas Red) that was selected as label for the siRNA to evidence its attachment seemed to be quenched in acidic pH (pH < 7.0). This result negated the possibility to study the drug release from the IONPs as the extracellular cancer environment has a pH value of around 6.5. In this work, which is a continuation of the pilot study, the sputtering of the IONPs will be fully investigated and optimised. Furthermore, the fluorescence behaviour of the dye will be systematically studied and if necessary, a different label will be chosen to optimise the attachment and release of the siRNA to and from the NPs. Different types of commercial iron oxide nanoparticles will also be considered for the study.

1.6 AIMS AND OBJECTIVES

This work aims at developing a novel manufacturing method to produce iron oxide nanoparticles (IONPs) of narrow distribution size suitable for biomedical application and particularly for intracellular drug delivery. In addition, a method to attach and release a therapeutic drug to the iron oxide nanoparticles will be developed.

Project objectives:

- To develop a manufacturing method for producing free standing IONPs using Mantis NanoGen Trio system
- To optimise conditions and achieve high yield of IONPs

- To characterise the sputtered IONPs using several characterisation techniques
- To identify and investigate a fluorescent dye as a suitable tag for a therapeutic agent (i.e. siRNA) to visualise and measure its attachment and detachment from the IONPs.
- To optimise the method for attachment of dye-siRNA to PEG/PEI coated IONPs
- To optimise the release of dye-siRNA from PEG/PEI coated IONPs

The following chart shows the connection between the contributing parts of the research (Figure 1-8).

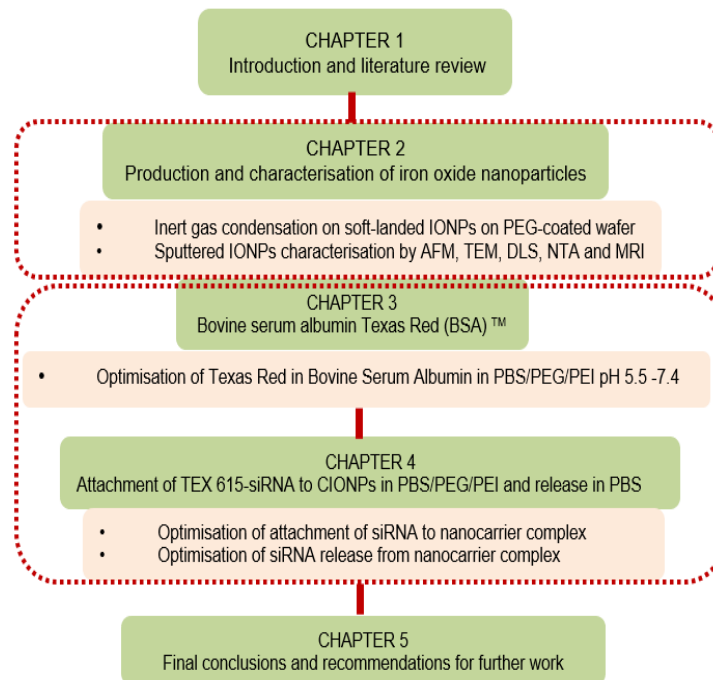


Figure 1-8: The two main sections of the experimental work and Chapters

CHAPTER 2

**PRODUCTION AND CHARACTERISATION OF
SPUTTERED, SOFT-LANDED IRON OXIDE
NANOPARTICLES**

2 PRODUCTION AND CHARACTERISATION OF IRON OXIDE NANOPARTICLES

2.1 INTRODUCTION

Physical vapour deposition denotes a range of vacuum deposition methods which are used for the application of a thin film or coat on a surface. Scientific vacuum systems (SVS), a sputtering systems manufacturer provides techniques like electron beam and deposition, evaporation and ion beam milling (SVS, 2022). The SVS used in this research has been specifically configured to meet the requirements of magnetron sputtering by inert gas condensation technique, using Mantis NanoGen Trio magnetrons suspended in an agglomeration chamber and coupled to the top of the SVS main chamber. Inert gas condensation technique is one of the physical vapour deposition (PVD) methods. The most common PVD processes are sputtering (Pinto, 2018) and evaporation (Khudair and Mohmood, 2021).

The principle of sputtering iron oxide nanoparticles using inert gas condensation (IGC) is a process that involves the bottom-up technique of production of nanoparticles from bulk source material. Inert gas condensation consists of two major steps. The first step involves the sputtering of loosened, energised atoms from the surface of the iron oxide bulk material (called a target) and the second step involves the condensation of the sputtered material in pre-determinable nanoparticles size. Inert gas condensation system used in this research is composed of the main chamber from Scientific Vacuum Systems (SVS) which is fitted with a magnetron from Mantis deposition Ltd.

A vacuum generated in the agglomeration chamber produced pressure as low as $2 \times 10E^{-6}$ Torr using a vacuum pump. After the evacuation of the agglomeration chamber, Argon was introduced into the chamber with Ar flow rate starting from 10 sccm. Once the high voltage (HV) was applied, the plasma was created, which is concentrated along a magnetic field. For this research, the substrate is a

polyethylene glycol (PEG)-coated silicon wafer. The silicon wafer is the substrate commonly used in this system and can withstand the conditions of pressure in the main chamber. PEG coating on the silicon wafer provides a soft landing for the sputtered iron oxide nanoparticles allowing free-standing nanoparticles to be obtained by dissolving the polymer sputtered layer (Hemben et al., 2021).

The SVS main chamber contains a drum upon which there is a table on which the substrate is positioned upon for the deposition of nanoparticles. Generally, the sputtering system can be used for sputtering other materials like tin, titanium, and copper, however, to produce iron oxide nanoparticles for this research, only iron oxide targets were used in the presence of Argon gas to generate a beam of energised, particulate mixture of iron oxide sputtered atoms released from the target to interact with Argon atoms. The schematic for generation of a plasma by inert gas condensation using Mantis NanoGen trio is shown in Figure 2-1.

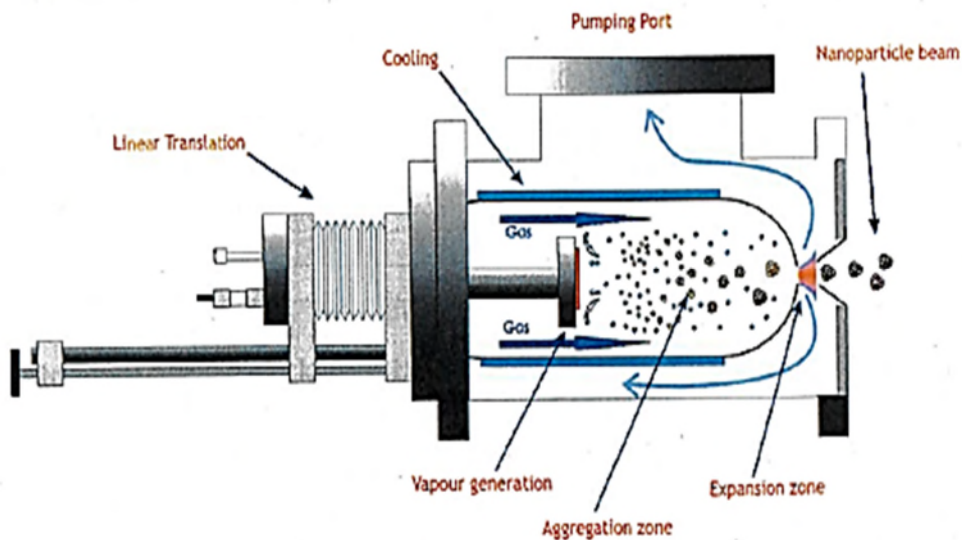


Figure 2-1: Mantis (mantisdeposition.com/nanoparticlegenerators, 2019).

Metallic coatings are used for developing anti-bacterial surfaces, medical devices like prostheses and catheters, food packaging industry, textile surfaces (e.g., health worker equipment) and air filtering systems. Metallic nanoparticles have

found application in water treatment plants, where they are used to attach to microorganisms (Mihut et al., 2019). Magnetron sputtered targets of gold have been deposited on polyethylene glycol solution in ligand controlled Au nanoparticle synthesis (Wang et al., 2022) while copper has been used in conductivity experiments (Iqbal et al., 2021). Magnetron sputtered silver nanoparticles have also found use as a catalyst (Solomon et al., 2021). Zinc oxides are known to have antimicrobial properties and magnetron sputtered zinc oxide nanoparticles are used for formaldehyde sensing (Zhang et al., 2021).

As mentioned earlier, metallic nanoparticles can be sputtered via a magnetron on a range of substrates to form a coating. For this study, however, inert gas condensation has been used to produce free-standing iron oxide nanoparticles for potential use in drug delivery (Hemben et al., 2021). The sputtered iron oxide nanoparticles have been characterised by Nanoparticle Tracking Analysis (NTA) (Hole et al., 2013; Dragovic et al., 2015; Luo et al., 2018), Transmission Electron Microscopy (TEM) (Mahdavi, et al., 2013), and Dynamic Light Scattering (DLS) (Behera et al., 2012; Yang et al., 2014; Mi et al., 2017). The small sizes of these nanoparticles enabled them for intercellular diffusion (Barth et al., 2005) through the cell membrane of cancer cells.

The enhanced therapeutic efficacy of targeted nanocarriers has been established in cancer treatment using multiple animal models that target tumours and deliver drugs for targeted radiotherapy, imaging-guided radiotherapy and precision medicine (Mi et al., 2015). Notably, the effects of NPs, such as iron oxide, selenium, silver, and gold NPs, alone or with different therapies (e.g. chemical agents or photocatalytic therapy) on malignant cells have also been reported (Gao et al., 2014; Xiong et al., 2014; Gobbo et al., 2015; Kovács et al., 2016; Petrushev et al., 2016). For example, it has been shown that by precisely shaping the structural properties of the iron oxide nanoparticles, drugs loaded onto the nanoparticles can be efficiently guided and selectively delivered toward targeted locations (Vangijzegem et al., 2019).

Iron oxide and magnetic nanoparticles have attracted significant attention in drug delivery systems for cancer research (Kaamyabi et al., 2016; Nosrati, et al., 2018; Rostami et al., 2018) due to their characteristics like small size, magnetic susceptibility, biocompatibility, stability, availability for surface modification and the ability to be controlled by the application of an external magnetic field (Arias et al., 2011; Wu and Wu, 2016). For nanoparticles to be used, surface coatings and specific modifications are required (Nosrati et al., 2017; Nosrati et al., 2018). Identifying suitable coating materials is important in obtaining stable nanoparticles since the coatings can generate inter-particulate repulsive forces preventing aggregation (Králová et al., 2011; Bae et al., 2012; Galisteo-gonzález and Molina-bolívar, 2014; Jahanban-esfahlan et al., 2016; Salehiabar et al. 2018).

Several studies on investigation of nano drug carriers (Hamidreza et al., 2017; Aghajanzadeh et al., 2018; Zamani et al., 2018) have been reported in literature and bio compatibility of the nanoparticles evaluated (Nosrati et al., 2017).

Magnetic nanoparticles have been known to have characteristics which encourage their potential use in catalysis including nanomaterial-based catalysts (Astruc, 2020), biomedicine (Nikzamir et al., 2021) and tissue specific targeting (Park et al., 2008), magnetically tuneable colloidal photonic crystals (Peterson et al., 2015), microfluidics (Salafi et al., 2017), magnetic resonance imaging (Yallapu et al., 2011), magnetic particle imaging (Yallapu et al., 2011), data storage (Singamaneni et al., 2011), environmental remediation (Singh et al., 2018) nanofluids (Hwang et al., 2008), optical filters (Algorri et al., 2016), defect sensors (Choi et al., 2020), magnetic cooling (Lin et al., 2006) and cation sensors (Ajayaghosh, 2005).

The research described in this Thesis is focused on the production and characterisation of free-standing iron oxide nanoparticles (IONPs) from Fe_3O_4 . The nanoparticles were prepared by the Mantis NanoGen Trio system. The novel production approach has resulted in a polymer-coated nanocarrier complex with potential for use in biological systems (Hemben et al., 2021).

2.2 MATERIALS

2.2.1 General chemicals and instrumentation

Phosphate buffered saline (PBS) tablets (pH 7.4), Polyethylene glycol (PEG) 1000 MW and RNase free water were purchased from Sigma (Dorset, UK) while acetone was purchased from Fisher Scientific (Loughborough, UK). Commercial IONPs in powder form (15-20 nm) were purchased from Nanomaterials Inc. (Texas, USA).

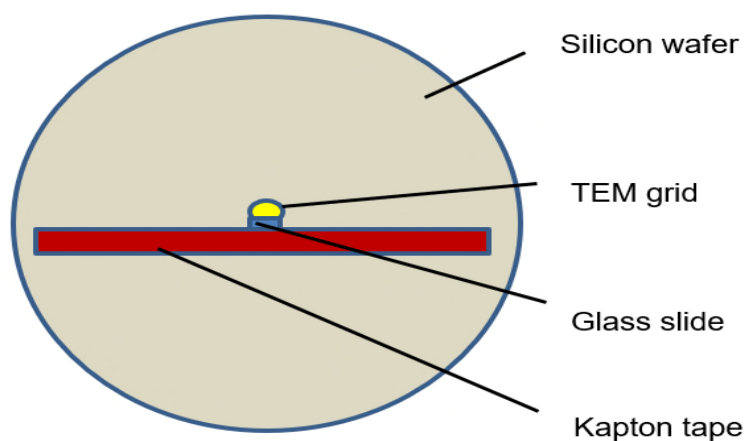
NanoGen Trio was obtained from Mantis Deposition Ltd. (Thame, UK); *In-house* Cu TEM grid from Open University (Milton Keynes, UK). Plasma cleaner was obtained from Diener Plasma Surface Technology (Ebhausen, Germany). Spin coater was obtained from Electronic Microsystems Ltd (Sutton Coldfield, UK). Contact angle meter with Attension software was obtained from Biolin Scientific (Stockport, UK). DektakXTstylus profiler was obtained from Bruker (Coventry, UK). Nuclear Magnetic Resonance (NMR) tubes (5 mm) placed inside 9.4T microimaging system were obtained from Bruker (Coventry, UK). Images were analysed using Prospa3.1 (Magritek, New Zealand) processing software. Edwards 306 carbon coater machine Glo (plasma) discharge Island Scientific Ltd. (Isle of Wight, UK). Atomic force microscope (AFM) equipment was obtained from Digital Instruments (Boston, USA); centrifugal vacuum concentrator Eppendorf 5301 from Sigma (Dorset, UK). Dynamic light scattering was conducted using (Malvern Panalytical Ltd., 2022). NanoSight LM20 was obtained from Malvern Panalytical Ltd. (Worcester, UK) with a CCD camera.

2.3 METHODS

The production of iron oxide nanoparticles by inert gas condensation using Mantis NanoGen Trio from Mantis Deposition Ltd. (Thame, UK) was intended to deposit soft-landed-iron oxide nanoparticles which would then be suspended in solution as free-standing IONPs. The same method was used to obtain nanoparticles directly on a 3 mm, *in-house*, Cu TEM grid, from The Open University (Milton Keynes, UK) for *in-situ* characterisation of the sputtered IONPs.

2.3.1 Preparation of silicon wafer with copper TEM grid

A silicon wafer purchased from Agar Scientific (Essex, UK) was carefully removed from the storage container with a pair of tweezers and placed on a clean surface. A TEM grid 200 mesh from Agar Scientific (Essex, UK), was attached to the silicon wafer using a glass slide and kept in place using Kapton tape. The glass slide was placed on the edge of the TEM grid to hold it in place on the silicon wafer and the tape was applied to prevent the TEM grid shifting out from under the glass slide (Scheme 2-1). Kapton tape can withstand the sputtering conditions during deposition of the nanoparticles in the main chamber. In another experiment, however, another TEM grid was first immersed in PEG solution and placed on a silicon wafer as described above to obtain soft-landed IONPs on the TEM grid.



Scheme 2-1: TEM grid held onto the silicon wafer by glass slide and Kapton tape

2.3.2 Preparation of PEG in acetone

A solution of PEG (1000 g/mol) in acetone with a concentration of 20 mg/mL was prepared in a fume hood by weighing and dissolving 0.2 g PEG on an electric balance product of Ohaus (Leicester, UK). The PEG was dissolved in 10 mL of acetone in a glass container. The acetone solution was stirred in the fume

cupboard for about 30 minutes until complete dispersion of PEG. The container was then sealed to prevent evaporation and placed in the cupboard at room temperature until required for coating of the plasma cleaned silicon wafer.

2.3.3 Coating of the silicon wafer with PEG in acetone

Prior to adding PEG solution to the silicon wafer, and to assess the volume of PEG spin-coated on the surface, the wafers were weighed before and after spin coating. The difference in weight is the estimated amount of PEG coating the silicon wafer.

The silicon wafer substrate which is suitable for use under sputtering conditions in Mantis NanoGen Trio system was coated with a PEG solution, prepared as described in section 2.3.2. It was not noticed straight away that the surface of the wafer was not fully wettable, resulting in poor coverage of the surface with PEG solution. Therefore, the silicon wafer was plasma cleaned to improve wettability of the substrate surface. After plasma cleaning, the surface of the substrate as more hydrophilic.

2.3.4 Plasma cleaning of the silicon wafer

Plasma cleaning (Figure 2-2) of the silicon wafer became necessary to avoid poor distribution and streaking of PEG in acetone during preparation of the substrate surface. The silicon wafer was cleaned in plasma cleaner from Diener Plasma Surface Technology (Ebhausen, Germany).



Figure 2-2: Plasma Cleaner prior to loading silicon wafer (Diener, 2022).

The silicon wafer was plasma cleaned in a Diener plasma cleaner using Oxygen gas at 0.8 mbar and 50 Watts, for 3 minutes to remove impurities from the surface and increase wettability (of the wafer surface) to enhance the spin coating of PEG in acetone on the silicon wafer.

2.3.5 Spin coating of the silicon wafer with PEG in acetone

Spin coating of the silicon wafer with the PEG acetone solution (0.20 mg/L) was conducted on a photoresist spin coater obtained from Electronic Microsystems Ltd model ISC-8 (Sutton Coldfield, UK) (Figure 2-3).



Figure 2-3: The spin coater used for coating the silicon wafer with PEG

The silicon wafer was fixed on the spin coater by vacuum and the PEG solution prepared as in section 2.3.2, was dropped onto the plasma cleaned silicon wafer. Approximately 2 mL of solution was added to cover the entire surface of the wafer. The wafer was then spin coated at 3000 rpm for 60 seconds. Once the run was completed the PEG-coated wafer was 'released' from the holder. The coating process was repeated on several, plasma cleaned silicon wafers and the wafers were all placed under the fume hood on a hot plate from Torrey Pines Scientific (California, USA), at 37°C (as this would be the mimicked temperature within the human body, used all through the later parts of the release studies in this work) for 5 minutes to ensure complete drying of the deposited PEG film (Figure 2- 4).

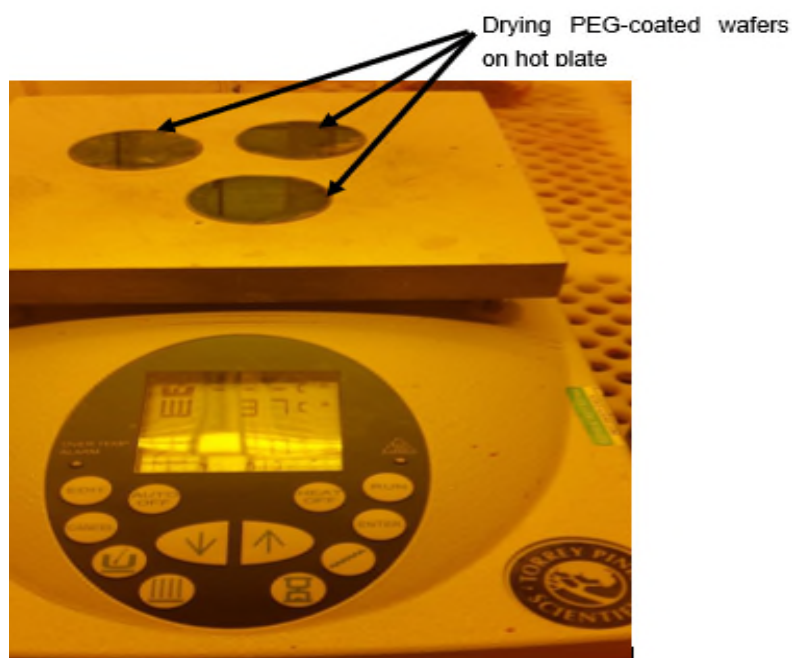


Figure 2-4: Drying PEG-coated wafers on a hot plate

2.3.6 Contact angle measurements for plain and PEG coated silicon wafer

To determine the difference in contact angle between the plain and PEG-coated wafer, contact angle measurements were taken using a contact angle meter,

Biolin Scientific (Stockport, UK) with the Attension software to analyse a live measurement (Figure 2-5).

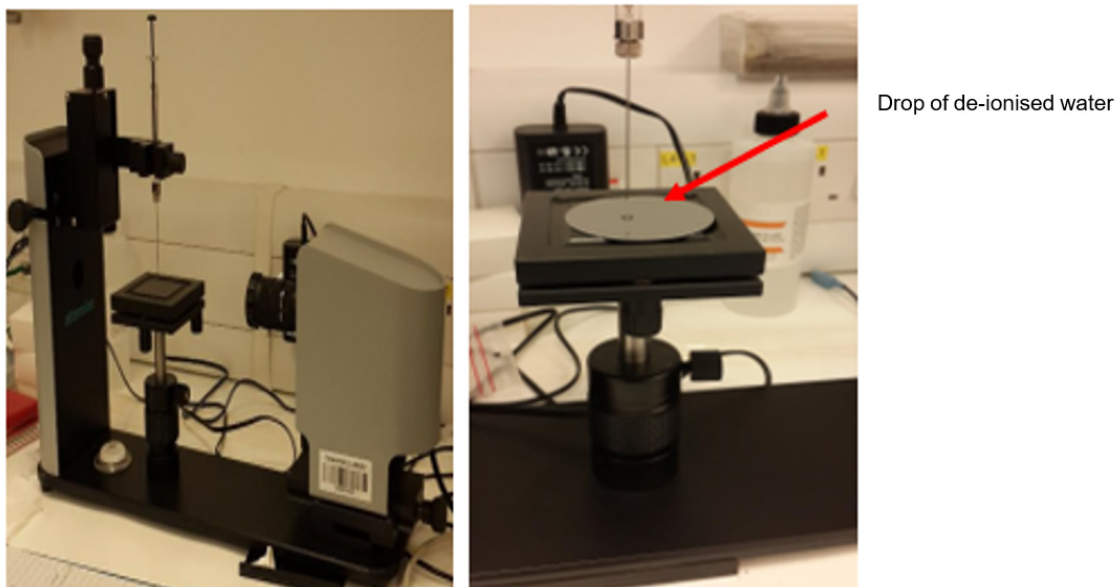


Figure 2-5: Contact angle measurements set up

Contact angle measurements of a drop of de-ionised water were taken at 20°C. For measurements, firstly the drop of de-ionised water was placed at least three times on the surface of the plain silicon wafer and the angle measured and averaged. The process was repeated for the PEG-coated silicon wafer.

To assess the thickness of the PEG layer on the PEG-coated wafer, measurements were taken using DektakXT stylus profiling.

2.3.7 DektakXT stylus profile of the PEG – coated silicon wafer

To assess the thickness of the coating of PEG on the silicon wafer, a spatula was used to scratch a line through the PEG layer and viewed with the DektakXT stylus profiler Bruker (Coventry, UK) (Figure 2-6).

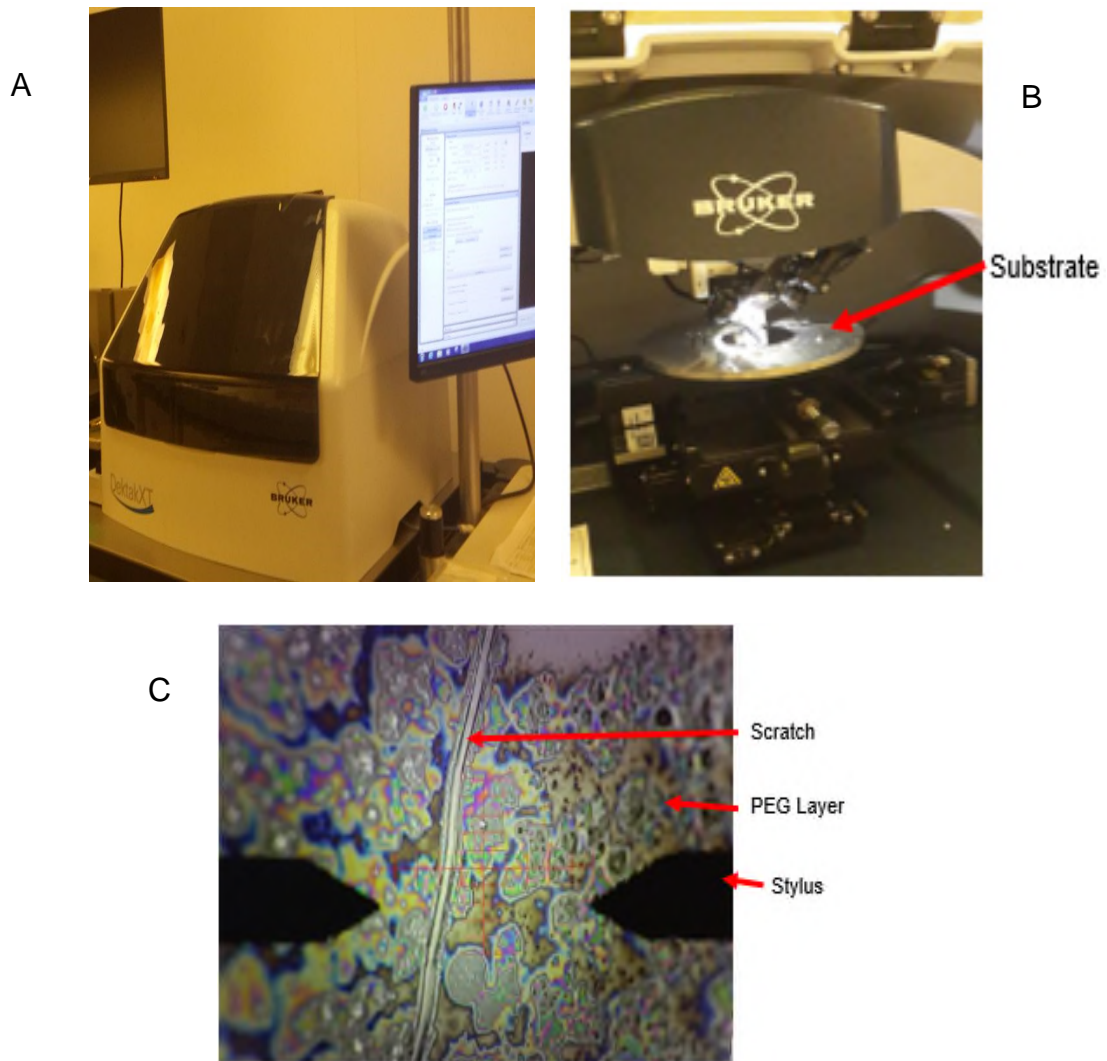


Figure 2-6: Scratch depth of PEG on silicon wafer

As mentioned above, DektakXT stylus profiler (2-6 image A), was the instrument used to scan the depth of the scratch in the PEG layer. Just prior to focusing on the scratch, the PEG-coated silicon wafer was placed on the stage in the DektakXT main cavity (2-6 image B). Just before measurements, the scratch drawn in the PEG layer using a spatula was seen (2-6 image C).

The average of five measurements was taken along the length of the scratch. The PEG-coated wafer was then loaded in the SVS main chamber in preparation for sputtering using Mantis NanoGen Trio.

2.3.8 Mantis NanoGenTrio

The NanoGen Trio source designed for synthesis of complex alloy nanoparticles, generates nanoparticles by a "terminated gas condensation" method. In this method, three coplanar magnetron targets are sputtered independently. Composition of the resulting nanoparticles depends on the material of the targets (Kusior et al., 2016; www.mantisdeposition.com, 2019). Inert gas condensation technique was used to produce iron oxide nanoparticles by sputtering an iron oxide (Fe_3O_4) target 15.4 mm diameter x 3.18 mm thick typically 99.9% pure, obtained from Testbourne Ltd. (Hampshire, UK). The target was attached to a magnetron, Mantis NanoGen Trio from Mantis Deposition Ltd. (Thame, UK). The target attached to the magnetron was suspended within the agglomeration chamber and fixed on top of the main deposition chamber, Scientific Vacuum Systems (Wokingham, UK). This nanoparticle deposition system is configured to deposit layers of nanoparticles from three independent magnetrons (Figure 2-7).

Magnetron heads

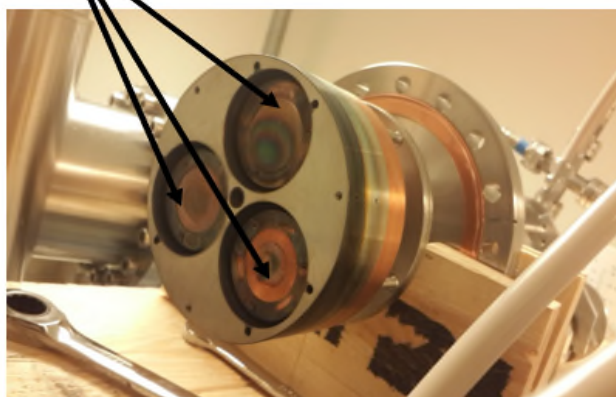


Figure 2-7: Three magnetron heads on Mantis NanoGen Trio

Three (3) 1" iron oxide (magnetite) targets from which the nanoparticles produced in this research (1-6 nm \varnothing) were sputtered in argon for soft landing on PEG thin film – coated silicon wafer. The working distance was 13.8 cm. The independent magnetron heads are the sources of power transmission to the targets, suspended in an agglomeration chamber (Figure 2-8).



Figure 2-8: Agglomeration chamber

The agglomeration chamber which is coupled to the Scientific Vacuum Systems (SVS) main chamber (Figure 2-9) is the site where the nanoparticle sputtering, and agglomeration take place.

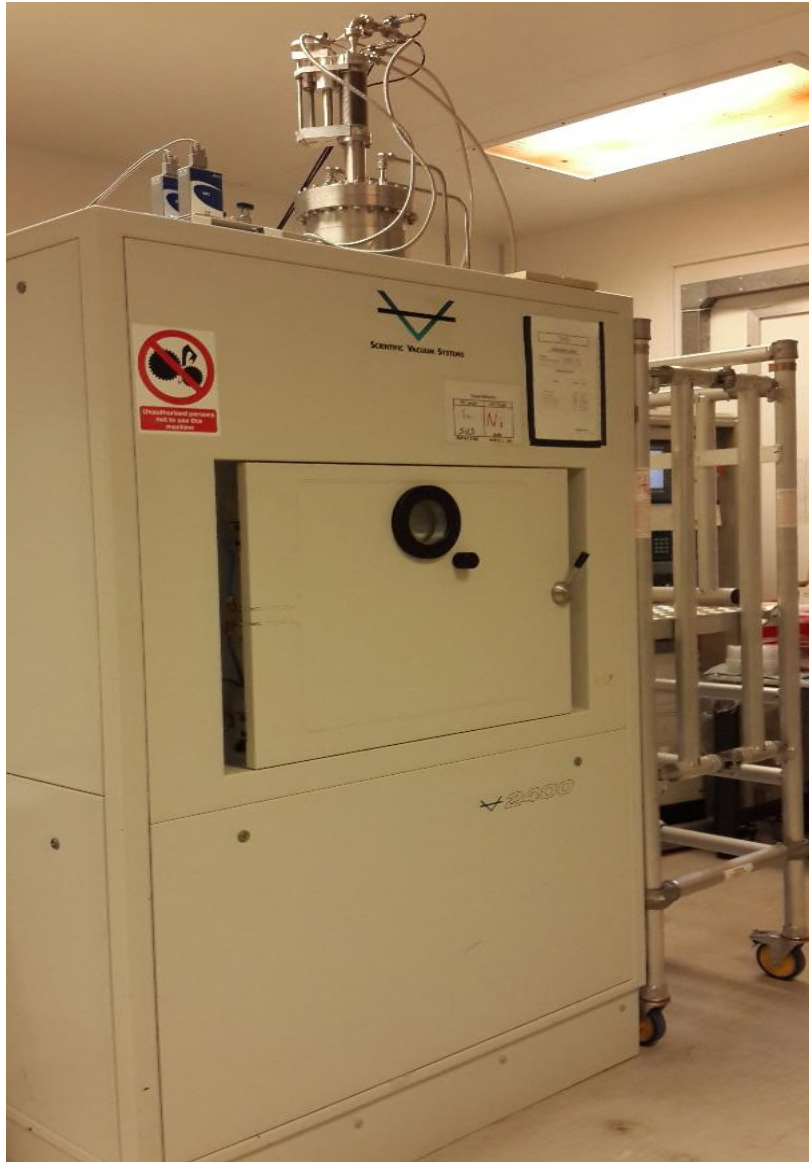


Figure 2-9: Mantis NanoGen Trio coupled to SVS main chamber

The mantis NanoGen Trio was connected to the main (SVS) chamber through the agglomeration chamber.

The magnetrons supplied the power via the cables energise the inert gas (e.g., Argon) which was supplied to the agglomeration chamber.

During energy exchange between the excited gas particles, the iron oxide targets attached to the magnetrons and suspended in the agglomeration chamber were bombarded by the charged Argon particles. As a result of the continuous energy

transfer among the gas particles and the targets, iron oxide atoms were ejected from the surface of the targets creating a plasma. Eventually, a stable plasma was formed and could be observed through a peep hole on top of the agglomeration chamber as a purple/pink glow. Following optimisation of parameters an equilibrium was attained, demonstrated by a pink glow of a stable plasma.

To establish the optimal conditions for the process to produce IONPs at room temperature, the sputtering parameters were optimised by varying the rate of argon flow (sccm), throttle position (%) and power = voltage × current.

As a high voltage was applied to the iron oxide targets, the plasma comprising argon atoms, positively charged argon ions and free electrons, was created after about 2 hours, increasing very gradually, the power to the magnetron. During the process of parameters optimisation, positively charged argon ions were continuously generated by electrons colliding with the argon atoms. As the iron oxide target is negatively charged, the argon ions were attracted towards the target. When the argon ions collided with the negatively charged target, iron oxide atoms were therefore released from the target surface in the process known as sputtering. The sputtered atoms of iron oxide continued to interact within the agglomeration chamber until the iron oxide atoms eventually attained a ground state and condensed and deposited on the PEG-coated silicon wafer (Figure 2-10).

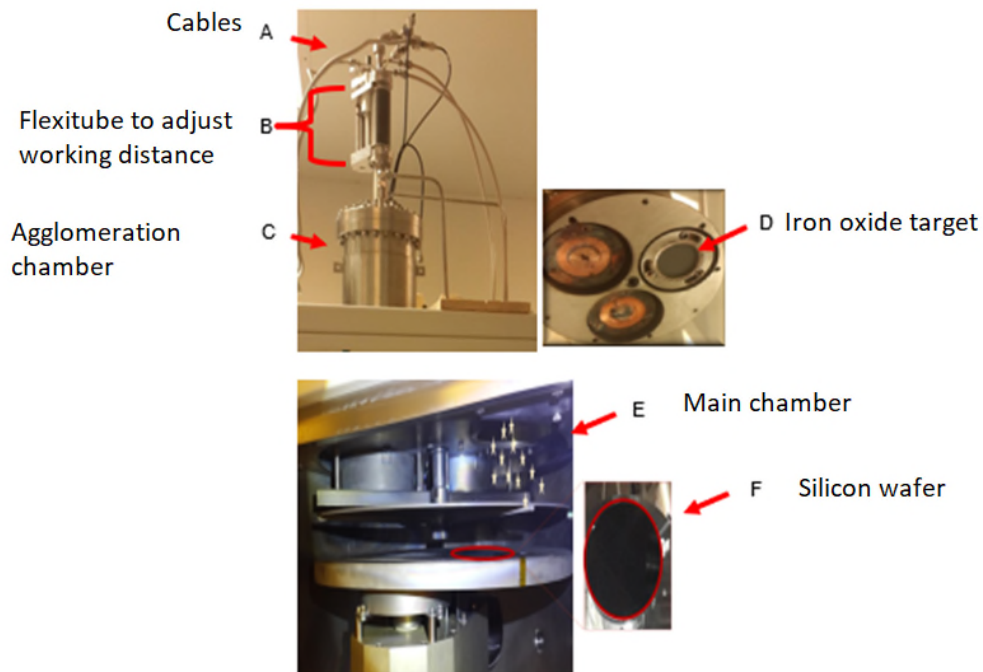


Figure 2-10: Generation of IONPs by inert gas condensation

As mentioned previously, the Mantis is supplied with cables (2-10 A) to transmit high voltage (HV) and current to the magnetrons in an electron beam. The Mantis is coupled to the scientific vacuum systems (SVS) main chamber, the flexi tube makes adjustable the working distance from the top of the Mantis to the magnetron head (2-10 B) which feeds into the agglomeration chamber (2-10 C). Suspended in the agglomeration chamber and attached to the magnetron is the iron oxide target (2-10 D) and sputtered iron oxide nanoparticles are channelled to the main chamber (2-10 E) as the iron oxide nanoparticles emerge from the Mantis aperture connected to the agglomeration chamber. The IONPs are eventually deposited on a substrate (2-10 F).

During the process of iron oxide nanoparticles production, nanoparticles optimisation and nanoparticles size pre-selection was performed using the intuitive MesoQ Controller software connected to a display panel (Figure 2-11).

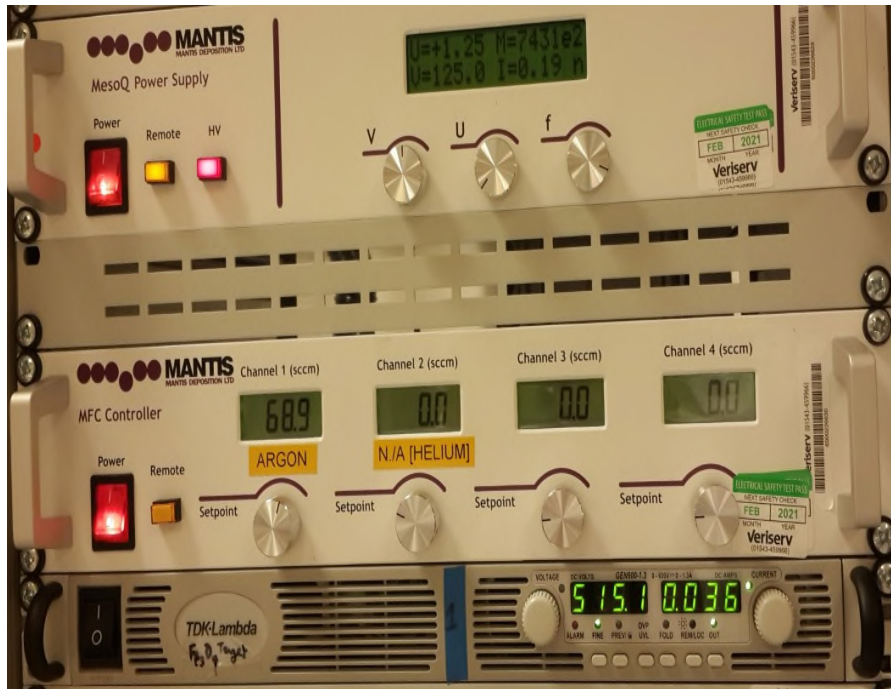


Figure 2-11: MesoQ Controller display panel

When the panel is turned on the display allows the control and monitoring of the nanoparticles production process. Buttons for power supply, current, voltage, argon and iron oxide targets enable monitoring of the sputtering process.

For this research, production of iron oxide nanoparticles that can permeate the cell membrane of tumour cells was achieved by optimising the process to obtain nanoparticles with a narrow and specific size. The preferred size of nanoparticles was then filtered via a set of channels within the apparatus, the quadruple filters, (Figure 2-12) through which the nanoparticles of pre-selected size are directed down to the substrate.

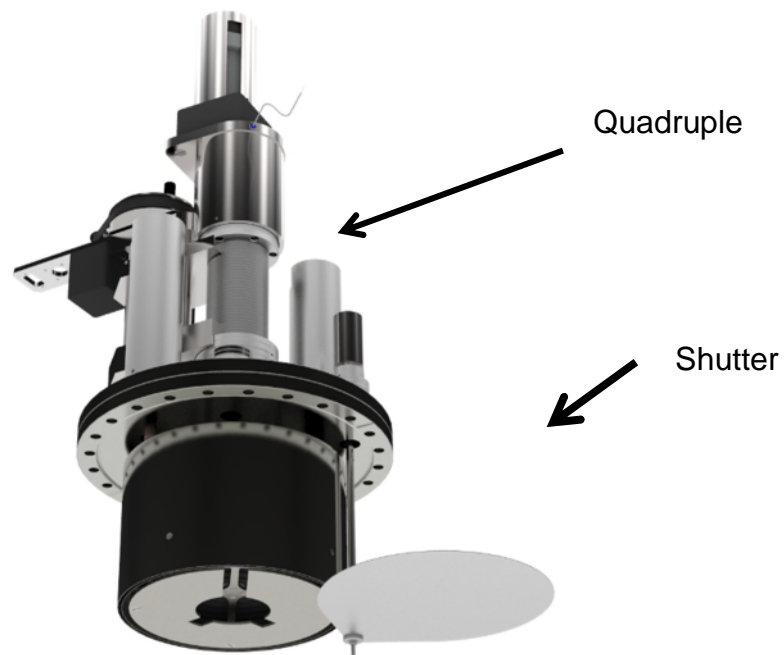


Figure 2-12: Nanoparticle filtration (www.mantisdeposition.com, 2019)

When the shutter was closed, the sputtered nanoparticles did not deposit on the substrate. The shutter can be controlled on the SVS panel (Figure 2-13) and seals off a section of the main chamber above the substrate. The shutter acts as a diaphragm, compartmentalising the main chamber. When the shutter is opened, the shutter moves such that the mantis source aligns with the silicon wafer substrate therefore sputtered nanoparticles can deposit directly on the substrate.

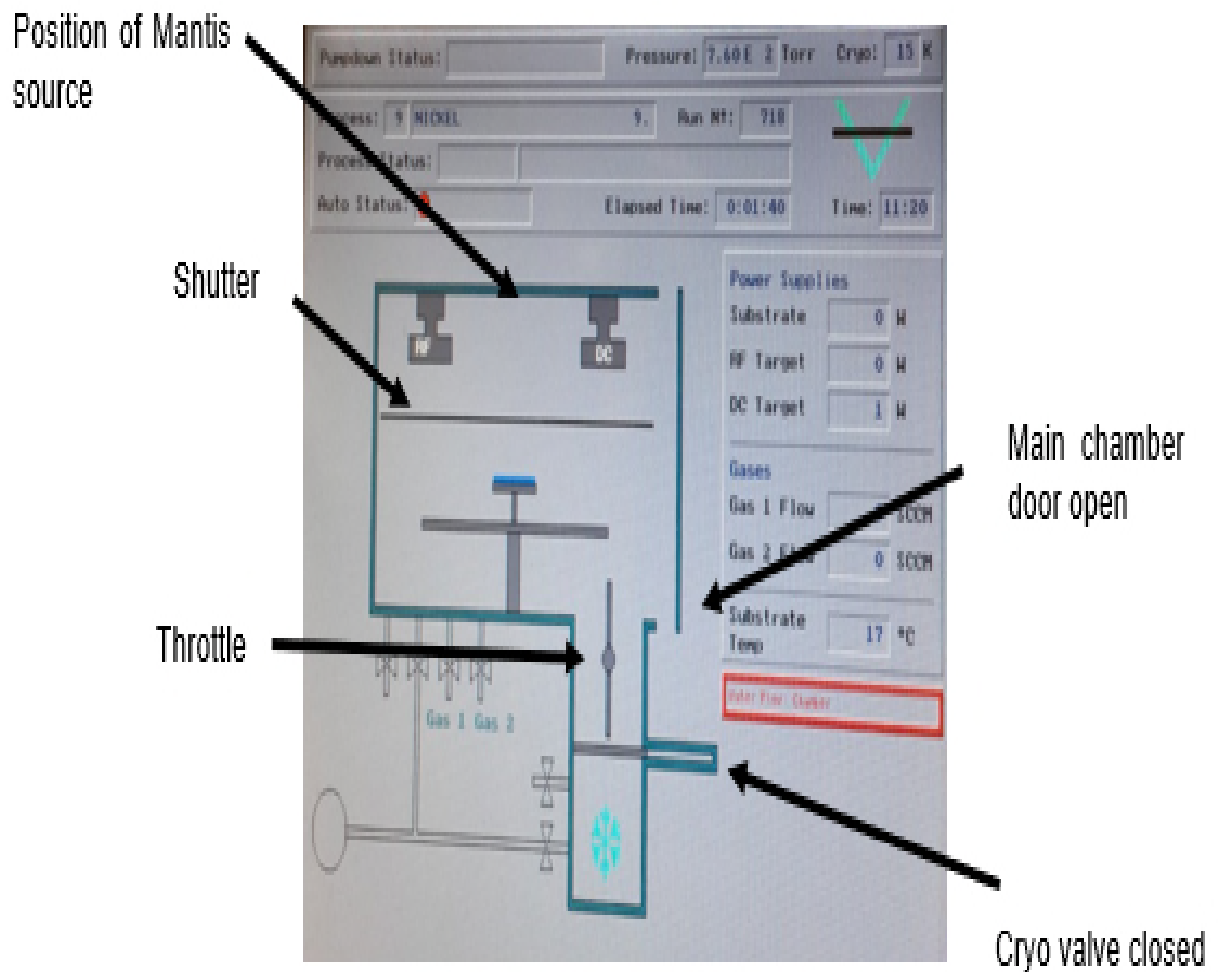


Figure 2-13: Scientific Vacuum Systems display panel

The SVS main chamber display shown in Figure 2-13 (above) was photographed when the main chamber had been vented, and just prior to loading of the silicon wafer. The door to the main chamber can be seen to be open while the cryo valve is closed off as the pressure in the main chamber was atmospheric (7.60×10^2 Torr) during loading of the PEG-coated silicon wafer or TEM grid (substrates). The throttle position was set at zero to reduce pressure in the main chamber while venting. The shutter had been left closed above the radio frequency (RF) and direct current (DC) sources not used in this research. This shutter when closed above RF and DC sources, leaves the Mantis source open for nanoparticles deposition. Though the mantis source is not visible in the section, Mantis was coupled between the RF and DC sources. Closing the shutter over the RF and

DC sources opens the Mantis source directly above the substrate for line-of-sight deposition of nanoparticles.

In another form of sputtering, reactive sputtering technique, chemically reactive gases mass react with both the effected target material and the target surface (Safi, 2000). In reactive sputtering a reactive gas is added to the inert gas in an electrical and chemical process to form a new material that deposits on the substrate.

2.3.9 Optimisation of sputtering process parameters

Before beginning the sputtering process, preliminary checks of the pressure in main chamber, throttle position and temperature were confirmed to be approximately 1.92×10^{-5} Torr, cryo Temperature 14-15K; Throttle 0%; Working distance (WD) 13.8 cm; Argon 10 sccm (flow rate). Sputtering was carried out at ambient temperature (approximately 25°C).

After a stable plasma had been achieved, pre-sputtering was conducted for 15 minutes with the shutter closed. Pre-sputtering was carried out to clean the surface of the target and to reduce the chances of contamination from residual particles due to any previous use of the mantis NanoGen Trio and SVS systems. During this research, iron oxide nanoparticles were sputtered using both low and high power (Table 2-1).

Table 2-1: Sputtering parameters

t ₀ minutes		t ₃₀ minutes		t ₆₀ minutes		t ₉₀ minutes		t ₁₂₀ minutes	
Volts (V)	Amps (A)	Volts (V)	Amps (A)	Volts (V)	Amps (A)	Volts (V)	Amps (A)	Volts (V)	Amps (A)
454.0	0.110	455.0	0.110	456.0	0.109	438.0	0.109	458.0	0.103
459.7	0.109	404.5	0.108	456.0	0.107	468.0	0.107	468.0	0.107
460.0	0.109	465.4	0.106	467.0	0.106	461.1	0.107	463.0	0.109
468.0	0.107	466.5	0.107	468.0	0.107	467.0	0.101	466.0	0.107

458.5	0.114	472.1	0.114	488.0	0.110	488.0	0.100	487.0	0.110
492.1	0.100	490.0	0.100	492.3	0.100	491.2	0.100	493.5	0.100
531.9	0.038	531.6	0.030	529.0	0.030	528.3	0.030	524.2	0.031

Following pre-sputtering, shutter was opened to expose the substrate to the mantis source to deposit IONPs on the substrate; the parameters were again noted as WD 13.8 cm; Throttle 50% - 80%; Argon 10-100 sccm; Pressure in main chamber approximately 2.74×10^{-3} Torr.

During sputtering, the process was monitored to control the power to the magnetron so as not to exceed 50 Watts, according to manufacturer's recommendations and to avoid melting the magnetron. An average of 20 Watts for low power sputtering and 45 Watts for high power sputtering was used to produce IONPs for this research. This was done by adjusting the current and finding the product of the current and the voltage. Each sputtering session did not exceed 2 hours to prevent the iron oxide nanoparticles from forming several layers on the substrate (Khanna et al., 2018) which would lead to tension and breaking off of aggregated, iron oxide nanoparticles.

Table 2-2 shows the parameters that were used to obtain a stable plasma with a particular iron oxide target and when the pressure in the main chamber was initially 2.59×10^{-3} Torr; at 15K with the throttle closed.

Table 2-2: Process parameters

Pressure main chamber (Torr)	Cryo pump Temperature (K)	WD (cm)	Throttle position (%)
2.84×10^{-5}	15	13.8 cm	0
5.30×10^{-5}	15	13.8 cm	50
2.99×10^{-4}	16	13.8 cm	60

1.90×10^{-3}	15	13.8 cm	70
-----------------------	----	---------	----

Following sputtering of soft – landed iron oxide nanoparticles on the PEG-coated silicon wafer, the wafer was removed from the main chamber of the SVS and submerged in 15 mL of RNase free water (obtained sealed from the manufacturer), then ultra-sonicated for 3 minutes at room temperature to dissolve the PEG-layer (Figure 2-14).

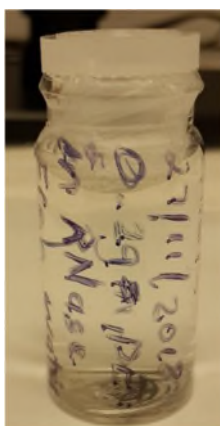


Figure 2-14: PEG-IONPs in RNase free water stored in a labelled container

The silicon wafer was first coated with PEG solution. The iron oxide nanoparticles were then sputtered on the PEG-coated silicon wafer. After sputtering the PEG-coated silicon wafer bearing sputtered IONPs was immersed in RNase free water to suspend the IONPs, in PEG solution. The sputtered iron oxide nanoparticles were first collected in a bottle and stored for a few days at room temperature (short storage time). For longer storage, the sample was transferred to a falcon tube and stored at -20°C to prevent microbial growth that might occur due to the presence of PEG.

Iron oxide nanoparticles sputtered directly on TEM grids along with the IONPs suspended in solution were characterised by TEM at The Open University, Milton Keynes, UK.

2.3.10 Characterisation of IONPs by TEM

The TEM grids used for the characterisation work were produced *in-house* by the Open University (Milton Keynes, UK), on paper backing (Figure 2-15).

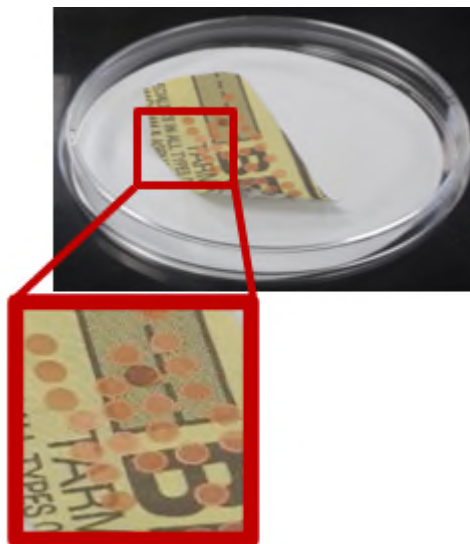


Figure 2-15: Plasma removal of TEM grids from the lining

The 3 mm copper TEM grids were made with a polymer base and then topped with carbon for added thickness.

Preparation of the TEM grids involved the use of Edwards 306 carbon coater machine Glo (plasma) discharge Island Scientific Ltd. (Isle of Wight, UK). The plasma treatment was used to make the carbon coating of the TEM grid more hydrophilic (Figure 2-16).



Figure 2-16: Glo plasma discharge to clean in-house TEM grids

Plasma treatment of the Tem grids was necessary to aid removal of the TEM grids stuck down by adhesive, from the paper backing, without damaging the TEM grid.

Fine tweezers were used to hold the TEM grids, while 20 μL samples of the sputtered PEG-IONPs dispersed in solution were deposited on the TEM grids using a micropipette and left to dry overnight (Figure 2-17).

Sputtered IONPs in
PEG solution

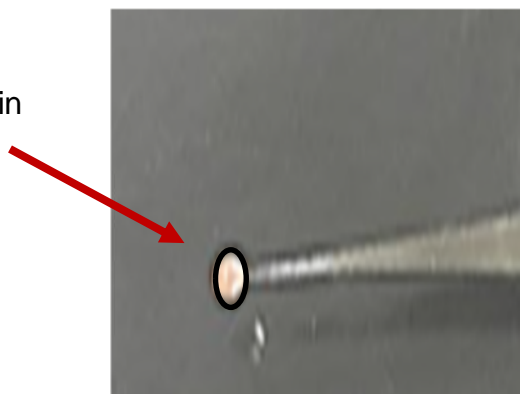


Figure 2-17: The drop of sputtered IONPs on the TEM grid

Once the sample was dry, the IONPs were characterised using TEM at 80 kV JEOL JEM-400 in collaboration with The Open University, (Milton Keynes, UK) (Figure 2-18).



Figure 2-18: Transmission electron microscope

Further characterisation of the sputtered IONPs was carried out by atomic force microscopy.

2.3.11 AFM characterisation of sputtered IONPs on bare silicon wafer

Atomic force microscopy (AFM) using equipment from Digital Instruments (Boston, USA) was one of the methods used to characterise the sputtered PEG IONPs dispersed in solution. The silicon wafer was first plasma cleaned to improve wettability and then ~200 μL of the PEG-IONP solution was deposited on the silicon wafer using a pipette. The drops were allowed to dry overnight. The topography of the silicon wafer blotted with sputtered IONPs in PEG solution was assessed by the AFM. The cantilever recorded changes in the surface between the coated wafer and the plain wafer in plasma cleaned silicon wafer.

An estimation of the size of nanoparticles, PEG IONPs was done by dynamic light scattering (DLS), one of the common methods using in estimating particles size in solution.

2.3.12 DLS characterisation of sputtered IONPs

Dynamic light scattering (DLS) investigations were carried out using the Malvern Instruments, Zetasiser Nano (Figure 2-19).

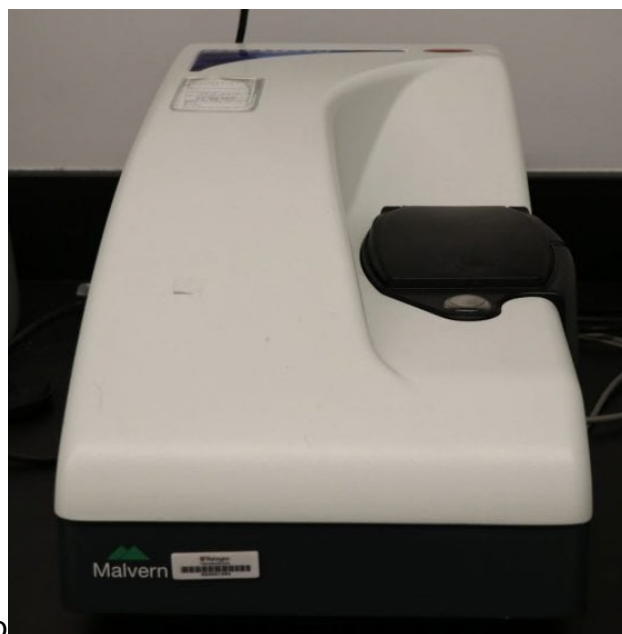


Figure 2-19: Dynamic light scattering (Malvern Panalytical Ltd., 2022)

DLS measurements were conducted to assess the PEG-IONPs size distribution and to measure by estimation, the amount of PEG surrounding the nanoparticles after production. Laser light reflecting off the particles in solution gave an indication of variation between samples.

To prepare the PEG-IONPs samples, the solution with dispersed PEG-IONPs, obtained after sputtering, was evaporated (3×) at 50°C for two hours in a centrifugal vacuum concentrator, Eppendorf 5301 from Sigma (Dorset, UK). This was done to concentrate the iron oxide nanoparticles suspended in the solution, so that the DLS technique might better distinguish between IONPs-PEG solution and PEG only solution. To prepare a control with just PEG, a substrate (wafer) was spin-coated with PEG (0.20 g/L) and directly dissolved in 15 mL of RNase free water with ultrasonication for 3 min. Then, similarly to the solution with the PEG-IONPs, this was concentrated (3×) by the vacuum concentrator and measured by DLS (Hemben et al., 2021). DLS measurements were done at 22°C with samples (1.2 mL) diluted 100-1000 (which is the range of concentration) in water. The sample volume measured is of the same concentration as the

concentrated sample mentioned earlier. Each sample was measured the sample to assess particle size, at least three times.

Further characterisation of IONPs size and concentration was carried out by Nanoparticle Tracking Analysis (NTA).

2.3.13 NTA characterisation of sputtered IONPs

Nanoparticle Tracking Analysis aided the visualisation of sputtered IONPs in real time. NanoSight LM20 from Malvern Panalytical Ltd. (Worcester, UK) (Figure 2-20) with a CCD camera and a red laser light was used to determine the size of the PEG-IONPs (obtained when the silicon wafer on which sputtered IONPs had been deposited was immersed in RNase free water, thus dispersing the sputtered IONPs in PEG solution) in RNase free water (concentrated 3×). The measurements were displayed by viewing the 'Thumbprint' via NanoSight 3.4 version software connected to a monitor display. At the start, before loading each sample, measurements were performed with 1 mL of 100 nm polystyrene to ensure proper functioning of the instrument.



Figure 2-20: NanoSight LM20 (Nanoparticle Tracking Analysis, 2021).

Next, 1 mL of each sample was injected into the instrument column and captured for 60s at a constant temperature of 22°C. Fractions of the same samples were

injected several times into the instrument to obtain 3-5 measurements for the calculation of an average result (Hemben et al., 2021). The number of measurements was determined based on reproducibility of the results during the initial measurements taken.

To compare the approximate concentration (particles/mL) of sputtered IONPs the NTA measurements were compared with those of powdered, commercial IONPs (CIONPs). Powdered commercial iron oxide nanoparticles (CIONPs) (5 g), with size range between 15-20 nm in diameter, were purchased from Nanomaterials Inc. (Texas, USA). The CIONPs were weighed (1 g), under a fume hood fitted with HEPA filter and placed in an Eppendorf tube. The remaining quantity (4 g) of powdered CIONPs was then labelled and stored in the hazardous chemical's cupboard. From the 1g aliquot, 5 mg was weighed under fume hood fitted with HEPA filter and suspended in 50 mL of RNase free water to produce a working concentration of 0.1 mg/mL. The solution was then uniformly dispersed using Branson ultra sonifier digital model 250 sonic probe, Branson Instruments (GA, USA) at 10% amplitude for 15 minutes at ambient temperature (25°C). Finally, the suspension was diluted in RNase free water to 0.001 mg/mL CIONPs (15-20 nm). NTA measurements were then taken.

2.3.14 MRI characterisation of water relaxation in the presence of sputtered IONPs

Sputtered IONPs were dispersed in RNase free water, concentrated 3 times (3x), dispensed into Nuclear Magnetic Resonance (NMR) tubes (5 mm) and placed inside 9.4T microimaging system Bruker (Coventry, UK). These measurements were done in collaboration with Sir Peter Mansfield Imaging Centre, University of Nottingham, UK. The samples were serially diluted using PEG (3 mg/mL) in RNase free water. The serial dilutions aided the construction of a range of concentrations to be tested. The samples were then placed in 5 mm glass NMR tubes. Central 5 mm slices were used for all T1, T2 and T* measurements. The 2.7-6.5 μM levels of elemental iron per mL were used to produce images for r1 and r2 (relaxivity ratio) determination. r1 value in the above iron concentration

range was evaluated from T1 values determined from spin-echo images collected with fixed echo delay (TE=30 ms) and multiple repetition delays (TR=380), 1383, 3383, 7383 and 15383 ms using exponential fitting built-in function in Prospa3.1 (Magritek, New Zealand) processing software. r2 value in the above iron concentration range was evaluated from T2 values determined from 30 spin-echo images collected with fixed echo delay (TE=30 ms) and a repetition delay TR 15383 ms using exponential fitting using built-in function in Prospa3.1 (Magritek, New Zealand) processing software. Similar methodologies to determine relaxivity of IONPs have been used before (Khaleghi et al., 2016; Metelkina et al., 2017). The r1 and r2 relaxivity were determined from linear fitting of both relaxation rates as a function of iron concentration in each solution of nanoparticles. The ratio of transverse to longitudinal relaxivity was used to assess the contrast efficiency of the particles for MRI. All measurements were performed at room temperature.

2.4 RESULTS AND DISCUSSION

2.4.1 Preparation of the silicon wafer substrate

To assess the volume of PEG spin coated on the surface, the wafers were weighed in triplicate before and after spin coating. The estimated difference in weight of the wafer before and after spin-coating was found to be 15.8 mg \pm 0.6 mg (Hemben et al., 2021), which was dispersed in 15 mL of RNase free water gave a concentration of PEG \sim 1 mg/mL.

Preparation of the silicon wafer as substrate for iron oxide nanoparticles deposition by inert gas condensation technique involved the use of polymer to coat the silicon wafer, both to obtain free-standing nanoparticles at the end of the process and to enhance the biocompatibility of the resulting IONPs (Baldim et al., 2019).

The silicon wafer was chosen as suitable material to deposit inert gas condensed IONPs as the wafer has been known to withstand the sputtering conditions in the main chamber of the SVS. Furthermore, coating the wafer with PEG enabled the sputtered IONPs to be obtained following soft-landing IONPs deposited on the

polymer film. As mentioned previously, once dissolved in RNase-water, the free-standing, PEG-coated IONPs were obtained. This preparation enabled the PEG to physically attach to the sputtered IONPs in solution, where the PEG forms a coat around the IONPs, preventing aggregation of IONPs and making them more stable in physiological conditions mimicked in this study. Another advantage of PEG is found in the polymer's ability to induce autophagy, which in turn protects against possible cytotoxic effect of IONPs.

During substrate preparation, contact angle measurements of the plasma cleaned, PEG-coated silicon wafer were carried out to characterise the spin-coated PEG layer. The measurements determined the contact angle of water and PEG on the thin film and plain silicon wafer to establish the hydrophobicity and hydrophilicity by measuring contact angle (Figure 2-21).

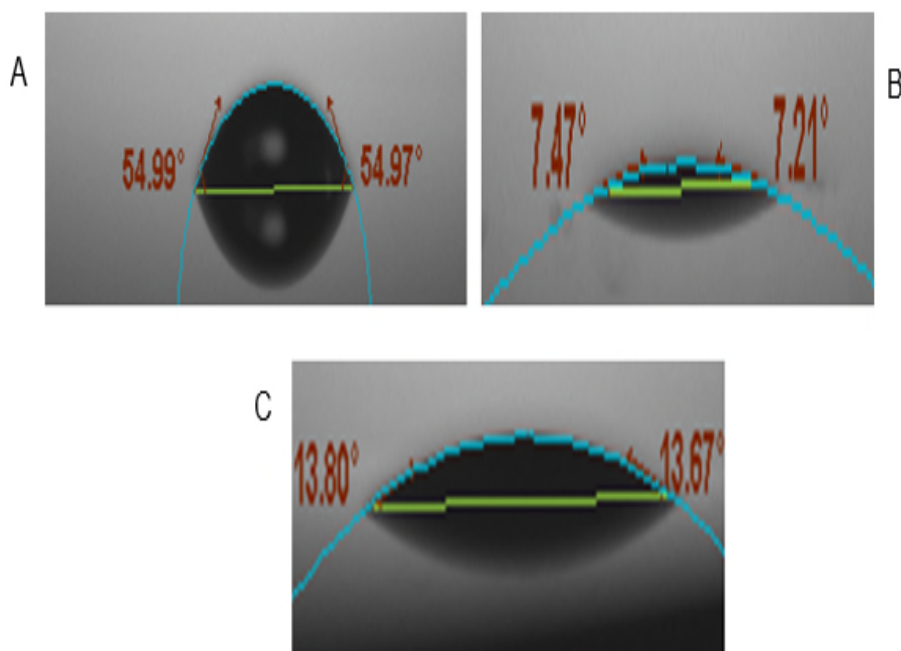


Figure 2-21: Contact angle measurements

The contact angle was measured by Attension software on bare silicon wafer (A) PEG-coated wafer (B) and IONPs deposited on PEG coated wafer (C) using a drop of de-ionised water, on the surface of the coated and plain silicon wafers, before sample application and after deposition of PEG on the silicon wafer. The

results showed that the contact angle value for the plain (not coated) silicon wafer was approximately 55°. The PEG-coated silicon wafer however, showed an approximate contact angle of 7.5°. Following, the inert gas condensation of IONPs on the PEG-coated silicon wafer, the contact angle measurement was seen around 14°.

The results suggested that the coating of the PEG on the wafer had been successful as the surface showed a more hydrophilic wafer surface when coated, compared to the plain, non-coated wafer (Hemben et al., 2021). Further change to the surface of the silicon wafer was seen following the sputtering process, suggesting that IONPs have been successfully soft-landed (by deposition of IONPs on the PEG layer) on the PEG-coated substrate.

As described in section 2.3.7, the DektakXT was used to measure the difference in thickness between the plasma cleaned silicon wafer and the PEG thin coat by taking 5 readings along the length of the scratch.

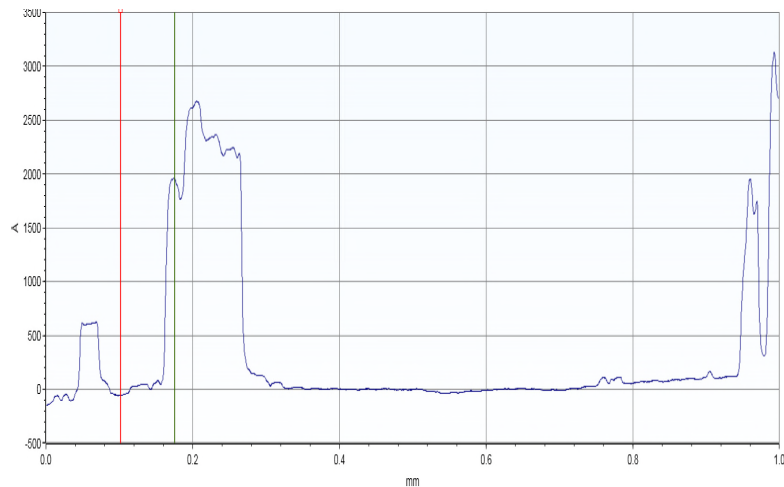


Figure 2-22: DektakXT profiler measurements.

One of the readings obtained along the scratch is shown in Figure 2-22. Four more readings are reported in Appendix C. The five readings were 0.201, 0.264, 0.268, 0.277 and 0.269 µm giving an average 0.256 ± 0.031 µm.

2.4.2 Production of IONPs by Inert gas condensation technique

Iron oxide nanoparticles were sputtered using Mantis NanoGen Trio using iron oxide targets attached to a magnetron and suspended in an agglomeration chamber filled with argon gas to which power was applied. The 1-inch magnetron was used to sputter iron oxide nanoparticles 1-6 nm with an approximate power of 20-49 Watts (Hemben et al., 2021), taking care not to exceed 50 Watts (Section 2.3.9). The size of the sputtered nanoparticles was determined while the IONPs passed through the quadruple MesoQ mass spectrometer. The sputtering results presented as spectral evolution graphs, show the current measured at the exit of the quadruple filter, against size of sputtered IONPs. The electrical current measured at the quadruple exit may be used as an indication of the number of particles of the selected mass that are being produced by the NanoGen trio source (Kusior et al., 2016). Later, during characterisation of the sputtered IONPs, size was determined by visualising TEM images. The advantage of using the Mantis NanoGen Trio system over other IONPs production methods is due to the option to pre-select, ahead of deposition, the desired size of nanoparticles. Results of the sputtered IONPs from target on magnetron source are shown in Figure 2-23.

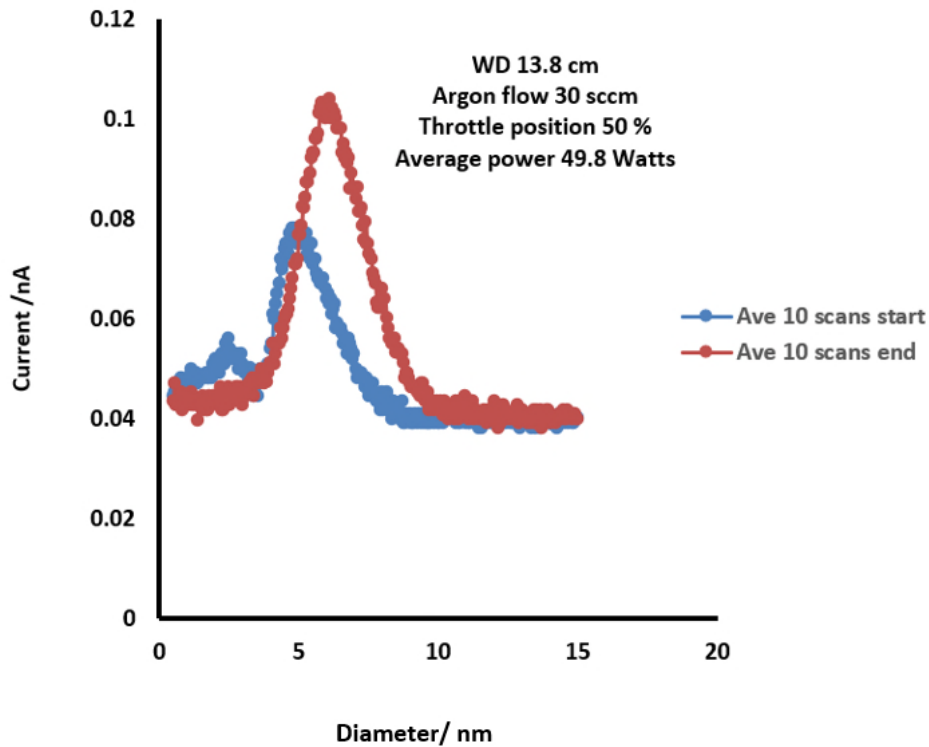


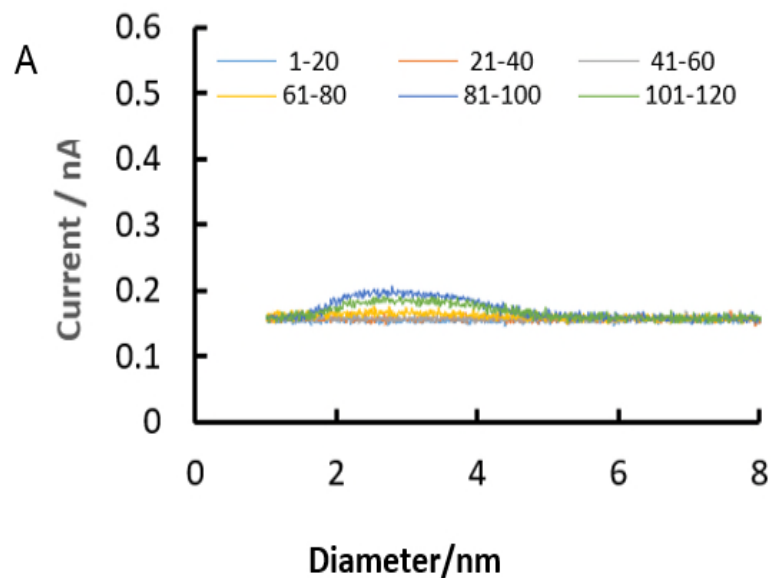
Figure 2-23: Spectral evolution graphs from IONPs sputtering

Spectral evolution graphs obtained from the sputtering of iron oxide targets were plotted in averages of 10 scans at the start of the deposition of IONPs on the substrate when the stable plasma had been achieved, and at the end of sputtering. At the start of sputtering and during the development of a stable plasma, the particles continue to interact in the agglomeration chamber and if a particular size is required to be sputtered, then the MesoQ controller software is set to the desired nanoparticles size and the shutter opened for the filtered particles to be deposited on a wafer.

Before the stable plasma was achieved, only a flat line (background noise) was observed. When a plasma was struck and maintained, spectral evolution graphs were seen. With a stable plasma, pre-sputtering was carried out as explained in the methods (section 2.3.8). As pre – sputtering was concluded, and the shutter was opened to deposit IONPs on the substrate.

At the start of the process, the throttle position was 0% while pressure in the main chamber was 2.89×10^{-5} Torr; 17K, WD 13.8 cm. During optimisation of process parameters, the throttle position was increased gradually to 70% while Ar gas flow was increased until the plasma was increased from 10 sccm to 96.8 sccm. One target was used to successfully produce nanoparticles even when the other two targets were not in use; an average of 20 scans was then plotted. The evolution scans are a representation of nanoparticles as they are being produced.

Process parameters were optimised in this research to confirm the size selection and the range for high power (40-49 Watts) and low power (19-20 Watts) sputtering (Figure 2-24).



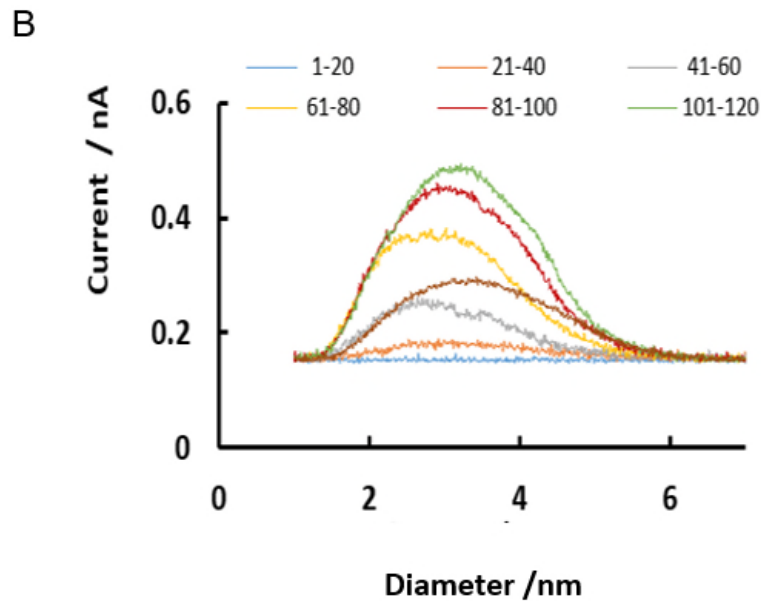


Figure 2-24: Spectral evolution graphs from low power sputtering (A) and high-power sputtering (B).

The low power sputtering shows spectral evolutions curves and therefore the formation of nanoparticles with a similar particle size distribution as for the high-power sputtering (Figure 2-23 and 2-24). The optimisation of the process parameters has helped to establish the repeatability of the process of obtaining particles with the desired size and size distribution.

High power sputtering was achieved when the stable plasma was established, while increasing the amount of energy applied to the magnetron. As the energy increase was made, the current generated by the nanoparticles in the Meso Q quadruple filter was also seen to increase in the spectral formation (maximum of 0.5 nA) indicating the presence of a higher number of nanoparticles formed. Low power sputtering on the other hand was achieved when the energy applied to the system was maintained at the first instance, and no further increase of energy was made to the process. In this second case, although nanoparticles were still formed in a slightly smaller range (~ 2-4 nm), a lower current (maximum of 0.2 nA) was observed indicating a much smaller production of particles.

Furthermore to investigate size pre-selection via MesoQ software, at fixed values of WD and temperature, size and size distribution of IONPs can be controlled altering the rate of flow of the Ar (Tang et al., 2003) in relation to the power and the throttle position. To assess the effect of the inert gas (argon) flow rate at fixed WD and room temperature (20°C), in this work, IONPs were sputtered using different Ar flow rates and by applying enough power to achieve a stable plasma. The parameters used for the optimisation process are shown in Table 2-3.

Table 2-3: Optimisation of sputtering process parameters

Throttle position (%)	WD (cm)	Argon flow (sccm)	Average power (Watts)
50	13.8	30	49.95
80	13.8	100	41.20
70	13.8	70	49.20

The effect of rate of flow of argon gas on the spectral evolution graphs is shown in Figure 2-25.

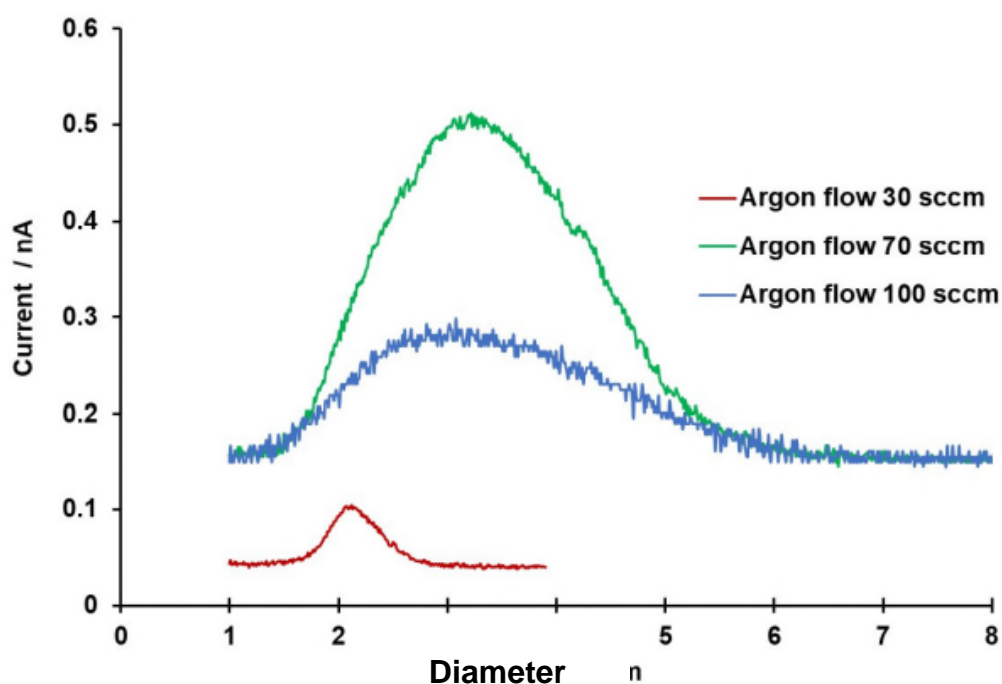


Figure 2-25: Effect of argon flow (30-100 sccm) on spectra evolution graph

During sputtering all data from the MesoQ controller and displayed on the monitor were exported to Excel. In graphical presentation, average of spectra was used to represent the evolution of the sputtering process. An average of 20 scans was usually plotted to visualise the results.

The results showed that IONPs production was not as high when lower argon flow rates were used (e.g. 30 sccm) and the production was at its maximum with the intermediate values of flow rate tested (70 sccm), when currents higher than 0.5 nA were recorded. The Ar flow rate seems to affect not only the number of nanoparticles produced, but also their size and size distribution. In fact, at an argon flow rate of 30 sccm IONPs with size around 2 nm were sputtered, while flow rates of both 70 and 100 sccm produced particles with size between ~ 1–6 nm. Therefore, by adjusting the sputtering conditions, the process can be repeated to obtain IONPs with the desired dimension and size distribution.

Inert gas condensation sputtering technique has the advantage of size pre-selection, whereas in other wet methods of nanoparticles production such as

green synthesis, using plant extracts, the nanoparticles yield and size range is not predetermined (Kanagasubbulakshmi and Kadirvelu, 2017).

During the sputtering process, once the plasma had been struck, the current stabilised on the MesoQ power supply display and the voltage trended downward before stabilising for a given current and gas flow (mantisdeposition.com, 2019). After the plasma had struck the power of the sputtering process was maintained by adjusting the 'current' knob.

For this research, it was found that a single target could potentially be sputtered for a total of 40 hours before changing for a new target. This estimation was made during inspection of the magnetron following about 20 hours cumulative sputtering. Most of the runs were conducted using one target only (as mentioned earlier) as this was successful in sputtering and deposition of nanoparticles. Also, in opening the main chamber after a sputtering session, care was taken to using gloves and a fine dust mask.

The higher the throttle position, the higher the pressure and the more frequent was the collision of argon gas and iron oxide particles in the plasma. Also, increasing the argon flow up to stable plasma increases the carrier gas concentration. Excess argon can have a damping effect on the plasma, reducing the deposition rate. Finally, sputtering power is determined by adjustment of the current to the magnetron. Optimum parameters for the sputtering IONPs for the purpose of this work is argon flow of 70 sccm, throttle position of 70 %, WD 13.8 cm and approximately 45 W. Higher working distance allows more time for the agglomeration of IONPs before they regain the ground state and deposit on the wafer. The optimised parameters showed highest yield with respect to spectral evolution at 70 sccm of Ar, 13.8 cm working distance. These conditions gave an estimated yield of 0.5 $\mu\text{g}/\text{mL}$ in 1 mg/mL of PEG (which became 1.55 $\mu\text{g}/\text{mL}$ in 3 mg/mL of PEG following 3 \times concentration) after a total of 2 hours sputtering on a combination of 3 substrates.

To achieve similar coating effect on the wafer, low intensity sputtering may be used for longer than 2 hours, while high intensity sputtering may be used for up

to 2 hours. If the deposition is performed for longer than 2 hours, the IONPs will start creating layers and adhere to one another. A thin coating is therefore recommended for the purpose of obtaining PEG-coated free-standing IONPs suspended in RNase free water. Performing sputtering for longer time might also cause particles' aggregation and mechanical means of dispersion may be then required.

Using one target reduced the risk of losing multiple targets due to cracking because of the thermoplastic refractory properties of iron oxide. Thermoplasticity is a feature of the target material in its bulk form. Once ramping down of the process takes place, a very gradual decrease of energy is required so as not to crack (as a result of too rapid heat change) the target, which upon inspection may need to be replaced. Iron oxide is often described as a ceramic. The targets thus require a very gradual increase and decrease of power at the beginning and end of the process. Monitoring of the process during sputtering was necessary to retain the power at or below 50 Watts during high intensity sputtering (to prevent the 1" magnetrons from melting). The manufacturer's recommendation is not to exceed 50 Watts sputtering power. In low powered sputtering at around 10 Watts, the voltage was monitored to maintain a steady plasma. Sputtering parameters varied slightly per session along with Argon flow (sccm) and throttle position at 50 – 70%.

Although in this work the sputtering was performed for two hours, the time needed to fully use up an iron oxide target (by sputtering) however, was estimated to be approximately 40 hours, by which time the target will have worn thin. This assumption was made while changing targets and replacing with new ones. Also, during replacement of used target for new ones, the vacuum seal (Figure 2-26) had also to be replaced for a new one as it was seen to have worn down around the edges.



Figure 2-26: Worn vacuum seal

During the changing of the seals, the magnetron head was inspected and the areas surrounding the target and target holder was found to be covered in deposits of iron oxide, which were then washed and polished using sandpaper and tap water under the fume hood.

The change of targets is necessary to replace worn targets with new ones. Generally, for the iron oxide target, a new one is required after about 40 hours of sputtering. During target change, targets may be seen to have cracked due to thermal plasticity resulting from rapid loss of heat from the target at the end of the sputtering process. Cracked targets when removed from the magnetron head tend to fragment (Figure -2-27).



Figure 2-27: Broken iron oxide target.

A target cracked by due to rapid cooling will break once it is removed from the magnetron to which it was attached during sputtering.

The ceramic nature of the iron oxide target makes it a brittle target to sputter, therefore the power used for sputtering must be ramped up very gradually. Likewise, the ramping down of the power at the end of sputtering session must be very gradual (approximately 0.01V per minute).

This sputtering process requires a lot a patience, especially with iron oxide. Iron oxide is not a quick material with which to establish a stable plasma and the entire process from start to finish can take up to 6 hours (2 hours for ramp up, 2 hours for sputtering with stable plasma and the last two hours for a gradual decrease of energy to the system and final ramping down).

While replacing targets and vacuum seals (mentioned above), it is recommended to clean the target holders (in vacuum chamber) to remove the build-up of sputtered nanoparticles (Figure 2-28).



Figure 2-28: Target holders before (A) cleaned after sputtering (B).

During IONP generation, the target seating (the component in B) can get fouled over time. During the target changing process, the seating is cleaned along with the target holder (the larger component in A) to remove accumulated masses of IONPs which have become stuck to the components. Cleaning is carried out

gently using non-flammable material and water as friction could cause the deposit to ignite.

During the optimisation of the process parameters, the targets were regularly removed and checked for wear. Worn targets present a risk of sputtering through and causing damage to the magnetron head.

In a similar sputtering study, it has been shown that by adjusting the parameters of the process—such as the pressure in the aggregation chamber, the ratio of He to Ar gas, and the magnetron-sputter power—NP mean diameter can be tuned from 1 to 100 nm (Sundararajan et al., 2014 ; Xing et al., 2016; Xing et al., 2017). Notably, also NP ferromagnetic properties can be changed by ion irradiation (Jiang et al., 2011; Vernieres et al., 2017).

Furthermore, the farther the distance (WD) between the magnetron head and the agglomeration chamber, the larger the size of IONPs produced (mantisdeposition.com- accessed 2019). In this research, the WD was fixed at 13.8 cm, which is the maximum adjustable working distance of the flexi tube from the top of the magnetron head to the target. The maximum WD of 13.8 cm keeps the IONPs in the interactive phase with the argon gas for as long as possible, to keep the sputtered IONPs for as long as possible in the agglomeration chamber during the 2-hour sputtering session used to produce IONPs in this work.

During sputtering, it was also found that parameters such as current and voltage needed to establish a stable plasma, varied within a small range (Table 2.1). The variation was attributed to the age of the target, new targets taking longer to strike a stable plasma than previously sputtered (used) targets. The iron oxide target can be used to produce nanoparticles for up to 40 hours in total, before changing targets, and vacuum seal. For this reason, some variation can occur in the absolute values of current and voltage, as the target wears down with continued use. For this research, 2 hours of sputtering were applied to the target to produce IONPs, and IONPs produced from the various sputtering sessions were all suspended in PEG solution. Adjustment of the current was therefore necessary

to maintain the stable plasma while making sure that the power (current × voltage) did not exceed 50 Watts.

During the process to obtain a stable plasma, throttle position was progressed from 50%, 60%, 70% and even 80% to increase pressure in the main chamber during pre-sputtering, and before striking plasma. When sputtering IONPs, one or all the three magnetrons could be used. Using all three targets at the same time may shorten the time of sputtering to <2 hours to obtain a thin layer of IONPs on the PEG-coated wafer. In addition, the powering of three magnetrons simultaneously will increase the output of energised argon whose molecules hit the targets and eject the particles into the agglomeration chamber, thereby increasing the intensity of the sputtering. This can be a suggestion for further work to investigate spectral evolution resulting from the use of multiple targets simultaneously.

Iron oxide nanoparticles produced by inert gas condensation and suspended in PEG solution were characterised by TEM, AFM, DLS, NTA and MRI.

2.4.3 Transmission Electron Microscopy (TEM)

NanoGen Trio iron oxide sputtering (2 hours) of nanoparticles has shown that free standing IONPs (1 – 6 nm \varnothing) soft -landed on thin film, PEG-coated silicon wafer can be achieved. After dissolution of the PEG-coated silicon wafer and sample preparation as described in section 2.3.1, IONPs were visualised and nanoparticle size was analysed by TEM at The Open University, Milton Keynes, UK and comparison made with blank TEM grid (Figure 2-29).

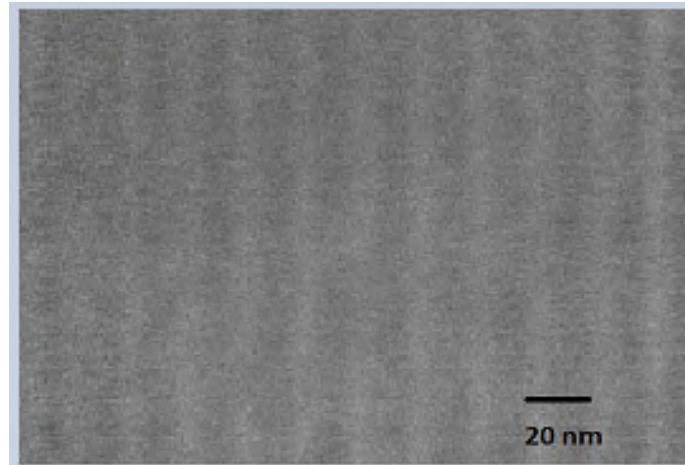


Figure 2-29: Bare TEM grid

A bare Cu TEM grid was visualised. The TEM grid was not coated with IONPs nor PEG and was scanned by electron microscopy to see the structure of the grid for later comparison with the coated TEM grid. The bare TEM grid is not coated with a film.

Next, the samples prepared as explained in section 2.3.10 were characterised by TEM (Figure 2-30).

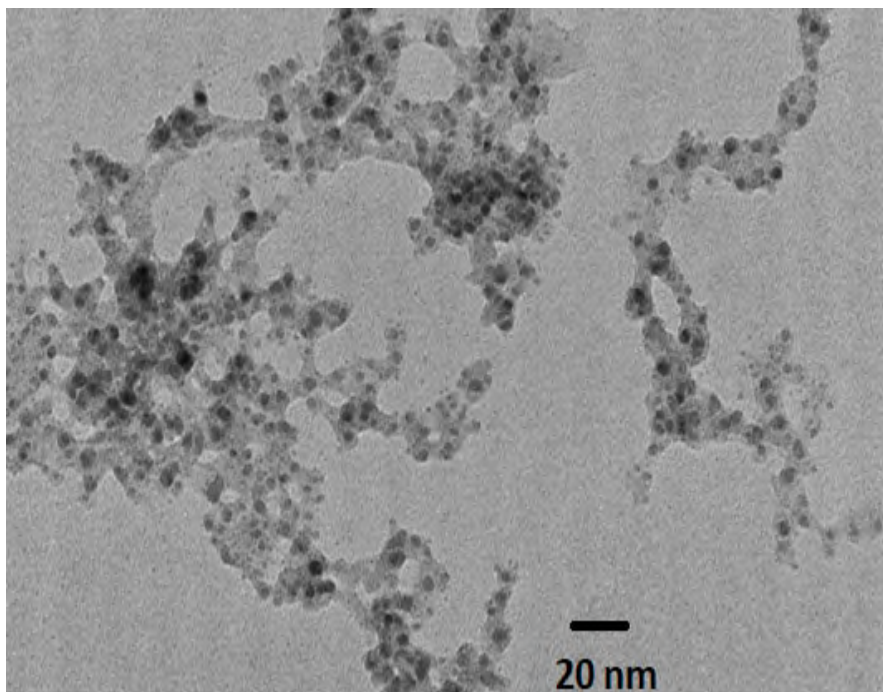


Figure 2-30: PEG coated IONPs dried on the TEM grid.

As mentioned above, 20 μL of sputtered IONPs in PEG solution was air dried on a TEM grid and viewed under the TE microscope (Figure 2-30). The dried-up PEG seemed to have trapped the sputtered IONPs on the TEM grid during the drying process. Nevertheless, most of the IONP cores can be individually seen, discounting the presence of multi-core NPs. Furthermore, to visualise better individual, stand-alone sputtered IONPs, it was necessary to conduct further experiments.

Therefore, in another experiment, IONPs were sputtered directly on the Cu TEM grid (Figure 2-31). The figure shows that the size of IONPs sputtered directly on bare TEM grid was around 5-6 nm were sputtered. The image also shows almost spherical IONPs.

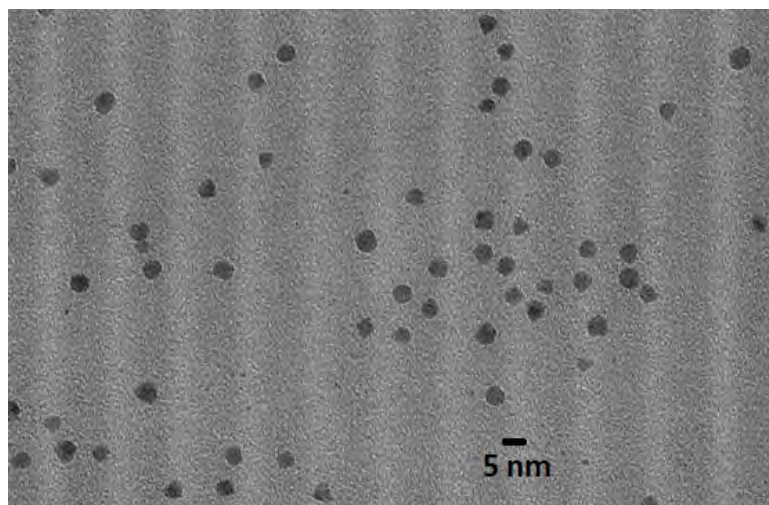


Figure 2-31: Sputtered IONPs directly on the TEM grid.

Further experiments were conducted to demonstrate soft-landed sputtered IONPs on a PEG-coated TEM grid (Figure 2-32).

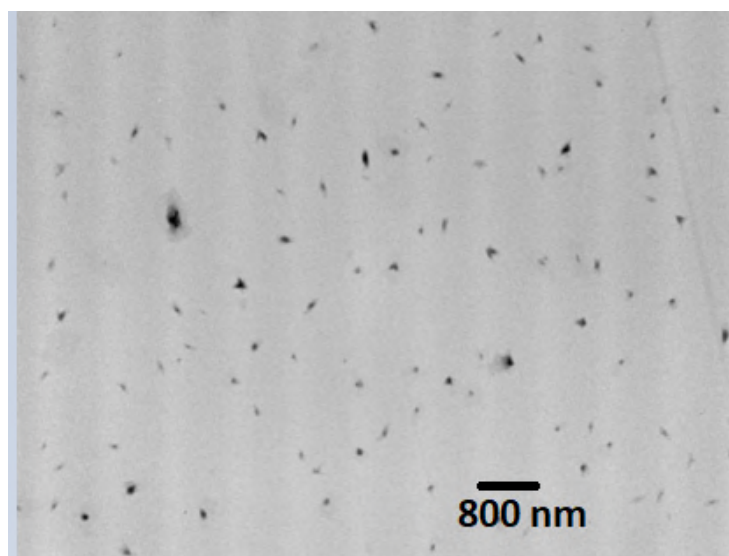


Figure 2-32: Soft-landed sputtered IONPs on a PEG-coated TEM grid.

The TEM grid was dipped in PEG solution prepared in section 2.3.2, before the IONPs were sputtered on the PEG layer. The figure shows that the sputtered

IONPs were successfully deposited on a PEG-coated TEM grid. In fact, the indentations of the IONPs landed on the PEG layer can be clearly seen.

TEM imaging has been widely used as a characterisation technique for iron oxide nanoparticles (Nwoko et al., 2019). The sputtered IONPs characterised by TEM in this work were seen encapsulated in PEG as a dried sample, as the preparation of the samples was applied to a TEM grid and allowed to dry. The sputtered IONPs which were deposited directly on the TEM grid offered clearer images of the soft-landed IONPs, embedded in the PEG layer (Figure 2.32). Soft-landing of IONPs on a PEG-coated silicon wafer enables the suspension of IONPs by washing the coated wafer in RNase free water to produce PEG-IONPs solution. The sputtered IONPs deposited directly on the bare TEM grid (Figure 2-31) produced the clearest TEM images of all, as the distinct form of spherical IONPs was seen.

This novel method of producing IONPs by inert gas condensation (for the purpose of producing a nanocarrier complex) has demonstrated the production of IONPs with better control in size and morphology than the nanoparticles produced by wet methods. As mentioned in section 1.5 (in Table 1-1), other methods of producing nanoparticles give rise to nanoparticles ranging in size from 15-100 nm.

The generally accepted size for nanoparticles used in cancer therapy is between 5 and 100 nm, as too small and the particles may easily be removed from circulation by the body's excretory processes, while too large particles will result in the retention of nanoparticles in the bodies organs. In this research the nanoparticles produced are between 1 and 6 nm diameter, which is very close to the desirable size for intracellular drug delivery (10 nm) (Feng et al., 2018). Such a narrow size distribution is also desirable because it helps in predicting the pharmacokinetics and biodistribution profile, which are highly size dependent (Han, 2016). The IONPs produced in this work are produced in a size- controlled manner which can be pre-set in the MesoQ instrument to obtain a specific size or size distribution of IONPs. This statement is supported by the TEM image of 5

nm sputtered IONPs shown in Figure 2-32. Producing IONPs in this way can be more efficient and inexpensive as the use of chemical precursors (Nikam et al., 2018) is not necessary and also, once the plasma has stabilised, a 2-hour process is sufficient to produce a batch of IONPs that does not need further purification and can be visualised, suspended in PEG solution and characterised. This method of producing IONPs also lends versatility to the production of IONPs with potential for various characterisation techniques and which may be obtained in a range of pre-selected or targeted outcomes. Wet methods however have the disadvantage of not being easily scalable and reproducible, as the changes in volume of chemicals and reagents tends to affect size and morphology (Nikam et al., 2018). This is not so with inert gas condensation as the production of sputtered IONPs can be increased by increasing the time by other 30-60 minutes (before multi-layers formation) to achieve more than 0.5 $\mu\text{g}/\text{mL}$ IONPs in 1 mg/mL PEG solution, once the deposit of IONPs has been washed and the IONPs suspended solution. In addition, more than one PEG-coated wafer in the main chamber during a sputtering session may increase the production rate of IONPs. Fortunately, the source material for top to bottom production of IONPs is 99% pure iron oxide target, ensuring that there is no need for further purification of the sputtered IONPs. During chemical synthesis, conventional heating generates a thermal gradient in the reaction solution in the absence of efficient mixing; this can alter the local nucleation and growth of the nanomaterials and could lead to variations in shape and size distributions (Nikam et al., 2018). Next, characterisation of sputtered IONPs was conducted by AFM.

2.4.4 Atomic Force Microscopy (AFM)

AFM was used to characterise the surface of the plain and IONP – coated silicon wafer to determine topographical changes on the surface of the substrate (Figure 2-33).

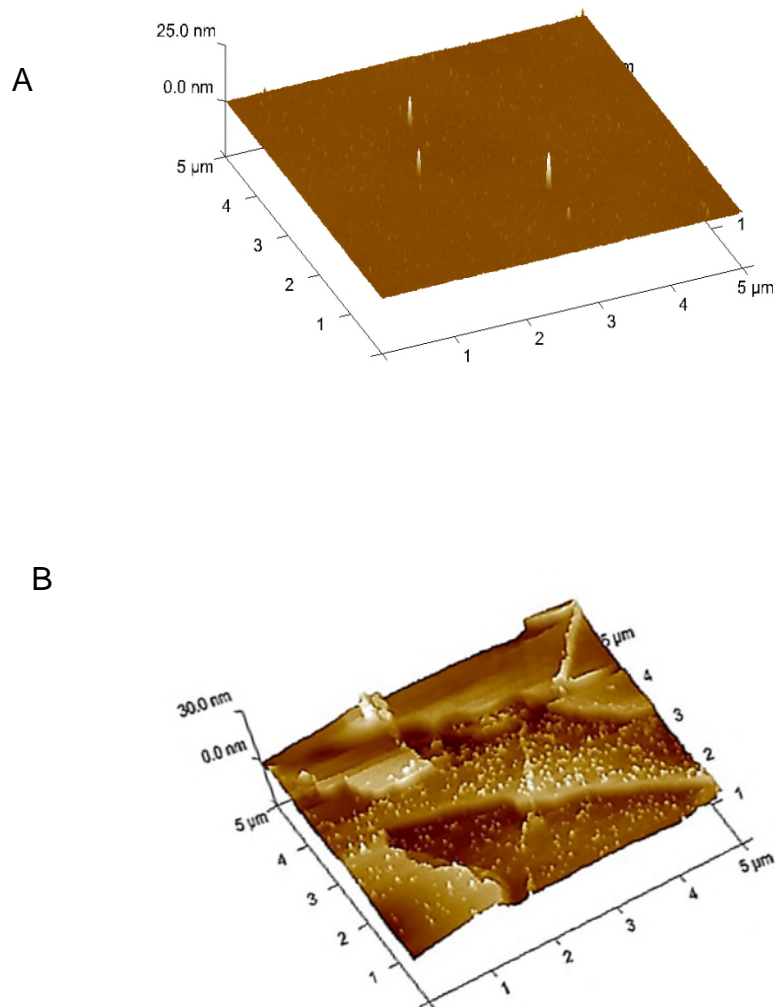


Figure 2-33: AFM of bare silicon wafer (A) and PEG-IONPs on the substrate (B).

The AFM showed a difference between the surface for the wafer that had dried sample of PEG-IONP and the plain wafer. The AFM was not intended to determine the thickness of PEG layer, but to visualise the change on the wafer surface. The preparation of PEG-IONPs suspended in RNase free water was blotted on the silicon wafer; the PEG IONPs solution was dropped on the surface of the silicon wafer and air dried, as described in section 2.3.11. Dropping was necessary to avoid the lifting of the PEG while carrying out the AFM measurements. The AFM technique helped to assess the variation of surface

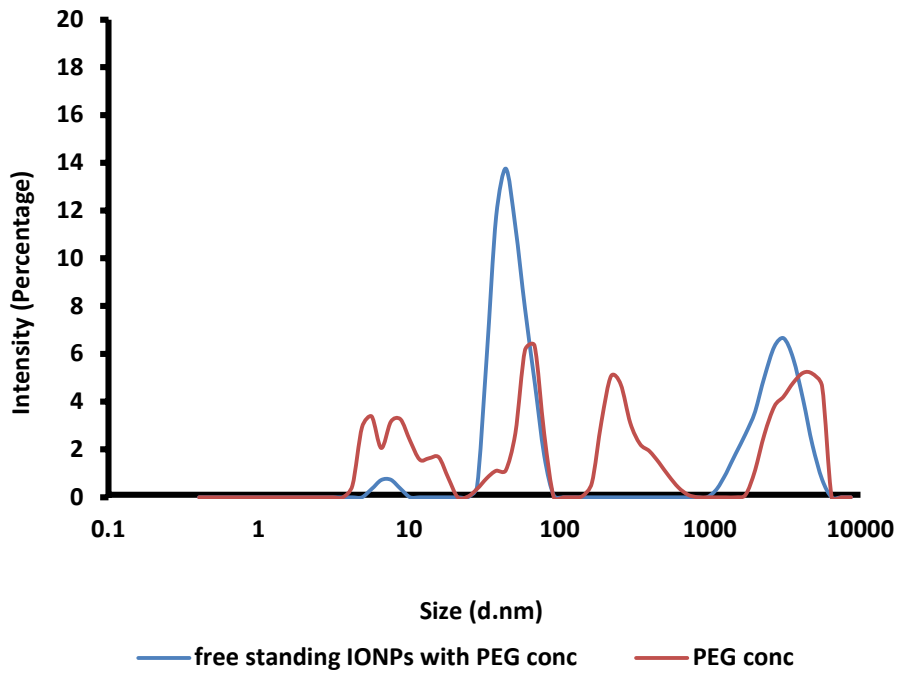
topography with deposition method via direct sputtering on PEG- coated plasma cleaned silicon wafer.

The AFM analysis showed bright spots on the surface of the wafer that had blotted-on sample of PEG-IONPs, when compared with the wafer that had no sample dried on it. Atomic force microscopy was used in this work to characterise (Zhang et al., 2015) sputtered IONPs in a blot by applying the solution of pegylated, sputtered IONPs (100 μ L) to the surface of the silicon wafer. It was imperative to blot rather than sputter onto the silicon slice as the PEG layer would have been picked up by the tip of the cantilever. Soft-landing sputtered IONPs on a silicon wafer and the blotting of the sample enabled some visualisation of the sputtered IONPs on the surface of the silicon wafer for the purpose of characterisation of the sputtered IONPs.

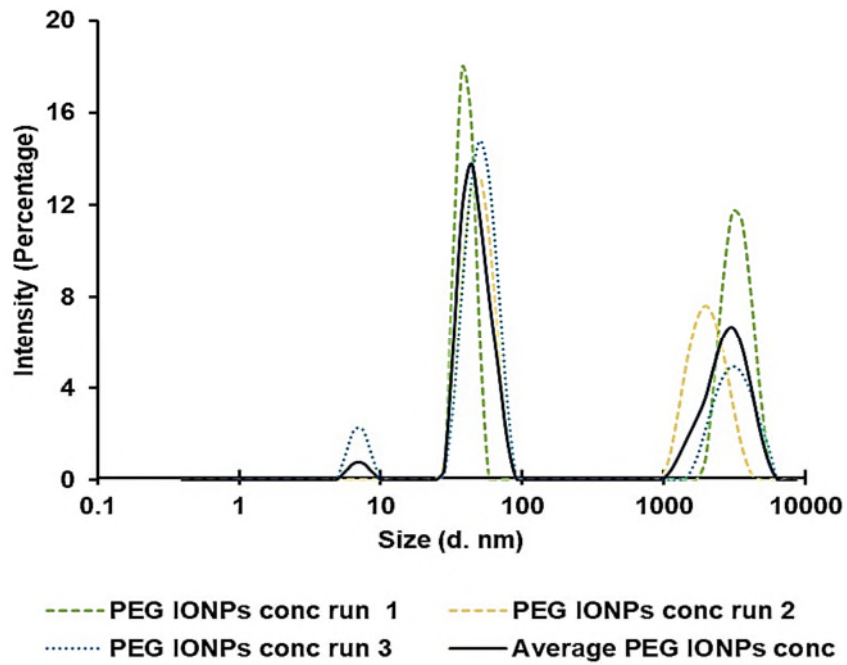
2.4.5 Dynamic light scattering (DLS)

DLS technique was used to estimate the size and size distribution of the PEG-coated IONPs. In addition, a solution containing only PEG, prepared as described in section 2.3.2, was also concentrated 3 times, and measured as the control (Figure 2-34A). The concentration of both PEG solutions was approximately 3 mg/mL.

A



B



C

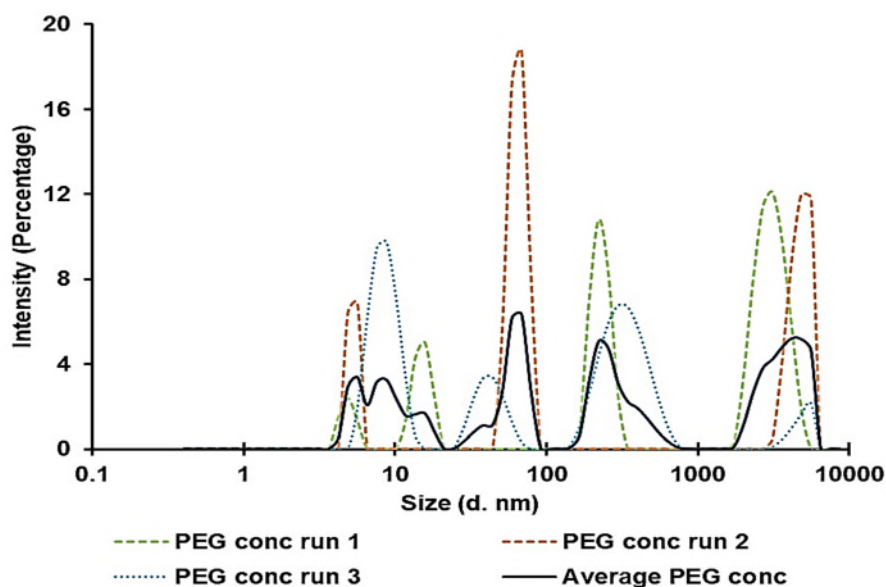


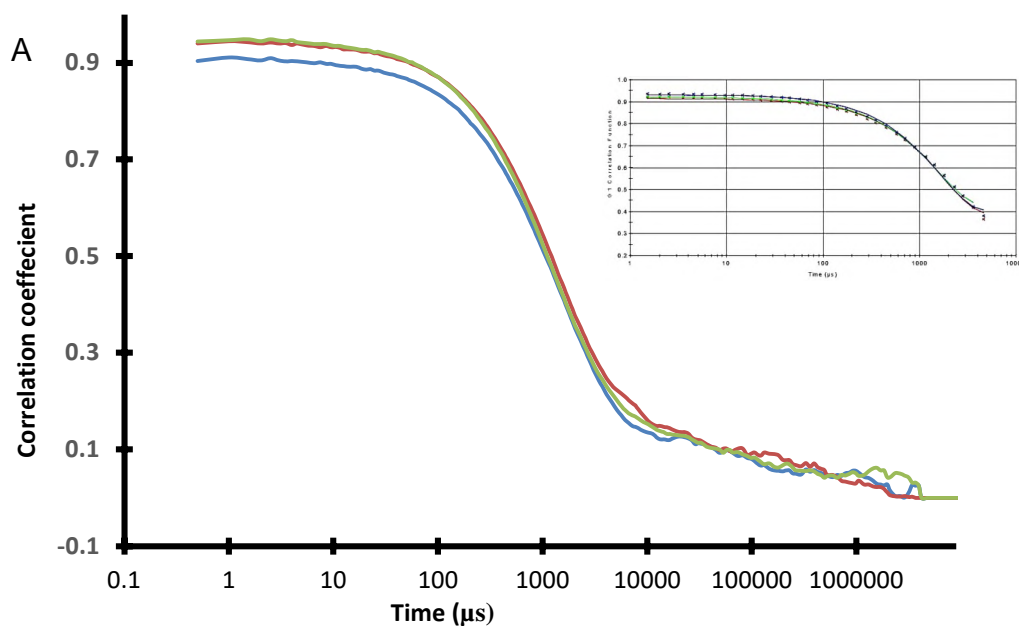
Figure 2-34: Dynamic light scattering of free standing IONPs in PEG Vs PEG alone (A), concentrated PEG-IONPs solution (B) and concentrated PEG solution (C), as control. Averaged signal as well as individual runs are depicted (Hemben et al., 2021).

Figure 2-34 A shows variation in peak size between free-standing IONPs and the PEG concentrated samples. Furthermore, there are distinct peaks in the PEG IONPs, solution at 7 nm (bare IONPs), 47 nm (IONPs coated with PEG) and over 2860 nm (most likely aggregation of PEG).

In the above results, the three measurements of PEG only samples demonstrate a large variability on the sizes of the particles seen (Figure 2-34C). This is likely due to an actual absence of nanomaterials present in the PEG only sample and the attempt of the machine to measure nanoparticles anyway. In the case of PEG-IONPs, however, the DLS measurements seem more reproducible with less variation at specific points, implying that there are IONPs contained in the samples (Figure 2-34B).

There was also a polydispersity index (PDI) of 0.707 ± 0.098 , for the PEG-IONPs solution. The DLS measurement of the PEG solution shown in Figure 2-34C depicts a collection of peaks with a higher PDI (0.846 ± 0.160) possibly demonstrating the absence of discrete nanoparticles.

DLS correlograms and cumulative fits are good indicators for the quality of the measurements. Therefore, for both types of samples these two were also analysed to better understand the origin of the peaks observed in the PEG only solution. Whereas the correlograms and cumulative fits of three consecutive measurements of the PEG-IONPs sample (shown in Figure 2.35A) are consistent and demonstrated a decent fit (see inset), those of the PEG only sample (Figure 3.5B) are highly variable and present a much worse fit (see inset). This means that the PEG only sample is not suitable for DLS analysis due to the lack of discrete nanomaterials and the peaks identified cannot be trusted.



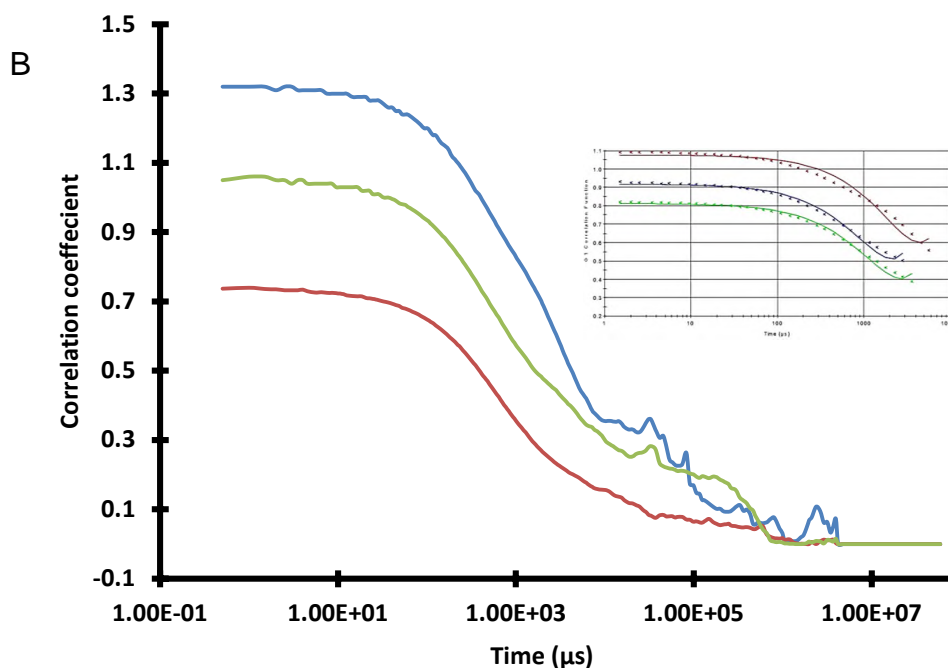


Figure 2-35: DLS correlograms and cumulative fits (insets) for PEG-IONP(A) and PEG only (B) samples

The PEG-IONPs measurements suggest that the IONPs may be coated with approximately 40 nm of PEG. Comparatively, each of the characterisation methods has been used progressively, to support and analyse the sputtered IONPs. The results of each characterisation method may show some variation on the exact size of individual nanoparticles due to the inherent different feature evaluated by each technique. However, all the characterisation techniques used in this work show clear indication of the presence of dispersed IONPs when contrasted against the blank in that experiment.

2.4.6 Nanoparticle Tracking Analysis (NTA)

NTA measurements were taken using red laser at 21°C (Figure 2-36).

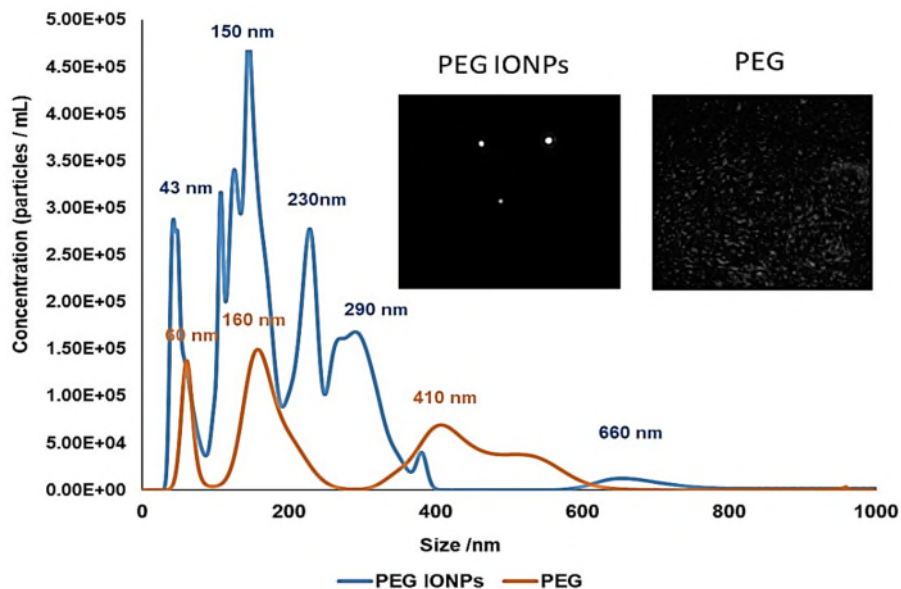


Figure 2-36: NTA analysis of sputtered IONPs (Hemben et al., 2021).

NTA measurements of concentrated (3×) PEG IONPs solution (blue) and concentrated (3×) PEG solution (orange), as control are depicted in Figure 2-36. The histograms shown in the figure are average of 3 measurements. The two insets show screenshots of representative NTA videos for both PEG IONPs, with the IONPs reflecting light, and PEG only solution as control.

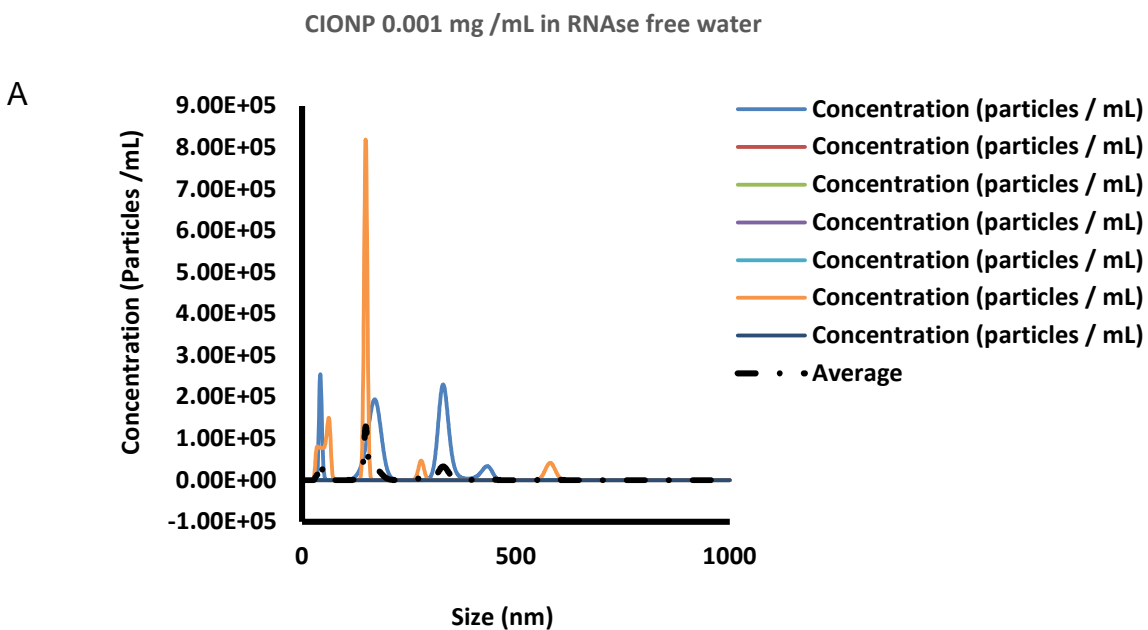
In Figure 2-36 above, the PEG-IONPs solution (blue) shows higher concentration of particles/mL when plotted against the PEG only solution (orange).

In a highly concentrated PEG sample (3 mg/mL), aggregation may be seen and could be due to settling of the sample in the syringe during measurements, as the individual measurements are taken when the sample is advanced after prompting from the instruments program. As a result, different fractions of the sample are measured each time and an average measurement calculated. Therefore, the PEG-IONPs particle seemed to have an average size of $\sim 143 \pm 100$ nm. Also, as mentioned above, the instrument shows variation between the sample containing IONPs and the PEG only sample. All measurements were acquired taking into consideration that some characterisation techniques are estimations and do not give absolute size values. In the case of NTA experiments,

the real-time visualisation of IONPs in a PEG IONP sample (see brighter spots in the inset of Figure 2-36) is a validation of the presence of IONPs in the sample. The sputtered IONPs were seen as reflective bodies as the laser shone on the particles, which came in and out of focus as a result of being in random Brownian motion. In stark contrast, the PEG only sample measurements show no reflective, motile particles, in the sample.

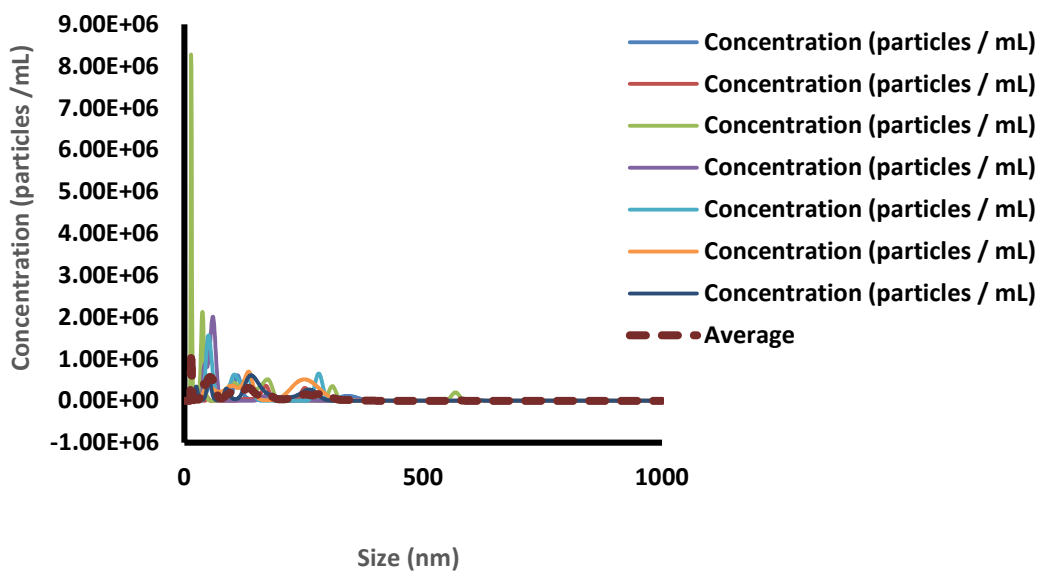
As an estimation of the concentration of the sputtered IONPs was necessary for further characterisation (i.e. magnetic characterisation), a set of NTA experiments was carried out using the CIONPs prepared over a range of concentrations.

Figure 2-37 shows the NTA measurement of the commercial IONPs (CIONPs) which were 15-20 nm diameter, suspended in RNase free water. Solutions of CIONPs (50 mL, 0.001-0.1 mg/mL) in RNase free water were ultra-sonicated as described in section 2.3.13, prior to NTA measurements and then each solution was measured seven times.



CIONPs 0.01 mg/mL in RNase free water

B



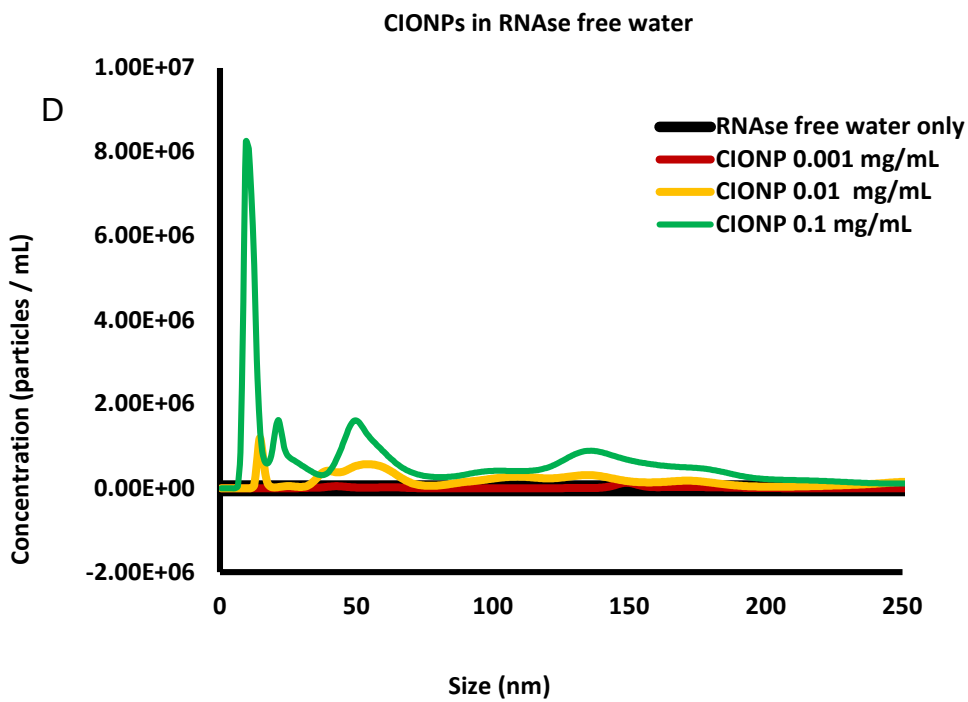
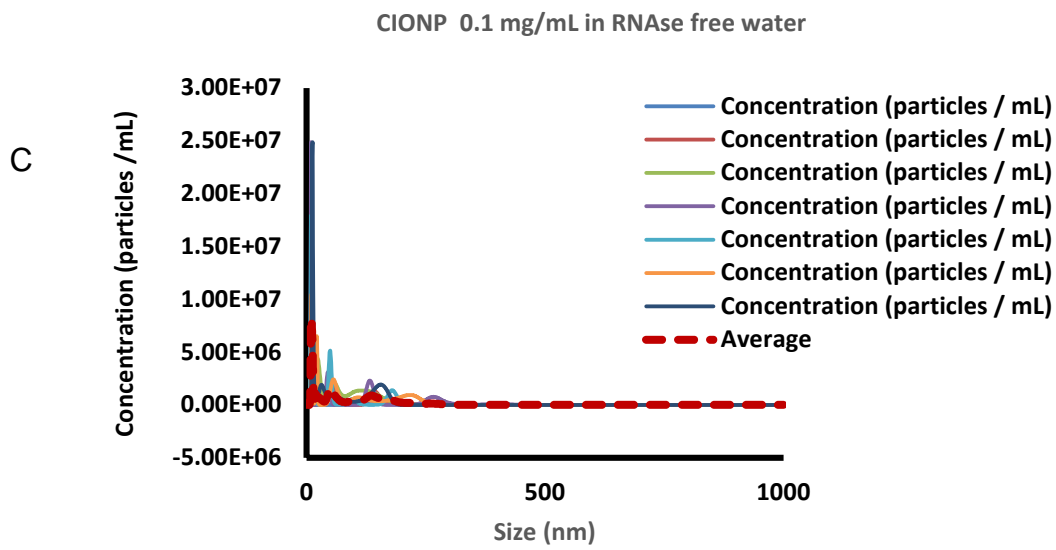


Figure 2-37: Nanoparticle Tracking Analysis CIONP 0.001 mg/mL (A), CIONP 0.01 mg/mL (B), CIONP 0.1 mg/mL (C) and average measurements (D).

Although seven measurements were carried out for all the CIONPs concentrations tested, for the lowest amount of CIONPs tested (Figure 2-37 A),

three measurements did not show any signal probably because the sample was near the limit of quantification of the instrument. The average plots from the three concentrations of CIONPs in RNase free water were compared (2-37 D).

RNase free water was used as control. The X axis scale for Figure 3-37 D was changed to a narrower interval to better see the separation in the measurements.

From the above NTA experiments, results show increasing signal with higher concentration of commercial iron oxide nanoparticles (CIONPs).

The value of the Y axes (particles/mL) read for the different concentrations of the CIONP were then compared to the values obtained for the PEG-IONPs and their concentration (particles/mL) estimated. The comparison showed that the highest point on the blue curve (shown in Figure 2-36 above) comprising PEG / sputtered IONPs which was 474,609 particles/mL and the highest point on the orange curve which contains PEG only in RNase free water was seen to be 145,375 particles/mL. The difference between the PEG IONPs and PEG only curves was 329,234 particles/mL.

Next, from Figure 2-38, the highest point on the y axis on the 0.1 mg/mL CIONPs in RNase free water was 8,242,741 particles/mL; the highest point in the 0.01 CIONPs in RNase free water was 1,183,907 particles/mL. The highest point on the 0.001 mg/mL CIONPs in RNase free water was 128,665 particles/mL (Table 2-4).

Table 2-4: Points to derive regression curve of concentration of CIONPs

CIONPs (mg/mL)	Particles/mL (Y axis)
0.001	128665
0.01	1183907
0.1	8242741

The values above were plotted against the nanoparticles concentration and to obtain the regression curve shown in Figure 2-38.

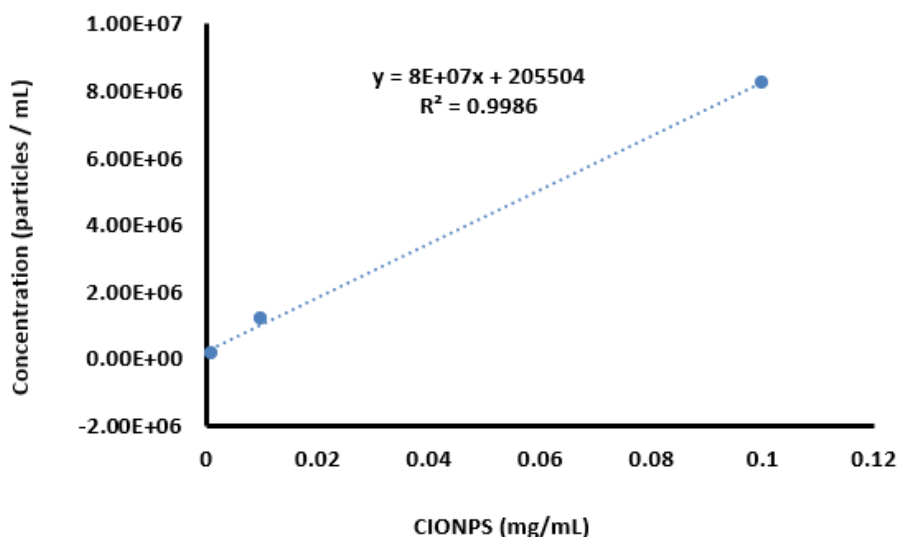


Figure 2-38: Regression curve depicting CIONPs concentration

The regression curve of the points (Table 2-4) shows the R^2 as 0.9986. From the regression equation, 'y' value, calculated for the sputtered PEG-IONPs (329.234), was fitted in the equation of the regression curve to calculate a value for x. The concentration of sputtered IONPs was found to be ~ 0.001547 mg/mL (1.55 μ g/mL).

Following the estimation of concentration of sputtered IONPs further characterisation was carried out to determine the magnetic properties of the nanoparticles.

NTA has been used in studies conducted on exosomes, microvesicles, extracellular vesicles characterisation, viral vaccine research and development, development of drug delivery systems and protein aggregation studies. The NTA utilised in this research used approximately 1 mL sample volume with minimal

sample preparation and consumables. The analysed sample is not affected by the process in which a laser beam (red) was shone through the samples. During tracking of the sputtered and commercial IONPs, real-time monitoring was done, and the nanoparticles were confirmed by visual validation because of Brownian motion of the nanoparticles. The NTA software analyses individual nanoparticles simultaneously (particle by particle) and via the Stokes-Einstein equation, calculates their hydrodynamic diameters.

Stoke-Einstein relationship of the particle diameter can be calculated as a function of the diffusion coefficient D at a Temperature T and a Viscosity η of the liquid (K_B Boltzmann's constant).

$$D = \frac{4 K_B T}{3\pi\eta d}$$

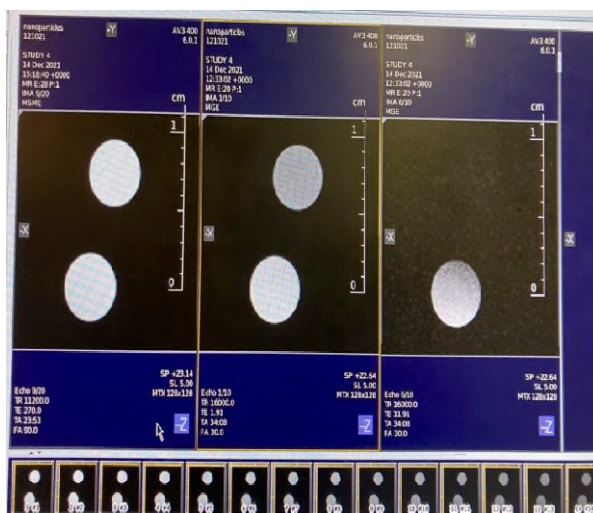
Equation 2-1: Stoke-Einstein equation

NTA utilises the properties of both light scattering and Brownian motion to obtain the nanoparticle size distribution of samples in the liquid suspension. The camera captures the video of the particles moving under Brownian motion. NTA is a particle characterisation technique which can be used to determine size as well as concentration. Nanoparticle tracking analysis was used to visually track and validate sputtered and commercial nanoparticles in solution (Nanoparticle Tracking Analysis, 2021). The NTA results showed the variation in spectra due to the concentration of sputtered IONPS in PEG solution when compared with the PEG only sample in RNase free water.

2.4.7 Magnetic resonance imaging

The efficiency of MRI contrast agents depends on the ratio of their transverse (r_2) and longitudinal (r_1) relaxivity. The efficiency of a T2 contrast agent is optimal when r_2/r_1 ratio is the highest. To determine the r_2/r_1 ratio in the presence of free-standing sputtered PEG IONPs, the transverse relaxation (T2) and longitudinal relaxation (T1) of water protons in aqueous solutions of PEG IONPs were studied for a range of concentrations. The concentrations were obtained by diluting the sample over a range of values as mentioned in the methods section, before applying the magnetic field. The influence of the IONPs on proton relaxations is highlighted in top panel of images in Figure 2-39 A which shows the gradient echo images of water phantoms (center) and of a sample containing the IONPs. As gradient echo time increases, water molecules are exposed to greater magnetic field inhomogeneities therefore, the image containing phantom nanoparticles disappears. With variation in the magnetic field, the contrast of the magnetic nanoparticles is seen less. To determine r_1 and r_2 relaxivity the dependence of the relaxation rates $R_1(=1/T_1)$ and $R_2(=1/T_2)$ on the concentration of iron contained by IONPs was evaluated. The relaxivity r_1 and r_2 were determined by linear fitting the data as displayed in Figure 2-39 B.

A



B

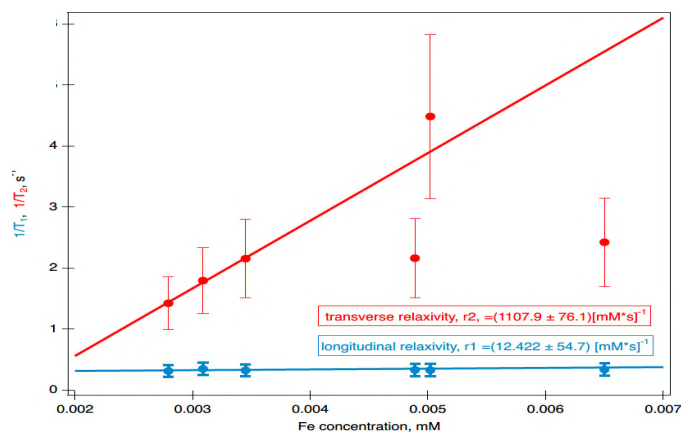


Figure 2-39: MRI plot of sputtered IONPs (A, B).

For B, the concentrations of 2.7-6.5 μM were plotted versus both $1/T_1$ or longitudinal relaxation (blue line) and $1/T_2$ or transverse relaxation (red line).

When $1/T_2$ was assessed, two dilutions corresponding to 5 and 6.5 μM of iron oxide nanoparticles in the samples were outside the predicted linear dependence of relaxation rate with iron concentration. This is associated with different local fields during the experiments, as dilutions could not be tested simultaneously due to lack of sufficient sample volumes and had to be tested sequentially. Although all possible precautions were taken to apply the same magnetic field during the

testing, it is likely that the testing conditions were slightly different between measurements resulting in these two concentrations being outside the predicted linear dependence. In addition, although the diluent (PEG in RNase free water) for preparing the dilutions (and for the blank) was estimated to be the same concentration as the one in the sputtered sample, it is possible that the two were slightly different implying that the composition of the higher concentration samples was slightly different than the most diluted ones, resulting again in the poor fitting. Despite this, Figure 2-36 B shows an $r_1 = 12.52 \pm 54 \text{ mM s}^{-1}$ and $r_2 = 1108 \pm 76 \text{ mM s}^{-1}$ with a determined r_2/r_1 ratio of 88.5, demonstrating that our PEG IONPs surpasses the best commercially available agent (Resovist) by nearly a factor of 2. The ratio (r_2/r_1) of Resovist is around 50 (Skopalik et al., 2014).

Magnetic resonance imaging (MRI) has been used for many years to diagnose diseases including Alzheimer's disease (Wolz et al., 2011), breast cancer (Deike-Hofmann et al., 2019) tuberculosis (Naselli et al., 2022). The MRI technique has also been applied as a mode of characterising magnetic nanoparticles (Estelrich et al., 2015 ; Eklund et al., 2021). Magnetic properties of iron oxide nanoparticles make them useful in magnetic resonance imaging as they are exploited as contrast agents. In this research, MRI was used to explore the sputtered IONPs for magnetic properties and assess whether they would be good contrast agents for MRI and could potentially be visualised by MRI during treatment. Magnetic resonance imaging has been used to establish and track the progress of magnetic nanoparticles in soft tissue following treatment of tumours, by manipulating magnetic nanoparticles using a magnetic field. In addition, as soon as the magnetic nanoparticles are found in the cells to which they have been delivered, the magnetic nanoparticles can be heat-treated, if that is the choice of procedures for the cancer type and progression, or the magnetic nanoparticles can be subtly manipulated. Biological imaging has been conducted, using iron oxide nanoparticles as these are US Food and Drug Administration (FDA)-approved for use in magnetic resonance imaging MRI due to their suitability for use as contrast agents to enhance image resolution (Stueber et al., 2021).

Regarding the relaxation process, MRI images are classified into longitudinal relaxation time weighted images (T1 contrast) and transverse relaxation time weighted images (T2 contrast) (Javed et al., 2017). Small-sized IONPs with diameter (<4nm) are preferred as T1 contrast agents while nanoparticles having diameter greater than 4 nm that are used as T2 contrast agents. IONPs-based MR contrast agents provide high spatial resolution with excellent visualisation to human body's fine structure.

A focus on the research of magnetic iron oxide nanoparticles involves the use of magnetic resonance imaging and the formation of contrast agent, over the past decade for improving the accuracy of diagnosis. Ultra-super paramagnetic iron oxide nanoparticles (USPIO) with core diameter smaller than 5 nm are expected to become next generation contrast agents owing to their excellent MRI performance, long blood circulation time upon proper surface modification, renal clearance capacity, and remarkable biosafety profile (Chen et al., 2022). USPIO nanoparticles are also used to develop T2/T1 switchable contrast agents in assembly/disassembly methods. In this work and as fully described in Chapter 2, sputtered IONPs between 1-6 nm produced by inert gas condensation technique, have the potential for use in cancer treatment, as the sputtered IONPs are of suitable size to cross the cell wall of the cancer cell (Hemben et al., 2021). In addition, the results of MRI characterisation in this research showed that the sputtered IONPs suspended in PEG solution are good contrast agents for MRI visualisation. The results of MRI in this work also show longitudinal relaxation (T1) to be clearly distinct from the transverse relaxation (T2) and are therefore an excellent candidate for use in *in-vivo* and *in-vitro* experiments.

Nowadays, new contrast agent USPIO nanoparticles have demonstrated several applications in the diagnosis of different diseases like vascular pathological changes and inflammations apart from malignant tumours (Chen et al., 2022). Magnetic resonance imaging has been used to characterise iron oxide nanoparticles (Chen et al., 2022). The promising T1 performance of small IONPs (≤ 5 nm) is due to their high surface-to-volume ratio increasing the exposure of surface Fe ions to the surrounding water/hydrogen (Chen et al., 2020). In contrast

to IONPs used for T2 contrast enhancement, their performance is not dominated by the high magnetic moment. The exact mechanism controlling T1 performance is still not clear but may rely on the accessibility of water molecules to surface iron ions.

Therefore, in this study, the observed r_2/r_1 ratio of 88.5 show the potential of the sputtered IONPs, to be used as good contrast agent and might indicate their ability to be trackable by MRI and therefore suitable for use in future studies for drug delivery targeting neuroendocrine prostate cancer. The future work will involve conducting the MRI characterisation of the IONPs with a higher amount of sample, which will permit measuring the entire range of concentrations at the same time, avoiding any variability in the testing. This will be followed by *in-vitro* and *in-vivo* studies, visualised directly by MRI, to investigate the internalisation of the nanoparticles by the tumour cells.

2.5 CONCLUSIONS

In conclusion, this Chapter has reported the process of optimising the conditions for sputtering IONPS with a diameter around 5 nm (1-6 nm, see TEM figure 2-31). The particles were produced by inert gas condensation at ambient temperature (around 25°C), throttle position 70% and Argon flow 70 sccm, over a two-hour sputtering and deposition session on a PEG-coated silicon wafer. The characterisation of the IONPs has shown that PEG has been successfully used to soft-land the sputtered IONPs. The PEG-IONPs solution characterised by TEM reveals IONPs dried up in the polymer layer (Figure 2-30), although individual cores can also be clearly seen, implying that it is unlikely to have multicore nanoparticles. Some of the IONPs looked clustered together, which may be caused by a pre-concentration effect during the drying. Further TEM images done directly on the TEM grid, showed individually deposited IONPs produced by inert gas condensation. Further characterisation by AFM provided capture of shiny spots implying the presence of IONPs in the PEG-IONPs solution, while DLS and NTA analyses confirmed the presence of a high concentration of PEG in comparison to the sputtered IONPs. The IONPs produced in this study are

smaller than 10 nm, a size which have shown high cellular uptake by tumour cells and can therefore potentially be used during drug delivery investigations (Feng et al., 2018). Another advantage of the sputtering method used to produce the IONPs is that the material obtained was immediately usable in further investigations without the need of purification or separation steps, which are required in chemical production of nanoparticles. The magnetic, sputtered IONPs showed promise as a good contrast agent and therefore the possibility of enhancing *in-vitro* tracking of the IONPs in cancer cells. In conclusion, inert gas condensation method has shown production of nanoparticles with a size suitable for potential use in targeted drug delivery.

CHAPTER 3

BOVINE SERUM ALBUMIN (BSA) TEXAS RED™ CONJUGATE FLUORESCENCE EXPERIMENTS WITH COMMERCIAL IRON OXIDE NANOPARTICLES

3 BOVINE SERUM ALBUMIN (BSA)TEXAS RED™

3.1 INTRODUCTION

Bovine serum albumin (BSA) is isolated from the blood of cows (Kim et al., 2022) as a by-product of the cattle industry and has many biomedical applications. BSA is known to be a low cost, stable, relatively non-reactive molecule that is used in enzyme linked immunosorbent assays (ELISA) (Zhang et al., 2022) and immunohistochemistry (Dettmar et al., 2018) as a blocker for non-specific binding of antibodies during reactions. The blocker ensures the antibodies bind specifically to the compound of interest. Thanks to the blocking process, the background noise due to the matrix is minimised as BSA forms a layer of relatively non-reactive sites, thereby improving the specific signal response of the assay. BSA is also used as a nutrient in cell and microbial culture (Tang et al., 2005). In restriction digests of genetic material, BSA is used to stabilise enzymes during the digestion of DNA and to prevent adhesion of the enzyme to reaction tubes, pipette tips, and other vessels. BSA is also used in protein quantitative assay to determine protein concentration (Zhou et al., 2019). BSA has been used to block enzymes in polymerase chain reaction (PCR) (Kreader, 1996), as a template to synthesise nanostructures (Akshaya et al., 2019) and as a protein conjugate probe.

Bovine Serum Albumin (BSA) Texas Red™ conjugate is a reagent consisting of the dye Texas Red linked to BSA and is commonly used as a tracer in biomedical applications (Prausnitz et al., 1993). The dye has also been used for the measurement of plasma volume in rats (Gillen et al., 1994), for the detection and localisation of small amounts of DNA sequences (Kahn et al., 1997) and electroporation of cells involving the construction of a fluorescent hapten-protein conjugate to monitor the highly specific events required for CD 4+ T lymphocyte recognition of antigenic proteins (Weaver and Voss, 1998). This BSA Texas Red™ conjugate is also suited for applications in which well-defined molecular

weight tracers are needed. These applications include studying the rate of endocytosis and exocytosis and following intracellular protein processing (Thermofisher.com, 2019). BSA Texas Red™ was selected as molecular probe for this research as the reagent has already been used in drug delivery studies as the dye is attached to protein molecules (Nhan et al., 2013). BSA Texas Red™ conjugate is part of a group of fluorescent labels which are listed in Table 3-1 and are commonly used for a variety of applications.

Table 3-1: BSA conjugates (Adapted from Molecular Probes, 2005)

Fluorescent label	Excitation wavelength (nm)	Emission wavelength (nm)
DNP	357	NA
Fluorescein	494	520
Alexa Fluor 488	497	520
BODIPY FL	501	509
tetramethyl rhodamine	541	572
Alexa Fluor 555	555	565
Texas Red	596	615
Alexa Fluor 594	590	622
Alexa Fluor 647	650	668
Alexa Fluor 480	679	702

Texas Red (C₃₁H₂₉ClN₂O₆S₂) is a purple, organic fluorescent dye, with molar mass 625.15 g/mol. When the dye is excited with an incident red laser light, it absorbs the energy, while emitting some of the absorbed light at a lower energy and longer wavelength due to energy conversion to kinetic and heat energy. The dye has found use in microscopic, anatomical procedures for staining cells, and cell sorting experiments (Quayle et al., 2018). Texas Red attached to a strand of nucleic acid can act as a molecular beacon for highlighting specific sequences of

DNA or RNA in quantitative assay (Kuang et al., 2017). Texas Red dye comprises a combination of mono sulfonyl chlorides and a sulphonate group (Figure 3-1A).

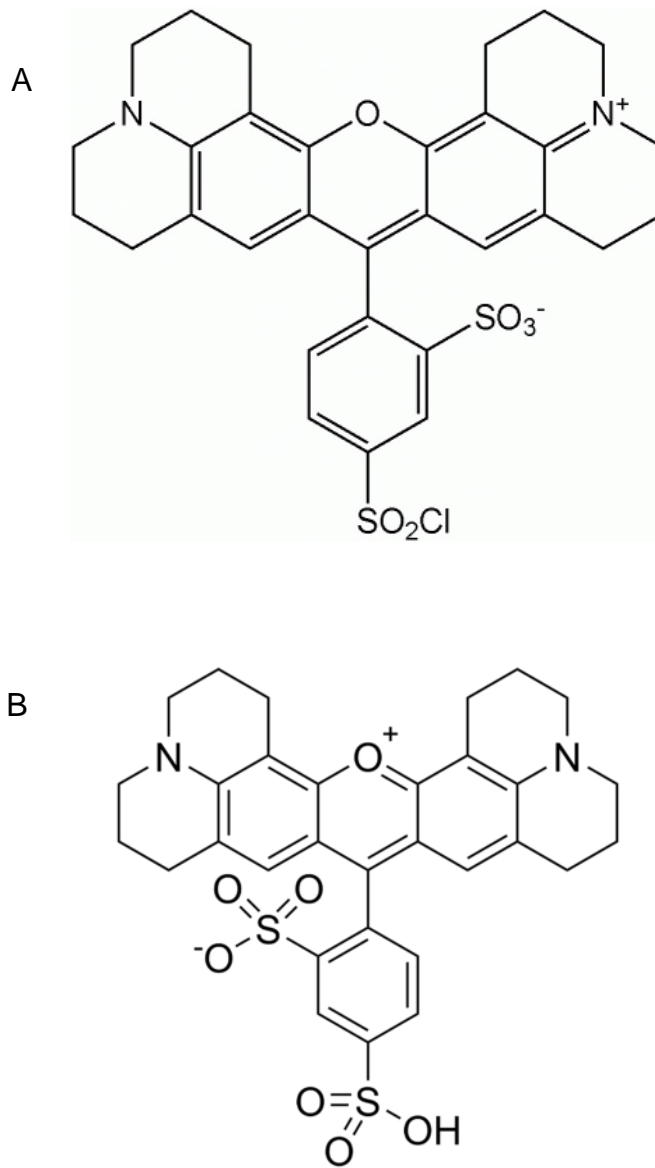


Figure 3-1: Texas Red dye chemical structure A) Texas Red B) Sulforhodamine 101 (Aldrich, 2021).

The SO_3 and SO_2Cl groups may be exchanged; Texas red can be used as a protein marker as it readily forms conjugates via the sulphonyl chloride group.

When water is added, the sulphonyl chloride group of the unreacted Texas Red molecules hydrolyses to sulfonate. The molecule is transformed to

sulforhodamine 101 which is highly soluble in water (Titus et al., 1982). When attached to a protein, Texas Red can play the role of fluorescent labelling agent. Also, highly specific antigen-antibody interactions can be monitored by attaching Texas Red to the antibody to track the antigen. Texas Red can also be used to label toxins. BSA Texas Red™ conjugate has also been used in many biomedical applications including cell tracing, tracking and cellular imaging (Thermofisher.com, 2019).

In this study, BSA Texas Red™ conjugate was used as a label to visualise and optimise the attachment of a drug (siRNA), and to enable tracking of the mechanism of attachment to and release of siRNA from pegylated iron oxide nanoparticles (PEG-IONPs) and subsequent release of the siRNA from the nanocarrier complex. This research work was a continuation of a preliminary pilot study (Serfimowicz, 2018), during which total quenching of the dye in acidic pH in presence of IONPs was reported. Therefore, here initially, preliminary tests involved using BSA Texas Red™ to assess the stability of its fluorescence signal in both acidic and neutral pH environments in presence and absence of IONPs. At the very beginning of the study, the suitability of the dye was assessed by performing fluorescence measurements to confirm the excitation and emission spectrum reported by the supplier (Figure 3-2).

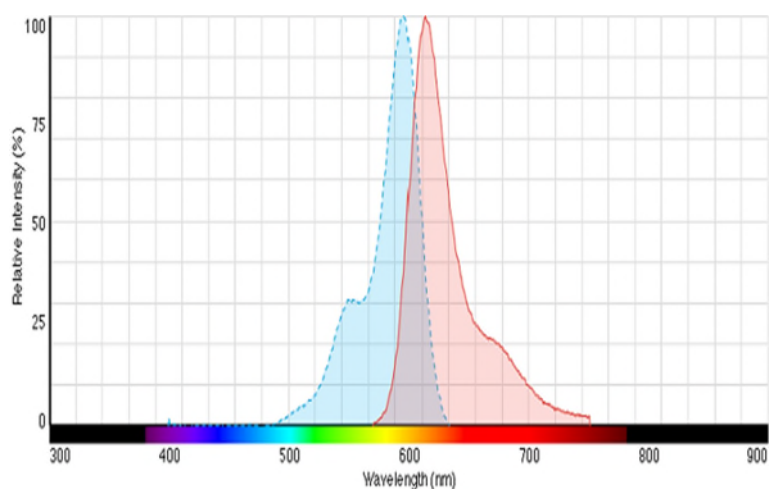


Figure 3-2: Fluorescence spectra (excitation in blue and emission in red) for BSA Texas Red™ conjugate (Thermofisher.com, 2019).

Similar spectra to those reported in Figure 3-2, were obtained in this study, and will be described later in the Chapter. While BSA Texas Red™ conjugate has been used in protein adsorption studies (Suci and Hlady, 1990; Alcantar et al., 2000), the conjugate has been known to attach via strong electrostatic or hydrophilic interactions to polyethylene glycol (PEG) (Abuchowski et al., 1977) as an encapsulating agent.

In the past 10 years, nanotechnology has introduced a range of nanoparticles (NPs) that can be used in biomedical applications. Metallic NPs can exhibit unique optical and magnetic properties, depending on their composition. In addition, NPs can be functionalised to impart the desired characteristics (Macovei et al., 2022). NPs have been employed successfully *in-vivo* and *ex-vivo*, by supplying the genetic agent in the living cells still in the body and by extracting the cells from the body to be modified outside of the body for replacement thereafter. Currently, the most important application areas for NPs in diagnostics are biomarker analysis (Reddy, et al, 2017), cancer diagnosis (Vallabani and Singh, 2018) immunoassays (Lin et al., 2021) and diagnostic imaging (Shahdeo et al., 2022).

Frequently used molecular labels include enzymes catalysts (Zhao et al., 2021) or fluorescent molecules (Chung and Zhang, 2021). The organic dyes used in diagnostic assays have the advantage of sensitivity by the emission of fluorescence or colour changes. They also have some disadvantages such as photobleaching and have been known to have asymmetric emission spectra. In addition, some dyes such as fluorescein and rhodamines display quenching when present in solution at high concentration (Demchenko, 2005). Despite the disadvantages mentioned above, organic dyes are frequently used as labels due to their low cost and ease of use. Furthermore, covalently attaching the dye to the polymer can help by preventing leakage, which has occurred with entrapped dyes, which were able to diffuse out of the polymer matrix (Demchenko, 2005).

NPs, due to their large surface to volume ratio, can accommodate hundreds of dye molecules to increase the intensity of emission. Fundamentally, the selection

of a suitable dye for biomedical applications should aim for high signal and shielding from the surrounding environment. A high Stokes shift allows for ease of fluorescent signal without interference due to overlapping of the excitation and emission spectra of the dye (Demchenko, 2005). Dyes for potential *in-vivo* or *ex-vivo* use must be non-toxic and their biodistribution understood (Canfarotta et al., 2013).

The pilot study (Serfimowicz, 2018) mentioned above, and carried out prior to this research work, was conducted to start the development of a nanocarrier complex. The previous study had omitted a systematic investigation of the dye prior to its use and reported fluorescence quenching in acidic pH. Therefore, as part of this research, BSA Texas Red™ has been tested in both acidic and neutral/basic pH, as well as in PBS, PEG, and in presence of commercial iron oxide nanoparticles, to assess the suitability of the dye for its use as label to optimise the chemistry for preparing a nanocarrier complex.

3.2 MATERIALS

3.2.1 General chemicals and instrumentation

The BSA Texas Red™ conjugate was purchased from Life Technologies (Woolstone, UK). The pH strips, the pre-suspended solution of iron oxide (Fe₃O₄) nanoparticles (IONPs) with 20 nm average particle size and a concentration of 5mg/mL, polyethylene glycol 1000 g/mol (PEG 1000) and RNase free water were purchased from Sigma Aldrich (Merck Life Science UK Ltd.) (Gillingham, UK). Polyethylene imine 600 g/mol (PEI 600) 99% was purchased from Polysciences, Inc. (Warrington, USA) and commercial IONPs in powder form (15-20 nm) were purchased from Nanomaterials Inc. (Texas, USA).

Gene2Vortex was purchased from Scientific Industries (St Neots, UK); magnetic stirrer/hot plate 1103 Jenway (Staffordshire, UK); analytical balance Entris II BCE was from Sartorius (Birmingham, UK). Stuart Gyro-rocker SSM3, Mini 230V from Techne (Staffordshire, UK), 96 well NUNC microtiter plates and Varioskan Flash spectrophotometer microplate reader from Thermo Fisher Scientific

(Loughborough, UK). Data capture was via SKanIT RE 2.4.5 software was used. Branson ultra sonifier digital model 250 sonic probe was obtained from Branson Instruments (GA, USA).

3.3 METHODS

3.3.1 Reconstitution of BSA Texas Red™ conjugate in RNase free water.

BSA Texas Red™ conjugate was first reconstituted in the original container to a concentration of 5 mg/mL by adding 1 mL RNase free water to the 5 mg contents and it was vortexed briefly using Gene2Vortex Scientific Industries (St Neots, UK). Aliquots of 50 µL were extracted using a pipette and delivered into Eppendorf tubes then the tubes were stored in the dark at -20°C.

3.3.2 Phosphate buffered saline pH 7.4

PBS solution (a mimic for physiological saline) was then prepared by adding 1 tablet of PBS pH 7.4 to 200 mL deionised water according to manufacturer's instructions and stirred using a magnetic stirrer/hot plate 1103 Jenway (Staffordshire, UK) until completely dissolved.

3.3.3 Preparation of PEG in PBS

PEG 1000 (1 mg/mL) was prepared by weighing 0.02 g on an analytical balance Entris II BCE, Sartorius (Birmingham, UK) and transferred to a glass container. The PBS solution (20 mL) was then added, and the solution was stirred on the magnetic stirrer at ambient temperature (25°C) until clear. The pH was then adjusted to 5.5, 7.0, 7.4 and 7.6 by drop-wise addition using 0.1M NaOH or 0.1M HCl, and then tested using pH strips. The solutions were stored at 4°C and used within a week.

3.3.4 Preparation of PBS/PEG/PEI

PEG 1000 and PEI 600 (1 mg/mL and 0.6 mg/mL respectively) were prepared by weighing 0.02 g of PEG 1000 and 0.012 g PEI 600 on an analytical balance and transferred to a glass container. The PBS solution (20 mL) was then added, and

the solution was stirred on the magnetic stirrer at ambient temperature (25°C) until clear. The PBS/PEG/PEI buffers were adjusted to pH 5.5 and 7.4 as required, using 0.1M NaOH or 0.1M HCl and the buffer kept at 4°C until use.

3.3.5 Preparation of BSA Texas Red™ conjugate in PBS

To test fluorescence of lower dye concentrations, BSA Texas Red™ conjugate aliquots were diluted to concentrations of 0.5 µg/mL, 1 µg/mL, 1.5 µg/mL, 2 µg/mL and 2.5 µg/mL. The pH of the buffers was adjusted to pH 5.5, 7, 7.4, and 7.6 then the samples were incubated for 0,5,10,20,30, and 60 minutes at ambient temperature (25°C), using Stuart Gyro-rocker SSM3, Mini 230V from Techne (Staffordshire, UK), which allowed shaking the solutions while incubating. Photometric measurements were taken after dispensing solution on 96 well NUNC microtiter plate and reading the absorbance by a Varioskan Flash spectrophotometer microplate reader (Figure 3-3) from Thermo Fisher Scientific (Loughborough, UK). Data capture was via SKanIT RE 2.4.5 software. With the lower concentrations of dye, both the excitation and the emission wavelengths were investigated in detail. For this, scans were first recorded fixing the emission wavelength at 615 nm and scanning the excitation wavelength between 500-600 nm. Similarly, to study the emission wavelength, in following measurements the excitation wavelength was fixed at 590 nm, while the emission wavelength was varied between 600-630 nm.

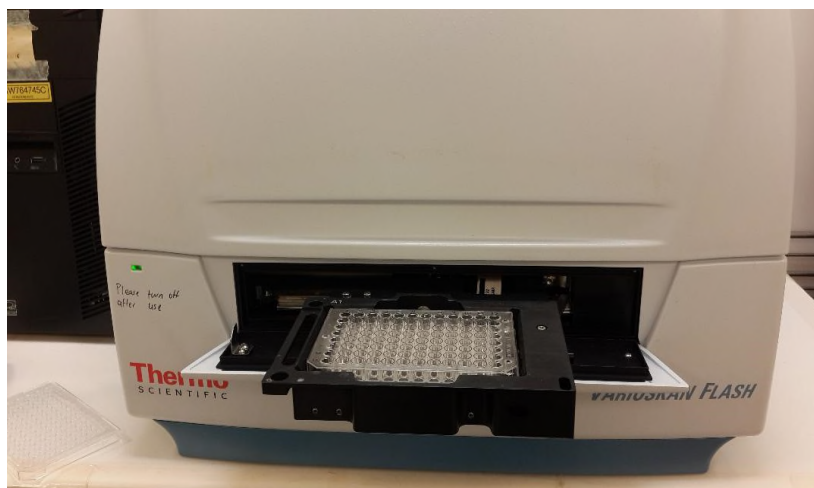


Figure 3-3: Varioskan plate reader used to read fluorescence of solution of BSA Texas Red™ conjugate at different concentrations and incubation time.

The experiment was then repeated under the same conditions of temperature and pH using fixed values for both the excitation and emission wavelengths as 590 nm and 615 nm respectively. These values were then used to measure the higher dye concentrations and all the subsequent experiments using these excitation and emission wavelengths were conducted using both pre-suspended commercial iron oxide nanoparticles (CIONPs) and the powdered CIONPs.

3.3.6 Commercial IONPs in PBS/PEG/PEI

Commercial IONPs or CIONPs (0.1 mg/mL) were dispersed in PBS/PEG/PEI pH 5.5, 7, 7.4 and 7.6. To these solutions, BSA Texas Red™ conjugate was then diluted to a concentration of 10 µg/mL. The concentrations were selected after some preliminary, investigations showed the concentrations used were much too high to produce interpretable results.

3.3.7 Fluorescence of pre-suspended and powdered CIONPs

To investigate the effect of pre-suspended CIONPs (<20 nm) on fluorescence of PBS samples, the pre-suspended CIONPs stock solution was diluted in PBS to concentrations ranging from 0.5 µg/mL, 1 µg/mL, 1.5 µg/mL, 2 µg/mL, and 2.5 µg/mL. The samples were dispensed in triplicate in a microtiter plate and fluorescent measurements taken with excitation wavelength of 590 nm and

emission of 615 nm. After the measurements were taken the samples were aspirated from the microtiter wells and placed in Eppendorf tubes on a magnetic sample holder to try to extract the pre-suspended CIONPs from solution. After 60 minutes, the samples of pre-suspended CIONPs remained in solution. The experiment was repeated using the powdered CIONPs initially with 1 mg/mL and then later with 0.1 mg/mL.

3.3.8 Powdered commercial IONPs in PBS/PEG/PEI

Powdered commercial iron oxide nanoparticles (CIONPs) (1 g) were taken from of the stock (5 g) and placed in an Eppendorf tube. Weighing of the CIONPs was done under a fume hood fitted with high efficiency particulate air (HEPA) filter to minimise risk due to inhalation of nanoparticles. The remaining quantity (4 g) of powdered CIONPs was then labelled and stored in the hazardous chemical's cupboard. Next, a quantity of 0.005 g was weighed (out of the 1 g CIONPs) and suspended in 50 mL of PBS/PEG/PEI pH 7.4 and PBS/PEG/PEI pH 5.5 to produce a working concentration of 0.1 mg/mL. The CIONPs were initially sonicated in a James ultrasonic bath for 60 minutes at 30°C, however, when the particles failed to uniformly disperse, a Branson digital, high power sonifier was used to disperse the CIONPs (Figure 3-4).

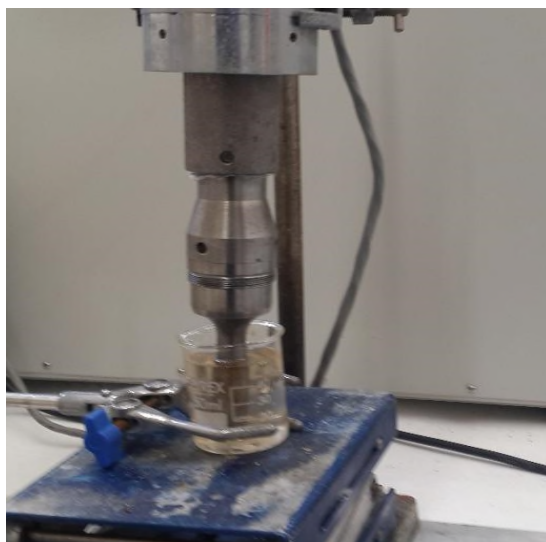


Figure 3-4: Branson ultrasonication of CIONPs in PBS/PEG/PEI

A 50 mL solution of CIONPs (0.1 mg/mL) in PBS/PEG/PEI were ultra-sonicated at 10% amplitude for 15 minutes at ambient temperature (25°C). The dispersed CIONPs were then transferred in falcon tubes and stored at 4°C.

Before sonication the powdered CIONPs when added to PBS/PEG/PEI tend to aggregate and precipitate, visibly at the bottom of the tube. Ultrasonicated CIONPs dispersed in PBS/PEG/PEI matrix take on a characteristic light brown colour of uniformly distributed CIONPs in solution.

The CIONPs in solution had been dispersed for 60 minutes. Prolonged sonication has been known to affect the viscosity and thermal conductivity of samples (Afzal et al., 2019). The samples were therefore ultrasonicated for 15 minutes to just completely disperse the CIONPs powder.

3.4 RESULTS AND DISCUSSION

3.4.1 Fluorescence of BSA Texas Red™ in PBS solution

A range of excitation and emission wavelengths values, reported in Table 3-2 were studied to identify the testing conditions producing the most sensitive fluorescence signal for the BSA Texas Red™.

Table 3-2: Excitation and Emission wavelengths of BSA Texas Red in PBS

	A	B	C	D	E	F
Excitation (nm)	580	585	590	575	590	570
Emission (nm)	620	625	615	615	630	610

The above values were chosen by varying the wavelengths before taking measurements to find the highest point of excitation and emission as read by the spectrophotometer. For this, dilutions of BSA Texas Red™ conjugate with

concentration between 0-2 $\mu\text{g}/\text{mL}$ prepared in PBS (pH 7.4) were tested. The values obtained for 1.5 $\mu\text{g}/\text{mL}$ are shown in Figure 3-5.

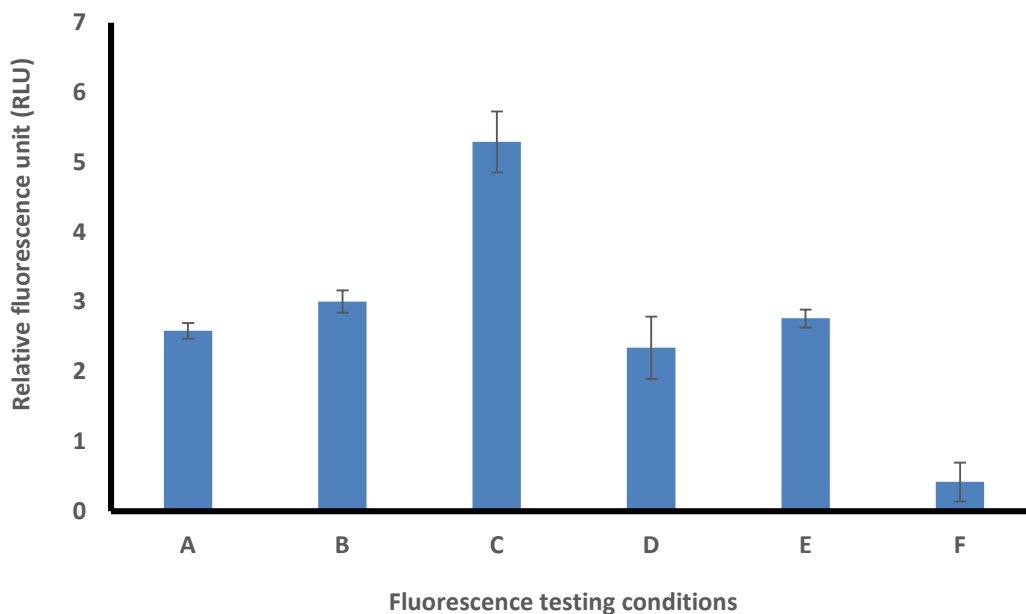


Figure 3-5: Fluorescence values for 1.5 $\mu\text{g}/\text{mL}$ of BSA Texas Red TM conjugate when varying the testing conditions.

The results indicate the highest signal was obtained with excitation at 590 nm and emission at 615 nm. These wavelengths were then used to produce a calibration curve for the BSA Texas Red TM conjugate with a range of values 0-2.5 $\mu\text{g}/\text{mL}$ (Figure 3-6).

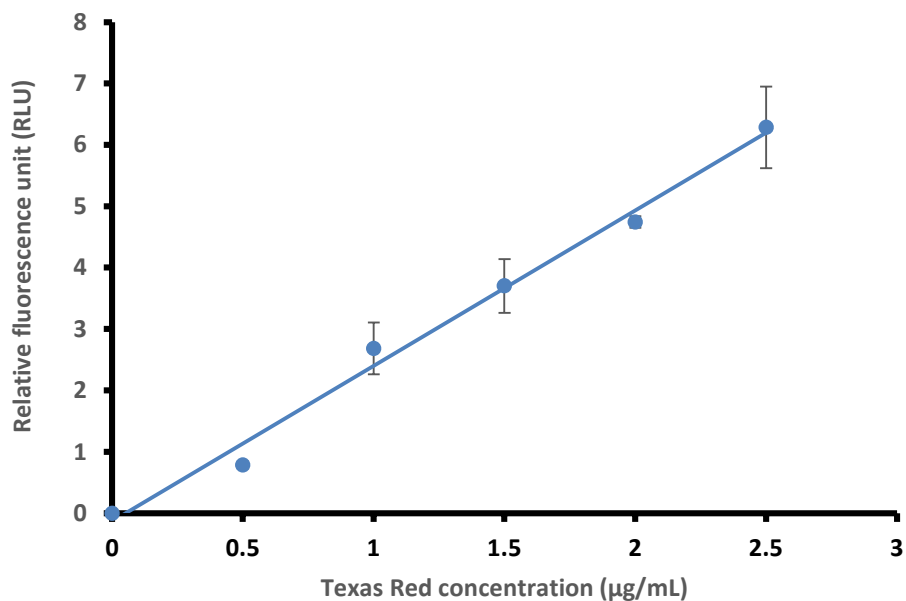


Figure 3-6: Calibration curve for BSA Texas Red™ conjugate obtained with excitation fixed at 590 nm and emission at 615 nm.

Then as described in section 3.3.5, to study the behaviour of the fluorescent dye in detail, measurements were taken, scanning both the excitation and emission wavelengths over a range of values (excitation wavelength between 500-600 nm and emission wavelength between 600-640 nm). The excitation spectrum (with emission at 615) and the emission spectrum (with excitation at 590) shown in Figure 3-6 evidenced a Stoke shift of 25 nm (Figure 3-7).

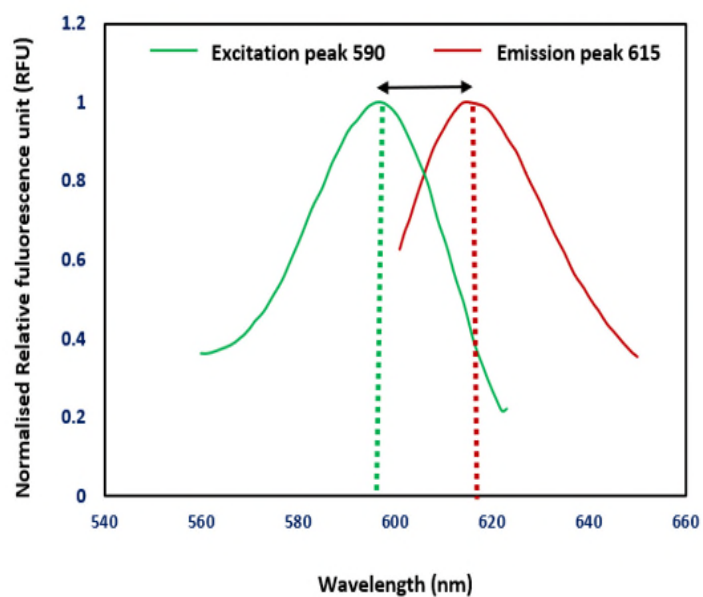


Figure 3-7: BSA Texas Red™ conjugate excitation and emission scans for 10 µg/mL BSA Texas Red prepared in PBS.

The results from the BSA Texas Red™ conjugate are comparable to the excitation and emission spectra reported in section 3.1; Table 3-1 (Probes, 2005).

3.4.2 BSA Texas Red™ conjugate in PBS

Using the above wavelengths, the BSA Texas Red™ conjugate was investigated at different pH (Figure 3-8).

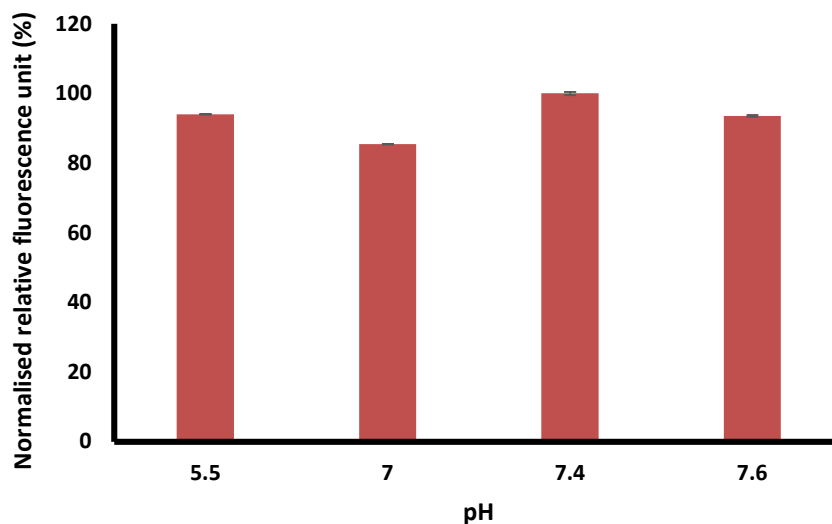


Figure 3-8: Effect of pH signals on BSA Texas Red™ conjugate (10 µg/mL).

The results in Figure 3.9 were obtained using an excitation wavelength of 590 nm and an emission wavelength of 615 nm.

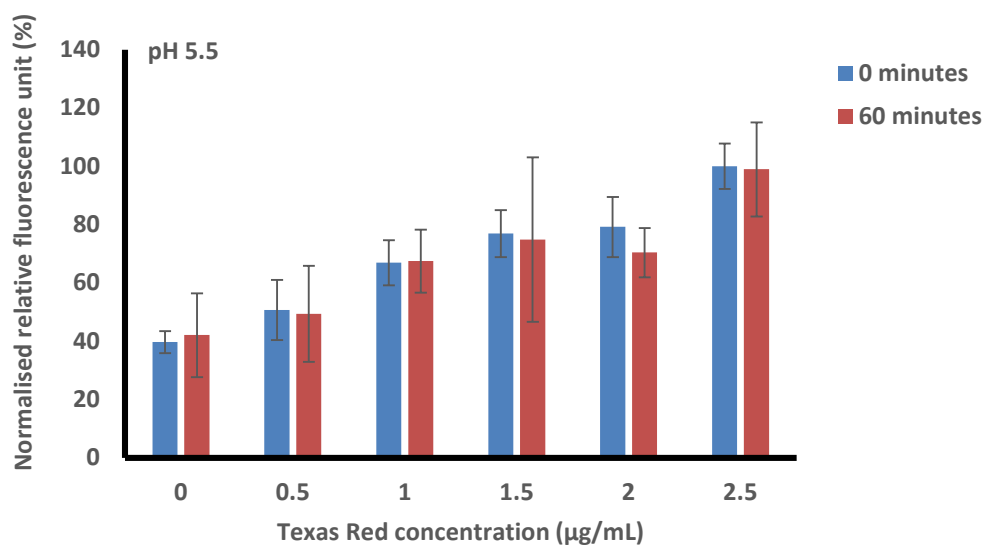
BSA Texas Red™ conjugate were assessed in samples of pH measurement of 5.5, 7, 7.4 and 7.6. All measurements were taken immediately, using a dye concentration of 10 µg/mL in PBS with the different pH values. The data was normalised to make the comparison easier. The average and standard deviation were calculated using three replicates.

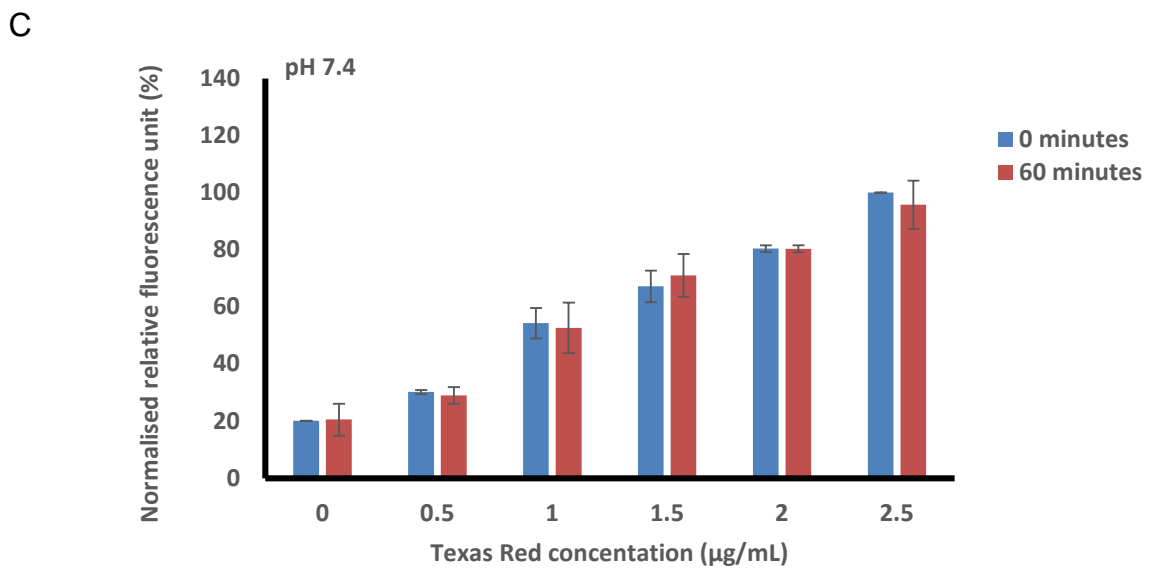
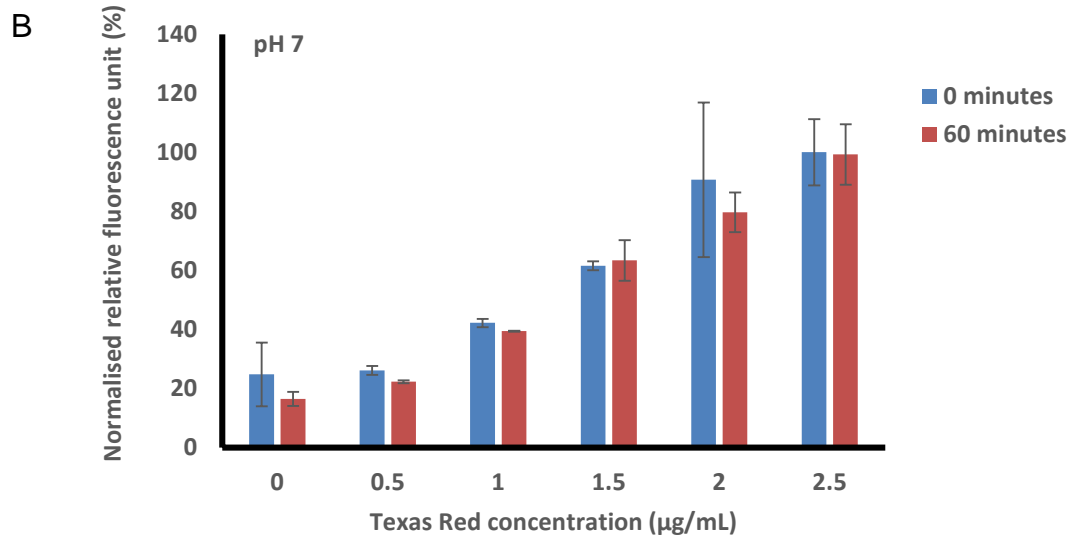
The results showed a stable, fluorescence signal for the dye not affected by the interval of pH tested. The signal response from the above experiments differs from the results of the previously conducted pilot research (Serfimowicz, 2018) which reported significant quenching, especially at pH 5.5. It is thought that during the pilot research the commercial IONPs used were different, were from an old batch and also that they were not properly dispersed. The behaviour of the aggregates may then have been responsible for the quenching of dye's

fluorescence in acidic buffer solution. Furthermore, the way in which the CIONPs were produced may have contributed.

After experimenting with high concentration of the dye (10 $\mu\text{g/mL}$), the concentration was lowered to assess the effect of the pH (5.5-7.6) on the fluorescence signal of lower concentrations (0.5-2.5 $\mu\text{g/mL}$) of the dye (Figure 3-9 A-D).

A





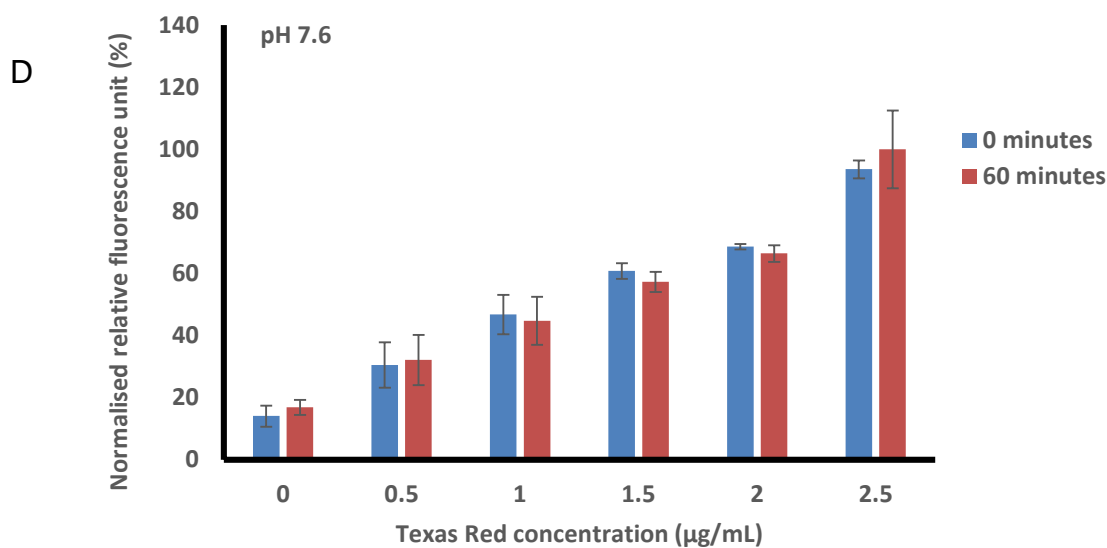


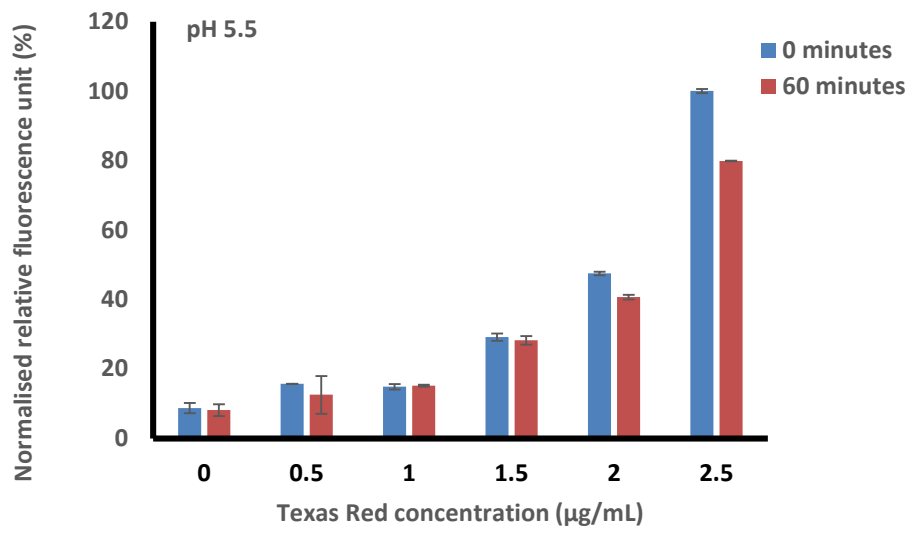
Figure 3-9: Fluorescence emission of BSA Texas Red™ conjugate in PBS at 0 minutes and 60 minutes of incubation.

Dye concentrations between 0 – 2.5 µg/mL were prepared in PBS pH 5.5-7.6 (A-D). Average and standard deviations were calculated with 3 replicates.

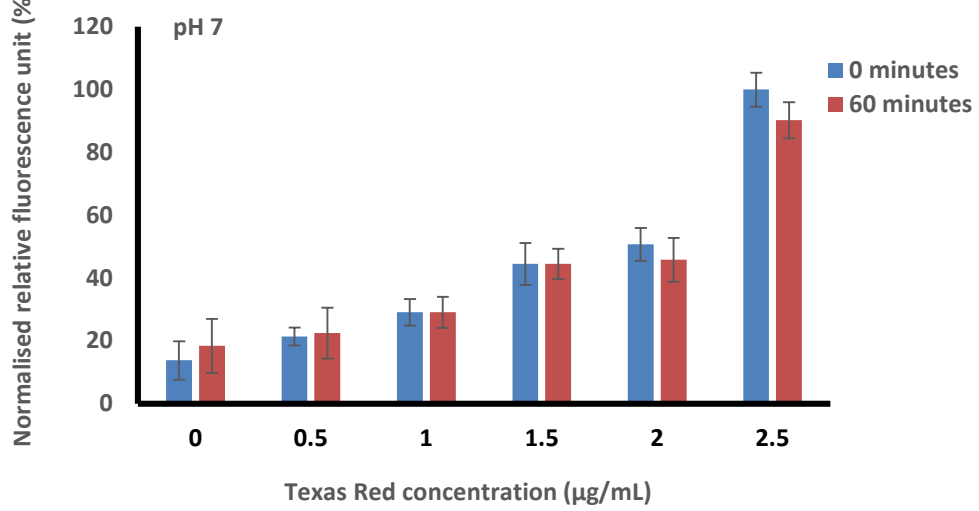
The results showed no noticeable quenching of the fluorescent signal with time. There is a negligible signal seen in the blank sample in all the spectrophotometric measurements and results. This is the background noise read by the instrument when measuring non fluorescence samples. The results also show that the increase of concentration in the samples shows a progressive increase in the fluorescent signal, as expected. In addition, such fluorescent signal was stable and did not change during 60 minutes in any of the pH values tested.

To further confirm the effect of the pH on the fluorescence of dye, the experiments were repeated taking particular care in preparing the dilutions (Figure 3-10 A-D).

A



B



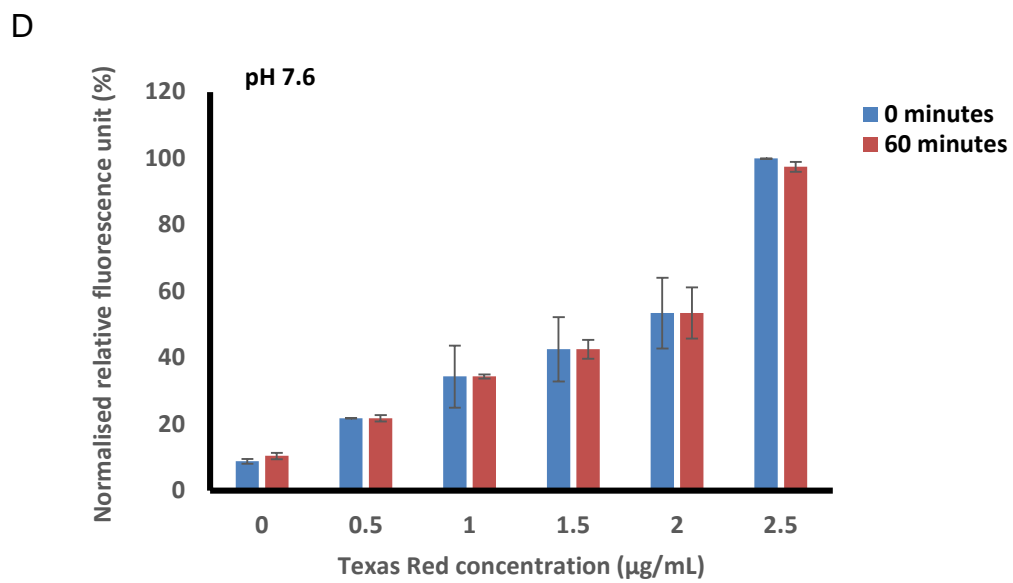
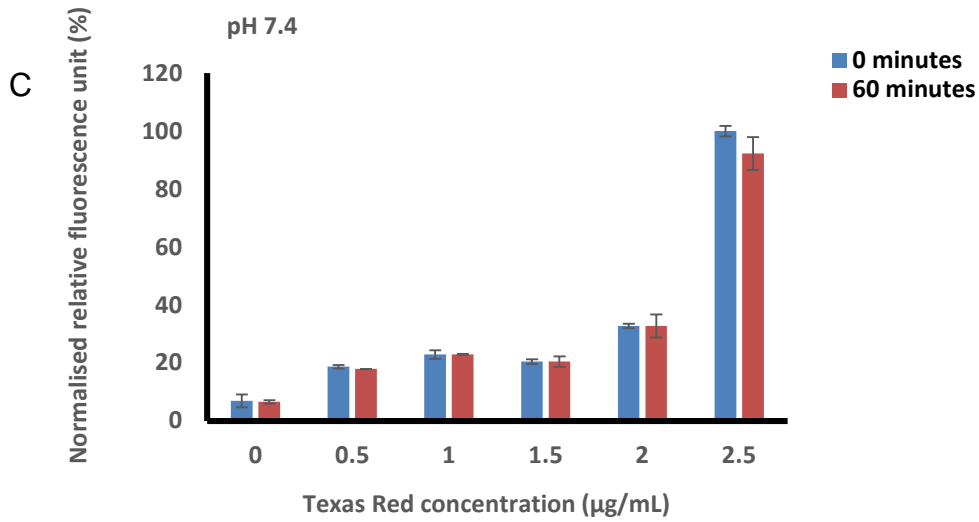


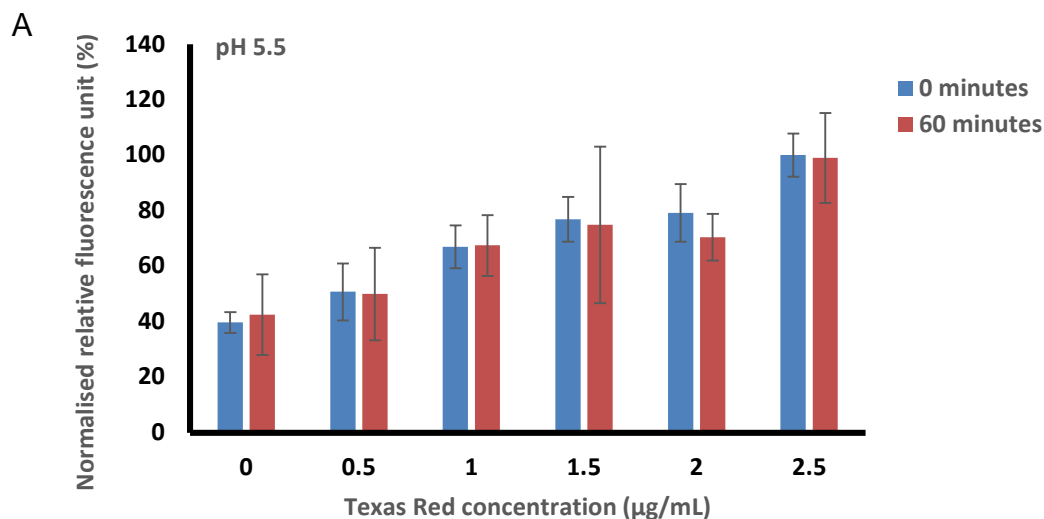
Figure 3-10: Fluorescence emission of Lower concentrations of BSA Texas Red™ conjugate (0.5-2.5 $\mu\text{g/mL}$).

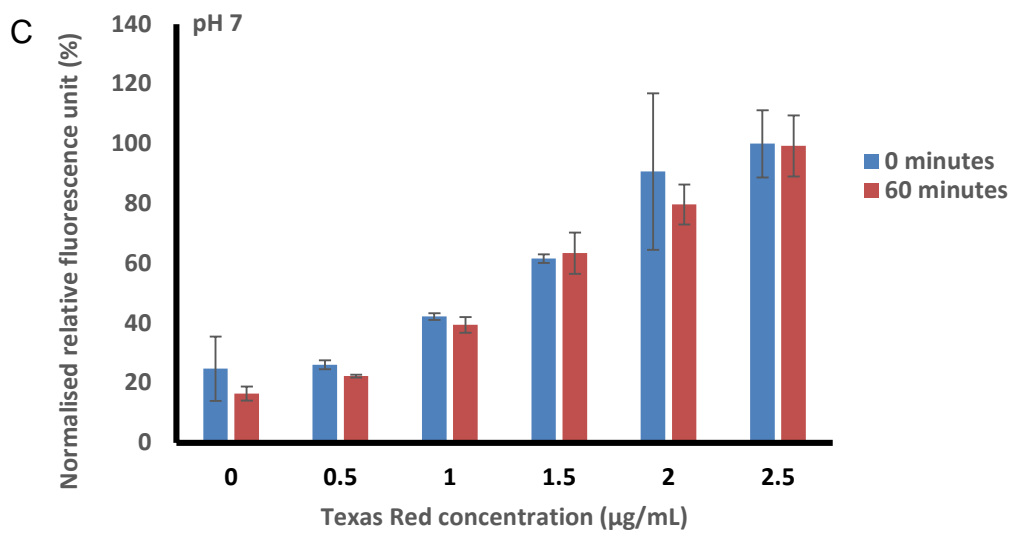
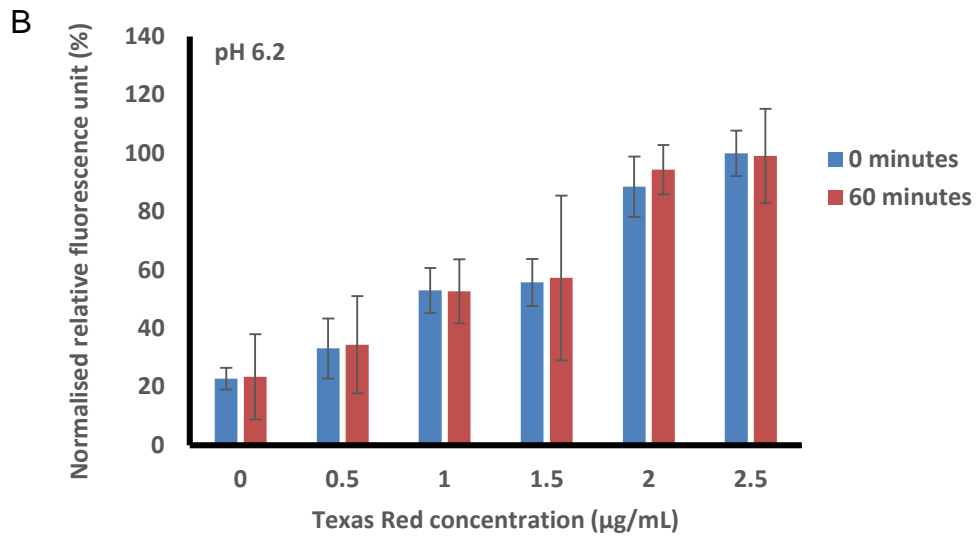
Fluorescence emissions in PBS with pH measurements of 5.5 (A), 7 (B), 7.4 (C) and 7.6 (D). Average and standard deviations were calculated with three replicates.

In these experiments, the results showed that at 0 minutes, the fluorescence emissions appeared slightly higher than after an incubation of 60 minutes. Nevertheless, the result was not correlated to the pH and it was most likely due to a small degree of quenching happening with time. Therefore, the results showed clearly that the fluorescence signal is stable in both acidic and neutral pH implying that BSA Texas Red™ conjugate is a suitable dye for conducting further experiments.

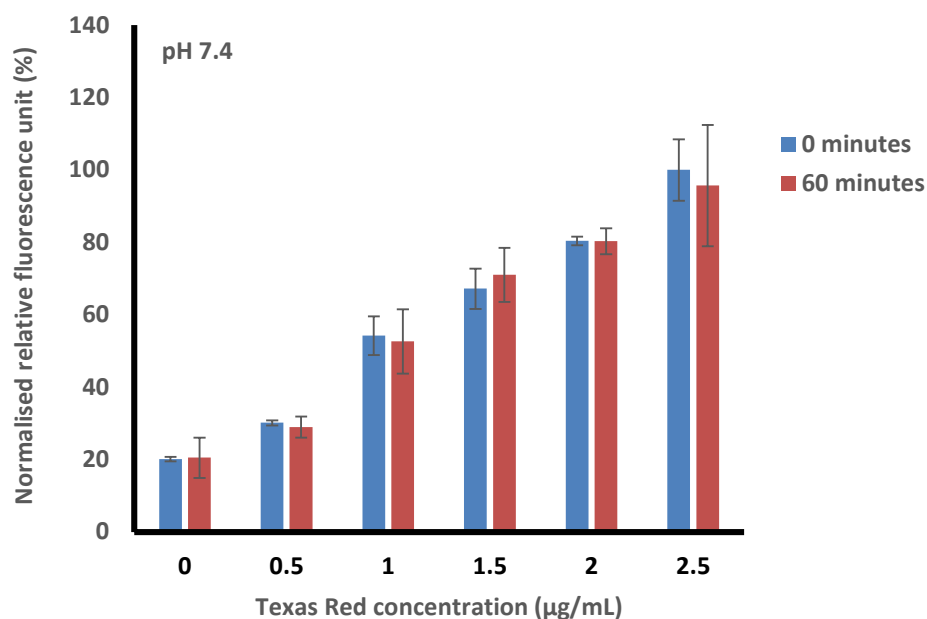
3.4.3 Fluorescence of BSA Texas Red™ in PBS/PEG solution

As the previous study done at Cranfield (Serfimowicz, 2018) showed quenching of the dye in acidic pH when in PBS/PEG solution, the experiment was repeated in PBS/PEG as part of this research, continuing from the pilot, and the results showed no loss of fluorescence signal of BSA Texas Red™ conjugate in the presence PBS/PEG matrix, which may be attributed to the fresh and different types of CIONPs used in all experiments (Figure 3-11).





D



E

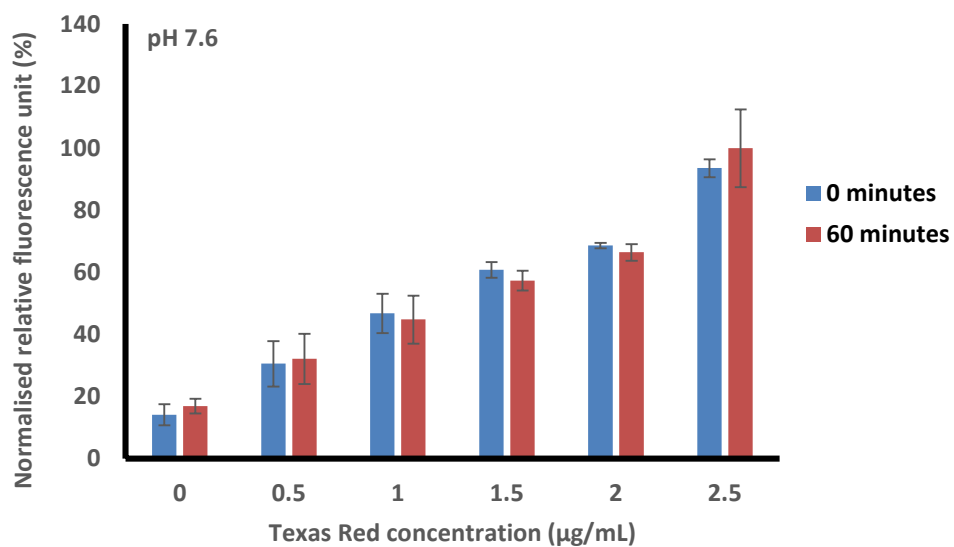


Figure 3-11: Fluorescence emission of BSA Texas Red™ conjugate in the presence PBS/PEG at 0 minutes and 60 minutes.

Averages and standard deviations were calculated with three replicates. Dilutions of dye (2.5 µg/mL) were prepared in PBS/PEG (1 mg/mL). The dilutions were then adjusted to pH 5.5, 6.2, 7, 7.4 and 7.6.

The fluorescence was then read at 0 minutes and 60 minutes to assess the effect of time and pH on the signal (Figure 3-12).

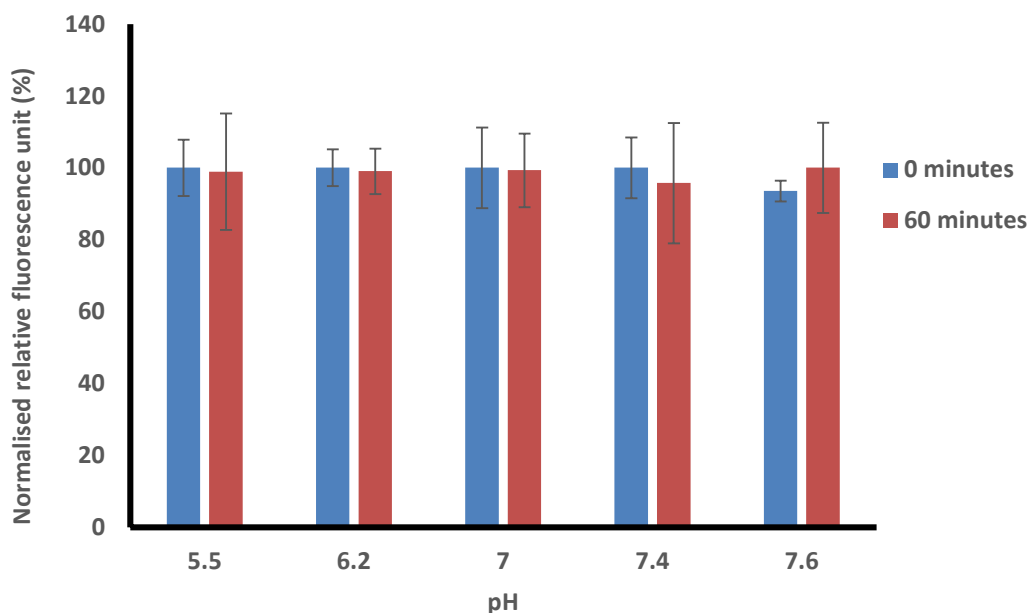


Figure 3-12: Fluorescence emission of BSA Texas Red™ conjugate (2.5 µg/mL) in PBS/PEG 5.5, 6.2, 7, 7.4 and 7.6.

Average and standard deviations were calculated with three replicates.

The results showed that over time there is no noticeable fluorescence quenching of the dye. This result implies that the dye can be used at low concentrations (0-2.5 µg/mL) and is therefore suitable as a tag to develop the chemistry for the drug delivery studies in this work. To confirm this further and to conduct further experiments, the dye was also incubated with commercial IONPs (CIONPs) adding PEI in the buffer.

3.4.4 Effect of pre-suspended CIONPs on fluorescence of BSA Texas Red™ conjugate in PBS/PEG/PEI solution.

Pre-suspended CIONPs (1mg/mL) dispersed in PBS/PEG/PEI (PBS pH 7.4, PEG 1 mg/mL, and PEI 0.6 mg/mL) were initially used in this work to assess the fluorescence signal over 60 minutes' incubation (Figure 3-13).

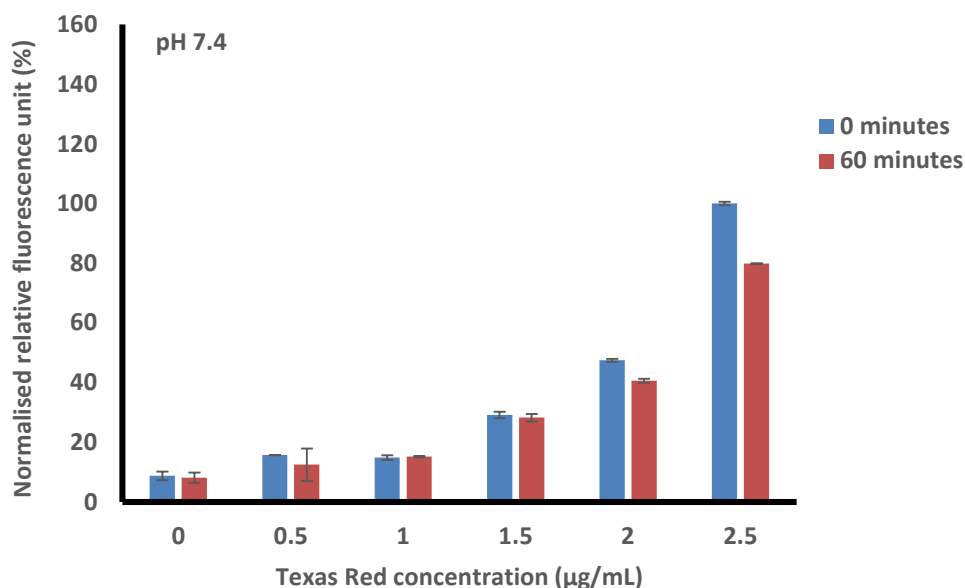


Figure 3-13: Fluorescence signal of Pre-suspended CIONPs (1 mg/mL) in BSA Texas Red™ conjugate in PBS/PEG/PEI.

Signal was read at 0 and 60 minutes. The BSA Texas Red™ conjugate 0.5-2.5 µg/mL were prepared in PBS/PEG/PEI pH 7.4. Average and standard deviations were calculated with three replicates.

The signal appeared to increase with concentration of the dye and a small quenching of the signal was seen after 60 minutes as also seen sometimes in previous experiments without the nanoparticles. In preparation for investigations using CIONPs, the pre-suspended CIONPs, (a solution of CIONPs obtained in liquid form) were suspended in buffer as described in section 3.3.8. Their behaviour when placed on a magnetic sample holder (Figure 3-14) was compared with the powdered CIONPs (a dry product of IONPs purchased as a

powder, then sonicated in solution to disperse them prior to fluorescence investigation).

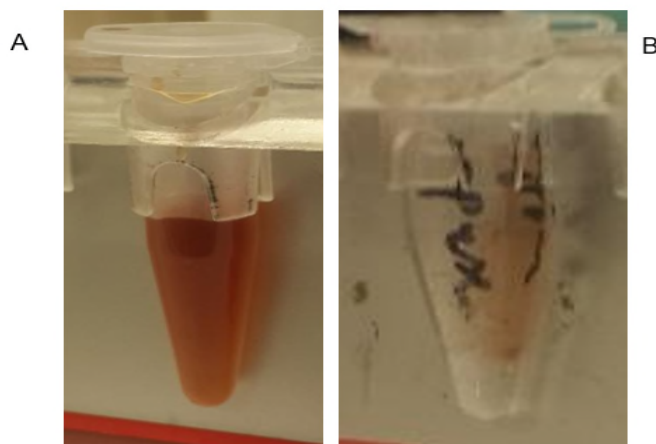


Figure 3-14: Pre-suspended CIONPs (A) powdered CIONPs (B) magnetic behaviour when extracted on an Eppendorf magnetic sample holder.

When the powdered nanoparticles were put on the magnetic rack they immediately magnetised and dropped out of solution aligning on the side of the tube, leaving the supernatant clear (Figure 3-14B). The pre-suspended CIONPs remained suspended in solution while on the magnetic sample holder even after 24 hours at ambient temperature (Figure 3.14 A).

The pre-suspended CIONPs though not affecting the fluorescent response were therefore not used for later investigations as extraction of CIONPs from the surrounding solution was essential to investigate the release of tagged particles attached in a nanocarrier complex in PBS during later stages of the research.

3.4.5 Powdered CIONPs effect on fluorescence

Powdered commercial iron oxide (CIONPs) were then used to test the fluorescence in PBS/PEG/PEI and studied in the same conditions as the dye. Short chain, non-toxic PEI was used with PEG in the buffer. The use of PEG/PEI together makes the matrix more amenable for use as an encapsulant and vehicle to trojan the IONPs in the intended potential role for targeted drug delivery. In fact, the positively charged amino groups in PEI can facilitate the crossing of the

negatively charged cell membrane. The fluorescence signal of PBS alone, PBS/PEG/PEI, PBS/PEG/PEI/IONPs and finally PBS/PEG/PEI/IONPs with BSA Texas Red™ conjugate (TEX 615) both at pH 5.5 and 7.4 are shown in Figure 3-15 A and B respectively.

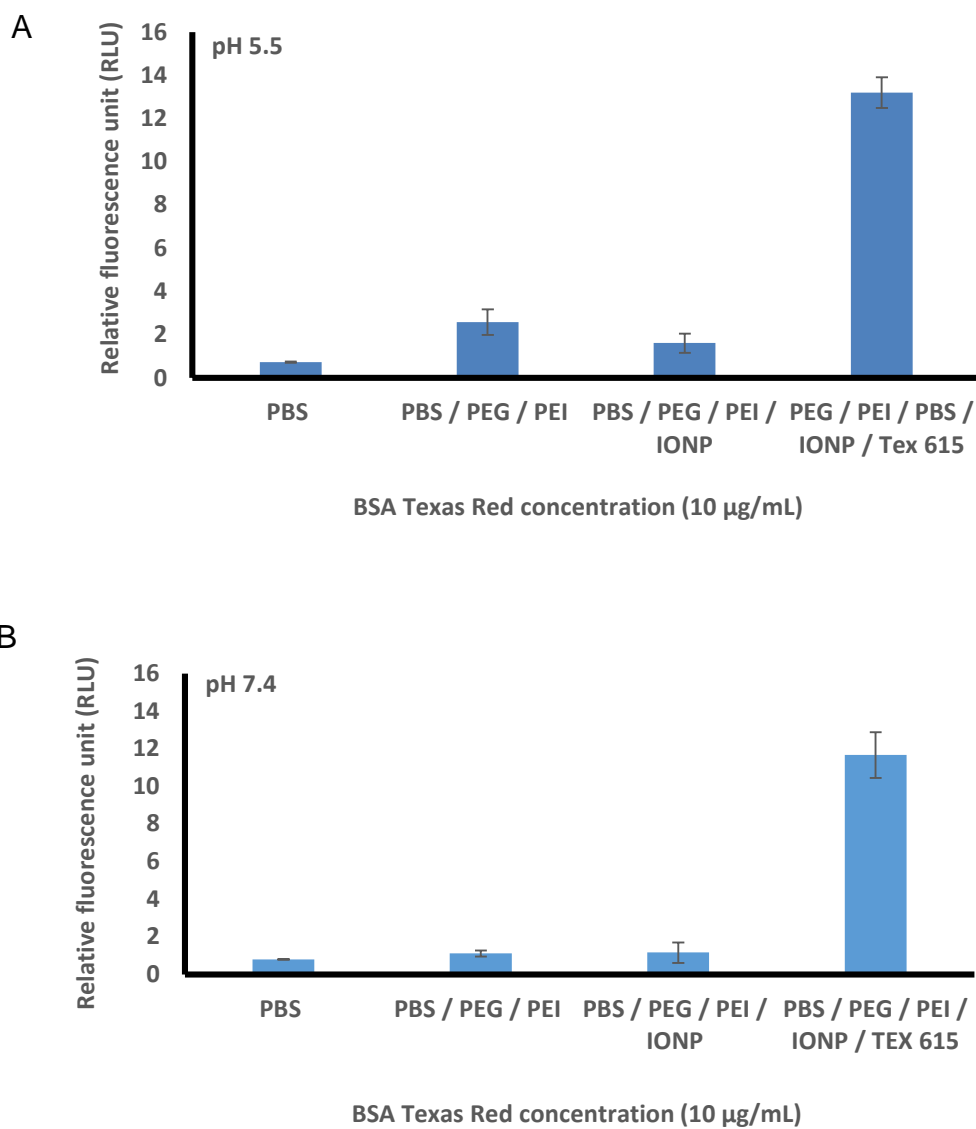
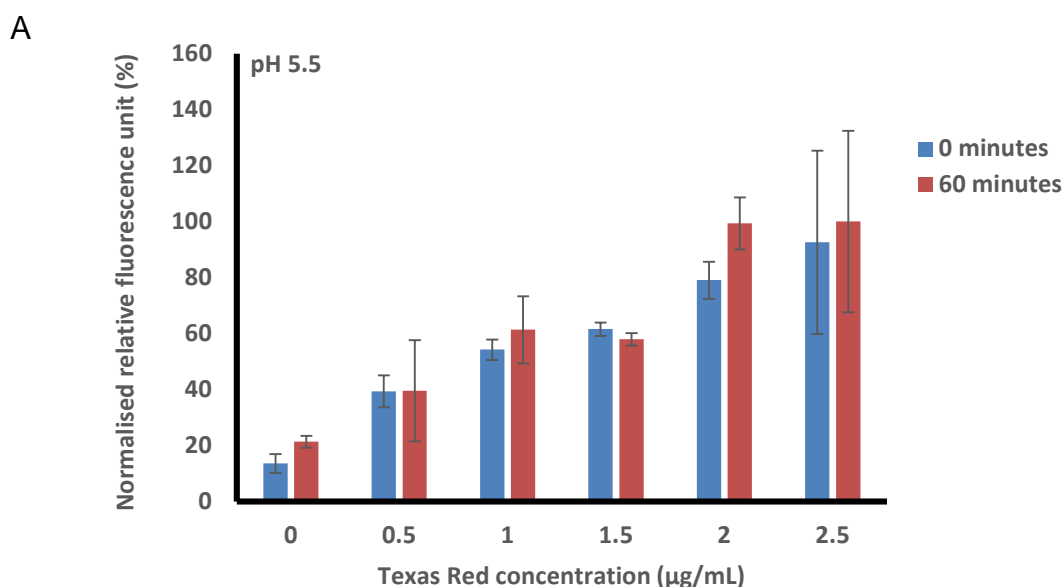


Figure 3-15: Fluorescence emissions obtained for PBS, PBS/PEG/PEI, PBS/PEG/PEI/IONP and PBS/PEG/PEI/IONPTEX 615 at pH 5.5 and 7.4

A concentration of 10 $\mu\text{g/mL}$ of BSA Texas Red™ conjugate was used for the experiments and average and standard deviations were calculated with three replicates.

The above results suggest that the PBS/PEG/PEI/IONPs do not interfere with the fluorescence signal of the BSA Texas Red™ conjugate at both pH 5.5 and 7.4, confirming their suitability for the study.

In another experiment, to investigate the effect of the CIONPs on the fluorescence signal of BSA Texas Red™ conjugate with time and different pH values, the signals of a range of dye concentrations between 0-2.5 $\mu\text{g/mL}$ were measured both at time 0 and after 60 minutes of incubation both at pH 5.5 and 7.4. The results show a stable fluorescent signal in all concentrations tested (Figure 3-16).



B

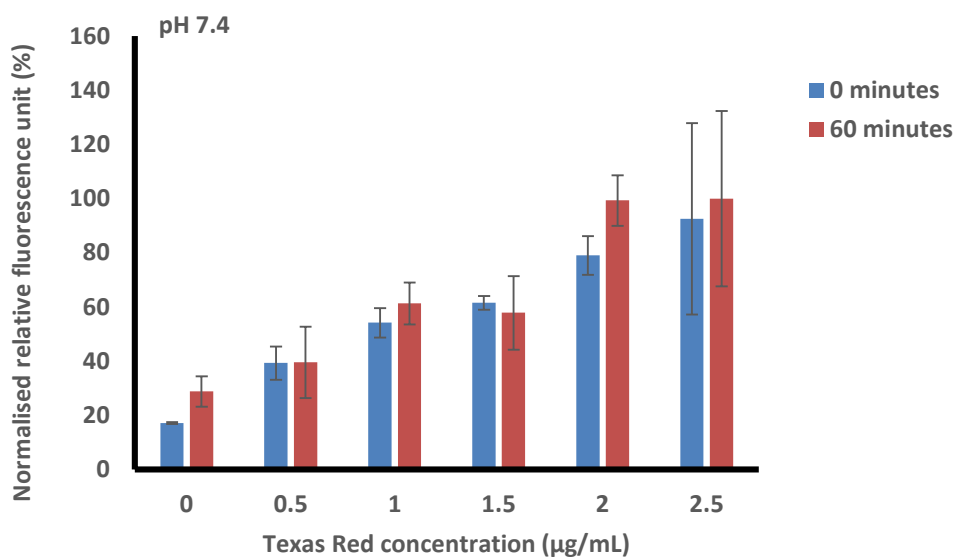


Figure 3-16: Fluorescence signal of BSA Texas Red™ conjugate in the presence of CIONPs (1 mg/mL) prepared in PBS/PEG/PEI (pH 5.5 and 7.4).

Signal was read at 0 and 60 minutes. BSA Texas Red™ conjugate concentration range between 0-2.5 µg/mL were used. Average and standard deviations were calculated with three replicates.

The results showed no quenching of the dye in presence of the CIONPs either with time or at two different values, demonstrating that the dye and these nanoparticles are suitable for the drug delivery studies.

After assessing the fluorescence response derived from PBS/PEG/PEI/CIONP, the next set of experiments, described in the next Chapter, focused on the development of method for the attachment of siRNA to the nanoparticles in the presence of PBS/PEG/PEI and subsequent release of the siRNA from the nanocarrier complex.

3.5 CONCLUSIONS

BSA Texas Red™ conjugate fluorescence stability was studied in different pH values. Contrary to the results obtained during the pilot study, the investigations carried out here confirmed that the dye had no loss of signal in acidic or neutral

pH, both in the presence and absence of both PEG/PEI and commercial IONPs. These finding highlights that the problem seen in the pilot study was due to the different type of CIONPs used. The results have demonstrated that Texas Red dye is a stable fluorescence label to visualise the attachment and release of siRNA to and from the IONPs, which is described in the next chapter.

CHAPTER 4

ENCAPSULATION AND RELEASE OF TEX 615-siRNA FROM NANOCARRIER COMPLEX USING COMMERCIAL IRON OXIDE NANOPARTICLES

4 ENCAPSULATION OF TEX 615-siRNA TO CIONPs IN PBS/PEG/PEI AND RELEASE IN PBS

4.1 INTRODUCTION

The synthesis and optimisation of nanocarrier complexes involving the use of iron oxide nanoparticles for drug delivery to treat cancer tumours has been in use for some time now (Zhao et al., 2018). Cancer treatments including radiotherapy, surgery, and chemotherapy are still required to treat or manage cancers, even though some have variable or limited success, depending on the diagnosis, prognosis and severity of the cancer (Moser and Meunier, 2014). The main disadvantage of the methods for treating cancers utilised in the past thirty years borders on the potentially harmful side effects that chemotherapy and radiation may have on healthy tissue surrounding the tumour (Zugazagoitia et al., 2016). There are differences in the internal and external environment of the tumour which must be considered while targeting the tumour with nanocarrier treatments. Intracellular pH (pH_i) is essentially identical or slightly more basic in tumour compared to normal tissue (Gerweck and Seetharaman, 1996); an average pH_i of 7.2 can be found in both tumour and normal tissue (Gerweck and Seetharaman, 1996). Generally, pH_e values of the normal tissues (brain tissues, subcutaneous tissues, etc.) are in the range of 7.2–7.5. However, pH_e of tumour tissues is mildly acidic in the range of 6.4–7.0 (Hao et al., 2018). This may suggest that drug release studies may involve pH investigations, as the nanocarrier will have to transport the drug to the required tumour site and either release it in the extracellular acidic environment or cross this before releasing it inside the cells though this will depend on the application method; whether the cancer drug will be administered through invasive or non-invasive methods. For treatments that need to work within cells such as genetically based drugs, it may be considered necessary to harvest tumour cells, treat the tumour cells *ex-vivo* (Yang et al., 2012; Chen and Chien, 2019), (outside the body) and re-introduce the 'genetically modified' cancer cells into the body. Alternatively, drug administration *in-vivo* (Dorai et al., 2001; Kim et al., 2018) involves introducing the genetic drug into modified cancer treatment to living cancer cells while the cells are still in the body.

Genes are popular candidates for therapeutic applications targeting diseases like cancer due to their ability to produce bioactive proteins (Wirth et al., 2013). The application of biomimetics in medicine and pharmaceuticals is a promising method for the treatment of diseases like cancer (Oroojalian et al., 2021). Methods for transferring genes into cells, include particle bombardment (Zhang et al., 2002), receptor mediated gene delivery (Martin et al., 2012), electroporation (Raffa et al., 2012), calcium phosphate precipitation (Tang et al., 2015), lipomal delivery (Olusanya et al., 2018) and viral vector delivery (Dai and Zhang, 2019).

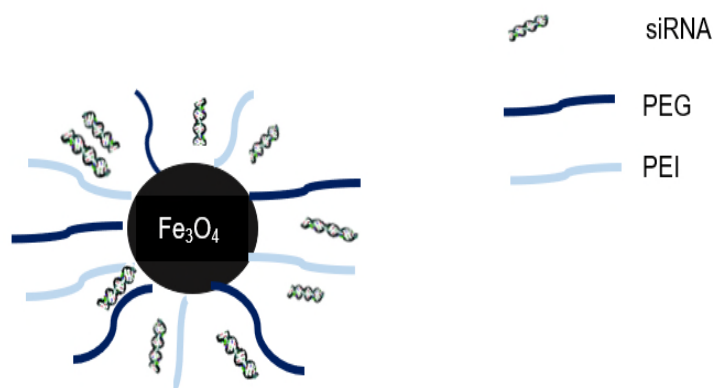
The nanocarrier complex treatment of cancer cells is currently an option in the treatment of cancers by targeting the tumour and delivering the drug directly to the affected site via a traceable vehicle. Targeted treatment has the potential to reduce the adverse effects of current cancer drug therapies on healthy tissue and regulate the amount of drug delivered to cancer cells. In this study, RNA with known potential as a biomarker and therapeutic agent for metastatic prostate cancer (Crea et al., 2014) is used in this research as the drug that will be attached by adsorption to the iron oxide nanoparticles.

The use of biocompatible polymers to coat metallic nanoparticles can help regulate the drug delivery and reduce any biocompatibility issues. Hydrophobic, physical interaction enables the attachment of biocompatible polymers such as PEG/PEI to the iron oxide nanoparticle. In addition, to ensure biocompatibility, the PEG/PEI covering the nanocarrier will also serve as protection for the siRNA preventing proteolytic enzymes from destroying it before it reaches the target tumour. Furthermore, the polymers aid the ingress of the pay-loaded particle through the membrane of the cancer cell (Lu and Zhang, 2018) while regulating release of the drug inside the cancer cells (Charmi et al., 2019). Naked siRNA is labile and would be quickly degraded by serum nucleases. Thus, numerous studies employing siRNA utilise polymeric, chemical modifications that increase its stability. Studies have shown that the gene inhibition kinetics of unmodified and nuclease-stabilised siRNA were essentially the same when electroporated into cells, by the use of an electric current creating pores in the cell membrane to

increase cell permeability enhancing the introduction of drugs, chemicals and DNA into cells (Bartlett and Davis, 2007; Pagant and Liberatore, 2021; Kurotsu et al., 2022).

siRNA is a double – stranded nucleic acid. It has an anionic phosphodiester backbone and can interact electrostatically with cationic agents (Gary et al., 2007). When compared to DNA which contains the sugar deoxyribose, the RNA backbone contains ribose with a hydroxyl group in the 2' position of the pentose ring instead of a hydrogen atom (Kay et al., 2001).

Bare RNA however, does not withstand the chemical effect of nucleases (Hashiba et al., 2017). Immunological response may also rapidly degrade and destroy the exposed nucleic acid before it arrives at the targeted tumour cells. Hydrophilicity, relatively large size and negatively charged phosphate groups may work against permeation of cell and nuclear membranes. In this work, the synthesis and formulation of a nanocarrier complex has been developed. Such a nanocarrier has potential to deliver siRNA to the tumour cell, in the presence of a polymer (PEG/PEI) coat to protect the labile siRNA from proteolytic enzymes which may destroy the siRNA before it reaches the tumour site (Scheme 4-1).



Scheme 4-1: Scheme of nanocarrier complex prepared in this study

The above figure depicts the core IONPs used in this research. The siRNA attaches to the IONPs in PEG/PEI layer. Tumour-targeting ability, minimal toxicity, stability outside the cell membrane, accurate siRNA release in the cytoplasm, and MR-tracing ability makes the iron oxide nanoparticle an effective therapeutic molecule for use in drug delivery to cancer cells (Killian and Von Heijne, 2000).

The release of the siRNA into the tumour cells has been known to occur as the pH gradient of the internal environment of the tumour is neutral or approaching neutral, while the immediate external environment of the cancer tumour cells is acidic. Acidic pH derived from cancer cells can induce failed reprogramming and tumour progress in normal cells surrounding cancer cells (Tavakol, 2014). Polymeric nanoparticles can be made from synthetic polymers, including poly(lactic acid) (PLA) and poly(lactic co-glycolic acid) (Hrkach et al., 1997) or from natural polymers such as chitosan (Alonso et al., 1997) and collagen (El-Samaligy et al., 1983) and may be used to encapsulate drugs without chemical modification. A variety of polymer formulations have been proposed in literature as potential carriers, most of which facilitate gene delivery by encapsulating, and in some cases, condensing nucleic acids into nano-sized particles which can then be taken up by cells (Killian and Von Heijne, 2000). Crucial to successful delivery of the gene to a cell is the polymer's ability to protect its contents from degradation in the extracellular environment. A well-designed carrier will also promote cellular uptake and intracellular release of the nucleic acid (Gary et al., 2007).

There has been significant interest and research conducted on nanoparticles for drug delivery, imaging, and bio-diagnostic applications (Kong et al., 2017). In general, controlled-release polymer systems facilitate drug delivery in the optimum amounts for an extended time, thus increasing the efficacy of the drug (Farokhzad and Langer, 2006). Nanoparticles for targeted drug delivery require precise design of the nanoparticles tuning several parameters which must be considered together to attain the highest therapeutic efficacy (Cabral and

Kataoka, 2014; Vangijzegem, 2019). The inherent sensitivity of RNA molecules both inside and outside the cell directed attention towards degradation by ribonucleases (Rana, 2007). siRNA can be labelled to track its progress through the extracellular and then intracellular phases of its transportation to the site of the tumour using a fluorescent dye.

Iron oxide nanoparticles bound to siRNA can be detected by magnetic resonance imaging (MRI), due to the magnetic behaviour of the nanoparticles. Out of the many types of RNA (Figure 4-1), siRNA is suitable for use in targeted drug research. siRNA has many properties including inhibition of protein synthesis.

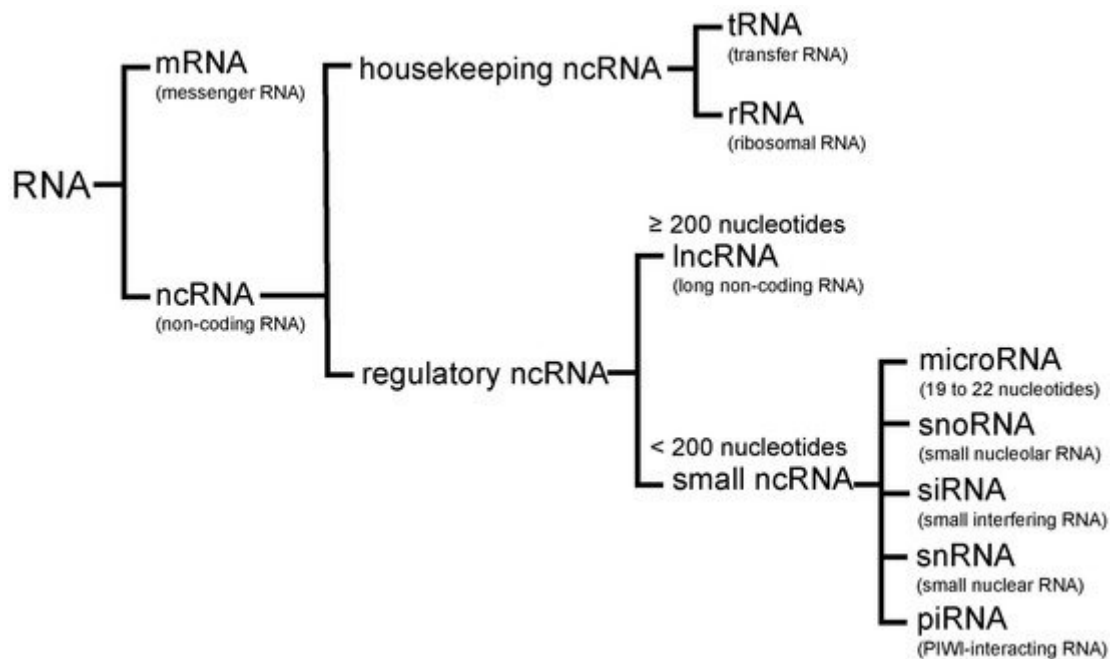


Figure 4-1: Types of RNA (Inamura, 2017).

RNA families have varied roles in the intracellular regulatory mechanisms of cell interaction. RNAs are divided into two main groups: messenger RNA (mRNA) and non-coding RNA (ncRNA). NcRNAs include housekeeping ncRNA, which consists of transfer RNA (tRNA) and ribosomal RNA (rRNA), and regulatory ncRNA. Regulatory ncRNAs are classified into long ncRNA (lncRNA) and small ncRNA. Small ncRNAs are subclassified into microRNA, small nucleolar RNA

(snoRNA), small interfering RNA (siRNA), small nuclear RNA (snRNA), and PIWI-interacting RNA.

Small interfering RNA (siRNA) is used in this work, and is composed of a double strand, to be interchangeably called double stranded siRNA (DsiRNA). SiRNA possesses distinct features. It is commonly between 20-24 base pairs in length. In double stranded RNA the core is a duplex structure.

Polymers are the ideal candidates to serve as nucleic acid carriers as they offer the versatility and ease of manipulation required for a wide range of gene therapy applications (Gary et al., 2007). Even if enzymatic degradation was not a concern, the efficiency of transfecting cells with naked siRNA *in-vitro* or *in-vivo* would be very low because the negative charge on the molecules renders them unlikely candidates to cross the negatively charged cell membrane for cellular internalisation. Unfortunately, enzymatic degradation of nucleic acids, particularly siRNA, is a very real concern which further necessitates the need for a protective carrier.

In this research, a nanocarrier complex has been developed and optimised. The complex comprised siRNA labelled with a fluorescent dye, TEX 615-siRNA (for visualisation) bound to iron oxide nanoparticles and covered in a mixture of PEG and non-toxic, short chain PEI, as mentioned previously. Following the successful attachment of the siRNA to the IONPs, the nanocarrier complex was then used to assess its release in PBS with pH 6.4 and pH 7.4 mimicking the extracellular and intracellular cancer environment.

4.2 MATERIALS

4.2.1 General chemical and instrumentation

TEX 615 (Texas Red) dye conjugated to siRNA (to produce TEX 615-siRNA) was purchased from Integrated DNA technologies (Leuven, Belgium); Polyethylene glycol and RNase free water were purchased from Sigma Aldrich (Kidlington, UK). Polyethylene imine (PEI) 600 g/mol 99% was purchased from Polysciences, Inc. (Warrington, USA). pH strips, and commercial iron oxide nanoparticles

(CIONPs) (pre-suspended) in solution were purchased from ThermoFisher Scientific (Loughborough, UK) and powdered IONPs (15-20 \varnothing nm) were purchased from Nanomaterials Inc. (Texas, USA).

Entris II BCE Analytical Balance, Sartorius (Birmingham, UK) was used to weigh the chemicals. Stuart Gyro-rocker SSM3, Mini 230V from Techne (Staffordshire, UK) was used for mixing and solubilising the samples. The magnetic sample holder used to precipitate the CIONPs was purchased from Eppendorf (Stevenage, UK). Shimadzu CTO-20A Prominence HPLC Column Oven used to incubate the samples at 37°C (to mimic the internal environment of the human body) was from Shimadzu Corporation (Kyoto, Japan). Dispersion of powdered iron oxide nanoparticles was carried out using a Branson ultra sonifier digital model 250 sonic probe, Branson Instruments (GA, USA). Zetasizer Nano Instrument (Nano S) was from Malvern Panalytical Ltd. (Great Malvern, UK) was used to determine the hydrodynamic diameter of the nanoparticles. Magnetic stirrer/hot plate 1103 Jenway (Staffordshire, UK) and Gene2Vortex Scientific Industries (St Neots, UK) were used to prepare buffer solutions. Fluorometric measurements were conducted using the computer-controlled spectrophotometer microplate reader, Varioskan Flash, and the 96-well NUNC microplates used were from Thermo Fischer Scientific (Roskild, Denmark). Data capture was via SKanIT RE 2.4.5 software.

4.3 METHODS

4.3.1 Optimisation of loading of TEX 615-siRNA to CIONPs

Before the siRNA experiments could begin, the lyophilised TEX 615-siRNA (stock concentration 5 nMol) also simply referred to here as siRNA, was dissolved by adding 100 μ L RNase free water to the vial and vortexing briefly according to manufacturer's instructions, to obtain a TEX 615-siRNA concentration of 50 μ M. According to manufacturer's directions, the mixture was then heated in a beaker to 94°C for 2 minutes, then allowed to cool to room temperature. Aliquots of 10 μ L were made and stored at -20°C until required.

The loading efficiency in percentage (LE%) was then calculated as follows:

$$\text{LE \%} = \left[\frac{\text{fluorescence of total drug added} - \text{fluorescence of free non-attached drug}}{\text{fluorescence of total drug added}} \right] * 100$$

Optimisation of pH: PBS/PEG/PEI/CIONPs (pH 5.5 and 7.4) were all prepared as described in section 3.3.7. Samples of PBS/PEG/PEI (1) and PBS/PEG/PEI/CIONPs (2) were compared with PBS/PEG/PEI/siRNA (3) and PBS/PEG/PEI/CIONPs/siRNA (4) at the two pH values (Table 4-1).

Table 4-1: Powdered commercial IONP (CIONP) nanocarrier complex

Sample	pH 5.5 and pH 7.4
1	PBS/PEG/ PEI (PEG 1mg/mL and PEI 0.6 mg/mL)
2	PBS/PEG/PEI (PEG 1mg/mL and PEI 0.6 mg/mL) CIONP (0.1 mg/mL)
3	PBS/PEG/PEI (PEG 1mg/mL and PEI 0.6 mg/mL) siRNA (2 μ M)
4	PBS/PEG/PEI (PEG 1mg/mL and PEI 0.6 mg/mL) siRNA (2 μ M) CIONP (0.1 mg/mL)

To prepare 500 μ L of samples in Table 4-1, a volume of 2 μ L of TEX 615-siRNA (50 μ M) was added to 498 μ L of PBS/PEG/PEI/CIONP pH 5.5 and 7.4 to obtain PBS/PEG/PEI/CIONP/siRNA (2 μ M) and vortexed briefly. The mixture was allowed to stand in the dark for 15 minutes to aid physical attachment of siRNA to the CIONPs. A 100 μ L volume of each sample was then added in triplicate to a 96 well plate and fluorescence measurements taken at 0 minutes. The samples were then returned to the vial and incubated at ambient temperature (25°C) in the dark on a Stuart Gyro-rocker for 60 minutes to further enhance the attachment of siRNA to the CIONPs. After incubation, the samples were delivered to the microtiter wells again, and photometric measurements taken at 60 minutes to observe the effect of time on the fluorescent signal.

Next, the CIONPs samples were aspirated again from the wells and delivered back into the Eppendorf tubes. The tubes containing samples were then placed on an Eppendorf magnetic sample holder and the CIONPs ‘extracted’ from solution by magnetic field attraction. As soon as the samples appeared clear of CIONPs, the colourless supernatant was carefully aspirated while the Eppendorf tubes containing the magnetised CIONPs were still in place on the magnetic sample holder. Next, 100 μ L of the aspirated supernatant was dispensed into a microtiter well plate to take the fluorometric measurements for CIONPs ‘extracted’ from solution of PBS/PEG/PEI/CIONPs. This fluorescence value indicated the amount of siRNA that failed to attach to the CIONPS (non-attached drug.) All photometric measurements were exported from SkanIT software and plotted in MS Excel.

Optimisation of PEG/PEI: In order to study the influence of the concentration and the ratio between PEG/PEI on the loading of TEX 615-siRNA, experiments were performed in the conditions described in Table 4.2, using the same methodology as explained for the pH study.

Table 4-2: Conditions tested for the optimisation of PEG/PEI ratio using 0.1 mg/mL CIONP and 2 μ M TEX 615 -siRNA

Sample	Nanocarrier complex
A	PBS/PEG 0.01 mg/mL PEI 0.01 mg/mL; PEG/PEI =1
B	PBS/PEG 1 mg/mL PEI 0.6 mg/mL; PEG/PEI =1.7
C	PBS/PEG 2.0 mg/mL PEI 0.6 mg/mL; PEG/PEI =3.33
D	PBS/PEG 3 mg/mL PEI 3 mg/mL; PEG/PEI =1

4.3.2 Release of TEX 615-siRNA from CIONPs

Following the development of the attachment of TEX 615-siRNA to CIONP samples in PBS/PEG/PEI, further experiments were conducted to investigate the release of TEX 615-siRNA in PBS, mimicking the physiological conditions of the body.

At the beginning of release experiments, the samples were prepared as described in section 4.3.1.

The CIONPs (0.1 mg/mL) in the PBS/PEG/PEI/CIONPs/siRNA samples were extracted out of solution by placing the samples in an Eppendorf magnetic sample holder until the supernatant had been seen as clear, and the CIONPs were aligned along the surface of the tube in contact with the magnetic sample holder (Figure 4-2).

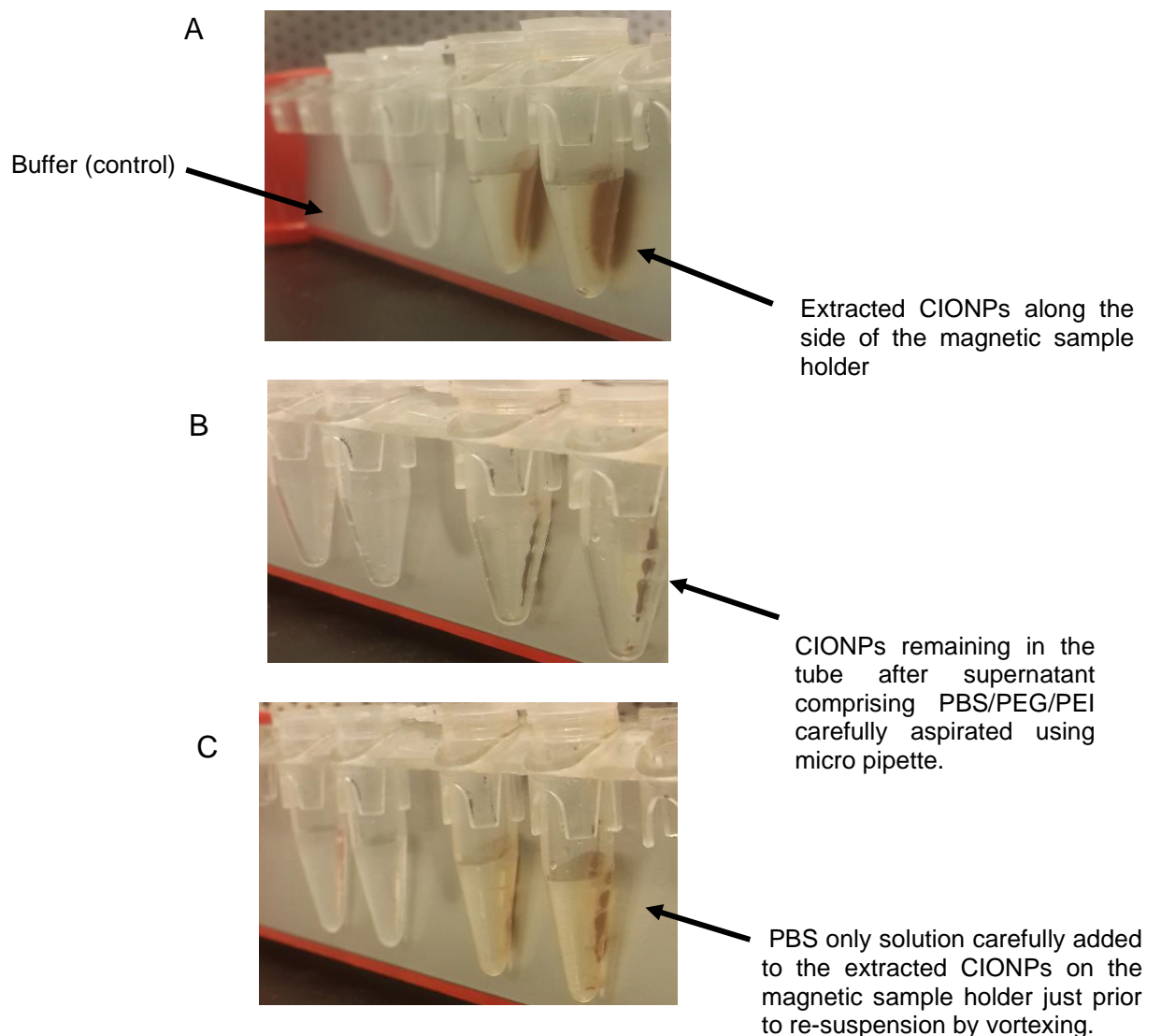


Figure 4-2: Extracted CIONPs from PBS/PEG/PEI/CIONPs/siRNA samples (A) Supernatant removed revealing only CIONPs out of solution (B) PBS added to resuspend CIONPs for siRNA release experiments (C).

In each of the images in Figure 4-2, there are four samples; from left to right, solution in tube 1 contains only PBS/PEG/PEI; tube 2 contains PBS/PEG/PEI/siRNA (2 μ M); tube 3 contains PBS/PEG/PEI/CIONP (0.1 mg/mL); tube 4 contains PBS/PEG/PEI/CIONP/siRNA (2 μ M) (Section 4.3.1; Table 4-1). Once the CIONPs had been extracted, the supernatant was removed, leaving behind only CIONPs with the siRNA attached. These were then resuspended in 500 μ L of PBS with pH 5.5, 6.4 and 7.4. PBS mimics the environment in the body with pH 7.4 being the pH within healthy and tumour cells; even though in some types of cancer cells the pH is known to be slightly less than pH 7.4 and pH 6.4 mimicking the acid extracellular environment. Photometric measurements were taken immediately, at 0 minutes. After measurements, samples were returned to their tubes and incubated in an oven for 60 minutes at 37°C. Just prior to incubation, the tubes containing samples were sealed with parafilm to minimise possible evaporation of the samples during incubation at 37°C (as mentioned earlier to mimic the physiological temperature of the human body's internal environment). Following incubation, the samples were dispensed in triplicate in microtiter plate and fluorescence measurements taken at 60 minutes. After measurements, the CIONPs were extracted again using the magnetic sample holder, and supernatant was removed. The supernatant was then tested for fluorescence at 60 minutes-extracted, since the CIONPs had been held by the magnet and only the supernatant was scanned for fluorescence signal. This fluorescence signal indicated the amount of siRNA released in the fresh PBS (drug released in solution). After the measurements, the supernatant was returned to the vials. The process of extraction, aspiration, and resuspension of CIONPs (maintaining the same volume of PBS without changing the buffer) was further repeated at hourly intervals: 0, 60, 120, 180, 240, 320 and 420 minutes. The results were exported and plotted in MS Excel.

The percentage of release was calculated as follows by considering 100% the actual total amount of siRNA loaded on the CIONPs (total amount of drug loaded).

Release % = (fluorescence of drug released in solution / fluorescence of total amount of drug loaded) * 100.

The results of photometric measurements were exported to Excel and plotted using the average of three measurements. Furthermore, the average reading was expressed as a percentage of the highest fluorescence value (fluorescence of the re-suspended CIONPs in PBS at time 0). Correlation of variation rather than standard deviation was calculated to assess the reproducibility of the experiments.

4.4 RESULTS AND DISCUSSION

4.4.1 Attachment of TEX 615-siRNA to CIONPs

Firstly, to assess the effect of PBS/PEG/PEI/CIONP on the fluorescence of TEX 615-siRNA in two different pH values 5.5 and 7.4, experiments similar to those reported in Chapter 3 for the BSA Texas Red conjugate were carried out. Results showed that up to 60 minutes of incubation there was no effect of the CIONPs on the fluorescence signal of TEX 615-siRNA at the two different pH values (Figure 4-3 A and B).

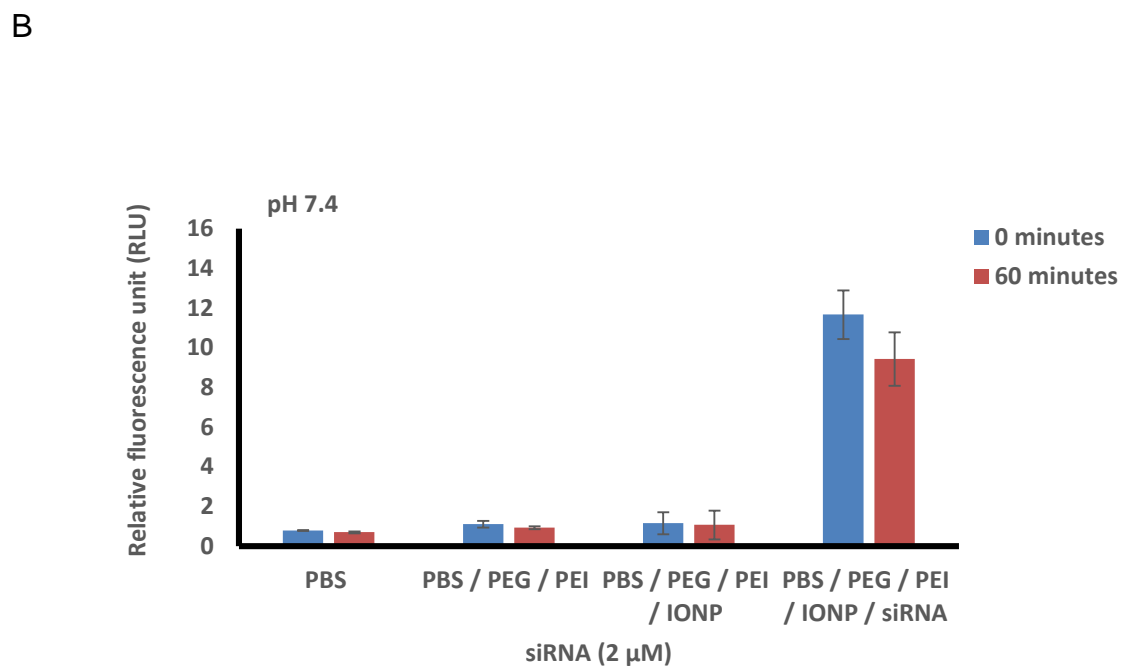
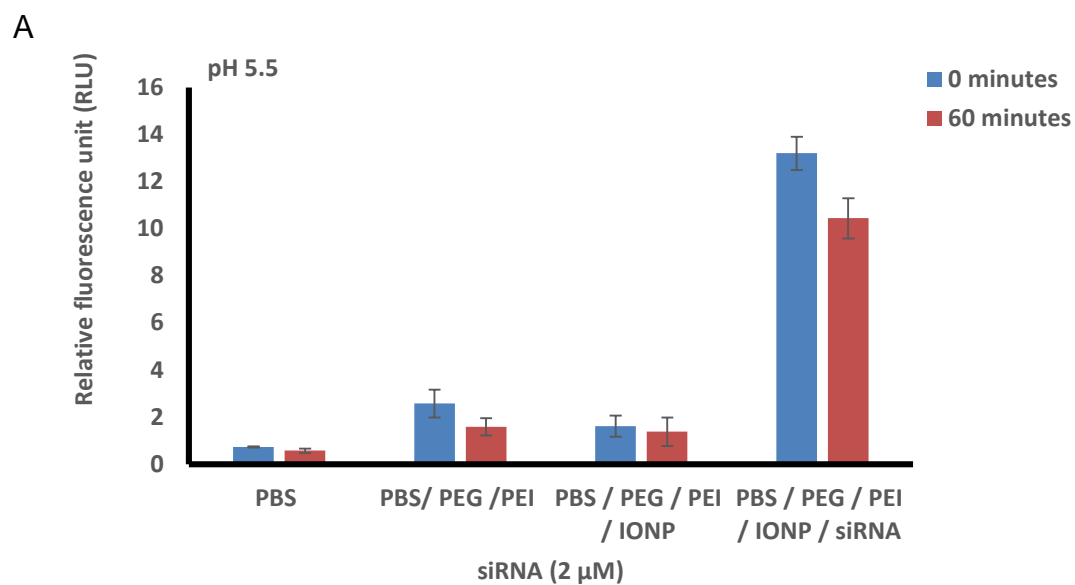


Figure 4-3: Fluorescence emission of TEX 615-siRNA at pH 5.5 (A) and 7.4 (B) in presence of CIONPs up to 60 minutes incubation.

PBS/PEG/PEI/CIONP/siRNA samples were measured at excitation 590 nm and emission at 615 nm. The samples were measured for fluorescence signal at 0 and 60 minutes. Average and standard deviation were calculated using three replicates.

The results also show a small quenching of the fluorescence signal after 60 minutes' incubation at both pH values. This loss may be attributed to the bleaching of the dye over time, rather than to an effect of the CIONPs. The dye is normally stored in the dark and is prone to photo decay, which is inevitable during the entire process of dilution, incubation and taking fluorescence measurements. Therefore, this makes the TEX 615 a suitable dye to tag the siRNA to study its attachment to IONPs.

Most siRNA-containing nanoparticles can be toxic to animals and humans, (Zuckerman et al., 2014) because the nanocarriers are prepared by electrostatically complexing siRNAs with excess cationic polymers or lipids (a combination of PEG and PEI in this work). It may be recommended to conduct specific toxicity studies relating to the use of polymers as biocomplexing materials for drug delivery. This may need to be conducted in collaboration with an animal model research group.

Therefore, the siRNA attachment to the CIONPs, its stability in neutral and slightly acidic conditions imitating the physiological environment and pH-dependent release were the most intensively studied aspects during this part of research.

Optimisation of the pH: To investigate the attachment of TEX 615-siRNA to the CIONPs, experiments were carried out as explained in Materials and Methods section 4.3.1. (Table 4.1), using PEG and PEI in pH 5.5 and 7.4. For the measurements, a 100 μ L volume of each control and sample was added in triplicate to a 96 well plate and the results are reported in Figure 4-4 A and B.

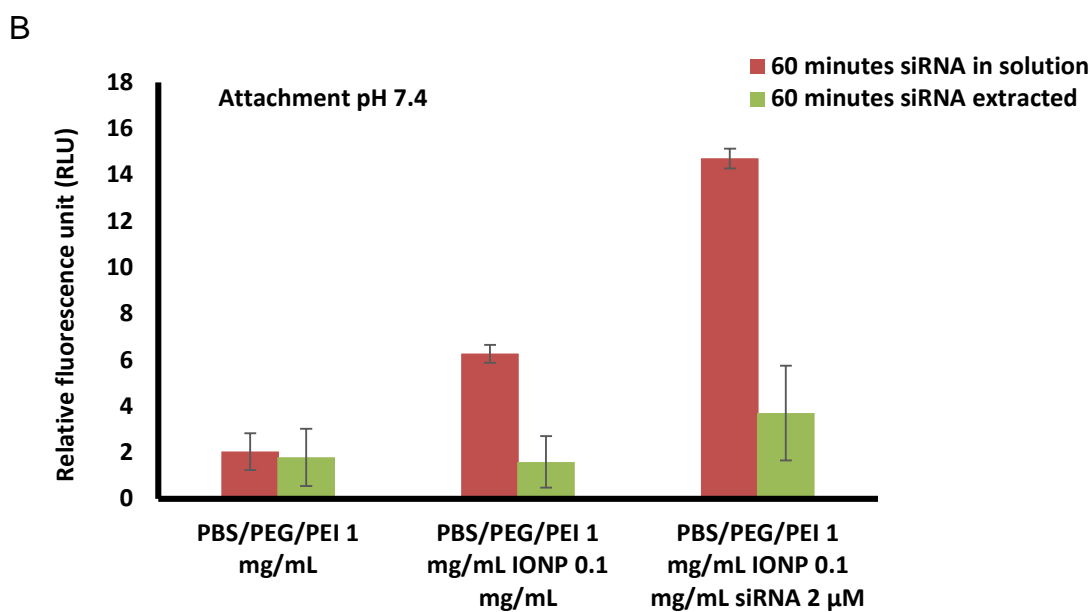
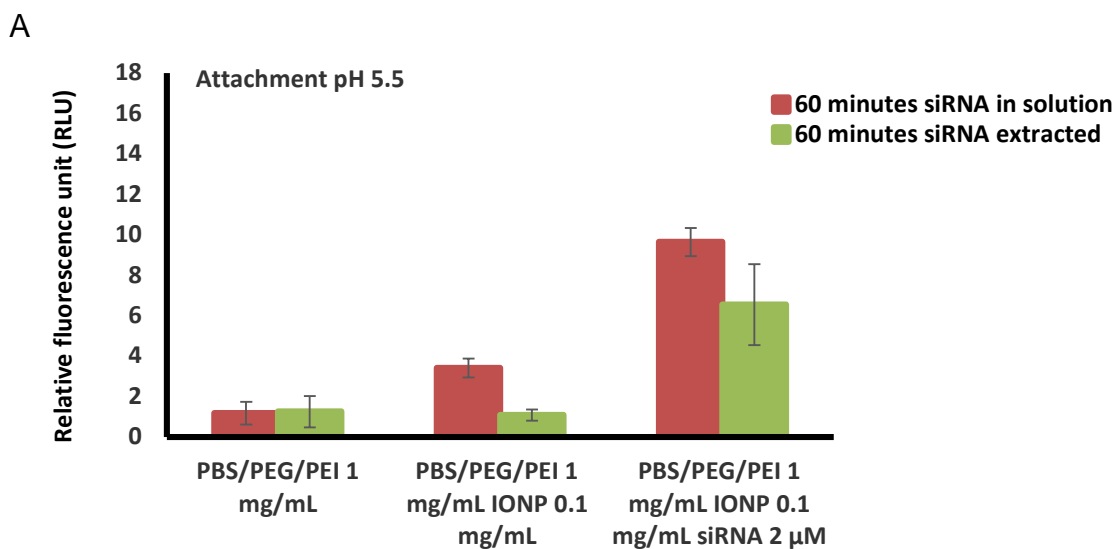


Figure 4-4: Example of relative fluorescence values obtained when testing the attachment of TEX 615-siRNA to CIONPs in nanocarrier complex.

PBS/PEG 1 mg/mL PEI 0.6 mg/mL CIONP 0.1 mg/mL TEX 615-siRNA 2 μ M were tested at 60 minutes incubation when the nanocarrier complex was in solution and after the CIONPs had been extracted from solution at pH 5.5 (A) and pH7.4 (B).

Figure 4-4 A and B show significant attachment of the labelled siRNA to the CIONPs, to both pH values, with the higher attachment observed at pH 7.4. In fact, after 60 minutes of incubation, the fluorescence value of CIONPs in solution was significantly higher than the fluorescence of the supernatant after CIONPs magnetic precipitation (extracted) indicating that the TEX 615-siRNA had successfully attached to the metal nanoparticles. The attachment of the TEX 615-siRNA to the PEG/PEI IONPs is more likely to be due to a combination of hydrophobic and electrostatic interaction between the siRNA and the two polymers. As the pKa of PEI is around 7.9, the polymer is positively charged at slightly alkaline condition (7.4) promoting stronger interaction with the negatively charged backbone of siRNA. This was confirmed in these results as there was a higher attachment at pH 7.4 than 5.5 and 6.4 (Figure 4-5).

The siRNA attached to the CIONPs was then calculated in percentage considering 100% of the fluorescence value of the samples after 60 minutes of incubation and with the CIONPs in solution (siRNA total), before magnetic extraction. The fluorescence value of the supernatant after CIONPs extraction was then measured and the percentage of the siRNA (non-attached) estimated. By subtracting the non-attached percentage from the total, the siRNA amount attached was finally calculated.

The same experiment was then carried out at pH 6.4 and in addition to 5.5 and 7.4 and the attachments in percentage at the three different pH values are shown in Figure 4-5.

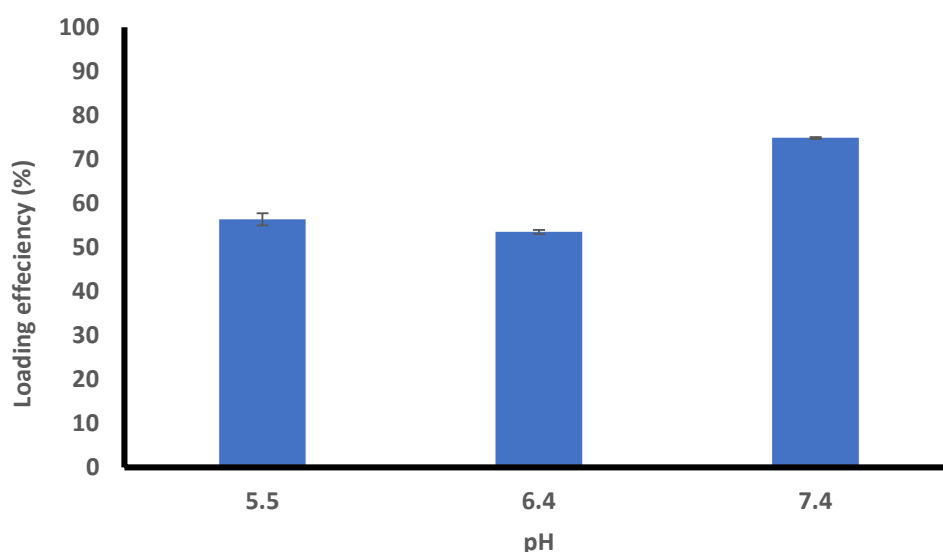


Figure 4-5: Attachment of TEX 615-siRNA to CIONPs

The results in this experiment show the effect of pH on attachment of siRNA to the CIONPs. Average and standard deviation of three measurements.

Figure 4-5 further confirmed that the highest siRNA attachment was seen as pH 7.4. Therefore, subsequent experiments were carried out only at pH 7.4 but by varying the concentration of PEG and PEI.

Optimisation of PEG/PEI: To optimise the ratio of PEG/PEI, the experiments were conducted as explained in materials and methods section, Table 4-2. The amount of TEX 615-siRNA attached to the nanoparticles in nanocarrier complex was calculated in percentage as already explained above. The amount of PEG/PEI used for this was optimised and the optimal ratio of polymer was established to obtain a high amount of siRNA attached to the CIONPs. The results are reported in Figure 4-6.

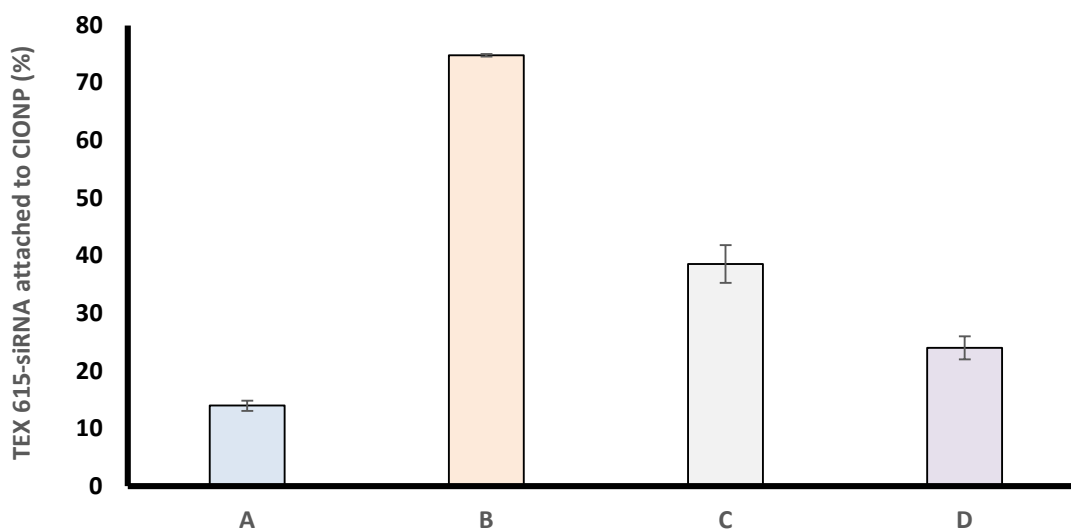


Figure 4-6: Percentage of TEX 615-siRNA attached to CIONPs.

The samples are different concentrations of PEG and PEI. The concentrations of samples A-D are given in the Table 4.2.

Figure 4-6 shows that among the concentrations tested, the nanocarrier complex prepared with PEG 1 mg/mL and PEI 0.6 mg/mL (condition B) gave the highest siRNA attachment. This could be explained by the fact that a certain amount of PEG and PEI is necessary to promote the hydrophobic and electrostatic interaction to attach the siRNA to the IONPs. If the concentration of PEG/PEI is too low, it may be inadequate for an effective attachment. The ratio between PEG/PEI also seems to be very important. The best attachment was observed in sample B, for a ratio of 1.7 in the figure above, whereas worse results were seen for higher and lower ratios. This means that a balance between hydrophobic and electrostatic interaction is necessary to obtain the optimal attachment.

Following successful demonstration of attachment of TEX 615-siRNA to the CIONPs and the optimisation of the binding conditions (e.g. pH and the amount of PEG and PEI), the release of TEX 615-siRNA in PBS buffer was conducted (as described in methods section 4.3.2).

4.4.2 Release of TEX 615-siRNA from CIONPs

To observe the release of TEX615-siRNA from CIONPs, the experiments were conducted at 37°C as explained in section 4.3.2. The release was calculated in percentage considering 100% of the fluorescence value of the nanocarrier complex resuspended in PBS with CIONPs in solution. The results are shown in Figure 4-7 to 4-9.

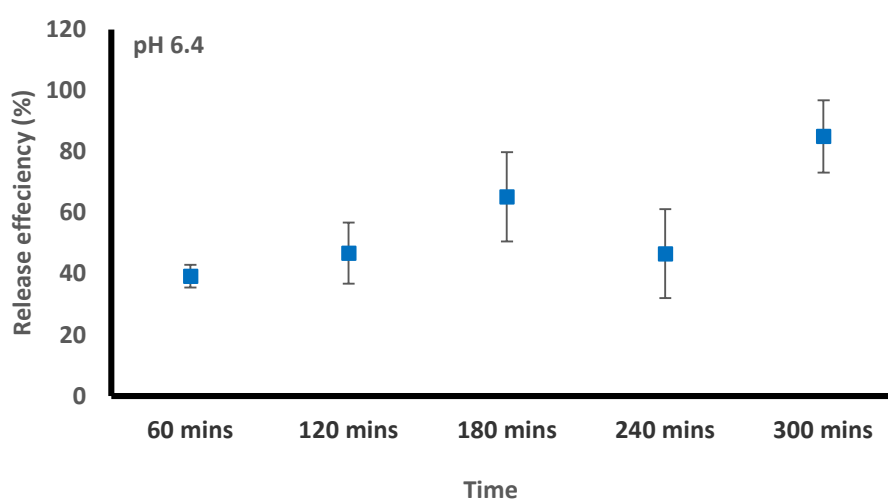


Figure 4-7: Release of siRNA (%) from CIONPs in PBS pH 6.4.

Percentage of siRNA found in supernatant after extraction of CIONPs is plotted over 0-300 minutes. Average values and error bars were calculated over three replicates.

The release curve shows the trend of the release starting from 39.3% at the beginning of the release experiments and after 60 mins of incubation. Progressively with time, the increase of siRNA released in PBS was seen reaching a maximum value of 85 % following 300 mins of incubation at 37°C. At

240 minutes of incubation however, there was some loss of signal seen. This is attributed to the sample volume discrepancy during repeated delivery and aspiration of the samples. This was however noted and corrected in the next samples (at 300 minutes).

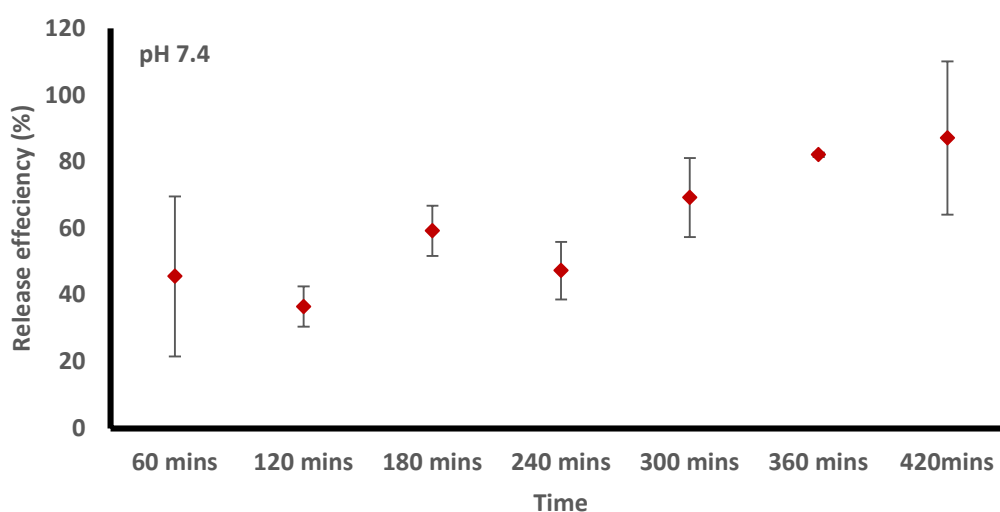


Figure 4-8: Release of siRNA (%) from CIONPs in PBS pH 7.4.

Percentage of siRNA found in supernatant after extraction of CIONPs is plotted over 0-420 minutes. Average values and error bars were calculated over three replicates.

For the experiments above (Figure 4-7 and 4-8) the CIONP/siRNA complex, obtained after the attachment experiments, was resuspended and incubated in the PBS solutions with the two pH values for up to 420 minutes. During such incubation, fluorescence reading of the supernatants (after CIONPs extraction) were performed every 60 minutes to assess the amount of siRNA (in percentage) released from the CIONPs with time. This was done to mimic the delivery in

extracellular matrix or within the cells at the tumour site. The percentage of siRNA released over time at 37°C in pH 6.4 and 7.4 are compared in Figure 4-9.

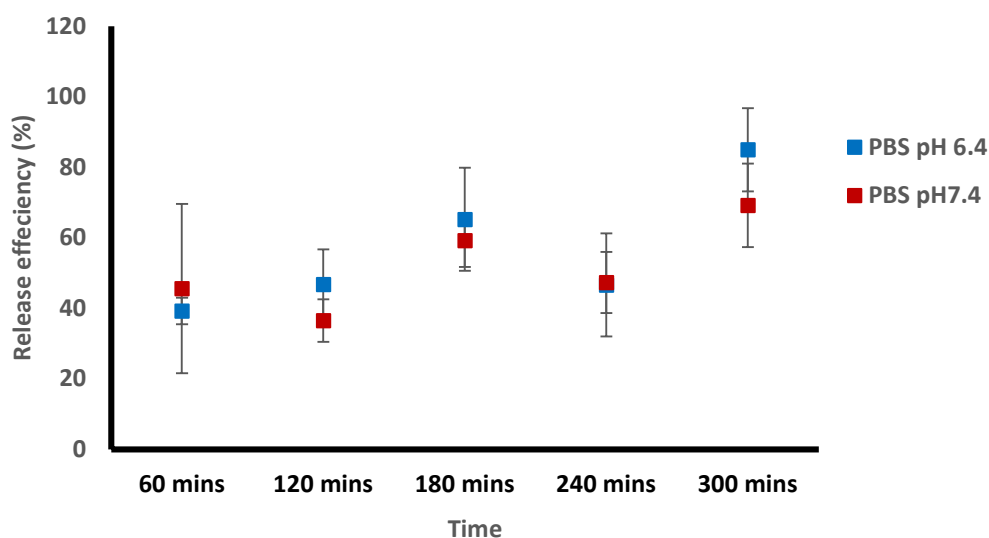


Figure 4-9: Release (%) of TEX 615-siRNA in PBS with pH 7.4 and 6.4.

When the results of photometric measurements were exported to Excel, the values of the averages of three measurements were taken and standard deviation obtained. The average reading was expressed as a percentage of the total amount of siRNA attached to the CIONPs as explained in the Methods section. Figure 4-9 shows, that although at pH 6.4 PEI is not as positively charged and therefore might have weaker interactions with siRNA, no significant differences between the release profile observed at the two pH values were seen, indicating that the acidic pH would not significantly accelerate the siRNA release in the extracellular cancer environment. This would give a chance to the nanocarrier to cross the cell membranes and to the drug to be release intracellularly.

It is reported in literature that the environment of the cancer is acidic due to an increased cancer cell activity. Tumours are highly heterogeneous entities (Welch, 2016). A review on similarities between tumour progression, heterogeneity development, and evolutionary theory (Heppner, 1984) supported researchers' and clinicians' thinking about how to address heterogeneity in experimental design and treatment of cancers.

The pH of solid tumours is acidic resulting from fermentative metabolism and poor perfusion. It is understood that acid pH supports local invasive growth and metastasis. Hydrogen ion diffusion from the immediate environment of the tumour into surrounding tissues, bringing about changes in the tissues that result in the spread of the tumour to surrounding cells. In this research, pH values 6.4 and 7.4 were investigated for the drug release from the CIONPs, demonstrating the relevance of the research to potentially provide a targeted focus to the treatment of the tumour.

In every case, the peritumoral pH was acidic and heterogeneous and the regions of highest tumour invasion corresponded to areas of lowest pH. Tumour invasion did not occur into regions with normal or near-normal pH_e (Estrella et al., 2013).

In the 1930s, Warburg noted 'the remarkable extent to which living tumour cells are able to convert carbohydrate into lactic acid' (Shirlaw, 1931).

In literature there are examples of several different release mechanisms from nanoparticles. Some mechanisms of release are triggered by enzymatic reaction. During cargo release, the superparamagnetic iron oxide nanoparticle (SPION) (Kievit & Zhang, 2011) requires a means of evading the activity of degradation enzymes. Interestingly, PEI used in this research, as part of the nanocarrier complex has been utilised as a proton sponge as it contains primary, secondary and tertiary amines, which have pKa ranging from 5 to 10 (Kievit and Zhang, 2011), with an average value around 7.4 (Dickhaus & Priefer, 2016). PEI has been incorporated onto the CIONPs in this work in combination with PEG. In the final application, PEI may enhance escape of the nanocarrier complex from endosomal destructive enzymes and with its positively charged amino acid

groups, will aid the approach of the negatively charged cell membranes and therefore the internalisation, into the tumour cells. Such positive charge of PEI may also enhance via electrostatic interactions the attachment of the negatively charged siRNA.

As can be seen previously, a nanocarrier complex has been successfully developed in this work. The nanocarrier showed the potential for use in the delivery of siRNA to neuroendocrine prostate cancer cells (Hemben et al., 2021). Prior to this research however, wide interest in metallic nanoparticles for the formation of theranostic particles for targeted drug therapy has been attributed to the metallic properties of iron oxide nanoparticles. These NPs have potential for use in biomedical areas owing to their magnetic properties (Cui et al., 2013). Fluorescent and optical properties enable tracking of NPs deposited in the body, and tracked the NPs settled in the spleen and liver (Martínez Vera et al., 2014). In this type of tracking, however, the nanoparticles will need to be labelled with a tag.

Iron oxide nanoparticles were chosen as the core of the nanocarrier complex in this study, as these types of nanoparticles have already been used in targeted drug delivery. In addition, the polymeric coating used in this work, polyethylene glycol (PEG) and polyethyleneimine (PEI) have found application in biomedical research (Artzi et al., 2011). As mentioned earlier, PEG enhances the biocompatibility of the nanoparticles and PEI enhances the crossing of the nanoparticles through the cell membrane. With respect the formation of the nanocarrier complex used in this work, the production method of sputtering iron oxide target to obtain iron oxide nanoparticles and then suspend them in polymer solution is a novel approach to produce a nanocarrier complex.

As seen earlier, the investigations also involved the use of commercial, powdered iron oxide (Fe_3O_4) nanoparticles (CIONPs) as part of the nanocarrier complex. The use of CIONPs became necessary to carry out further investigations and characterisations following the production of sputtered iron oxide (Fe_3O_4), demonstrating free-standing iron oxide nanoparticles in a solution of RNase free

water and PEG. The use of CIONPs enabled the development of a method of attachment and release of siRNA to be conducted in parallel with the development, optimisation, and characterisation of the sputtered IONPs without first conducting several sputtering sessions to accumulate sufficient sputtered IONPs.

This research carries forward from the pilot study investigating drug release mechanism from the developed nanocarrier complex. This work used fluorescence spectroscopy to measure the fluorescence signal in samples containing the dye attached to the anti-cancer agent (siRNA), which is known to inhibit protein synthesis. In this work the dye was used to visualise the attachment and release and will not be used in the clinical application for triggered release of the drug in cancer cells. Furthermore, the magnetic contrast property of the IONPs can be used in conjunction with MRI to assess the interaction of IONPs with cells. Signal response of the fluorescent dye was therefore measured in samples in pH range 5.5-7.4. From the release studies (Chapter 4), the pH of PBS in which release of the siRNA was seen at almost 70% in pH 7.4 (after 6-7 hours) which is the pH_e (Zhou et al., 2017).

Nanoparticles loaded with siRNAs protected by a polymer layer proffer longevity of siRNAs in circulatory system, enhancing resistance against destruction by serum nuclease, give the siRNA the ability to target cancer cells; actively by ligand-receptor interaction or passively by the enhanced permeability and retention (EPR) effect (Shi et al., 2017).

An increasing number of surface coatings can be developed and applied to yield environmentally sensitive nanoparticles with superior performance (Peer et al., 2007). According to Davis et al., 2008, nanoparticles in the size range 1–100 nm are emerging as a class of therapeutics for cancer. pH change and redox potential are major chemical stimuli to trigger drug release from cargos (Chen et al., 2011). Stimuli-responsive nanocarriers have been developed to release drugs with efficacy into tumour tissues upon changes in physical and chemical environments, such as redox potential, pH, temperature and ultrasound. In

relation to other materials, the primary features determining nanoparticle properties include chemical composition of the material, surface functionalisation, shape and bio physiochemical interactions at the nano-bio interface (Nel et al., 2009).

Targeted drug delivery uses particles comprising an iron oxide nanoparticle (IONP) core attached to a protein inhibitor, all encapsulated in polyethylene glycol (PEG). Iron oxide nanoparticles serve as the vehicle which carries siRNA for delivery to the site of the tumour. One of the major challenges is to provide a surface coating material that can not only prevent contamination of IONPs in blood, but which can also provide active functional groups for controllable conjugation of biomolecules onto the nanoparticles to enhance the specific targeting property (Lin et al., 2009). One way to prevent deposition of biological impurities of the IONPs in blood is to apply a polymeric coating such as PEG which has also been used in this work. PEG is one of the most used polymers in biomedical research.

4.5 CONCLUSIONS

In this Chapter, the work done has successfully demonstrated the physical adsorption of siRNA anticancer drug to the commercial IONPs (15-20 nm). Following the optimisation of the pH and the concentration / ratio of PEG/PEI to achieve optimal attachment, a maximum value of 75% was obtained at pH 7.4 and PEG/PEI 1mg/mL / 0.6 mg/mL (PEG/PEI=1.7) using 2 μ M of siRNA and 0.1 mg/mL CIONPs. A higher uptake might be achieved by increasing the concentration of the nanoparticles. The release of siRNA in PBS by simple diffusion was conducted from the PEG/PEI siRNA nanocarrier complex. It was found that approximately 40% of the siRNA was released in PBS 7.4 in the first 60 minutes, and approximately 85% was seen after 5 hours (300 minutes). Similar results were obtained in PBS pH 6.4, demonstrating the stability of the nanocarrier complex, and that the external acidic tumour environment would not accelerate the unwanted release of siRNA in the extracellular matrix. Whereas in

literature, pH has been used to trigger the release of therapeutic agents, in this study, this was not desired to avoid premature release in the extracellular matrix.

Even though a triggered release mechanism was not developed in this work, the release of siRNA was established and evidenced in the signal change in the samples over time. In general, the release was not very rapid, potentially giving time to intracellular uptake of siRNA.

These results have demonstrated that 40% of the pay-loaded drug was released in the first hour in a mimicked, physiological environment. This might be considered too quick for effective intracellular drug delivery and additional work is required to find conditions to slow down the release, possibly by tuning further the amount of PEG/PEI used for coating the IONPs. It can be postulated that there is a possibility for the siRNA to be destroyed if the release of the drug is not close to the cancer cells, and the intended effect of targeted drug delivery missed. To this end, localised administration of the nanocarrier at or as near as it is safely possible, to the tumour cells will more likely achieve the desired effect of the drug.

CHAPTER 5

FINAL CONCLUSIONS AND RECOMMENDATIONS FOR FURTHER WORK

5 FINAL CONCLUSIONS AND RECOMMENDATIONS FOR FURTHER WORK

5.1 FINAL CONCLUSIONS

Prostate cancer is the most widely occurring cancer in men in the UK (Cancer Research UK, 2016). Neuroendocrine prostate cancer (NEPC) is seen in 2% of all prostate cancer cases. NEPC is considered particularly lethal as it is known to be resistant to current treatments (Puranik et al., 2021). NEPC can arise following initial diagnosis and treatment of prostate cancer.

This work has two broad sections, in the first section the production and characterisation of iron oxide nanoparticles by inert gas condensation using Mantis NanoGen Trio was achieved. The sputtering method produced iron oxide nanoparticles of around 5 nm (1-6 nm) at ambient temperature following the optimised sputtering conditions of throttle position and 70% and Argon flow 70 sccm after two hours of sputtering. Dispersed nanoparticles were obtained in solution containing a relatively high amount of PEG. The PEG-IONPs were characterised by TEM, AFM, DLS, NTA and MRI to confirm the production of stable, free-standing magnetic PEG-coated nanoparticles. By using NTA and commercial IONPs as 'standard', the concentration of the sputtered IONPs for a two-hours sputtering session on three substrates was estimated to be around 1.55 µg/mL in 5 mL solution, which means a total of 7.75 µg. Although it is not straightforward to assess how this yield compares with other synthetic techniques, which might require further purification steps and a more 'hands on' approach, the amount produced here could be simply increased by sputtering for slightly longer (before unwanted aggregates are produced) and by positioning even more than three silicon wafer substrates.

The second major part of the work investigated the attachment and release of the anti-cancer agent, siRNA to and from the nanocarrier complex. This section of the work stemmed from the pilot study in which a molecular label, Texas Red-siRNA conjugate TM had failed to produce a fluorescence signal in acidic pH, particularly in presence of the commercial IONPS used at the time. This work

demonstrated that with a different type of commercial nanoparticles, the dye was actually stable in both acidic and neutral conditions and could be used as label to visualise the siRNA. Experiments using commercially sourced TEX Red-siRNA (TEX 615-siRNA) enabled tracking of the siRNA to confirm physical attachment of siRNA to CIONPs and siRNA release from PEG/PEI nanocarrier complex. The amount of PEG/PEI used for this was optimised and the optimal ratio of polymer was established to obtain a high amount of siRNA attached to the CIONPs (80% at pH 7.4). Following the release study, a relatively high amount of siRNA was seen to be released from the nanocarrier within the first hour in PBS (~ 40%) at 37 °C even though the release was not triggered by pH nor temperature but relied on the dissolution with time of the PEG/PEI coating. Although this work has successfully highlighted the potential to use such IONPs and the attachment and release method of siRNA from CIONPs for biomedical applications, there were a few limitations to the research study, and these are described in the next section.

5.2 LIMITATIONS

One of the major limitations to this study is that near the end of this research work, the sputtering system was unable to achieve a stable plasma, thereby posing a limitation of the further sputtering of IONPs on PEG PEI-coated silicon wafer and TEM grid. For this reason, this work does not contain work on variations of the soft-landed productions of IONPs.

In the near future, the short chain polyethyleneimine (PEI) should also be used to thin-coat the silicon wafer prior sputtering as this was not possible in this work due to the failure of Pfeiffer pump and subsequent inability to achieve a stable plasma even when the previously used parameters of Argon flow, sccm throttle position 50-80%, and current and voltage were selected. The sputtered IONPs that were obtained by dissolving soft-landed IONPs in solution, were with PEG only solution. It is recommended that the PEI may be used in combination with PEG to thin coat the silicon wafer in further investigations to study its effect on the attachment and the release of siRNAs from the sputtered IONPs nanocarrier complex. It is anticipated that after sputtering IONPs on the PEG/PEI coated

substrate, the siRNA would be added to the RNAase free water used to disperse the sputtered IONPs. The siRNA should then be adsorbed on the PEG/PEI layer on the IONPs, and the resulting solution will be ready for the release studies and its subsequent use in *in-vitro* and *in-vivo* experiments.

Another important limitation to the work presented here is that due to the disruption with COVID and the lockdown, the parts of the research related to *in-vivo* and *in-vitro* investigation initially intended to take place in collaboration with the Open University, Milton Keynes, UK were not carried out. Based on the promising results found in this work, it is recommended that the cellular internalisation of nanocarrier complex be investigated in a further study. In addition, biocompatibility *in-vitro* and *in-vivo* study of the sputtered PEG/PEI/IONPs once these are produced, should be carried out to confirm safety of the materials.

5.3 FURTHER WORK

It is recommended that the sputtering of iron oxide targets be carried out for longer than 2 hours to obtain a higher amount of free-standing IONPs suspended in the ligand (PEG). This is important for characterisation and for applications requiring a high yield of discrete, non-aggregated nanoparticles. This method also has potential to become a scalable method, by exploring the possibility of multiple substrates placed in the main chamber during a session of sputtering, for manufacturing IONPs to be used in other targeted drug delivery studies.

PEG concentrations used to coat the silicon wafer should be varied to determine the effect of a thinner or thicker layer of PEG on the silicon wafer prior to IONPs sputtering. Similarly, a combination of PEG/PEI should be used on the silicon wafer and the sputtered IONPs should be dispersed in a TEX 615-siRNA (RNAase free) solution, enabling to assess its attachment and release to the IONPs and how the concentration and ratio between PEG/PEI affect the performance.

The siRNA- IONPs should then be used for *in-vitro* studies to assess the cellular uptake and the siRNA release. This will also allow to optimise further the quantity of PEG/PEI until optimal performance is achieved.

In the future, the identification of a receptor (e.g., antibody) to attach to the IONPs-siRNA complex that will guide delivery to the cancer cells may be also investigated.

Alternatively, the research should aim to administer the nanocarrier closer to the environment of the tumour for quick tumour cells internalisation preventing rapid decay of the siRNA due to unsuppressed and fast release (within the first hour) of nearly half of the drug from the IONPs.

REFERENCES

- Abuchowski, A., Van Es, T., Palczuk, N. C., & Davis, F. F. (1977). Alteration of immunological properties of bovine serum albumin by covalent attachment of polyethylene glycol. *Journal of Biological Chemistry*, 252(11), 3578–3581. [https://doi.org/10.1016/s0021-9258\(17\)40291-2](https://doi.org/10.1016/s0021-9258(17)40291-2)
- Adimoolam, M. G., Amreddy, N., Nalam, M. R., & Sunkara, M. V. (2018). A simple approach to design chitosan functionalized Fe₃O₄ nanoparticles for pH responsive delivery of doxorubicin for cancer therapy. *Journal of Magnetism and Magnetic Materials*, 448, 199–207. <https://doi.org/10.1016/j.jmmm.2017.09.018>
- Afzal, A., Nawfal, I., Mahbubul, I. M., & Kumbar, S. S. (2019). An overview on the effect of ultrasonication duration on different properties of nanofluids. *Journal of Thermal Analysis and Calorimetry*, 135(1), 393–418. <https://doi.org/10.1007/s10973-018-7144-8>
- Aghajanzadeh, M., Zamani, M., Molavi, H., Khieri Manjili, H., Danafar, H., & Shojaei, A. (2018). Preparation of Metal–Organic Frameworks UiO-66 for Adsorptive Removal of Methotrexate from Aqueous Solution. *Journal of Inorganic and Organometallic Polymers and Materials*, 28(1), 177–186. <https://doi.org/10.1007/s10904-017-0709-3>
- Ahmadzada, T., Reid, G., & McKenzie, D. R. (2018). Fundamentals of siRNA and miRNA therapeutics and a review of targeted nanoparticle delivery systems in breast cancer. *Biophysical Reviews*, 10(1), 69–86. <https://doi.org/10.1007/s12551-017-0392-1>
- Ajayaghosh, A. (2005). Chemistry of squaraine-derived materials: Near-IR dyes, low band gap systems, and cation sensors. *Accounts of Chemical Research*, 38(6), 449–459. <https://doi.org/10.1021/ar0401000>
- Akhtar, N., Akram, M., Asif, H. M., Usmanghani, K., Ali Shah, S. M., Ahmad Rao, S., Uzair, M., Shaheen, G., & Ahmad, K. (2011). Gene therapy: A review article. *Journal of Medicinal Plants Research*, 5(10), 1812–1817.
- Akhter, Sohail; Ahmad, Iqbal; Ahmad, Mohammad Zaki; Ramazani, Farshad; Singh, Anjali; Rahman, Ziyaur; Ahmad, Farhan Jalees; Storm, Gert; Kok, R. J. (2013). Nanomedicines as Cancer Therapeutics: Current Status. *Current Cancer Drug Targets*, 13(4), 362–378.
- Akshaya, K. B., Varghese, A., Sudhakar, Y. N., & George, L. (2019). Electrocatalytic oxidation of morin on electrodeposited Ir-PEDOT nanograins. *Food Chemistry*, 270(July 2018), 78–85. <https://doi.org/10.1016/j.foodchem.2018.07.074>

- Aksu Demirezen, D., Yıldız, Y. Ş., Yılmaz, Ş., & Demirezen Yılmaz, D. (2019). Green synthesis and characterization of iron oxide nanoparticles using *Ficus carica* (common fig) dried fruit extract. *Journal of Bioscience and Bioengineering*, 127(2), 241–245. <https://doi.org/10.1016/j.jbiosc.2018.07.024>
- Alberts, I. L., Seide, S. E., Mingels, C., Bohn, K. P., Shi, K., Zacho, H. D., Rominger, A., & Afshar-Oromieh, A. (2021). Correction to: Comparing the diagnostic performance of radiotracers in recurrent prostate cancer: a systematic review and network meta-analysis (*European Journal of Nuclear Medicine and Molecular Imaging*, (2021), 48, 9, (2978-2989), 10.1007/s00259-021-052). *European Journal of Nuclear Medicine and Molecular Imaging*, 48(9), 3014–3016. <https://doi.org/10.1007/s00259-021-05300-8>
- Alcantar, N. A., Aydil, E. S., & Israelachvili, J. N. (2000). Polyethylene glycol-coated biocompatible surfaces. *Journal of Biomedical Materials Research*, 51(3), 343–351. [https://doi.org/10.1002/1097-4636\(20000905\)51:3<343::AID-JBM7>3.0.CO;2-D](https://doi.org/10.1002/1097-4636(20000905)51:3<343::AID-JBM7>3.0.CO;2-D)
- Aldrich, S. (2021). *Texas Red Dye*. <https://www.sigmaaldrich.com/GB/en/sds/sigma/s7635>
- Algorri, J. F., Poudereux, D., García-Cámara, B., Urruchi, V., Sánchez-Pena, J. M., Vergaz, R., Caño-García, M., Quintana, X., Geday, M. A., & Otón, J. M. (2016). Metal nanoparticles-PDMS nanocomposites for tunable optical filters and sensors. *Optical Data Processing and Storage*, 2(1), 1–6. <https://doi.org/10.1515/odps-2016-0001>
- Alim Khan, Benboubetra, M., Pakeeza Z. Sayyed, K. W. N., Fox, S., & Beck, G. (2008). Sustained Polymeric Delivery of Gene Silencing Antisense ODNs, siRNA, DNAzymes and Ribozymes: In Vitro and In Vivo Studies. *Journal of Drug Targeting*, 12(6), 393–404. <https://doi.org/10.1080/10611860400003858>
- Allen, T. M., & Cullis, P. R. (2004). Drug Delivery Systems: Entering the Mainstream. *Science*, 303(5665), 1818–1822. <https://doi.org/10.1126/science.1095833>
- Allerson, C. R., Sioufi, N., Jarres, R., Prakash, T. P., Naik, N., Berdeja, A., Wanders, L., Griffey, R. H., Swayze, E. E., & Bhat, B. (2005). Fully 2'-modified oligonucleotide duplexes with improved in vitro potency and stability compared to unmodified small interfering RNA. *Journal of Medicinal Chemistry*, 48(4), 901–904. <https://doi.org/10.1021/jm049167j>
- Alonso, M. J., Calvo, P., & Remun, C. (1997). Novel hydrophilic chitosan-polyethylene oxide nanoparticles as protein carriers. *Journal of Applied Polymer Science*, 63(1), 125–132. [https://doi.org/10.1002/\(SICI\)1097-](https://doi.org/10.1002/(SICI)1097-)

4628(19970103)63:13.0.CO;2-4

- Amoozgar, Z., & Yeo, Y. (2012). Recent advances in stealth coating of nanoparticle drug delivery systems. *Wiley Interdisciplinary Reviews: Nanomedicine and Nanobiotechnology*, 4(2), 219–233. <https://doi.org/10.1002/wnan.1157>
- An, F. F., Cao, W., & Liang, X. J. (2014). Nanostructural systems developed with positive charge generation to drug delivery. *Advanced Healthcare Materials*, 3(8), 1162–1181. <https://doi.org/10.1002/adhm.201300600>
- Ankerhold, U. (2013). *Magnetic nanoparticle-based cancer therapy* *. <https://doi.org/10.1088/1674-1056/22/2/027506>
- Ansari, C., Tikhomirov, G. A., Hong, S. H., Falconer, R. A., Loadman, P. M., Gill, J. H., Castaneda, R., Hazard, F. K., Tong, L., Lenkov, O. D., Felsher, D. W., Rao, J., & Daldrop-Link, H. E. (2014). Development of novel tumor-targeted theranostic nanoparticles activated by membrane-type matrix metalloproteinases for combined cancer magnetic resonance imaging and therapy. In *Small* (Vol. 10, Issue 3, pp. 566–575). <https://doi.org/10.1002/smll.201301456>
- Antonin de Fougères, Muthiah Manoharan, Rachel Meyers, H.-P. V. (2005). RNA Interference In Vivo: Toward Synthetic Small Inhibitory RNA-Based Therapeutics. *Methods in Enzymology*, 392, 278–296.
- Aravind, A., Jeyamohan, P., Nair, R., Veerananarayanan, S., Nagaoka, Y., Yoshida, Y., Maekawa, T., & Kumar, D. S. (2012). AS1411 aptamer tagged PLGA-lecithin-PEG nanoparticles for tumor cell targeting and drug delivery. *Biotechnology and Bioengineering*, 109(11), 2920–2931. <https://doi.org/10.1002/bit.24558>
- Arenas-Alatorre, J., Tehuacanero C., S., Lukas, O., Rodríguez-Gómez, A., Hernández Reyes, R., Tapia-del León, C., & Lara V., J. (2019). Synthesis and characterization of iron oxide nanoparticles grown via a non-conventional chemical method using an external magnetic field. *Materials Letters*, 242, 13–16. <https://doi.org/10.1016/j.matlet.2019.01.098>
- Argenziano, M., Bessone, F., Dianzani, C., Cucci, M. A., Grattarola, M., Pizzimenti, S., & Cavalli, R. (2022). Ultrasound-Responsive Nrf2-Targeting siRNA-Loaded Nanobubbles for Enhancing the Treatment of Melanoma. *Pharmaceutics*, 14(2). <https://doi.org/10.3390/pharmaceutics14020341>
- Arias, J. L., Reddy, L. H., Othman, M., Gillet, B., Desmaële, D., Zouhiri, F., Dosio, F., Gref, R., & Couvreur, P. (2011). Squalene based nanocomposites: A new platform for the design of multifunctional pharmaceutical theragnostics. *ACS Nano*, 5(2), 1513–1521. <https://doi.org/10.1021/nn1034197>

- Artzi, N., Oliva, N., Puron, C., Shitreet, S., Artzi, S., Bon Ramos, A., Groothuis, A., Sahagian, G., & Edelman, E. R. (2011). In vivo and in vitro tracking of erosion in biodegradable materials using non-invasive fluorescence imaging. *Nature Materials*, *10*(9), 704–709. <https://doi.org/10.1038/nmat3095>
- Ashrafizadeh, M., Hushmandi, K., Moghadam, E. R., Zarrin, V., Kashani, S. H., Bokaie, S., Najafi, M., Tavakol, S., Mohammadinejad, R., Nabavi, N., Hsieh, C. L., Zarepour, A., Zare, E. N., Zarrabi, A., & Makvandi, P. (2020). Progress in delivery of siRNA-based therapeutics employing nano-vehicles for treatment of prostate cancer. *Bioengineering*, *7*(3), 1–40. <https://doi.org/10.3390/bioengineering7030091>
- Astruc, D. (2020). Introduction: Nanoparticles in Catalysis. *Chemical Reviews*, *120*(2), 461–463. <https://doi.org/10.1021/acs.chemrev.8b00696>
- Astruc, P. D. D. (2007). Transition-metal Nanoparticles in Catalysis: From Historical Background to the State-of-the Art. In B. E. D. D. Astruc (Ed.), *Nanoparticles and catalysis* (pp. 1–48). <https://doi.org/https://doi.org/10.1002/9783527621323.ch1>
- Atomic force microscope.* (2022). https://wiki.nanotech.ucsb.edu/wiki/File:ICON_AFM.jpg
- Aubry, E., Liu, T., Dekens, A., Perry, F., Mangin, S., Hauet, T., & Billard, A. (2019). Synthesis of iron oxide films by reactive magnetron sputtering assisted by plasma emission monitoring. *Materials Chemistry and Physics*, *223*(November 2018), 360–365. <https://doi.org/10.1016/j.matchemphys.2018.11.010>
- Bae, S., Ma, K., Kim, T. H., Lee, E. S., Oh, K. T., Park, E. S., Lee, K. C., & Youn, Y. S. (2012). Doxorubicin-loaded human serum albumin nanoparticles surface-modified with TNF-related apoptosis-inducing ligand and transferrin for targeting multiple tumor types. *Biomaterials*, *33*(5), 1536–1546. <https://doi.org/10.1016/j.biomaterials.2011.10.050>
- Bagalkot, V., & Gao, X. (2011). SiRNA-aptamer chimeras on nanoparticles: preserving targeting functionality for effective gene silencing. *ACS Nano*, *5*(10), 8131–8139. <https://doi.org/10.1021/nn202772p>
- Baldir, V., Bia, N., Graillet, A., Loubat, C., & Berret, J. F. (2019). Monophosphonic versus Multiphosphonic Acid Based PEGylated Polymers for Functionalization and Stabilization of Metal (Ce, Fe, Ti, Al) Oxide Nanoparticles in Biological Media. *Advanced Materials Interfaces*, *6*(7), 1–11. <https://doi.org/10.1002/admi.201801814>
- Barick, K. C., Aslam, M., Lin, Y. P., Bahadur, D., Prasad, P. V., & Dravid, V. P. (2009). Novel and efficient MR active aqueous colloidal Fe₃O₄ nanoassemblies. *Journal of Materials Chemistry*, *19*(38), 7023–7029.

<https://doi.org/10.1039/b911626e>

- Barth, R. F., Coderre, J. A., Vicente, M. G. H., & Blue, T. E. (2005). Boron neutron capture therapy of cancer: Current status and future prospects. *Clinical Cancer Research*, 11(11), 3987–4002. <https://doi.org/10.1158/1078-0432.CCR-05-0035>
- Bartlett, D. W., & Davis, M. E. (2007). Effect of siRNA nuclease stability on the in vitro and in vivo kinetics of siRNA-mediated gene silencing. *Biotechnology and Bioengineering*, 97(4), 909–921. <https://doi.org/10.1002/bit.21285>
- Beckman Coulter Inc. (2021). *Total PSA Analyser*. <https://www.beckmancoulter.com/>
- Behera, S. S., Patra, J. K., Pramanik, K., Panda, N., & Thatoi, H. (2012). Characterization and Evaluation of Antibacterial Activities of Chemically Synthesized Iron Oxide Nanoparticles. *World Journal of Nano Science and Engineering*, 02(04), 196–200. <https://doi.org/10.4236/wjnse.2012.24026>
- Beyerle, A., Irmeler, M., Beckers, J., Kissel, T., & Stoeger, T. (2010). Toxicity pathway focused gene expression profiling of PEI-based polymers for pulmonary applications. *Molecular Pharmaceutics*, 7(3), 727–737. <https://doi.org/10.1021/mp900278x>
- Bhattacharya, D., Das, M., Mishra, D., Banerjee, I., Sahu, S. K., Maiti, T. K., & Pramanik, P. (2011). Folate receptor targeted, carboxymethyl chitosan functionalized iron oxide nanoparticles: A novel ultradispersed nanoconjugates for bimodal imaging. *Nanoscale*, 3(4), 1653–1662. <https://doi.org/10.1039/c0nr00821d>
- Bosland, M. C., Özten, N., Eskra, J. N., & Mahmoud, A. M. (2015). A Perspective on Prostate Carcinogenesis and Chemoprevention. *Current Pharmacology Reports*, 1(4), 258–265. <https://doi.org/10.1007/s40495-015-0031-0>
- Bozzuto, G., & Molinari, A. (2015). Liposomes as nanomedical devices. *International Journal of Nanomedicine*, 10, 975–999. <https://doi.org/10.2147/IJN.S68861>
- Braun, J. E. A., Fritz, B. A., Wong, S. M. E., & Lowe, A. W. (1994). Identification of a vesicle-associated membrane protein (VAMP)-like membrane protein in zymogen granules of the rat exocrine pancreas. *Journal of Biological Chemistry*, 269(7), 5328–5335. [https://doi.org/10.1016/s0021-9258\(17\)37691-3](https://doi.org/10.1016/s0021-9258(17)37691-3)
- Bray, F., Ferlay, J., Soerjomataram, I., Siegel, R. L., Torre, L. A., & Jemal, A. (2018). Global cancer statistics 2018: GLOBOCAN estimates of incidence and mortality worldwide for 36 cancers in 185 countries. *CA: A Cancer Journal for Clinicians*, 68(6), 394–424. <https://doi.org/10.3322/caac.21492>

- C. M. Gillen, A. Takamata, G. W. Mack, and E. R. N. (1994). *Measurement of plasma volume in rats with use of fluorescent-labeled albumin molecules*. 485. <https://doi.org/https://doi.org/10.1152/jappl.1994.76.1.485>
- Cabral, H., & Kataoka, K. (2014). Progress of drug-loaded polymeric micelles into clinical studies. *Journal of Controlled Release*, 190, 465–476. <https://doi.org/10.1016/j.jconrel.2014.06.042>
- Canfarotta, F., Whitcombe, M. J., & Piletsky, S. A. (2013). Polymeric nanoparticles for optical sensing. *Biotechnology Advances*, 31(8), 1585–1599. <https://doi.org/10.1016/j.biotechadv.2013.08.010>
- Cao, X., Shang, X., Guo, Y., Zheng, X., Li, W., Wu, D., Sun, L., Mu, S., & Guo, C. (2021). Lysosomal escaped protein nanocarriers for nuclear-targeted siRNA delivery. *Analytical and Bioanalytical Chemistry*, 413(13), 3493–3499. <https://doi.org/10.1007/s00216-021-03297-5>
- Cao, Y., Mao, Z., He, Y., Kuang, Y., Liu, M., Zhou, Y., Zhang, Y., & Pei, R. (2020). Extremely Small Iron Oxide Nanoparticle-Encapsulated Nanogels as a Glutathione-Responsive T1 Contrast Agent for Tumor-Targeted Magnetic Resonance Imaging. *ACS Applied Materials and Interfaces*, 12(24), 26973–26981. <https://doi.org/10.1021/acsami.0c07288>
- Caruso, F., Hyeon, T., & Rotello, V. (2012). *Nanomedicine themed issue*. 7. <https://doi.org/10.1039/c1cs15248c>
- Charmi, J., Nosrati, H., Mostafavi Amjad, J., Mohammadkhani, R., & Danafar, H. (2019). Polyethylene glycol (PEG) decorated graphene oxide nanosheets for controlled release curcumin delivery. *Heliyon*, 5(4), e01466. <https://doi.org/10.1016/j.heliyon.2019.e01466>
- Cheheltani, R., Kim, J., Naha, P. C., & Cormode, D. P. (2018). Nanoparticle Contrast Agents for Medical Imaging. In *Nanobiotechnology* (1st ed., pp. 219–250). CRC Press.
- Chemla, Y. R., Grossman, H. L., Poon, Y., Mcdermott, R., Stevens, R., Alper, M. D., & Clarke, J. (2000). *Ultrasensitive magnetic biosensor for homogeneous immunoassay*.
- Chen, B., Guo, Z., Guo, C., Mao, Y., Qin, Z., Ye, D., Zang, F., Lou, Z., Zhang, Z., Li, M., Liu, Y., Ji, M., Sun, J., & Gu, N. (2020). Moderate cooling coprecipitation for extremely small iron oxide as a pH dependent: T 1-MRI contrast agent. *Nanoscale*, 12(9), 5521–5532. <https://doi.org/10.1039/c9nr10397j>
- Chen, C., Ge, J., Gao, Y., Chen, L., Cui, J., Zeng, J., & Gao, M. (2022). Ultrasmall superparamagnetic iron oxide nanoparticles: A next generation contrast agent for magnetic resonance imaging. *Wiley Interdisciplinary Reviews*:

Nanomedicine and Nanobiotechnology, 14(1), 1–22.
<https://doi.org/10.1002/wnan.1740>

- Chen, F. P., & Chien, M. H. (2019). Effects of phytoestrogens on the activity and growth of primary breast cancer cells ex vivo. *Journal of Obstetrics and Gynaecology Research*, 45(7), 1352–1362.
<https://doi.org/10.1111/jog.13982>
- Chen, J., Qiu, X., Ouyang, J., Kong, J., Zhong, W., & Xing, M. M. Q. (2011). *pH and Reduction Dual-Sensitive Copolymeric Micelles for Intracellular Doxorubicin Delivery*. 3601–3611. <https://doi.org/10.1021/bm200804j>
- Chen, L., Li, J., Zhang, M., Cai, S., Zhang, T., Cai, C., & Chen, Z. (2015). Super-resolved enhancing and edge deghosting (SEED) for spatiotemporally encoded single-shot MRI. *Medical Image Analysis*, 23(1), 1–14.
<https://doi.org/10.1016/j.media.2015.03.004>
- Chen, T., Zhao, T., Wei, D., Wei, Y., Li, Y., & Zhang, H. (2013). Core-shell nanocarriers with ZnO quantum dots-conjugated Au nanoparticle for tumor-targeted drug delivery. *Carbohydrate Polymers*, 92(2), 1124–1132.
<https://doi.org/10.1016/j.carbpol.2012.10.022>
- Cheng, F. Y., Su, C. H., Yang, Y. S., Yeh, C. S., Tsai, C. Y., Wu, C. L., Wu, M. T., & Shieh, D. Bin. (2005). Characterization of aqueous dispersions of Fe₃O₄ nanoparticles and their biomedical applications. *Biomaterials*, 26(7), 729–738. <https://doi.org/10.1016/j.biomaterials.2004.03.016>
- Cheng, L., Jiang, X., & Wang, J. (2013). *cells*. 3547–3569.
<https://doi.org/10.1039/c3nr34276j>
- Chin, A. B., & Yaacob, I. I. (2007). Synthesis and characterization of magnetic iron oxide nanoparticles via w/o microemulsion and Massart's procedure. *Journal of Materials Processing Technology*, 191(1–3), 235–237.
<https://doi.org/10.1016/j.jmatprotec.2007.03.011>
- Choi, P. G., Fuchigami, T., Kakimoto, K. I., & Masuda, Y. (2020). Effect of Crystal Defect on Gas Sensing Properties of Co₃O₄Nanoparticles. *ACS Sensors*, 5(6), 1665–1673. <https://doi.org/10.1021/acssensors.0c00290>
- Choi, S. W., Kim, W. S., & Kim, J. H. (2007). *Surface Modification of Functional Nanoparticles for Controlled Drug Delivery Surface Modification of Functional Nanoparticles*. 2691. <https://doi.org/10.1081/DIS-120021803>
- Choung, S., Kim, Y. J., Kim, S., Park, H., & Choi, Y. (2006). *Chemical modification of siRNAs to improve serum stability without loss of efficacy*. 342, 919–927.
<https://doi.org/10.1016/j.bbrc.2006.02.049>
- Chung, S., & Zhang, M. (2021). Microwave-Assisted Synthesis of Carbon Dot –

- Iron Oxide Nanoparticles for Fluorescence Imaging and Therapy. *Frontiers in Bioengineering and Biotechnology*, 9(July), 1–12. <https://doi.org/10.3389/fbioe.2021.711534>
- Cinti, C., Taranta, M., Naldi, I., & Grimaldi, S. (2011). Newly engineered magnetic erythrocytes for sustained and targeted delivery of anti-cancer therapeutic compounds. *PLoS ONE*, 6(2). <https://doi.org/10.1371/journal.pone.0017132>
- Corbett, V., Arnold, S., Anthony, L., & Chauhan, A. (2021). Management of Large Cell Neuroendocrine Carcinoma. *Frontiers in Oncology*, 11(August), 1–20. <https://doi.org/10.3389/fonc.2021.653162>
- Corot, C., Robert, P., Idée, J. M., & Port, M. (2006). Recent advances in iron oxide nanocrystal technology for medical imaging. *Advanced Drug Delivery Reviews*, 58(14), 1471–1504. <https://doi.org/10.1016/j.addr.2006.09.013>
- Crea, F., Venalainen, E., Ci, X., Cheng, H., Pikor, L., Parolia, A., Xue, H., Saidy, Nur, N. R., Lin, D., Lam, W., & Wang, C. C. & Y. (2016). The role of epigenetics and long noncoding RNA MIAT in neuroendocrine prostate cancer. *Epigenomics*, 8(5). <https://doi.org/10.2217/epi.16.6>
- Crea, F., Watahiki, A., Quagliata, L., Xue, H., Pikor, L., Parolia, A., Wang, Y., Lin, D., Lam, W. L., Farrar, W. L., Isogai, T., Morant, R., Castori-Eppenberger, S., Chi, K. N., Wang, Y., & Helgason, C. D. (2014). Identification of a long non-coding RNA as a novel biomarker and potential therapeutic target for metastatic prostate cancer. *Oncotarget*, 5(3), 764–774. <https://doi.org/10.18632/oncotarget.1769>
- Cui, K., Lu, X., Guan, J., Lu, Q., Fei, Z., & Dyson, P. J. (2013). Formation and properties of self-assembly-driven fluorescent nanoparticle sensors. *Chemistry - A European Journal*, 19(26), 8550–8557. <https://doi.org/10.1002/chem.201204349>
- Dai, Y., & Zhang, X. (2019). MicroRNA Delivery with Bioreducible Polyethylenimine as a Non-Viral Vector for Breast Cancer Gene Therapy. *Macromolecular Bioscience*, 19(4), 1–7. <https://doi.org/10.1002/mabi.201800445>
- Daldrup-Link, H. E., Golovko, D., Ruffell, B., DeNardo, D. G., Castaneda, R., Ansari, C., Rao, J., Tikhomirov, G. A., Wendland, M. F., Corot, C., & Coussens, L. M. (2011). MRI of tumor-associated macrophages with clinically applicable iron oxide nanoparticles. *Clinical Cancer Research*, 17(17), 5695–5704. <https://doi.org/10.1158/1078-0432.CCR-10-3420>
- Davis, M.E., Zuckerman, J. E., Choi, C. H. J., Seligson, D., Tolcher, A., Alabi, C. A., Yen, Y., & Heidel, J.D. and Ribas, A. (2010). Evidence of RNAi in humans from systemically administered siRNA via targeted nanoparticles. *Nature*, 464. 464(7291), 1067–1070.

- Davis, Mark E., Chen, Z. (Georgia), & Shin, D. M. (2008). Nanoparticle Therapeutics: An emerging treatment modality for cancer. *Nanoscience and Technology*, 7, 711–782. https://doi.org/10.1142/9789814287005_0025
- Davis, Mark E. (2002). *Non-viral gene delivery systems*. 128–131.
- Deike-Hofmann, K., Koenig, F., Paech, D., Dreher, C., Delorme, S., Schlemmer, H. P., & Bickelhaupt, S. (2019). Abbreviated MRI Protocols in Breast Cancer Diagnostics. *Journal of Magnetic Resonance Imaging*, 49(3), 647–658. <https://doi.org/10.1002/jmri.26525>
- Demchenko, A. P. (2005). Optimization of fluorescence response in the design of molecular biosensors. *Analytical Biochemistry*, 343(1), 1–22. <https://doi.org/10.1016/j.ab.2004.11.041>
- Derfus, A. M., Chen, A. A., Min, D. H., Ruoslahti, E., & Bhatia, S. N. (2007). Targeted quantum dot conjugates for siRNA delivery. *Bioconjugate Chemistry*, 18(5), 1391–1396. <https://doi.org/10.1021/bc060367e>
- Dettmar, A. K., Wiech, T., Kemper, M. J., Soave, A., Rink, M., Oh, J., Stahl, R. A. K., & Hoxha, E. (2018). Immunohistochemical and serological characterization of membranous nephropathy in children and adolescents. *Pediatric Nephrology*, 33(3), 463–472. <https://doi.org/10.1007/s00467-017-3817-y>
- Devi, H. S., Boda, M. A., Shah, M. A., Parveen, S., & Wani, A. H. (2019). Green synthesis of iron oxide nanoparticles using *Platanus orientalis* leaf extract for antifungal activity. *Green Processing and Synthesis*, 8(1), 38–45. <https://doi.org/10.1515/gps-2017-0145>
- DeVita, V. T., & Chu, E. (2008). A history of cancer chemotherapy. *Cancer Research*, 68(21), 8643–8653. <https://doi.org/10.1158/0008-5472.CAN-07-6611>
- Dickhaus, B. N., & Priefer, R. (2016). Determination of polyelectrolyte pKa values using surface-to-air tension measurements. *Colloids and Surfaces A: Physicochemical and Engineering Aspects*, 488, 15–19. <https://doi.org/10.1016/j.colsurfa.2015.10.015>
- Diener-zepto-plasma-cleaner*. (2022). <https://microscopy.tamu.edu/instrument/diener-zepto-plasma-cleaner/>
- Dorai, T., Cao, Y. C., Dorai, B., Buttyan, R., & Katz, A. E. (2001). Therapeutic potential of curcumin in human prostate cancer. III. Curcumin inhibits proliferation, induces apoptosis, and inhibits angiogenesis of LNCaP prostate cancer cells in vivo. *Prostate*, 47(4), 293–303. <https://doi.org/10.1002/pros.1074>

- Dragovic, R. A., Collett, G. P., Hole, P., Ferguson, D. J. P., Redman, C. W., Sargent, I. L., & Tannetta, D. S. (2015). Isolation of syncytiotrophoblast microvesicles and exosomes and their characterisation by multicolour flow cytometry and fluorescence Nanoparticle Tracking Analysis. *Methods*, 87(2015), 64–74. <https://doi.org/10.1016/j.ymeth.2015.03.028>
- Du, Y., Lai, P. T., Leung, C. H., & Pong, P. W. T. (2013). Design of superparamagnetic nanoparticles for magnetic particle imaging (MPI). *International Journal of Molecular Sciences*, 14(9), 18682–18710. <https://doi.org/10.3390/ijms140918682>
- E. A. Périgo, G. H., Sandre, O., Ortega, D., Garaio, E., Plazaola, F., & Teran, and F. J. (2015). *Fundamentals and advances in magnetic hyperthermia*. 2(4). <https://doi.org/Doi.org/10.1063/1.4935688>
- E. Gould, MD Victor, W. Franke, Mdi., MD Gregorio Chejfec, Mdb. W. Mdr., Werner, & Frank, W. (1986). Human Pathology Synaptophysin: A novel marker for neurons, certain neuroendocrine cells, and their neoplasms. *Hum Pathol*, 17(10), 979–983.
- Edward A. Neuwelt, M.D., Csanád G. Várallyay, M.D., Sándor Manninger, M.D., Diána Solymosi, M.D., Marianne Haluska, A. C. N. P., Matthew A. Hunt, M. D., Gary Nesbit, M. D., Alexander Stevens, P. D., Jerosch-Herold, M., & Jacobs, P. M. (2007). THE POTENTIAL OF FERUMOXYTOL NANOPARTICLE MAGNETIC RESONANCE IMAGING, PERFUSION, AND ANGIOGRAPHY IN CENTRAL NERVOUS SYSTEM MALIGNANCY: A PILOT STUDY. *Neurosurgery*, 60(4), 601–612. <https://doi.org/doi.org/10.1227/01.NEU.0000255350.71700.37>
- Eklund, M., Jäderling, F., Discacciati, A., Bergman, M., Annerstedt, M., Aly, M., Glaessgen, A., Carlsson, S., Grönberg, H., & Nordström, T. (2021). MRI-Targeted or Standard Biopsy in Prostate Cancer Screening. *New England Journal of Medicine*, 385(10), 908–920. <https://doi.org/10.1056/nejmoa2100852>
- Estelrich, J., Sánchez-Martín, M. J., & Busquets, M. A. (2015). Nanoparticles in magnetic resonance imaging: From simple to dual contrast agents. *International Journal of Nanomedicine*, 10, 1727–1741. <https://doi.org/10.2147/IJN.S76501>
- Estrella, V., Chen, T., Lloyd, M., Wojtkowiak, J., Cornell, H. H., Ibrahim-Hashim, A., Bailey, K., Balagurunathan, Y., Rothberg, J. M., Sloane, B. F., Johnson, J., Gatenby, R. A., & Gillies, R. J. (2013). Acidity generated by the tumor microenvironment drives local invasion. *Cancer Research*, 73(5), 1524–1535. <https://doi.org/10.1158/0008-5472.CAN-12-2796>
- Etienne Duguet , Sébastien Vasseur, Stéphane Mornet, J.-M. D. (2006). Magnetic nanoparticles and their applications in medicine. *Nanomedicine* :

Nanotechnology, Biology, and Medicine, 157–168.
<https://doi.org/10.2217/17435889.1.2.157>.

- Fan, S., Zheng, Y., Liu, X., Fang, W., Chena, X., Liao, W., Jing, X., Lei, M., Tao, E., Ma, Q., Zhang, X., Guo, R., & Liu, J. (2018). Curcumin-loaded plga-peg nanoparticles conjugated with b6 peptide for potential use in alzheimer's disease. *Drug Delivery*, 25(1), 1044–1055.
<https://doi.org/10.1080/10717544.2018.1461955>
- Farokhzad, O. C., & Langer, R. (2006). *Nanomedicine: Developing smarter therapeutic and*. 58, 1456–1459. <https://doi.org/10.1016/j.addr.2006.09.011>
- Feng, Q., Liu, Y., Huang, J., Chen, K., Huang, J., & Xiao, K. (2018). Uptake, distribution, clearance, and toxicity of iron oxide nanoparticles with different sizes and coatings. *Scientific Reports*, 8(1), 1–13.
<https://doi.org/10.1038/s41598-018-19628-z>
- Ferlay J, Ervik M, Lam F, Colombet M, Mery L, Piñeros M, et al. (2020). *World Health Organisation Fact Sheet*. Global Cancer Observatory: Cancer Today Lyon: International Agency for Research on Cancer.
<https://www.who.int/news-room/fact-sheets/detail/cancer>
- Ferlay, J., Parkin, D. M., & Steliarova-Foucher, E. (2010). Estimates of cancer incidence and mortality in Europe in 2008. *European Journal of Cancer*, 46(4), 765–781. <https://doi.org/10.1016/j.ejca.2009.12.014>
- Figuerola, A., Di Corato, R., Manna, L., & Pellegrino, T. (2010). From iron oxide nanoparticles towards advanced iron-based inorganic materials designed for biomedical applications. *Pharmacological Research*, 62(2), 126–143.
<https://doi.org/10.1016/j.phrs.2009.12.012>
- Ganji, M., Docter, M., Le Grice, S. F. J., & Abbondanzieri, E. A. (2016). DNA binding proteins explore multiple local configurations during docking via rapid rebinding. *Nucleic Acids Research*, 44(17), 8376–8384.
<https://doi.org/10.1093/nar/gkw666>
- Gao, F., Yuan, Q., Gao, L., Cai, P., Zhu, H., Liu, R., Wang, Y., Wei, Y., Huang, G., Liang, J., & Gao, X. (2014). Biomaterials Cytotoxicity and therapeutic effect of irinotecan combined with selenium nanoparticles. *Biomaterials*, 35(31), 8854–8866. <https://doi.org/10.1016/j.biomaterials.2014.07.004>
- Gary Beale, Andrew J. Hollins, Mustapha Benboubetra, Muhammad Sohail, Stephen P. Fox, I. B. (2008). *Gene Silencing Nucleic Acids Designed by Scanning Arrays: Anti-EGFR Activity of siRNA, Ribozyme and DNA Enzymes Targeting a Single Hybridization-accessible Region using the Same Delivery System*. 449-456 |.
<https://doi.org/10.1080/1061186042000207039>

- Gary, D. J., Puri, N., & Won, Y. Y. (2007). Polymer-based siRNA delivery: Perspectives on the fundamental and phenomenological distinctions from polymer-based DNA delivery. *Journal of Controlled Release*, 121(1–2), 64–73. <https://doi.org/10.1016/j.jconrel.2007.05.021>
- Ge, S., Shi, X., Sun, K., Li, C., Uher, C., Baker, J. R., Holl, M. M. B., & Orr, B. G. (2009). *Facile Hydrothermal Synthesis of Iron Oxide Nanoparticles with Tunable Magnetic Properties*. 13593–13599.
- Gerweck, L. E., & Seetharaman, K. (1996). Cellular pH gradient in tumor versus normal tissue: Potential exploitation for the treatment of cancer. *Cancer Research*, 56(6), 1194–1198.
- Ghafelehbashi, R., Tavakkoli, M., Mohammad, A., & Moradian, R. (2020). Materials Science & Engineering C A pH-responsive citric-acid / α - cyclodextrin-functionalized Fe₃O₄ nanoparticles as a nanocarrier for quercetin : An experimental and DFT study. *Materials Science & Engineering C*, 109(September 2019), 110597. <https://doi.org/10.1016/j.msec.2019.110597>
- Gobbo, O. L., Sjaastad, K., Radomski, M. W., Volkov, Y., & Prina-Mello, A. (2015). Magnetic nanoparticles in cancer theranostics. *Theranostics*, 5(11), 1249–1263. <https://doi.org/10.7150/thno.11544>
- Godbey, W. T., Wu, K. K., & Mikos, A. G. (1999). Size matters: Molecular weight affects the efficiency of poly(ethylenimine) as a gene delivery vehicle. *Journal of Biomedical Materials Research*, 45(3), 268–275. [https://doi.org/10.1002/\(SICI\)1097-4636\(19990605\)45:3<268::AID-JBM15>3.0.CO;2-Q](https://doi.org/10.1002/(SICI)1097-4636(19990605)45:3<268::AID-JBM15>3.0.CO;2-Q)
- Gorshtein, G., Grafinger, O., & Coppolino, M. G. (2021). Targeting SNARE-Mediated Vesicle Transport to Block Invadopodium-Based Cancer Cell Invasion. *Frontiers in Oncology*, 11(May), 1–6. <https://doi.org/10.3389/fonc.2021.679955>
- Grammatikopoulos, P., Steinhauer, S., Vernieres, J., Singh, V., & Sowwan, M. (2016). Nanoparticle design by gas-phase synthesis. *Advances in Physics: X*, 1(1), 81–100. <https://doi.org/10.1080/23746149.2016.1142829>
- Gregg, J. R., & Thompson, T. C. (2021). Considering the potential for gene-based therapy in prostate cancer. *Nature Reviews Urology*, 18(3), 170–184. <https://doi.org/10.1038/s41585-021-00431-x>
- Grimm, D. (2009). Small silencing RNAs: State-of-the-art. *Advanced Drug Delivery Reviews*, 61(9), 672–703. <https://doi.org/10.1016/j.addr.2009.05.002>
- Gupta, A. K., & Gupta, M. (2005). Synthesis and surface engineering of iron oxide

nanoparticles for biomedical applications. *Biomaterials*, 26(18), 3995–4021. <https://doi.org/10.1016/j.biomaterials.2004.10.012>

- GUSTAVO F. CARVALHAL, DEBORAH S. SMITH, DOUGLAS E. MAGER, CHRISTIAN RAMOS, and W. J. C. V. A. A. I. (1999). DIGITAL RECTAL EXAMINATION FOR DETECTING PROSTATE CANCER AT PROSTATE SPECIFIC ANTIGEN LEVELS OF 4 NG./ML. OR LESS. *Journal of Urology*, 161(3), 835–839. [https://doi.org/1016/S0022-5347\(01\)61785-3](https://doi.org/1016/S0022-5347(01)61785-3)
- H Bonkhoff, Stein, U., & Remberger, K. (1994). Multidirectional differentiation in the normal, hyperplastic, and neoplastic human prostate: simultaneous demonstration of cell-specific epithelial markers. *Hum Pathol*, 25(1), 42–46. [https://doi.org/10.1016/0046-8177\(94\)90169-4](https://doi.org/10.1016/0046-8177(94)90169-4)
- Hamidreza Kheiri Manjili, Ali Sharafi, E. A. & H. D. (2017). Pharmacokinetics and in_vitro and in_vivo delivery of sulforaphane by PCL–PEG–PCL copolymeric_based micelles, Artificial Cells,. *Nanomedicine, and Biotechnology*, 5(8), 1728–1739. <https://doi.org/10.1080/21691401.2017.1282501>
- Han, H. (2016). *Nnm-11-673.Pdf*. 11, 673–692.
- Hanahan, D., & Weinberg, R. A. (2011a). Hallmarks of cancer: the next generation. *Cell*, 144(5), 646–674. <https://doi.org/10.1016/j.cell.2011.02.013>
- Hanahan, D., & Weinberg, R. A. (2011b). Hallmarks of cancer: The next generation. *Cell*, 144(5), 646–674. <https://doi.org/10.1016/j.cell.2011.02.013>
- Hao, G., Xu, Z. P., & Li, L. (2018). Manipulating extracellular tumour pH: An effective target for cancer therapy. *RSC Advances*, 8(39), 22182–22192. <https://doi.org/10.1039/c8ra02095g>
- Hashiba, K., Sato, Y., & Harashima, H. (2017). pH-labile PEGylation of siRNA-loaded lipid nanoparticle improves active targeting and gene silencing activity in hepatocytes. *Journal of Controlled Release*, 262(July), 239–246. <https://doi.org/10.1016/j.jconrel.2017.07.046>
- Hedayatnasab, Z., Abnisa, F., & Daud, W. M. A. W. (2017). Review on magnetic nanoparticles for magnetic nanofluid hyperthermia application. *Materials and Design*, 123, 174–196. <https://doi.org/10.1016/j.matdes.2017.03.036>
- Heidenreich, A., Bellmunt, J., Bolla, M., Joniau, S., Mason, M., Matveev, V., Mottet, N., Schmid, H. P., Van Der Kwast, T., Wiegel, T., & Zattoni, F. (2011). EAU guidelines on prostate cancer. Part 1: Screening, diagnosis, and treatment of clinically localised disease. *European Urology*, 59(1), 61–71. <https://doi.org/10.1016/j.eururo.2010.10.039>
- Hemben, A., Chianella, I., & Leighton, G. J. T. (2021). Surface engineered iron

oxide nanoparticles generated by inert gas condensation for biomedical applications. *Bioengineering*, 8(3).
<https://doi.org/10.3390/bioengineering8030038>

Heppner, G. H. (1984). Tumor Heterogeneity. *Cancer Research*, 44(6), 2259–2265. <https://doi.org/10.1001/jamanetworkopen.2020.3677>

Hole, P., Sillence, K., Hannell, C., Maguire, C. M., Roesslein, M., Suarez, G., Capracotta, S., Magdolenova, Z., Horev-Azaria, L., Dybowska, A., Cooke, L., Haase, A., Contal, S., Manø, S., Vennemann, A., Sauvain, J. J., Staunton, K. C., Anguissola, S., Luch, A., ... Wick, P. (2013). Interlaboratory comparison of size measurements on nanoparticles using nanoparticle tracking analysis (NTA). *Journal of Nanoparticle Research*, 15(12).
<https://doi.org/10.1007/s11051-013-2101-8>

Hong, B. J., Chipre, A. J., & Nguyen, S. T. (2013). Acid-degradable polymer-caged lipoplex (PCL) platform for siRNA delivery: Facile cellular triggered release of siRNA. *Journal of the American Chemical Society*, 135(47), 17655–17658. <https://doi.org/10.1021/ja404491r>

Hong, R. Y., Feng, B., Chen, L. L., Liu, G. H., Li, H. Z., Zheng, Y., & Wei, D. G. (2008). Synthesis, characterization and MRI application of dextran-coated Fe₃O₄ magnetic nanoparticles. *Biochemical Engineering Journal*, 42(3), 290–300. <https://doi.org/10.1016/j.bej.2008.07.009>

Hrkach, J. S., Peracchia, M. T., Domb, A., Lotan, N., & Langer, R. (1997). Nanotechnology for biomaterials engineering: Structural characterization of amphiphilic polymeric nanoparticles by ¹H NMR spectroscopy. *Biomaterials*, 18(1), 27–30. [https://doi.org/10.1016/S0142-9612\(96\)00077-4](https://doi.org/10.1016/S0142-9612(96)00077-4)

<https://www.mantisdeposition.com/nanoparticlegenerators.html>- accessed 2019. (2021). <https://www.mantisdeposition.com/nanoparticlegenerators.html>- accessed 2019

<https://www.menshormonalhealth.com/pictures-of-prostate-cancer> (accessed December, 2018). (2018). <https://www.menshormonalhealth.com/pictures-of-prostate-cancer> (accessed December, 2018).

Huang, H. S., & Hainfeld, J. F. (2013). IJN-43770-intravenous-magnetic-nanoparticle-hyperthermia. *International Journal of Nanomedicine*, 8, 2521–2532. <https://www.ncbi.nlm.nih.gov/pmc/articles/PMC3720579/pdf/ijn-8-2521.pdf>

Hudson, D. L., O'Hare, M., Watt, F. M., & Masters, J. R. W. (2000). Proliferative heterogeneity in the human prostate: Evidence for epithelial stem cells. *Laboratory Investigation*, 80(8), 1243–1250. <https://doi.org/10.1038/labinvest.3780132>

- Hwang, Y., Lee, J. K., Lee, J. K., Jeong, Y. M., Cheong, S. ir, Ahn, Y. C., & Kim, S. H. (2008). Production and dispersion stability of nanoparticles in nanofluids. *Powder Technology*, 186(2), 145–153. <https://doi.org/10.1016/j.powtec.2007.11.020>
- Imir, O. B., Kaminsky, A. Z., Zuo, Q. Y., Liu, Y. J., Singh, R., Spinella, M. J., Irudayaraj, J., Hu, W. Y., Prins, G. S., & Erdogan, Z. M. (2021). Per-and polyfluoroalkyl substance exposure combined with high-fat diet supports prostate cancer progression. *Nutrients*, 13(11), 1–12. <https://doi.org/10.3390/nu13113902>
- Inamura, K. (2017). *Major Tumor Suppressor and Oncogenic Non-Coding RNAs: Clinical Relevance in Lung Cancer*. <https://doi.org/10.3390/cells6020012>
- Ioannidou, E., Moschetta, M., Shah, S., Parker, J. S., Ozturk, M. A., Pappas-Gogos, G., Sheriff, M., Rassy, E., & Boussios, S. (2021). Angiogenesis and anti-angiogenic treatment in prostate cancer: Mechanisms of action and molecular targets. *International Journal of Molecular Sciences*, 22(18). <https://doi.org/10.3390/ijms22189926>
- Iqbal, M. Z., Khan, J., Alam, S., Ali, R., Iqbal, M. J., Afzal, A. M., & Aftab, S. (2021). Enhanced electrochemical performance of battery-grade cobalt phosphate via magnetron sputtered copper interfacial layer for potential supercapattery applications. *International Journal of Energy Research*, 45(13), 18658–18669. <https://doi.org/10.1002/er.6974>
- JAE Y. RO, MD, PHD, BERNARD TETU, MD, FRCP (c); ALBERTO G. AYALA, M., & AND NELSON G. ORDONEZ, M. (1987). Small Cell Carcinoma of the Prostate 11. *Cancer*, 59, 1803–1809.
- Jahanban-esfahlan, A., Dastmalchi, S., & Davaran, S. (2016). International Journal of Biological Macromolecules A simple improved desolvation method for the rapid preparation of albumin nanoparticles. *International Journal of Biological Macromolecules*, 91, 703–709. <https://doi.org/10.1016/j.ijbiomac.2016.05.032>
- Jamkhande, P. G., Ghule, N. W., Bamer, A. H., & Kalaskar, M. G. (2019). Metal nanoparticles synthesis: An overview on methods of preparation, advantages and disadvantages, and applications. *Journal of Drug Delivery Science and Technology*, 53(June), 101174. <https://doi.org/10.1016/j.jddst.2019.101174>
- Javed, Y., Akhtar, K., Anwar, H., & Jamil, Y. (2017). MRI based on iron oxide nanoparticles contrast agents: effect of oxidation state and architecture. *Journal of Nanoparticle Research*, 19(11). <https://doi.org/10.1007/s11051-017-4045-x>
- Jiang, D. S., Long, S. Y., Huang, J., Xiao, H. Y., & Zhou, J. Y. (2005).

- Immobilization of *Pycnoporus sanguineus* laccase on magnetic chitosan microspheres. *Biochemical Engineering Journal*, 25(1), 15–23. <https://doi.org/10.1016/j.bej.2005.03.007>
- Jiang, Jinjin, Zhang, X., Tang, Y., Li, S., & Chen, J. (2021). Progress on ocular siRNA gene-silencing therapy and drug delivery systems. *Fundamental and Clinical Pharmacology*, 35(1), 4–24. <https://doi.org/10.1111/fcp.12561>
- Jiang, Jun, Zhou, Y., Mei, C., & Cao, J. (2021). Polyethylene glycol and silica sol penetration improves hydrophobicity and dimensional stability of wood after a short-time treatment. *European Journal of Wood and Wood Products*, 79(6), 1395–1404. <https://doi.org/10.1007/s00107-021-01710-5>
- Jin, R., Lin, B., Li, D., & Ai, H. (2014). ScienceDirect Superparamagnetic iron oxide nanoparticles for MR imaging and therapy : design considerations and clinical applications. *Current Opinion in Pharmacology*, 18, 18–27. <https://doi.org/10.1016/j.coph.2014.08.002>
- Johannsen, M., Gneveckow, U., Eckelt, L., Feussner, A., Waldöfner, N., Scholz, R., Deger, S., Wust, P., Loening, S. A., Jordan, A., Gneveckow, U., Eckelt, L., Feussner, A., & Waldöfner, N. (2009). *Clinical hyperthermia of prostate cancer using magnetic nanoparticles: Presentation of a new interstitial technique*. 6736. <https://doi.org/10.1080/02656730500158360>
- John T. Isaacs, & Coffey, D. S. (1989). Etiology and disease process of benign prostatic hyperplasia. *The Prostate*, 15, 35–50. <https://doi.org/10.1002/pros.2990150506>
- Jung, J., Solanki, A., Memoli, K. A., Kamei, K., Kim, H., Drahl, M. A., Williams, L. J., Tseng, H., & Lee, K. (2010). *Selective Inhibition of Human Brain Tumor Cells through* *Zuschriften*. 107–111. <https://doi.org/10.1002/ange.200905126>
- Kaaki, K., Herve, K., Chiper, M., Shkilnyy, A., Souce, M., Benoit, R., Paillard, A., Dubois, P., Saboungi, M., & Chourpa, I. (2011). *Magnetic Nanocarriers of Doxorubicin Coated with Poly (ethylene glycol) and Folic Acid: Relation between Coating Structure , Surface Properties , Colloidal Stability , and Cancer Cell Targeting*.
- Kaamyabi, S., Habibi, D., & Amini, M. M. (2016). Bioorganic & Medicinal Chemistry Letters Preparation and characterization of the pH and thermosensitive magnetic molecular imprinted nanoparticle polymer for the cancer drug delivery. *Bioorganic & Medicinal Chemistry Letters*, 26(9), 2349–2354. <https://doi.org/10.1016/j.bmcl.2016.03.020>
- Kadanyo, S., Gumbi, N. N., Matindi, C. N., Dlamini, D. S., Hu, Y., Cui, Z., Wang, H., Hu, M., & Li, J. (2022). Enhancing compatibility and hydrophilicity of polysulfone/poly (ethylene-co-vinyl alcohol) copolymer blend ultrafiltration

- membranes using polyethylene glycol as hydrophilic additive and compatibilizer. *Separation and Purification Technology*, 287(January), 120523. <https://doi.org/10.1016/j.seppur.2022.120523>
- Kahn, E., Lizard, G., Frouin, F., Roignot, P., Chardonnet, Y., & Di Paola, R. (1997). Laser scanning confocal microscopy and factor analysis of biomedical image sequences (FAMIS) to detect and characterise HPV DNA sequences by FISH in HeLa cells. *Cytometry*, 28(4), 269–279. [https://doi.org/10.1002/\(SICI\)1097-0320\(19970801\)28:4<269::AID-CYTO1>3.0.CO;2-7](https://doi.org/10.1002/(SICI)1097-0320(19970801)28:4<269::AID-CYTO1>3.0.CO;2-7)
- Kanagasubbulakshmi, S., & Kadirvelu, K. (2017). Green synthesis of Iron oxide nanoparticles using *Lagenaria siceraria* and evaluation of its Antimicrobial activity. *Defence Life Science Journal*, 2(4), 422. <https://doi.org/10.14429/dlsj.2.12277>
- Kay, M. A., Glorioso, J. C., & Naldini, L. (2001). Viral vectors for gene therapy : the art of turning infectious. 2001 *Nature Publishing Group*, 7(1), 33–40. <http://medicine.nature.com>
- Kean . S. (2019). *Polyethylene glycol*. 2022
- Khaleghi, S., Rahbarizadeh, F., Ahmadvand, D., Malek, M., & Madaah Hosseini, H. R. (2016). The effect of superparamagnetic iron oxide nanoparticles surface engineering on relaxivity of magnetoliposome. *Contrast Media and Molecular Imaging*, 11(5), 340–349. <https://doi.org/10.1002/cmml.1697>
- Khandhar, A. P., Ferguson, R. M., Arami, H., & Krishnan, K. M. (2013). Monodisperse magnetite nanoparticle tracers for in vivo magnetic particle imaging. *Biomaterials*, 34(15), 3837–3845. <https://doi.org/10.1016/j.biomaterials.2013.01.087>
- Khanna, L., Verma, N. K., & Tripathi, S. K. (2018). Burgeoning tool of biomedical applications - Superparamagnetic nanoparticles. *Journal of Alloys and Compounds*, 752, 332–353. <https://doi.org/10.1016/j.jallcom.2018.04.093>
- Khudair, G. H., & Mohmood, K. H. (2021). *Study of the effect of annealing during and after deposition on (crystal growth and some physical properties) of zinc sulfide (ZnS) nanoparticles prepared by vacuum thermal evaporation method (PVD)*. 12(14), 2013–2029.
- Kievit, F. M., & Zhang, M. (2011). Surface engineering of iron oxide nanoparticles for targeted cancer therapy. *Accounts of Chemical Research*, 44(10), 853–862. <https://doi.org/10.1021/ar2000277>
- Killian, J. A., & Von Heijne, G. (2000). How proteins adapt to a membrane-water interface. *Trends in Biochemical Sciences*, 25(9), 429–434. [https://doi.org/10.1016/S0968-0004\(00\)01626-1](https://doi.org/10.1016/S0968-0004(00)01626-1)

- Kim, B. J., Lee, J. E., Lee, S. H., Yu, J. H., Lee, J. H., Park, T. G., & Hyeon, T. (2008). *Designed Fabrication of a Multifunctional Polymer Nanomedical Platform for Simultaneous Cancer-Targeted Imaging and Magnetically Guided Drug Delivery* **. <https://doi.org/10.1002/adma.200701726>
- Kim, D., Kim, J. W., Jeong, Y. Y., & Jon, S. (2009). Antibiofouling polymer coated gold@iron oxide nanoparticle (GION) as a dual contrast agent for CT and MRI. *Bulletin of the Korean Chemical Society*, 30(8), 1855–1857. <https://doi.org/10.5012/bkcs.2009.30.8.1855>
- Kim, G. H., Hwang, H. Y., & An, T. (2022). In Situ BSA (Bovine Serum Albumin) Assisted Electroless Plating Method with Superior Adhesion Property. *Advanced Materials Interfaces*, 9(2), 1–7. <https://doi.org/10.1002/admi.202101203>
- Kim, H., Lin, Q., & Yun, Z. (2018). The hypoxic tumor microenvironment in vivo selects tumor cells with increased survival against genotoxic stresses. *Cancer Letters*, 431, 142–149. <https://doi.org/10.1016/j.canlet.2018.05.047>
- Kim, J., Park, S., Lee, J. E., Jin, S. M., Lee, J. H., Lee, I. S., Yang, I., Kim, J., Kim, S. K., & Cho, M. (2006). *Zuschriften*. 7918–7922. <https://doi.org/10.1002/ange.200602471>
- Kimura, T., Jia, J., Kumar, S., Choi, S. W., Gu, Y., Mudd, M., Dupont, N., Jiang, S., Peters, R., Farzam, F., Jain, A., Lidke, K. A., Adams, C. M., Johansen, T., & Deretic, V. (2017). Dedicated SNARE s and specialized TRIM cargo receptors mediate secretory autophagy . *The EMBO Journal*, 36(1), 42–60. <https://doi.org/10.15252/embj.201695081>
- Klenk, C., Gawande, R., Uslu, L., Khurana, A., Qiu, D., Quon, A., Donig, J., Rosenberg, J., Luna-fineman, S., Moseley, M., & Daldrup-link, H. E. (2014). Ionising radiation-free whole-body MRI versus ¹⁸F-fl uorodeoxyglucose PET / CT scans for children and young adults with cancer : a prospective , non-randomised , single-centre study. *Lancet Oncology*, 15(3), 275–285. [https://doi.org/10.1016/S1470-2045\(14\)70021-X](https://doi.org/10.1016/S1470-2045(14)70021-X)
- Kovács, D., Sz, K., Igaz, N., Spengler, G., Molnár, J., Tóth, T., Madarász, D., & Rázga, Z. (2016). *Silver nanoparticles modulate ABC transporter activity and enhance chemotherapy in multidrug resistant cancer*. 12, 601–610. <https://doi.org/10.1016/j.nano.2015.10.015>
- Krauland, A. H., & Alonso, M. J. (2007). Chitosan/cyclodextrin nanoparticles as macromolecular drug delivery system. *International Journal of Pharmaceutics*, 340(1–2), 134–142. <https://doi.org/10.1016/j.ijpharm.2007.03.005>
- Kreader, C. A. (1996). Relief of amplification inhibition in PCR with bovine serum albumin or T4 gene 32 protein. *Applied and Environmental Microbiology*,

- 62(3), 1102–1106. <https://doi.org/10.1128/aem.62.3.1102-1106.1996>
- Kuang, T., Chang, L., Peng, X., Hu, X., & Gallego-Perez, D. (2017). Molecular Beacon Nano-Sensors for Probing Living Cancer Cells. *Trends in Biotechnology*, 35(4), 347–359. <https://doi.org/10.1016/j.tibtech.2016.09.003>
- Kumar, R., Sahoo, G. C., Pandey, K., Das, V. N. R., Topno, R. K., Ansari, M. Y., & Das, P. (2016). Development of PLGA-PEG encapsulated miltefosine based drug delivery system against visceral leishmaniasis. *Materials Science and Engineering C*, 59, 748–753. <https://doi.org/10.1016/j.msec.2015.10.083>
- Kurotsu, S., Sadahiro, T., Harada, I., & Ieda, M. (2022). A biomimetic hydrogel culture system to facilitate cardiac reprogramming. *STAR Protocols*, 3(1), 101122. <https://doi.org/10.1016/j.xpro.2022.101122>
- Kurzer, F., & Douraghi-Zadeh, K. (1967). Advances in the chemistry of carbodiimides. *Chemical Reviews*, 67(2), 107–152. <https://doi.org/10.1021/cr60246a001>
- Kusior, A., Kollbek, K., Kowalski, K., Borysiewicz, M., Wojciechowski, T., Adamczyk, A., Trenczek-Zajac, A., Radecka, M., & Zakrzewska, K. (2016). Sn and Cu oxide nanoparticles deposited on TiO₂ nanoflower 3D substrates by Inert Gas Condensation technique. *Applied Surface Science*, 380, 193–202. <https://doi.org/10.1016/j.apsusc.2016.01.204>
- Laconte, L., Nitin, N., & Bao, G. (2005). Magnetic nanoparticle probes. *Materials Today*, 8(5 SUPPL. 1), 32–38. [https://doi.org/10.1016/S1369-7021\(05\)00893-X](https://doi.org/10.1016/S1369-7021(05)00893-X)
- Lai, W. F., & He, Z. D. (2016). Design and fabrication of hydrogel-based nanoparticulate systems for in vivo drug delivery. *Journal of Controlled Release*, 243, 269–282. <https://doi.org/10.1016/j.jconrel.2016.10.013>
- Lakshmi, P., Bhaskaran, S., & Saroja, C. (2011). Recent trends in vaccine delivery systems: A review. *International Journal of Pharmaceutical Investigation*, 1(2), 64. <https://doi.org/10.4103/2230-973x.82384>
- Lantada, D., & Endrino, J. . (2016). Microsystems for Enhanced Control of Cell Behavior. In Díaz Lantada (Ed.), *Nanomanufacturing Technologies for Biomedical Microsystems Interacting at a Molecular Scale* (pp. 147–162). Springer Berlin Heidelberg. https://doi.org/https://doi.org/10.1007/978-3-319-29328-8_9
- Laurent, S., Dutz, S., Häfeli, U. O., & Mahmoudi, M. (2011). Magnetic fluid hyperthermia: Focus on superparamagnetic iron oxide nanoparticles. *Advances in Colloid and Interface Science*, 166(1–2), 8–23.

<https://doi.org/10.1016/j.cis.2011.04.003>

- Layzer, J. M., Mccaffrey, A. P., Tanner, A. K., Huang, Z. A. N., Kay, M. A., & Sullenger, B. A. (2004). *In vivo activity of nuclease-resistant siRNAs*. 766–771. <https://doi.org/10.1261/rna.5239604>.The
- Lee, J. H., Huh, Y. M., Jun, Y. W., Seo, J. W., Jang, J. T., Song, H. T., Kim, S., Cho, E. J., Yoon, H. G., Suh, J. S., & Cheon, J. (2007). Artificially engineered magnetic nanoparticles for ultra-sensitive molecular imaging. *Nature Medicine*, 13(1), 95–99. <https://doi.org/10.1038/nm1467>
- Lee, S., Shim, G., Kim, S., Kim, Bong, Y., Chan-Wha Kim, Y. B., & Oh, and Y.-K. (2011). Enhanced Transfection Rates of Small-Interfering RNA Using Dioleoylglutamide-Based Magnetic Lipoplexes. *Nucleic Acids Research*, 21(3). <https://doi.org/doi.org/10.1089/nat.2010.0274>
- Lee, S. Y., Huh, M. S., Lee, S., Lee, S. J., Chung, H., Park, J. H., Oh, Y. K., Choi, K., Kim, K., & Kwon, I. C. (2010). Stability and cellular uptake of polymerized siRNA (poly-siRNA)/polyethylenimine (PEI) complexes for efficient gene silencing. *Journal of Controlled Release*, 141(3), 339–346. <https://doi.org/10.1016/j.jconrel.2009.10.007>
- Lewis, D. L., Hagstrom, J. E., Loomis, A. G., Wolff, J. A., & Herweije, & H. (2002). *Efficient delivery of siRNA for inhibition of gene expression*. 32(september), 107–108. <https://doi.org/10.1038/ng944>
- Li, C., Lu, H., Xu, G., Hu, F., Li, J., & Wang, L. (2022). Flexible graphene oxide/poly(ethylene glycol) composite films for lubrication application. *Materials Chemistry and Physics*, 277(November 2021), 125491. <https://doi.org/10.1016/j.matchemphys.2021.125491>
- Li, K., Nejadnik, H., & Daldrup-link, H. E. (2017). Next-generation superparamagnetic iron oxide nanoparticles for cancer theranostics. *Drug Discovery Today*, 22(9), 1421–1429. <https://doi.org/10.1016/j.drudis.2017.04.008>
- Li, L., Jiang, W., Luo, K., Song, H., Lan, F., Wu, Y., & Gu, Z. (2013). Superparamagnetic iron oxide nanoparticles as MRI contrast agents for non-invasive stem cell labeling and tracking. *Theranostics*, 3(8), 595–615. <https://doi.org/10.7150/thno.5366>
- Liang, W., & Lam, J. K. W. (2021). Endosomal Escape Pathways for Non Viral Nucleic Acid Delivery Systems. In Brian Ceresa (Ed.), *Molecular Regulation of Endocytosis* (pp. 429–441). Intech Open.
- Lim Ng, K. (2021). The Etiology of Prostate Cancer. *Prostate Cancer*, 17–28. <https://doi.org/10.36255/exonpublications.prostatecancer.etiology.2021>

- Lin, C., Blaauboer, C. J., Timoneda, M. M., Lok, M. C., van Steenberg, M., Hennink, W. E., Zhong, Z., Feijen, J., & Engbersen, J. F. J. (2008). Bioreducible poly(amido amine)s with oligoamine side chains: Synthesis, characterization, and structural effects on gene delivery. *Journal of Controlled Release*, *126*(2), 166–174. <https://doi.org/10.1016/j.jconrel.2007.11.012>
- Lin, C. R., Chiang, R. K., Wang, J. S., & Sung, T. W. (2006). Magnetic properties of monodisperse iron oxide nanoparticles. *Journal of Applied Physics*, *99*(8), 10–13. <https://doi.org/10.1063/1.2172891>
- Lin, J. J., Chen, J. S., Huang, S. J., Ko, J. H., Wang, Y. M., Chen, T. L., & Wang, L. F. (2009). Folic acid-Pluronic F127 magnetic nanoparticle clusters for combined targeting, diagnosis, and therapy applications. *Biomaterials*, *30*(28), 5114–5124. <https://doi.org/10.1016/j.biomaterials.2009.06.004>
- Lin, S., Shen, C., Lu, D., Wang, C., & Gao, H. J. (2013). Synthesis of Pt nanoparticles anchored on graphene-encapsulated Fe₃O₄ magnetic nanospheres and their use as catalysts for methanol oxidation. *Carbon*, *53*, 112–119. <https://doi.org/10.1016/j.carbon.2012.10.037>
- Lin, X., O'Reilly Beringshs, A., & Lu, X. (2021). Applications of Nanoparticle-Antibody Conjugates in Immunoassays and Tumor Imaging. *AAPS Journal*, *23*(2). <https://doi.org/10.1208/s12248-021-00561-5>
- Loeb, S., & Catalona, W. J. (2009). What is the role of digital rectal examination in men undergoing serial screening of serum PSA levels? *Nature Clinical Practice Urology*, *6*(2), 68–69. <https://doi.org/10.1038/ncpuro1294>
- Loeb, S., Martin G. Sanda, Dennis L. Broyles, S. S. S., H., B. C., John T. Wei, Alan W. Partin, G., Klee, e G., Kevin M. Slawin, L. S. M., Ron H.N. van Schaik, Daniel W. Chan, L. J. S., Cruz, A. B., Mizrahi, I. A., & Catalona, and W. J. (2015). Cancer, The Prostate Health Index Selectively Identifies Clinically Significant Prostate. *Urology*, *193*(4), 1163–1169. <https://doi.org/Doi.org/10.1016/j.juro.2014.10.121>
- Long, N. V., Yang, Y., Minh Thi, C., Minh, N. Van, Cao, Y., & Nogami, M. (2013). The development of mixture, alloy, and core-shell nanocatalysts with nanomaterial supports for energy conversion in low-temperature fuel cells. *Nano Energy*, *2*(5), 636–676. <https://doi.org/10.1016/j.nanoen.2013.06.001>
- Lu, X., & Zhang, K. (2018). PEGylation of therapeutic oligonucleotides: From linear to highly branched PEG architectures. *Nano Research*, *11*(10), 5519–5534. <https://doi.org/10.1007/s12274-018-2131-8>
- Lugnani, F. ., Simone, G. ., Biava, P. M. ., & Ablin, R. J. (2015). The Role of Neuroendocrine Cells in Prostate Cancer: A Comprehensive Review of Current Literature and Subsequent Rationale to Broaden and Integrate

Current Treatment Modalities. *Current Medicinal Chemistry*, 21(9), 1082-1092 (11).

Luo, P., Roca, A., Tiede, K., Privett, K., Jiang, J., Pinkstone, J., Ma, G., Veinot, J., & Boxall, A. (2018). Application of nanoparticle tracking analysis for characterising the fate of engineered nanoparticles in sediment-water systems. *Journal of Environmental Sciences (China)*, 64, 62–71. <https://doi.org/10.1016/j.jes.2016.07.019>

Ma, Q., Nakane, Y., Mori, Y., Hasegawa, M., Yoshioka, Y., Watanabe, T. M., Gonda, K., Ohuchi, N., & Jin, T. (2012). Multilayered, core/shell nanoprobe based on magnetic ferric oxide particles and quantum dots for multimodality imaging of breast cancer tumors. *Biomaterials*, 33(33), 8486–8494. <https://doi.org/10.1016/j.biomaterials.2012.07.051>

Macovei, I., Luca, S. V., Skalicka-Woźniak, K., Sacarescu, L., Pascariu, P., Ghilan, A., Doroftei, F., Ursu, E. L., Rumbu, C. M., Horhoge, C. E., Lungu, C., Vochita, G., Panainte, A. D., Nechita, C., Corciova, M. A., & Miron, A. (2022). Phyto-functionalized silver nanoparticles derived from conifer bark extracts and evaluation of their antimicrobial and cytogenotoxic effects. *Molecules*, 27(1). <https://doi.org/10.3390/molecules27010217>

Maeda, H. (2012). Macromolecular therapeutics in cancer treatment: The EPR effect and beyond. *Journal of Controlled Release*, 164(2), 138–144. <https://doi.org/10.1016/j.jconrel.2012.04.038>

Mahdavi, M., Ahmad, M. Bin, Haron, M. J., Namvar, F., Nadi, B., Ab Rahman, M. Z., & Amin, J. (2013). Synthesis, surface modification and characterisation of biocompatible magnetic iron oxide nanoparticles for biomedical applications. *Molecules*, 18(7), 7533–7548. <https://doi.org/10.3390/molecules18077533>

Mahdavi, M., Namvar, F., Ahmad, M. Bin, & Mohamad, R. (2013). Green biosynthesis and characterization of magnetic iron oxide (Fe₃O₄) nanoparticles using seaweed (*Sargassum muticum*) aqueous extract. *Molecules*, 18(5), 5954–5964. <https://doi.org/10.3390/molecules18055954>

Mahmoudi, M., Sant, S., Wang, B., Laurent, S., & Sen, T. (2011). Superparamagnetic iron oxide nanoparticles (SPIONs): Development, surface modification and applications in chemotherapy. *Advanced Drug Delivery Reviews*, 63(1–2), 24–46. <https://doi.org/10.1016/j.addr.2010.05.006>

Malvern Panalytical Ltd. (2022). <https://nano.wustl.edu/items/dynamic-light-scattering-malvern-zen3600/>

Martin, I., Dohmen, C., Mas-Moruno, C., Troiber, C., Kos, P., Schaffert, D., Lächelt, U., Teixidó, M., Günther, M., Kessler, H., Giralt, E., & Wagner, E.

- (2012). Solid-phase-assisted synthesis of targeting peptide-PEG-oligo(ethane amino)amides for receptor-mediated gene delivery. *Organic and Biomolecular Chemistry*, 10(16), 3258–3268. <https://doi.org/10.1039/c2ob06907e>
- Martínez Vera, N. P., Schmidt, R., Langer, K., Zlatev, I., Wronski, R., Auer, E., Havas, D., Windisch, M., Von Briesen, H., Wagner, S., Stab, J., Deutsch, M., Pietrzik, C., Fazekas, F., & Ropele, S. (2014). Tracking of magnetite labeled nanoparticles in the rat brain using MRI. *PLoS ONE*, 9(3), 20–24. <https://doi.org/10.1371/journal.pone.0092068>
- Marusyk, A., & Polyak, K. (2010). Tumor heterogeneity: Causes and consequences. *Biochimica et Biophysica Acta - Reviews on Cancer*, 1805(1), 105–117. <https://doi.org/10.1016/j.bbcan.2009.11.002>
- Marziyeh Salehiabar, Hamed Nosrati, Soodabeh Davaran, Hossein Danafar, H. K. M. (2018). *Facile Synthesis and Characterization of L-Aspartic Acid Coated Iron Oxide Magnetic Nanoparticles (IONPs) For Biomedical Applications*. 68(5), 280–285. <https://doi.org/10.1055/s-0043-120197>
- Maxwell, K. N., Cheng, H. H., Powers, J., Gulati, R., Ledet, E. M., Morrison, C., Le, A., Hausler, R., Stopfer, J., Hyman, S., Kohlmann, W., Naumer, A., Vagher, J., Greenberg, S. E., Naylor, L., Laurino, M., Konnick, E. Q., Shirts, B. H., AlDubayan, S. H., ... Pritchard, C. C. (2021). Inherited TP53 Variants and Risk of Prostate Cancer. *European Urology*, 81(3), 243–250. <https://doi.org/10.1016/j.eururo.2021.10.036>
- McCaffrey, A. P., Meuse, L., Pham, T. T. T., Conklin, D. S., Hannon, G. J., & Kay, M. A. (2002). RNA interference in adult mice. *Nature*, 418(6893), 38–39. <https://doi.org/10.1038/418038a>
- McCarthy, J. R., & Weissleder, R. (2008). Multifunctional magnetic nanoparticles for targeted imaging and therapy. *Advanced Drug Delivery Reviews*, 60(11), 1241–1251. <https://doi.org/10.1016/j.addr.2008.03.014>
- McNamara, K., & Tofail, S. A. M. (2015). Nanosystems: The use of nanoalloys, metallic, bimetallic, and magnetic nanoparticles in biomedical applications. *Physical Chemistry Chemical Physics*, 17(42), 27981–27995. <https://doi.org/10.1039/c5cp00831j>
- Meng, F., Cheng, R., Deng, C., & Zhong, Z. (2012). Intracellular drug release nanosystems In order to elicit therapeutic effects , many drugs including small molecule. *Materials Today*, 15(10), 436–442. [https://doi.org/10.1016/S1369-7021\(12\)70195-5](https://doi.org/10.1016/S1369-7021(12)70195-5)
- Meng, J., & Wang, J. (2015). Role of SNARE proteins in tumourigenesis and their potential as targets for novel anti-cancer therapeutics. *Biochimica et Biophysica Acta - Reviews on Cancer*, 1856(1), 1–12.

<https://doi.org/10.1016/j.bbcan.2015.04.002>

- Mi, P., Dewi, N., Yanagie, H., Kokuryo, D., Suzuki, M., & Sakurai, Y. (2015). *Hybrid Calcium Phosphate-Polymeric Micelles Incorporating Gadolinium Chelates for Imaging-Guided Gadolinium Neutron Capture Tumor Therapy*. 6, 5913–5921.
- Mi, P., Yanagie, H., Dewi, N., Yen, H., Liu, X., Suzuki, M., Sakurai, Y., Ono, K., Takahashi, H., Cabral, H., Kataoka, K., & Nishiyama, N. (2017). Block copolymer-boron cluster conjugate for effective boron neutron capture therapy of solid tumors. *Journal of Controlled Release*, 254(January), 1–9. <https://doi.org/10.1016/j.jconrel.2017.03.036>
- Mihut, D. M., Afshar, A., Lackey, L. W., & Le, K. N. (2019). Antibacterial effectiveness of metallic nanoparticles deposited on water filter paper by magnetron sputtering. *Surface and Coatings Technology*, 368(July 2018), 59–66. <https://doi.org/10.1016/j.surfcoat.2019.04.039>
- Mishra, P., Nayak, B., & Dey, R. K. (2016). PEGylation in anti-cancer therapy : An overview. *Asian Journal of Pharmaceutical Sciences*, 11(3), 337–348. <https://doi.org/10.1016/j.ajps.2015.08.011>
- Miyagishi, M. (2004). *Optimization of an siRNA-expression system with an improved hairpin and its significant suppressive effects in mammalian cells*. September 2003, 715–723. <https://doi.org/10.1002/jgm.556>
- Moghimi, S. M., Hunter, A. C., & Murray, J. C. (2005). *Nanomedicine : current status and future prospects*. <https://doi.org/10.1096/fj.04-2747rev>
- Mohammadi, S., & Babaei, A. (2022). Poly (vinyl alcohol)/chitosan/polyethylene glycol-assembled graphene oxide bio-nanocomposites as a prosperous candidate for biomedical applications and drug/food packaging industry. *International Journal of Biological Macromolecules*, 201(September 2021), 528–538. <https://doi.org/10.1016/j.ijbiomac.2022.01.086>
- Mohammed, L., Gomaa, H. G., Ragab, D., & Zhu, J. (2017). Magnetic nanoparticles for environmental and biomedical applications: A review. *Particuology*, 30, 1–14. <https://doi.org/10.1016/j.partic.2016.06.001>
- Moreira, D. M., Aronson, W. J., Terris, M. K., Kane, C. J., Amling, C. L., & Matthew R. Cooperberg, ; Paolo Boffetta, and S. J. F. (2014). *Cigarette Smoking Is Associated With an Increased Risk of Biochemical Disease Recurrence , Metastasis , Castration- Resistant Prostate Cancer , and Mortality After Radical Prostatectomy*. 197–204. <https://doi.org/10.1002/cncr.28423>
- Mornet, S., Vasseur, S., Grasset, F., Veverka, P., Goglio, G., Demourgues, A., Portier, J., Pollert, E., & Duguet, E. (2006). Magnetic nanoparticle design for medical applications. *Progress in Solid State Chemistry*, 34(2–4), 237–247.

<https://doi.org/10.1016/j.progsolidstchem.2005.11.010>

Moser, E. C., & Meunier, F. (2014). Cancer survivorship: A positive side-effect of more successful cancer treatment. *European Journal of Cancer, Supplement*, 12(1), 1–4. <https://doi.org/10.1016/j.ejcsup.2014.03.001>

Munnier, E., Cohen-Jonathan, S., Linassier, C., Douziech-Eyrolles, L., Marchais, H., Soucé, M., Hervé, K., Dubois, P., & Chourpa, I. (2008). Novel method of doxorubicin-SPION reversible association for magnetic drug targeting. *International Journal of Pharmaceutics*, 363(1–2), 170–176. <https://doi.org/10.1016/j.ijpharm.2008.07.006>

Nadal, R., Schweizer, M., Kryvenko, O. N., Epstein, J. I., & Eisenberger, M. A. (2014). Small cell carcinoma of the prostate. *Nature Reviews Urology*, 11(4), 213–219. <https://doi.org/10.1038/nrurol.2014.21>

Naghdi, S., & Mišković-Stanković, V. (2022). Review—A Review of the Corrosion Behaviour of Graphene Coatings on Metal Surfaces Obtained by Chemical Vapour Deposition. *Journal of The Electrochemical Society*, 169(2), 021505. <https://doi.org/10.1149/1945-7111/ac53cb>

Nanoparticle tracking analysis. (2021). <https://www.malvernpanalytical.com/en/products/technology/light-scattering/nanoparticle-tracking-analysis>

Naselli, N., Facchini, G., Lima, G. M., Evangelisti, G., Ponti, F., Miceli, M., & Spinnato, P. (2022). MRI in differential diagnosis between tuberculous and pyogenic spondylodiscitis. *European Spine Journal*, 31(2), 431–441. <https://doi.org/10.1007/s00586-021-06952-8>

Nel, A. E., Mädler, L., Velegol, D., Xia, T., Hoek, E. M. V., Somasundaran, P., Klaessig, F., Castranova, V., & Thompson, M. (2009). Understanding biophysicochemical interactions at the nano-bio interface. *Nature Materials*, 8(7), 543–557. <https://doi.org/10.1038/nmat2442>

Neuroendocrine prostate cancer. (2022). Neuroendocrine Cancer UK. <https://www.neuroendocrinecancer.org.uk/prostate/#:~:text=Neuroendocrine%20Cancer%20of%20the%20Prostate%20is%20rare%20%25E2%2580%2593,without%252>

Nhan, T., Burgess, A., Cho, E. E., Stefanovic, B., Lilge, L., & Hynynen, K. (2013). Drug delivery to the brain by focused ultrasound induced blood-brain barrier disruption: Quantitative evaluation of enhanced permeability of cerebral vasculature using two-photon microscopy. *Journal of Controlled Release*, 172(1), 274–280. <https://doi.org/10.1016/j.jconrel.2013.08.029>

Nikam, A. V., Prasad, B. L. V., & Kulkarni, A. A. (2018). Wet chemical synthesis of metal oxide nanoparticles: A review. *CrystEngComm*, 20(35), 5091–5107.

<https://doi.org/10.1039/C8CE00487K>

- Nikzamir, M., Akbarzadeh, A., & Panahi, Y. (2021). An overview on nanoparticles used in biomedicine and their cytotoxicity. *Journal of Drug Delivery Science and Technology*, 61(December 2020), 102316. <https://doi.org/10.1016/j.jddst.2020.102316>
- Nilsson, O. L. A., Jakobsen, A. L., Kölby, L., Bernhardt, P., Forssell-aronsson, E. V. A., & Ahlman, H. (2004). *Importance of Vesicle Proteins in the Diagnosis and Treatment of Neuroendocrine Tumors*. 283, 280–283. <https://doi.org/10.1196/annals.1294.032>
- Nosrati, H., Salehiabar, M., Attari, E., & Davaran, S. (2018). *Green and one - pot surface coating of iron oxide magnetic nanoparticles with natural amino acids and biocompatibility investigation*. June 2017, 1–10. <https://doi.org/10.1002/aoc.4069>
- Nosrati, H., Salehiabar, M., Davaran, S., Ramazani, A., Manjili, H. K., & Danafar, H. (2017). New advances strategies for surface functionalization of iron oxide magnetic nano particles (IONPs). *Research on Chemical Intermediates*, 43(12), 7423–7442. <https://doi.org/10.1007/s11164-017-3084-3>
- Nosrati, H., Salehiabar, M., Kheiri, H., & Danafar, H. (2018). International Journal of Biological Macromolecules Preparation of magnetic albumin nanoparticles via a simple and one-pot desolvation and co-precipitation method for medical and pharmaceutical applications. *International Journal of Biological Macromolecules*, 108, 909–915. <https://doi.org/10.1016/j.ijbiomac.2017.10.180>
- Nwoko, K. C., Raab, A., Cheyne, L., Dawson, D., Krupp, E., & Feldmann, J. (2019). Matrix-dependent size modifications of iron oxide nanoparticles (Ferumoxytol) spiked into rat blood cells and plasma: Characterisation with TEM, AF4-UV-MALS-ICP-MS/MS and spICP-MS. *Journal of Chromatography B: Analytical Technologies in the Biomedical and Life Sciences*, 1124(March), 356–365. <https://doi.org/10.1016/j.jchromb.2019.06.029>
- Oh, Y., & Gwan, T. (2009). siRNA delivery systems for cancer treatment ☆. *Advanced Drug Delivery Reviews*, 61(10), 850–862. <https://doi.org/10.1016/j.addr.2009.04.018>
- Okpalugo, J., Ibrahim, K., & Inyang, U. S. (2009). Toothpaste formulation efficacy in reducing oral flora. *Tropical Journal of Pharmaceutical Research*, 8(1), 71–77. <https://doi.org/10.4314/tjpr.v8i1.14714>
- Olga N. Metelkina, ab Rhys W. Lodge, c Polina G. Rudakovskaya, ab Vasiliy M. Gerasimov, a Carlos Herreros Lucas, c Ivan S. Grebennikov, a Igor V. Shchetinin, a Alexander G. Savchenko, a Galina E. Pavlovskaya, d Graham

- A. Rance, ORCID logo c Maria del Carm, c A. N. K. O. logo *ac and A. G. M. (2017). magnetite–carbon nanofibre materials for magnetic resonance imaging contrast agents. *Journal of Materials Chemistry B*, 5(8), 2167–2174. <https://doi.org/https://doi.org/10.1039/C6TC04141H>
- Olusanya, T. O. B., Ahmad, R. R. H., Ibegbu, D. M., Smith, J. R., & Elkordy, A. A. (2018). Liposomal drug delivery systems and anticancer drugs. *Molecules*, 23(4), 1–17. <https://doi.org/10.3390/molecules23040907>
- Oroojalian, F., Beygi, M., Baradaran, B., Mokhtarzadeh, A., & Shahbazi, M. A. (2021). Immune Cell Membrane-Coated Biomimetic Nanoparticles for Targeted Cancer Therapy. In *Small* (Vol. 17, Issue 12). <https://doi.org/10.1002/sml.202006484>
- Pagant, S., & Liberatore, R. A. (2021). In vivo electroporation of plasmid dna: A promising strategy for rapid, inexpensive, and flexible delivery of anti-viral monoclonal antibodies. *Pharmaceutics*, 13(11), 1–17. <https://doi.org/10.3390/pharmaceutics13111882>
- Parimi, V., Goyal, R., Poropatich, K., & Yang, X. J. (2014). Neuroendocrine differentiation of prostate cancer: a review. *American Journal of Clinical and Experimental Urology*, 2(4), 273–285. <http://www.ncbi.nlm.nih.gov/pubmed/25606573><http://www.pubmedcentral.nih.gov/articlerender.fcgi?artid=PMC4297323>
- Park, J. Y., Daksha, P., Lee, G. H., Woo, S., & Chang, Y. (2008). Highly water-dispersible PEG surface modified ultra small superparamagnetic iron oxide nanoparticles useful for target-specific biomedical applications. *Nanotechnology*, 19(36), 1–8. <https://doi.org/10.1088/0957-4484/19/36/365603>
- Patel, D., Moon, J. Y., Chang, Y., Kim, T. J., & Lee, G. H. (2008). Poly(d,l-lactide-co-glycolide) coated superparamagnetic iron oxide nanoparticles: Synthesis, characterization and in vivo study as MRI contrast agent. *Colloids and Surfaces A: Physicochemical and Engineering Aspects*, 313–314, 91–94. <https://doi.org/10.1016/j.colsurfa.2007.04.078>
- Pecot, C. V, Calin, G. A., Coleman, R. L., & Lopez-berestein, G. (2011). REVIEWS RNA interference in the clinic: challenges and future directions. *Nature Publishing Group*, 11(jANUARY), 59–67. <https://doi.org/10.1038/nrc2966>
- Peer, D., Karp, J. M., Hong, S., Farokhzad, O. C., Margalit, R., & Langer, R. (2007). *Nanocarriers as an emerging platform for cancer therapy*. 751–760.
- Pereira, S., Ma, G., Na, L., Hudoklin, S., Kreft, M. E., Kostevsek, N., & Al-Jamal, W. T. (2022). Encapsulation of doxorubicin prodrug in heat-triggered liposomes overcomes off-target activation for advanced prostate cancer

therapy. *Acta Biomaterialia*, 140, 530–546.
<https://doi.org/10.1016/j.actbio.2021.12.019>

- Peterson, R. D., Chen, W., Cunningham, B. T., & Andrade, J. E. (2015). Enhanced sandwich immunoassay using antibody-functionalized magnetic iron-oxide nanoparticles for extraction and detection of soluble transferrin receptor on a photonic crystal biosensor. *Biosensors & Bioelectronics*, 74, 815–822. <https://doi.org/10.1016/j.bios.2015.07.050>
- Petrushev, B., Simon, T., Berce, C., Dima, D., Tanase, A., Zdrengea, M., Suarasan, S., Dima, L., Stanciu, R., Jurj, A., & Buzoianu, A. (2016). *Gold nanoparticles enhance the effect of tyrosine kinase inhibitors in acute myeloid leukemia therapy*. 641–660.
- Pham, X. N., Nguyen, T. P., Pham, T. N., Tran, T. T. N., & Tran, T. V. T. (2016). Synthesis and characterization of chitosan-coated magnetite nanoparticles and their application in curcumin drug delivery. *Advances in Natural Sciences: Nanoscience and Nanotechnology*, 7(4). <https://doi.org/10.1088/2043-6262/7/4/045010>
- Pinto, G. (2018). *Sputtering Physical Vapour Deposition (PVD) Coatings : Trend Demands*. Dc. <https://doi.org/10.3390/coatings8110402>
- Pitek, A. S., Wen, A. M., Shukla, S., & Steinmetz, N. F. (2016). The Protein Corona of Plant Virus Nanoparticles Influences their Dispersion Properties, Cellular Interactions, and in Vivo Fates. *Small*, 12(13), 1758–1769. <https://doi.org/10.1002/smll.201502458>
- Plan Sangnier, A., Van De Walle, A. B., Curcio, A., Le Borgne, R., Motte, L., Lalatonne, Y., & Wilhelm, C. (2019). Impact of magnetic nanoparticle surface coating on their long-term intracellular biodegradation in stem cells. *Nanoscale*, 11(35), 16488–16498. <https://doi.org/10.1039/c9nr05624f>
- Portela-gomes, G. M., & Lukinius, A. (2000). Synaptic Vesicle Protein 2 , A New Neuroendocrine Cell Marker. *The American Journal of Pathology*, 157(4), 1299–1309. [https://doi.org/10.1016/S0002-9440\(10\)64645-7](https://doi.org/10.1016/S0002-9440(10)64645-7)
- Powell, I. J., Bock, C. H., Ruterbusch, J. J., & Sakr, and W. (2010). Evidence Supports a Faster Growth Rate and/or Earlier Transformation to Clinically Significant Prostate Cancer in Black Than in White American Men, and Influences Racial Progression and Mortality Disparity. *Journal of Urology*, 183(5), 1792–1797. <https://doi.org/10.1016/j.juro.2010.01.015>
- Prabaharan, M., & Mano, J. F. (2008). *Chitosan-Based Particles as Controlled Drug Delivery Systems*. 7544. <https://doi.org/10.1080/10717540590889781>
- Prausnitz, M. R., Lau, B. S., Milano, C. D., Conner, S., Langer, R., & Weaver, J.

- C. (1993). A quantitative study of electroporation showing a plateau in net molecular transport. *Biophysical Journal*, 65(1), 414–422. [https://doi.org/10.1016/S0006-3495\(93\)81081-6](https://doi.org/10.1016/S0006-3495(93)81081-6)
- Probes, M. (2005). *Bovine serum albumin conjugates*. <https://assets.thermofisher.com/TFS-Assets/LSG/manuals/mp13100.pdf>
- Probst, C. E., Zrazhevskiy, P., Bagalkot, V., & Gao, X. (2013). Quantum dots as a platform for nanoparticle drug delivery vehicle design. *Advanced Drug Delivery Reviews*, 65(5), 703–718. <https://doi.org/10.1016/j.addr.2012.09.036>
- Puranik, A. D., Dromain, C., Fleshner, N., Sathekge, M., Pavel, M., Eberhardt, N., Zengerling, F., Marienfeld, R., Grunert, M., & Prasad, V. (2021). Target heterogeneity in oncology: The best predictor for differential response to radioligand therapy in neuroendocrine tumors and prostate cancer. *Cancers*, 13(14). <https://doi.org/10.3390/cancers13143607>
- Qi, L., & Gao, X. (2008). *Quantum Dot □ Amphipol Nanocomplex Time Imaging of siRNA*. 2(7), 1403–1410.
- Qian, L., Yang, X., Li, S., Zhao, H., Gao, Y., Zhao, S., Lv, X., Zhang, X., Li, L., Zhai, L., Zhou, F., & Chen, B. (2021). Reduced O-GlcNAcylation of SNAP-23 promotes cisplatin resistance by inducing exosome secretion in ovarian cancer. *Cell Death Discovery*, 7(1). <https://doi.org/10.1038/s41420-021-00489-x>
- Qiu, Y., Tong, S., Zhang, L., Sakurai, Y., Myers, D. R., Hong, L., Lam, W. A., & Bao, G. (2017). Magnetic forces enable controlled drug delivery by disrupting endothelial cell-cell junctions. *Nature Communications*, 8, 1–10. <https://doi.org/10.1038/ncomms15594>
- Qizhen, C., Li, T., Cai, W., Zhang, Xianzhong, Xing, Chen, K., Yang, Yong, & Lei. (2006). Combined integrin siRNA therapy and radiotherapy of breast cancer. *Cancer Research*, 66(8), 1214.
- Quayle, L. A., Ottewill, P. D., & Holen, I. (2018). Chemotherapy resistance and stemness in mitotically quiescent human breast cancer cells identified by fluorescent dye retention. *Clinical and Experimental Metastasis*, 35(8), 831–846. <https://doi.org/10.1007/s10585-018-9946-2>
- Raffa, V., Riggio, C., Smith, M. W., Jordan, K. C., Cao, W., & Cuschieri, A. (2012). BNNT-mediated irreversible electroporation: Its potential on cancer cells. *Technology in Cancer Research and Treatment*, 11(5), 459–465. <https://doi.org/10.7785/tcrt.2012.500258>
- Rana, T. M. (2007). *Illuminating the silence: understanding the structure and function of small RNAs*. 8(January), 23–36. <https://doi.org/10.1038/nrm2085>

- Reddy, A. N., Anjaneyulu, K., Basak, P., Rao, N. M., & Manorama, S. V. (2012). A simple approach to the design and functionalization of Fe₃O₄-Au nanoparticles for biomedical applications. *ChemPlusChem*, 77(4), 284–292. <https://doi.org/10.1002/cplu.201100032>
- Reddy, U. A., Prabhakar, P. V., & Mahboob, M. (2017). Biomarkers of oxidative stress for in vivo assessment of toxicological effects of iron oxide nanoparticles. *Saudi Journal of Biological Sciences*, 24(6), 1172–1180. <https://doi.org/10.1016/j.sjbs.2015.09.029>
- Regazzi, R., Wollheim, C. B., Lang, J., Theler, J., Rossetto, O., Montecucco, C., Sadoul, K., Weller, U., Palmer, M., & Thorens, B. (1995). *VAMP-2 and cellubrevin are expressed in pancreatic -cells and are essential for Ca²⁺ + - but not for GTPyS-induced insulin secretion*. 14(12), 2723–2730. <https://doi.org/10.1002/j.1460-2075.1995.tb07273.x>
- Rindi, G., Paolotti, D., Fiocca, R., & Henry, B. W. J. (2000). *Vesicular monoamine transporter 2 as a marker of gastric enterochromaffin-like cell tumors*. 2, 217–223.
- Rios, N. S., Arana-Peña, S., Mendez-Sanchez, C., Lokha, Y., Cortes-Corberan, V., Gonçalves, L. R. B., & Fernandez-Lafuente, R. (2019). Increasing the enzyme loading capacity of porous supports by a layer-by-layer immobilization strategy using PEI as glue. *Catalysts*, 9(7). <https://doi.org/10.3390/catal9070576>
- Robert Borny , Thomas Lechleitner, Thomas Schmiedinger, Martin Hermann, Richard Tessadri, Günther Redhammer, Josef Neumüller, Donscho Kerjaschki, Gundula Berzaczy, Gürkan Erman, Martin Popovic, Johannes Lammer, M. F. (2015). Nucleophilic cross-linked, dextran coated iron oxide nanoparticles as basis for molecular imaging: synthesis, characterization, visualization and comparison with previous product. *Contrast Media and Molecular Imaging*, 10(1), 18–27. <https://doi.org/10.1002/cmml.1595>
- Roger, J., Pons, J. N., Massart, R., Halbreich, A., And, & Bacri, J. C. (1999). *Some biomedical applications of ferrofluids** (Vol. 5, Issue 3). Cambridge University Press. <https://doi.org/doi.org/10.1051/epjap:1999144>
- Rosnagel, S. M. (1999). Sputter deposition for semiconductor manufacturing. *IBM Journal of Research and Development*, 43(1–2), 163–179. <https://doi.org/10.1147/rd.431.0163>
- Rostami, M., Aghajanzadeh, M., Zamani, M., Manjili, H. K., & Danafar, H. (2018). Sono-chemical synthesis and characterization of Fe₃O₄@mTiO₂-GO nanocarriers for dual-targeted colon drug delivery. *Research on Chemical Intermediates*, 44(3), 1889–1904. <https://doi.org/10.1007/s11164-017-3204-0>

- S, T., N, S., A, T., RY, Osamura, & RY'. (1999). *Expression of Rab3, a Ras-related GTP-binding protein, in human nontumorous pituitaries and pituitary adenomas*. 12(6), 627–634.
- Safi, I. (2000). Recent aspects concerning DC reactive magnetron sputtering of thin films: A review. *Surface and Coatings Technology*, 127(2–3), 203–218. [https://doi.org/10.1016/s0257-8972\(00\)00566-1](https://doi.org/10.1016/s0257-8972(00)00566-1)
- Saha, K., Agasti, S. S., Kim, C., Li, X., & Rotello, V. M. (2012). Gold nanoparticles in chemical and biological sensing. *Chemical Reviews*, 112(5), 2739–2779. <https://doi.org/10.1021/cr2001178>
- Salafi, T., Zeming, K. K., & Zhang, Y. (2017). Advancements in microfluidics for nanoparticle separation. *Lab on a Chip*, 17(1), 11–33. <https://doi.org/10.1039/C6LC01045H>
- Sangeetha, J. ., Thomas, Susha; Arutchelvi, J. ., Doble, M., & Philip, J. (2013). Functionalization of Iron Oxide Nanoparticles with Biosurfactants and Biocompatibility Studies. *Biomedical Technology*, 9(5), 751-764(14). [https://doi.org/DOI: https://doi.org/10.1166/jbn.2013.1590](https://doi.org/DOI:https://doi.org/10.1166/jbn.2013.1590)
- Schleich, N., Danhier, F., & Préat, V. (2015). Iron oxide-loaded nanotheranostics: Major obstacles to in vivo studies and clinical translation. *Journal of Controlled Release*, 198, 35–54. <https://doi.org/10.1016/j.jconrel.2014.11.024>
- Schmechel, D. (1978). Neurone-specific enolase is a molecular marker for peripheral and central neuroendocrine cells. *Nature*, 276(5690), 834.
- Schroeder, A., Heller, D. A., Winslow, M. M., Dahlman, J. E., Pratt, G. W., Langer, R., Jacks, T., & Anderson, D. G. (2012). Treating metastatic cancer with nanotechnology. *Nature Reviews Cancer*, 12(1), 39–50. <https://doi.org/10.1038/nrc3180>
- Schron, D. S., Gipson, T., & Mendelsohn, G. (1984). The histogenesis of small cell carcinoma of the prostate an immunohistochemical study. *Cancer*, 53(11), 2478–2480. [https://doi.org/10.1002/1097-0142\(19840601\)53:11<2478::AID-CNCR2820531119>3.0.CO;2-Q](https://doi.org/10.1002/1097-0142(19840601)53:11<2478::AID-CNCR2820531119>3.0.CO;2-Q)
- Seeger, R. C., Danon, Y. L., Rayner, S. A., And, & Hoover, F. (1982). Definition of a Thy-1 determinant on human neuroblastoma, glioma, sarcoma, and teratoma cells with a monoclonal antibody. *Journal of Immunological Methods*, 128(2), 983–989.
- Serfimowicz, W. (2018). *PILOT STUDY OF siRNA NANOMEDICINE TARGETING CANCER TREATMENT*. Cranfield University.
- Seshi, B., True, L., Carter, D., & Rosai, J. (1988). Immunohistochemical

- characterization of a set of monoclonal antibodies to human neuron-specific enolase. *American Journal of Pathology*, 131(2), 258–269.
- Seton-Rogers, S. (2012). Therapeutics: SiRNAs jump the hurdle. *Nature Reviews Cancer*, 12(6), 376–377. <https://doi.org/10.1038/nrc3281>
- Shahdeo, D., Roberts, A., Kesarwani, V., Horvat, M., Chouhan, R. S., & Gandhi, S. (2022). *Polymeric biocompatible iron oxide nanoparticles labeled with peptides for imaging in ovarian cancer*. 0(February), 1–14.
- Shapira, A., Livney, Y. D., Broxterman, H. J., & Assaraf, Y. G. (2011). Nanomedicine for targeted cancer therapy : Towards the overcoming of drug resistance. *Drug Resistance Updates*, 14(3), 150–163. <https://doi.org/10.1016/j.drug.2011.01.003>
- Shchapova, E., Nazarova, A., Gurkov, A., Borvinskaya, E., Rzhechitskiy, Y., Dmitriev, I., Meglinski, I., & Timofeyev, M. (2019). Application of PEG-covered non-biodegradable polyelectrolyte microcapsules in the crustacean circulatory system on the example of the amphipod *Eulimnogammarus verrucosus*. *Polymers*, 11(8). <https://doi.org/10.3390/polym11081246>
- Sheng-Nan(孙圣男)Sun, 超 W. C., Zan-Zan(朱赞赞), Z., Yang-Long(侯仰龙), H., Venkatramana)†, S. S., & Zhi-Chuan(徐志川), and X. (2014). Magnetic iron oxide nanoparticles: Synthesis and surface coating techniques for biomedical applications Magnetic iron oxide nanoparticles: Synthesis and surface coating techniques for biomedical applications *. *Chin. Phys. B.*, 23(3), 037503-(1)-037503-(19). <https://doi.org/10.1088/1674-1056/23/3/037503>
- Shi, J., Kantoff, P. W., Wooster, R., & Farokhzad, O. C. (2017). Cancer nanomedicine : progress , challenges and opportunities. *Nature Publishing Group*, 17, 20–27. <https://doi.org/10.1038/nrc.2016.108>
- Shirlaw, J. T. (1931). The metabolism of tumours. *British Medical Journal*, 1(3653), 74. <https://doi.org/10.1136/bmj.1.3653.74-a>
- Siddiqi, K. S., ur Rahman, A., Tajuddin, & Husen, A. (2016). Biogenic Fabrication of Iron/Iron Oxide Nanoparticles and Their Application. *Nanoscale Research Letters*, 11(1). <https://doi.org/10.1186/s11671-016-1714-0>
- Sikora, K. (1998). Prostate Cancer. *World Health, World Health Organization.*, 51(5), 19–20. <https://apps.who.int/iris/handle/10665/331393>
- Sine, B., Ndiath, A., Bagayogo, N. A., Sarr, A., Thiam, A., Ondo, C. Z., Sow, O., Diaw, E. H. M., Sène, M., Sakho, B., Gassama, C. B., Ngom, I., Sow, Y., Diao, B., & Ndoeye, A. K. (2021). Positive Surgical Margins (PSM) after Open Retropubic Radical Prostatectomy: Evaluation of Patient Survival. *Open*

- Singamaneni, S., Bliznyuk, V. N., Binek, C., & Tsymbal, E. Y. (2011). Magnetic nanoparticles: Recent advances in synthesis, self-assembly and applications. *Journal of Materials Chemistry*, 21(42), 16819–16845. <https://doi.org/10.1039/c1jm11845e>
- Singh, J., Dutta, T., Kim, K. H., Rawat, M., Samddar, P., & Kumar, P. (2018). ‘Green’ synthesis of metals and their oxide nanoparticles: Applications for environmental remediation. *Journal of Nanobiotechnology*, 16(1), 1–24. <https://doi.org/10.1186/s12951-018-0408-4>
- Sinha, R., Kim, G. J., & Nie, S. (2006). *Review Nanotechnology in cancer therapeutics: bioconjugated nanoparticles for drug delivery*. 5(August), 1909–1918. <https://doi.org/10.1158/1535-7163.MCT-06-0141>
- Sioud, M. (2003). *Cationic liposome-mediated delivery of siRNAs in adult mice*. 312, 1220–1225. <https://doi.org/10.1016/j.bbrc.2003.11.057>
- Skopalik, J., Polakova, K., Havrdova, M., Justan, I., Magro, M., Milde, D., Knopfova, L., Smarda, J., Polakova, H., Gabrielova, E., Vianello, F., Michalek, J., & Zboril, R. (2014). Mesenchymal stromal cell labeling by new uncoated superparamagnetic maghemite nanoparticles in comparison with commercial Resovist--an initial in vitro study. *International Journal of Nanomedicine*, 9, 5355–5372. <https://doi.org/10.2147/IJN.S66986>
- Sohrabijam, Z., Saeidifar, M., & Zamanian, A. (2017). Colloids and Surfaces B: Biointerfaces Enhancement of magnetofection efficiency using chitosan coated superparamagnetic iron oxide nanoparticles and calf thymus DNA. *Colloids and Surfaces B: Biointerfaces*, 152, 169–175. <https://doi.org/10.1016/j.colsurfb.2017.01.028>
- Solomon, G., Kohan, M. G., Vagin, M., Rigoni, F., Mazzaro, R., Natile, M. M., You, S., Morandi, V., Concina, I., & Vomiero, A. (2021). Decorating vertically aligned MoS₂ nanoflakes with silver nanoparticles for inducing a bifunctional electrocatalyst towards oxygen evolution and oxygen reduction reaction. *Nano Energy*, 81(November 2020), 105664. <https://doi.org/10.1016/j.nanoen.2020.105664>
- Song, J., Ma, S., Sokoll, L. J., Eiguez, R. V., Höti, N., Zhang, H., Mohr, P., Dua, R., Patil, D., May, K. D., Williams, S., Arnold, R., Sanda, M. G., Chan, D. W., & Zhang, Z. (2021). A panel of selected serum protein biomarkers for the detection of aggressive prostate cancer. *Theranostics*, 11(13), 6214–6224. <https://doi.org/10.7150/thno.55676>
- SONG¹, E., LEE, S.-K., WANG, JIE, INCE, NEDIM, OUYANG, N., MIN², J., CHEN, J., LIEBERMAN, & JUDY, P. S. &. (2003). *ARTICLES RNA*

- interference targeting Fas protects mice from fulminant hepatitis.* 347–351. <https://doi.org/10.1038/nm>
- Sørensen, D. R., Leirdal, M., & Sioud, M. (2003). *Gene Silencing by Systemic Delivery of Synthetic siRNAs in Adult Mice.* 2836(03), 761–766. [https://doi.org/10.1016/S0022-2836\(03\)00181-5](https://doi.org/10.1016/S0022-2836(03)00181-5)
- Stark, W. J. (2011). *Nanoparticles in Biological Systems Angewandte.* 1242–1258. <https://doi.org/10.1002/anie.200906684>
- Steitz, B., Hofmann, H., Kamau, S. W., Hassa, P. O., Hottiger, M. O., von Rechenberg, B., Hofmann-Antenbrink, M., & Petri-Fink, A. (2007). Characterization of PEI-coated superparamagnetic iron oxide nanoparticles for transfection: Size distribution, colloidal properties and DNA interaction. *Journal of Magnetism and Magnetic Materials*, 311(1 SPEC. ISS.), 300–305. <https://doi.org/10.1016/j.jmmm.2006.10.1194>
- Stevens, P. D., Fan, J., Gardimalla, H. M. R., Yen, M., & Gao, Y. (2005). Superparamagnetic nanoparticle-supported catalysis of Suzuki cross-coupling reactions. *Organic Letters*, 7(11), 2085–2088. <https://doi.org/10.1021/ol050218w>
- Stratakis, E., & Kymakis, E. (2013). Nanoparticle-based plasmonic organic photovoltaic devices. *Materials Today*, 16(4), 133–146. <https://doi.org/10.1016/j.mattod.2013.04.006>
- Stueber, D. D., Villanova, J., Aponte, I., Xiao, Z., & Colvin, V. L. (2021). Magnetic nanoparticles in biology and medicine: Past, present, and future trends. *Pharmaceutics*, 13(7). <https://doi.org/10.3390/pharmaceutics13070943>
- Subbiah, R.; Veerapandian, M. ., & S. Yun, K. (2010). Nanoparticles: Functionalization and Multifunctional Applications in Biomedical Sciences. In *Current Medicinal Chemistry* (Vol. 17, Issue 36, pp. 4559-4577(19)). Bentham Science Publishers. <https://doi.org/https://doi.org/10.2174/092986710794183024>
- Suci, P., & Hlady, V. (1990). Fluorescence lifetime components of Texas red-labelled bovine serum albumin: Comparison of bulk and adsorbed states. *Colloids and Surfaces*, 51(C), 89–104. [https://doi.org/10.1016/0166-6622\(90\)80134-P](https://doi.org/10.1016/0166-6622(90)80134-P)
- Sumer, B., & Gao, J. (2008). *Theranostic nanomedicine for cancer.* 137–140.
- Sun, J., Ogunnaike, E. A., Jiang, X., & Chen, Z. (2021). Nanotechnology lights up the antitumor potency by combining chemotherapy with siRNA. *Journal of Materials Chemistry B*, 9(36), 7302–7317. <https://doi.org/10.1039/d1tb01379c>

- Sun, Z., Ni, W., Yang, Z., Kou, X., Li, L., & Wang, J. (2008). *pH-Controlled Reversible Assembly and Disassembly of Gold Nanorods***[†]. 1287–1292. <https://doi.org/10.1002/sml.200800099>
- SVS. (2022). *Scientific Vacuum Systems*. <https://www.svs.co.uk/sputtering/production-sputtering>
- Sztandera, K., Gorzkiewicz, M., & Klajnert-Maculewicz, B. (2019). Gold Nanoparticles in Cancer Treatment. *Molecular Pharmaceutics*, 16(1), 1–23. <https://doi.org/10.1021/acs.molpharmaceut.8b00810>
- Takami, S., Sato, T., Mousavand, T., Ohara, S., Umetsu, M., & Adschiri, T. (2007). *Hydrothermal synthesis of surface-modified iron oxide nanoparticles*. 61, 4769–4772. <https://doi.org/10.1016/j.matlet.2007.03.024>
- Tan, H. L., Sood, A., Rahimi, H. A., Wang, W., Gupta, N., Hicks, J., Mosier, S., Gocke, C. D., Epstein, J. I., Netto, G. J., Liu, W., Isaacs, W. B., De Marzo, A. M., & Lotan, T. L. (2014). Rb loss is characteristic of prostatic small cell neuroendocrine carcinoma. *Clinical Cancer Research*, 20(4), 890–903. <https://doi.org/10.1158/1078-0432.CCR-13-1982>
- Tan, S. C., & Yiap, B. C. (2009). DNA, RNA, and protein extraction: The past and the present. *Journal of Biomedicine and Biotechnology*, 2009. <https://doi.org/10.1155/2009/574398>
- Tan, X. C., Zhang, J. L., Tan, S. W., Zhao, D. D., Huang, Z. W., Mi, Y., & Huang, Z. Y. (2009). Amperometric hydrogen peroxide biosensor based on immobilization of hemoglobin on a glassy carbon electrode modified with Fe₃O₄/chitosan core-shell microspheres. *Sensors*, 9(8), 6185–6199. <https://doi.org/10.3390/s90806185>
- Tang, J., Myers, M., Bosnick, K. A., & Brus, L. E. (2003). Magnetite Fe₃O₄ nanocrystals: spectroscopic observation of aqueous oxidation kinetics. *Journal of Physics and Chemistry of Solids*, 107(30), 7501–7506. <https://doi.org/https://doi.org/10.1021/jp027048e>
- Tang, Jie, Li, L., Howard, C. B., Mahler, S. M., Huang, L., & Xu, Z. P. (2015). Preparation of optimized lipid-coated calcium phosphate nanoparticles for enhanced in vitro gene delivery to breast cancer cells. *Journal of Materials Chemistry B*, 3(33), 6805–6812. <https://doi.org/10.1039/c5tb00912j>
- Tang, Y., Shigematsu, T., Morimura, S., & Kida, K. (2005). Microbial community analysis of mesophilic anaerobic protein degradation process using bovine serum albumin (BSA)-fed continuous cultivation. *Journal of Bioscience and Bioengineering*, 99(2), 150–164. <https://doi.org/10.1263/jbb.99.150>
- Tavakol, S. (2014). Acidic pH derived from cancer cells may induce failed reprogramming of normal differentiated cells adjacent tumor cells and turn

them into cancer cells. *Medical Hypotheses*, 83(6), 668–672.
<https://doi.org/10.1016/j.mehy.2014.09.014>

Thermofisher.com. (2019).
<https://www.thermofisher.com/order/catalog/product/A23017>

Tischler, A. S., Mobtaker, H., Mann, K., Nunnemacher, G., Jason, W. J., Dayal, Y., Delellis, R. A., Adelman, L., & Wolfe, H. J. (1986). Anti-lymphocyte antibody Leu-7 (HNK-1) recognizes a constituent of neuroendocrine granule matrix. *Journal of Histochemistry and Cytochemistry*, 34(9), 1213–1216.
<https://doi.org/10.1177/34.9.2426347>

Titus, J.A., Haugland, R., Sharrow, S.O. and Segal, D.M. (1982). Texas red, a hydrophilic, red-emitting flourophore for use with flourescein in dual parameter flow microfluorometric and fluorescence microscopic studies. *Journal of Immunological Methods*, 50(2), 193–204.

Torchilin, V. P. (2014). Multifunctional, stimuli-sensitive nanoparticulate systems for drug delivery. *Nature Reviews Drug Discovery*, 13(11), 813–827.
<https://doi.org/10.1038/nrd4333>

Tortajada, L., Felip-León, C., & Vicent, M. J. (2022). Polymer-based non-viral vectors for gene therapy in the skin. *Polymer Chemistry, Table 1*, 718–735.
<https://doi.org/10.1039/d1py01485d>

Tosoian, J. J., Druskin, S. C., Andreas, D., Mullane, P., Chappidi, M., Joo, S., Ghabili, K., Agostino, J., Macura, K. J., Carter, H. B., Schaeffer, E. M., Partin, A. W., Sokoll, L. J., & Ross, A. E. (2017). Use of the prostate health index for detection of prostate cancer: Results from a large academic practice. *Prostate Cancer and Prostatic Diseases*, 20(2), 228–233.
<https://doi.org/10.1038/pcan.2016.72>

UgelstadA., BergeT., EllingsenJ., BjorgumR., SchmidP., StenstadO., N., A., NilsenS., & Nustad, F. (1987). Biomedical Applications of Monodisperse Magnetic Polymer Particles. In *Future Direction in Polymer Colloids* (pp. 355–370). Springer Berlin Heidelberg.

Ung, H. S. I. E. N. K. (1998). *Etk⁻Bmx*, a tyrosine kinase with a pleckstrin-homology domain, is an effector of phosphatidylinositol 3-kinase and is involved in interleukin 6-induced neuroendocrine differentiation of prostate cancer cells. 95(March), 3644–3649.

Unni, M., Uhl, A. M., Savliwala, S., Savitzky, B. H., Dhavalikar, R., Garraud, N., Arnold, D. P., Kourkoutis, L. F., Andrew, J. S., & Rinaldi, C. (2017). *Thermal Decomposition Synthesis of Iron Oxide Nanoparticles with Diminished Magnetic Dead Layer by Controlled Addition of Oxygen*.
<https://doi.org/10.1021/acsnano.7b00609>

- Unsoy, G., Yalcin, S., Khodadust, R., Gunduz, G., & Gunduz, U. (2012). Synthesis optimization and characterization of chitosan-coated iron oxide nanoparticles produced for biomedical applications. *Journal of Nanoparticle Research*, 14(11). <https://doi.org/10.1007/s11051-012-0964-8>
- Vallabani, N. V. S., & Singh, S. (2018). Recent advances and future prospects of iron oxide nanoparticles in biomedicine and diagnostics. *3 Biotech*, 8(6), 1–23. <https://doi.org/10.1007/s13205-018-1286-z>
- Vallet-Regí, M., Colilla, M., Izquierdo-Barba, I., & Manzano, M. (2018). Mesoporous silica nanoparticles for drug delivery: Current insights. *Molecules*, 23(1), 1–19. <https://doi.org/10.3390/molecules23010047>
- Van Leenders, G., Dijkman, H., Hulsbergen-Van De Kaa, C., Ruiters, D., & Schalken, J. (2000). Demonstration of intermediate cells during human prostate epithelial differentiation in situ and in vitro using triple-staining confocal scanning microscopy. *Laboratory Investigation*, 80(8), 1251–1258. <https://doi.org/10.1038/labinvest.3780133>
- Vangijzegem, T., Stanicki, D., & Laurent, S. (2019). Magnetic iron oxide nanoparticles for drug delivery: applications and characteristics. *Expert Opinion on Drug Delivery*, 16(1), 69–78. <https://doi.org/doi.org/10.1080/17425247.2019.1554647>
- Vauthier, C., & Labarre, D. (2008). Modular biomimetic drug delivery systems. *Journal of Drug Delivery Science and Technology*, 18(1), 59–68. [https://doi.org/10.1016/S1773-2247\(08\)50008-6](https://doi.org/10.1016/S1773-2247(08)50008-6)
- Vergés, M. A., Costo, R., Roca, A. G., Marco, J. F., Goya, G. F., Serna, C. J., & Morales, M. P. (2008). Uniform and water stable magnetite nanoparticles with diameters around the monodomain-multidomain limit. *Journal of Physics D: Applied Physics*, 41(13). <https://doi.org/10.1088/0022-3727/41/13/134003>
- Vernieres, J., Steinhauer, S., Zhao, J., Chapelle, A., Menini, P., Dufour, N., Diaz, R. E., Nordlund, K., & Djurabekova, F. (2017). *Gas Phase Synthesis of Multifunctional Fe-Based Nanocubes*. <https://doi.org/10.1002/adfm.201605328>
- Vigneswaran, H. T., Jagai, J. S., Greenwald, D. T., Patel, A. P., Kumar, M., Dobbs, R. W., Moreira, D. M., & Abern, M. R. (2021). Association between environmental quality and prostate cancer stage at diagnosis. *Prostate Cancer and Prostatic Diseases*, 24(4), 1129–1136. <https://doi.org/10.1038/s41391-021-00370-z>
- Von Harpe, A., Petersen, H., Li, Y., & Kissel, T. (2000). Characterization of commercially available and synthesized polyethylenimines for gene delivery. *Journal of Controlled Release*, 69(2), 309–322.

[https://doi.org/10.1016/S0168-3659\(00\)00317-5](https://doi.org/10.1016/S0168-3659(00)00317-5)

- Wagner, A. M., Knipe, J. M., Orive, G., & Peppas, N. A. (2019). Quantum dots in biomedical applications. *Acta Biomaterialia*, 94, 44–63. <https://doi.org/10.1016/j.actbio.2019.05.022>
- Wang, L., Omoda, T., Koyasu, K., & Tsukuda, T. (2022). Controlled Synthesis of Diphosphine-Protected Gold Cluster Cations Using Magnetron Sputtering Method. *Molecules*, 27(4), 1330. <https://doi.org/10.3390/molecules27041330>
- Wang, W., Zhang, M. J., & Chu, L. Y. (2014). Functional polymeric microparticles engineered from controllable microfluidic emulsions. *Accounts of Chemical Research*, 47(2), 373–384. <https://doi.org/10.1021/ar4001263>
- Weaver, D. J., & Voss, E. W. (1998). Analysis of rates of receptor-mediated endocytosis and exocytosis of a fluorescent hapten-protein conjugate in murine macrophage: Implications for antigen processing. *Biology of the Cell*, 90(2), 169–181. [https://doi.org/10.1016/S0248-4900\(98\)80338-9](https://doi.org/10.1016/S0248-4900(98)80338-9)
- Weigert, O., Pastore, A., Rieken, M., Lang, N., Hiddemann, W., & Dreyling, M. (2007). Sequence-dependent synergy of the proteasome inhibitor bortezomib and cytarabine in mantle cell lymphoma. *Leukemia*, 21(3), 524–528. <https://doi.org/10.1038/sj.leu.2404511>
- Weizenecker, J., Gleich, B., Rahmer, J., Dahnke, H., & Borgert, J. (2009). Three-dimensional real-time in vivo magnetic particle imaging. *Physics in Medicine and Biology*, 54(5). <https://doi.org/10.1088/0031-9155/54/5/L01>
- Welch, D. R. (2016). Tumor heterogeneity - A 'contemporary concept' founded on historical insights and predictions. *Cancer Research*, 76(1), 4–6. <https://doi.org/10.1158/0008-5472.CAN-15-3024>
- Weyts, K. F., & Goethals, E. J. (1988). New synthesis of linear polyethyleneimine. *Polymer Bulletin*, 19(1), 13–19. <https://doi.org/10.1007/BF00255018>
- WHO. (2022). *WHO Factsheet*. Cancer Factsheet. <https://www.who.int/news-room/fact-sheets/detail/cancer>
- Wiedenmann, B., Franke, W. W., Kuhn, C., Moll, R., & Gould, V. E. (1986). *Synaptophysin: A marker protein for neuroendocrine cells and neoplasms*. 83(May), 3500–3504.
- Williams, G. V. M., Prakash, T., Kennedy, J., Chong, S. V., & Rubanov, S. (2018). Spin-dependent tunnelling in magnetite nanoparticles. *Journal of Magnetism and Magnetic Materials*, 460, 229–233. <https://doi.org/10.1016/j.jmmm.2018.04.017>
- Winkler, H., & Westhead, E. (1980). The molecular organization of adrenal

- chromaffin granules. *Neuroscience*, 5(11), 1803–1823. [https://doi.org/https://doi.org/10.1016/0306-4522\(80\)90031-7](https://doi.org/https://doi.org/10.1016/0306-4522(80)90031-7)
- Winnik, F. M., & Maysinger, D. (2013). T 672 '. *Acc. Chem. Res.*, 46(3), 672.
- Wirth, T., Parker, N., & Ylä-Herttuala, S. (2013). History of gene therapy. *Gene*, 525(2), 162–169. <https://doi.org/10.1016/j.gene.2013.03.137>
- Wolz, R., Julkunen, V., Koikkalainen, J., Niskanen, E., Zhang, D. P., Rueckert, D., Soininen, H., & Lötjönen, J. (2011). Multi-method analysis of MRI images in early diagnostics of Alzheimer's disease. *PLoS ONE*, 6(10), 1–9. <https://doi.org/10.1371/journal.pone.0025446>
- World Health Organisation Factsheet*. (2018). <https://www.who.int/news-room/fact-sheets/detail/cancer>
- Wu, J. N., Fish, K. M., Evans, C. P., White, R. W., & Era, M. A. D. (2014). *No Improvement Noted in Overall or Cause-Specific Survival for Men Presenting With Metastatic Prostate Cancer Over a 20-Year Period*. 818–823. <https://doi.org/10.1002/cncr.28485>
- Wu, W., He, Q., & Jiang, C. (2008). Magnetic iron oxide nanoparticles: Synthesis and surface functionalization strategies. *Nanoscale Research Letters*, 3(11), 397–415. <https://doi.org/10.1007/s11671-008-9174-9>
- Wu, W., Wu, Z., Yu, T., Jiang, C., Kim, W., Wu, W., Wu, Z., Yu, T., & Jiang, C. (2015). nanoparticles: synthesis , surface functional strategies and biomedical applications Recent progress on magnetic iron oxide nanoparticles: synthesis , surface functional strategies and biomedical applications. *Science and Technology of Advanced Materials*, 16(2), 23501. <https://doi.org/10.1088/1468-6996/16/2/023501>
- Wu, Z., & Wu, W. (2016). *Shape control of inorganic nanoparticles from*. 1237–1259. <https://doi.org/10.1039/c5nr07681a>
- www.mantisdeposition.com. (2019a). <https://www.mantisdeposition.com/nanoparticlegenerators.html>
- www.mantisdeposition.com. (2019b). www.mantisdeposition.com
- Xie, S., Zhang, B., Wang, L., Wang, J., Li, X., Yang, G., & Gao, F. (2015). Superparamagnetic iron oxide nanoparticles coated with different polymers and their MRI contrast effects in the mouse brains. *Applied Surface Science*, 326, 32–38. <https://doi.org/10.1016/j.apsusc.2014.11.099>
- Xie, W., Guo, Z., Gao, F., Gao, Q., Wang, D., Liaw, B., & Cai, Q. (2018). *Therapeutic Shape-, size- and structure-controlled synthesis and biocompatibility of iron oxide nanoparticles for magnetic theranostics*. 8(12). <https://doi.org/10.7150/thno.25220>


- Xing, L., Brink, G. H., Chen, B., & Schmidt, F. P. (2016). *Synthesis and morphology of iron – iron oxide core – shell nanoparticles produced by high pressure gas condensation*.
- Xing, L., Brink, G. H., Kooi, B. J., & Palasantzas, G. (2017). *Preparation of tunable-sized iron nanoparticles based on magnetic manipulation in inert gas condensation (IGC)*. 024305(October 2016). <https://doi.org/10.1063/1.4974052>
- Xiong, X., Arvizo, R. R., Saha, S., Robertson, D. J., Bhattacharya, R., & Mukherjee, P. (2014). *Sensitization of ovarian cancer cells to cisplatin by gold nanoparticles*. 5(15).
- Xu, H., Cheng, L., Wang, C., Ma, X., Li, Y., & Liu, Z. (2011). Polymer encapsulated upconversion nanoparticle/iron oxide nanocomposites for multimodal imaging and magnetic targeted drug delivery. *Biomaterials*, 32(35), 9364–9373. <https://doi.org/10.1016/j.biomaterials.2011.08.053>
- Xu, L., Karunakaran, R. G., Guo, J., & Yang, S. (2012). Transparent, superhydrophobic surfaces from one-step spin coating of hydrophobic nanoparticles. *ACS Applied Materials and Interfaces*, 4(2), 1118–1125. <https://doi.org/10.1021/am201750h>
- Xuan, D., Chengyang, W., Mingming, C., Yang, J., & Jin, W. (2009). Electrochemical performances of nanoparticle Fe₃O₄/activated carbon supercapacitor using KOH electrolyte solution. *Journal of Physical Chemistry C*, 113(6), 2643–2646. <https://doi.org/10.1021/jp8088269>
- Yallapu, M. M., Othman, S. F., Curtis, E. T., Gupta, B. K., Jaggi, M., & Chauhan, S. C. (2011). Multi-functional magnetic nanoparticles for magnetic resonance imaging and cancer therapy. *Biomaterials*, 32(7), 1890–1905. <https://doi.org/10.1016/j.biomaterials.2010.11.028>
- Yang, C. L., Chen, J. P., Wei, K. C., Chen, J. Y., Huang, C. W., & Liao, Z. X. (2017). Release of doxorubicin by a folate-grafted, chitosan-coated magnetic nanoparticle. *Nanomaterials*, 7(4), 1–12. <https://doi.org/10.3390/nano7040085>
- Yang, K. M., Cho, H. II, Choi, H. J., & Piao, Y. (2014). Synthesis of water well-dispersed PEGylated iron oxide nanoparticles for MR/optical lymph node imaging. *Journal of Materials Chemistry B*, 2(21), 3355–3364. <https://doi.org/10.1039/c4tb00084f>
- Yang, Yanfang, Xie, X., Xu, X., Xia, X., Wang, H., Li, L., Dong, W., Ma, P., Yang, Y., Liu, Y., & Mei, X. (2016). Thermal and magnetic dual-responsive liposomes with a cell-penetrating peptide-siRNA conjugate for enhanced and targeted cancer therapy. *Colloids and Surfaces B: Biointerfaces*, 146, 607–615. <https://doi.org/10.1016/j.colsurfb.2016.07.002>

- Yang, Yang, Hu, Y., Wang, Y., Li, J., Liu, F., & Huang, L. (2012). Nanoparticle delivery of pooled siRNA for effective treatment of non-small cell lung cancer. *Molecular Pharmaceutics*, 9(8), 2280–2289. <https://doi.org/10.1021/mp300152v>
- Yemul, O., & Imae, T. (2008). Synthesis and characterization of poly(ethyleneimine) dendrimers. *Colloid and Polymer Science*, 286(6–7), 747–752. <https://doi.org/10.1007/s00396-007-1830-6>
- Yingyuad, P., Mével, M., Prata, C., Kontogiorgis, C., Thanou, M., & Miller, A. D. (2014). Enzyme-triggered PEGylated siRNA-nanoparticles for controlled release of siRNA. *Journal of RNAi and Gene Silencing*, 10(1), 490–499.
- Yoo, J., Irvine, D. J., Discher, D. E., & Mitragotri, S. (2011). Bio-inspired, bioengineered and biomimetic drug delivery carriers. *Nature Publishing Group*, 10(July). <https://doi.org/10.1038/nrd3499>
- Zhang, M., Tang, Y., Tian, X., Wang, H., Wang, J., & Zhang, Q. (2021). Magnetron co-sputtering optimized aluminum-doped zinc oxide (AZO) film for high-response formaldehyde sensing. *Journal of Alloys and Compounds*, 880, 160510. <https://doi.org/10.1016/j.jallcom.2021.160510>
- Zhang, Shaobo, Gu, J., Yang, N. S., Kao, C., Gardner, T. A., Eble, J. N., & Cheng, L. (2002). Relative promoter strengths in four human prostate cancer cell lines evaluated by particle bombardment-mediated gene transfer. *Prostate*, 51(4), 286–292. <https://doi.org/10.1002/pros.10081>
- Zhang, Song, Gong, M., Zhang, D., Yang, H., Gao, F., & Zou, L. (2014). Thiol-PEG-carboxyl-stabilized Fe₂O₃/Au nanoparticles targeted to CD105: Synthesis, characterization and application in MR imaging of tumor angiogenesis. *European Journal of Radiology*, 83(7), 1190–1198. <https://doi.org/10.1016/j.ejrad.2014.03.034>
- Zhang, X., Sun, W., & Cheng, Y. (2022). Aptamer labeled nanozyme-based ELISA for ampicillin residue detection in milk. *Chemical Papers*. <https://doi.org/10.1007/s11696-022-02084-5>
- Zhang, Z., Zou, X., Xu, L., Liao, L., Liu, W., Ho, J., Xiao, X., Jiang, C., & Li, J. (2015). Hydrogen gas sensor based on metal oxide nanoparticles decorated graphene transistor. *Nanoscale*, 7(22), 10078–10084. <https://doi.org/10.1039/c5nr01924a>
- Zhao, J., Bao, X., Meng, T., Wang, S., Lu, S., Liu, G., Wang, J., Sun, J., & Yang, X. (2021). Fe(II)-driven self-assembly of enzyme-like coordination polymer nanoparticles for cascade catalysis and wound disinfection applications. *Chemical Engineering Journal*, 420(P1), 129674. <https://doi.org/10.1016/j.cej.2021.129674>

- Zhao, M., Li, J., Du, L., Tan, C., & Xia, Q. (2011). *Targeted Cellular Uptake and siRNA Silencing by Quantum-Dot Nanoparticles Coated with β -Cyclodextrin Coupled to Amino Acids*. 5171–5179. <https://doi.org/10.1002/chem.201003523>
- Zhao, Y., Zhao, X., Cheng, Y., Guo, X., & Yuan, W. (2018). Iron Oxide Nanoparticles-Based Vaccine Delivery for Cancer Treatment. *Molecular Pharmaceutics*, 15(5), 1791–1799. <https://doi.org/10.1021/acs.molpharmaceut.7b01103>
- Zhou, J., Wang, Y., Bu, J., Zhang, B., & Zhang, Q. (2019). Ni²⁺-BSA Directional Coordination-Assisted Magnetic Molecularly Imprinted Microspheres with Enhanced Specific Rebinding to Target Proteins. *ACS Applied Materials and Interfaces*, 11(29), 25682–25690. <https://doi.org/10.1021/acsami.9b06507>
- Zhou, Z., Liu, X., Zhu, D., Wang, Y., Zhang, Z., Zhou, X., Qiu, N., Chen, X., & Shen, Y. (2017). Nonviral cancer gene therapy: Delivery cascade and vector nanoproperty integration. *Advanced Drug Delivery Reviews*, 115, 115–154. <https://doi.org/10.1016/j.addr.2017.07.021>
- Zlotta, A. R., Egawa, S., Pushkar, D., Govorov, A., Kimura, T., Kido, M., Takahashi, H., Kuk, C., Kovylyna, M., Aldaoud, N., Fleshner, N., Finelli, A., Klotz, L., Sykes, J., & Lockwood, G. (2013). *Prevalence of Prostate Cancer on Autopsy: Cross-Sectional Study on Unscreened Caucasian and Asian Men*. 105(14). <https://doi.org/10.1093/jnci/djt151>
- Zuckerman, J. E., Gritli, I., Tolcher, A., Heidel, J. D., Lim, D., & Morgan, R. (2014). *Correlating animal and human phase Ia / Ib clinical data with CALAA-01 , a targeted , polymer-based nanoparticle containing siRNA*. 111(31). <https://doi.org/10.1073/pnas.1411393111>
- Zugazagoitia, J., Guedes, C., Ponce, S., Ferrer, I., Molina-Pinelo, S., & Paz-Ares, L. (2016). Current Challenges in Cancer Treatment. *Clinical Therapeutics*, 38(7), 1551–1566. <https://doi.org/10.1016/j.clinthera.2016.03.026>

APPENDICES

Appendix A : Poster presentations 2019



Metallic nano carrier complex targeting neuroendocrine prostate cancer

Aver Hemben, Iva Chianella and Glenn Leighton

Introduction

Cancer treatment methods such as chemotherapy, radiation therapy, immunotherapy and hormone therapy have been used to treat cancers. These treatments affect cancerous as well as healthy tissues. Targeted drug delivery however can provide a focused approach to the treatment of cancers with the potential to eliminate the adverse side effects. This work follows from previous research conducted on synthesis of polymer encapsulated siRNA / iron oxide (Fe₃O₄) commercial nanoparticle complex in pilot study. The study highlighted extracellular drug release in relation to time and polymer composition of the pay loaded complex. Going forward, free standing Fe₃O₄ NPs (1 – 8 nm ø) soft landed on thin film, polymer-coated 4" silicon wafer have since been achieved. Physical vapour deposition (PVD) thin film sputtering via Mantis Nanogen Trio system was employed. Overall objective of this study is to synthesise a polymer / nanocarrier complex, pay - loaded with siRNA and with chemical properties suitable for intracellular targeted drug delivery in neuroendocrine prostate cancer (NEPC).

Methods

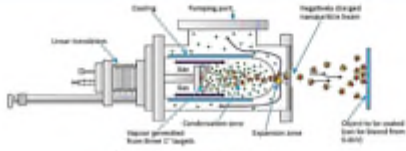


Fig. 1: Mantis Nanogen Trio system.




Fig. 2: PEGylated particle.

Results

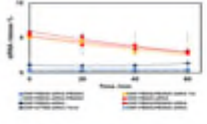


Fig. 3: siRNA release studies (obtained during previous phase of project).

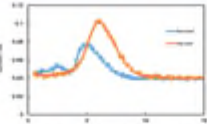


Fig. 4: Curve resolution pre and post sputtering.

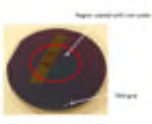


Fig. 5: Fe₃O₄ coating in center of silicon wafer.




Fig. 6: TEM free-standing Fe₃O₄ NPs in water.

Conclusions

- PVD sputtered magnetic targets produce 1-8 nm ø NPs potentially suitable size for intracellular targeted delivery.
- Water soluble polymer allows suspension of particles.
- NP dispersion may be reduced by using 2" substrate.

Further work

- Development of protocols to assess siRNA release at different pH values (using suitable fluorescent markers).
- Effect of pH on siRNA release from polymer /nano carrier complex.
- Identification and attachment of receptor specific for cancerous cell membrane biomarker for targeted delivery.
- *in vitro* and *in vivo* testing at Open University.

Dr Aver Hemben, Dr Iva Chianella and Dr Glenn Leighton.
ahemben@cranfield.ac.uk | ichianella1999@cranfield.ac.uk | gl.leighton@cranfield.ac.uk

Acknowledgements:
 Thanks to the Open University for supporting this research.

www.cranfield.ac.uk
 2019




Figure 1: Poster Manufacturing, May 2019



Metallic nanocarrier complex targeting neuroendocrine prostate cancer.

Introduction

Cancer treatment methods such as chemotherapy, radiation therapy, immunotherapy and hormone therapy have been used to treat cancers; affecting cancerous and healthy tissues. Targeted drug delivery can provide a focused approach to cancer treatment potentially to eliminating adverse effects. This work follows from pilot study conducted on synthesis of polymer encapsulated siRNA / iron oxide (Fe_3O_4) commercial nanoparticle complex. Physical vapour deposition (PVD) sputtered Fe_3O_4 NPs (1 – 8 nm ϕ) soft landed on thin film, polymer-coated 4" ϕ silicon wafer have since been produced via Mantis Nanogen Trio system. Overall objective of this study is to synthesise a polymer / nanocarrier complex, pay - loaded with siRNA and with chemical properties suitable for intracellular targeted drug delivery in neuroendocrine prostate cancer (NEPC).

Methodology

Fitted to the magnetron is iron oxide target suspended in agglomeration chamber filled with Argon to which is applied a HV and current to strike a plasma. Produced Iron oxide nanoparticles (IONPs) are filtered and deposited on silicon wafer substrate.

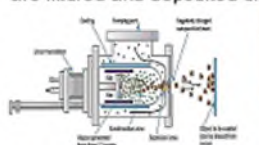


Fig.1a: Mantis Nanogen Trio.



Fig.1 b: IONP production.

Table 1: Process parameters

Target Fe_3O_4	
t = 4 minutes	
1	411 V 0.010 A
2	407.3 V 0.010 A
t = 16 minutes	
3	373 V 0.010 A
4	473.5 V 0.010 A



Fig. 2: PEGylated particle.

Results

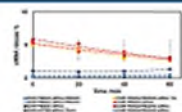


Fig.3: siRNA release in pilot study.



Fig. 4: Fe_3O_4 in Texas Red labelled PEG / PBS pH 5.5 – 7.6 up to 1 hr.

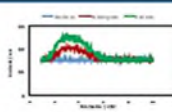


Fig. 5: Curve evolution pre and post sputtering.

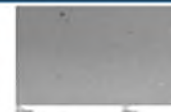


Fig. 6: TEM free-standing Fe_3O_4 NPs in water.

Conclusions

- PVD sputtered magnetite targets produce 1-8 nm ϕ NPs potentially suitable size for intracellular targeted delivery.
- Water soluble polymer allows suspension of the produced nanoparticles.

Further work

- Development of protocols to assess siRNA release at different pH values.
- Effect of pH on siRNA release from polymer / nano carrier complex.
- *In vitro* and *in vivo* testing at Open University.

Dr. Aver Hemben, Dr. Glenn Leighton and Dr. Iva Chianella

School of Aerospace, Transport and Manufacturing, Surface Engineering and Precision Institute.

a.hemben@cranfield.ac.uk; g.j.t.leighton@cranfield.ac.uk; i.chianella.1998@cranfield.ac.uk

www.cranfield.ac.uk

Figure 2: Cranfield Doctoral Network (CDN) presentation, September 2019
(Winner of PhD poster competition)

Table 1: Conferences and Seminars attended

S/no.	Conference / Seminar	Date
1	Oral presentation at National University of Columbia, Medellin	March 2019
2	Poster – Manufacturing Research Community Conference Cranfield University, UK	May 2019
3	Poster – NEPC Conference, Open University, UK	June 2019
4	Cranfield Doctoral Network Annual Conference <i>Prize winner for the Poster competition</i>	September 2019
5	Cranfield Doctoral Network (online) <i>Prize winner for the Poem competition</i>	October 2020

Appendix B : Presentation at University of Columbia 2019

Vehicle for drug delivery

Surface Engineering and Precision Institute (SEPi) at Cranfield University, U.K. is a world-leading Centre of excellence for innovative research into atomistic and particulate-based manufacturing techniques, for the production of protective and active surface coating systems. The mission is to transform innovative manufacturing research into engineered products. In March 2019, I was asked to visit and make presentations at the National University of Colombia, Medellin through a joint Royal Academy of Engineering Grant.



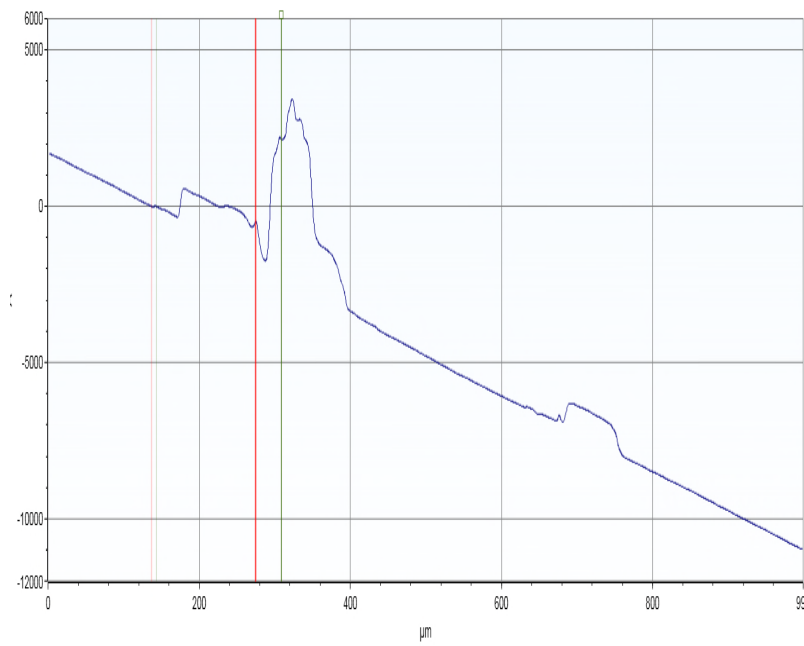
Interactive session with participants

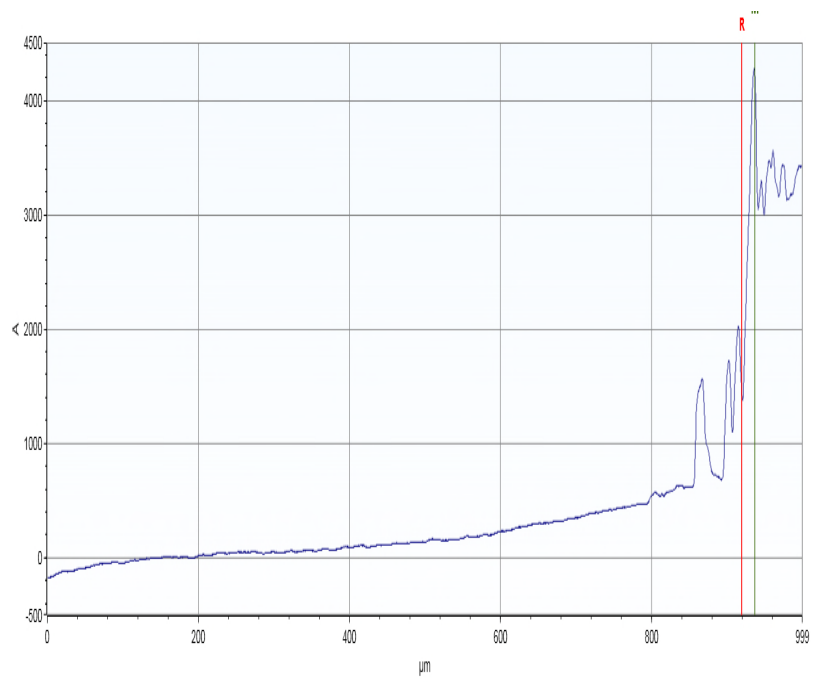
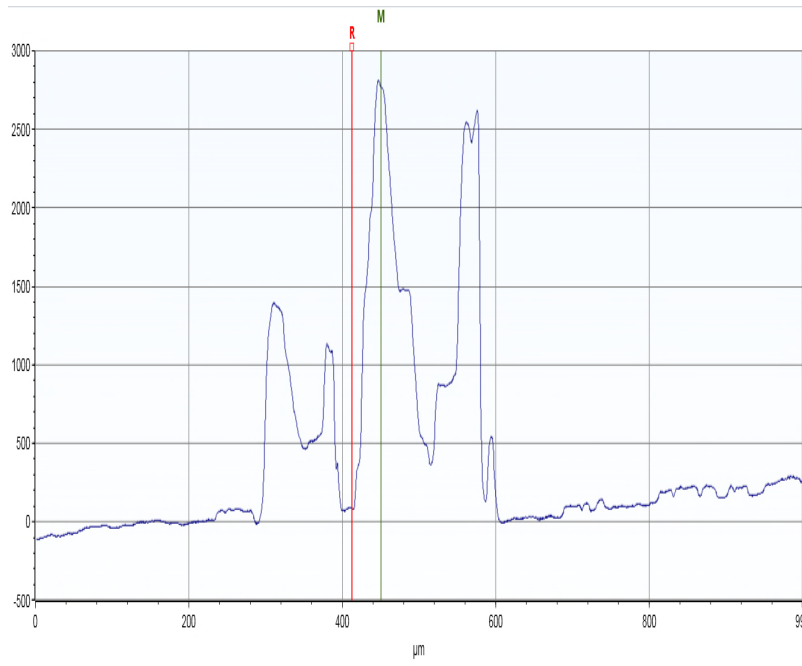
Major discussions included current research involving the production of metallic particles as the vehicle for delivering drugs to prostate cancer cells. These photographs were taken (Huawei Mate 9) to capture the presentations which bear upon Cranfield University research collaboration with the National University of Colombia, Medellin.

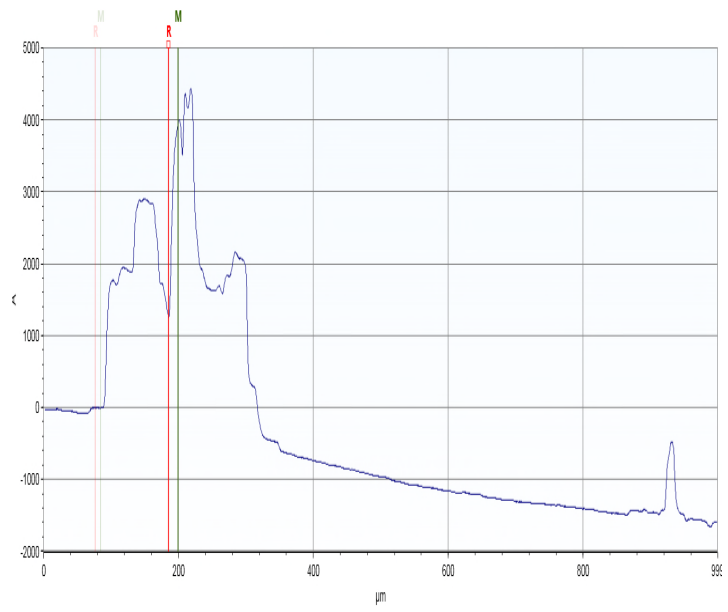
Figure 3: Oral presentation at National University of Columbia, Medellin, March 2019

This photo was also entered for a competition conducted at Cranfield University.

Appendix C : DektakXT measurements







Appendix D : Cranfield Doctoral Network Conference 2020

A poem by Aver Hemben

Metallic nanocarrier complex targeting neuroendocrine prostate cancer

Neuroendocrine prostate cancer, or NEPC
Is a form of prostate cancer
Sometimes chronic, you see

Cancers grow for many years
Sometimes showing no signs
Yet once found are managed
As well as can be advised

Several treatments exist
For the cancer types
Radio and chemotherapy
Surgery and such like

Some affect healthy tissues
And tissues diseased
Drug- loaded particles help side effects
While cancer cells recede

Tiny particles find uses
In many different ways
But targeted drug delivery
Is my focus today

I produce small iron particles
Also called IONPs
From larger bits of iron
Via gas condensation technique

After two hours of deposition
On a wax - coated wafer
IONPs are suspended
In ultra - pure water

Free-standing IONPs
Waxy coat 'n all
Seen by a microscope
Are really very small

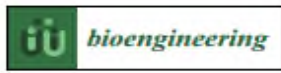
1-8 nm is suitable particle size
For payload delivery to cancer cells
To ensure the cancer dies

IONPs can leave the body
By very natural ways
Hence particle size is important
In preserving good health always

Future work, other colleagues involved,
More tests to perform
May show the role of IONPs
Treating NEPC some day

<https://intranet.cranfield.ac.uk/CDN/Pages/CDN-annual-conference.aspx>

Appendix E : Published paper 2021



Article

Surface Engineered Iron Oxide Nanoparticles Generated by Inert Gas Condensation for Biomedical Applications

Aver Hemben, Iva Chianella and Glenn John Thomas Leighton *

Surface Engineering and Precision Institute, Cranfield University, Bedfordshire MK430AL, UK;
hemben@cranfield.ac.uk (A.H.); i.chianella.1998@cranfield.ac.uk (I.C.)
* Correspondence: g.j.t.leighton@cranfield.ac.uk

Abstract: Despite the lifesaving medical discoveries of the last century, there is still an urgent need to improve the curative rate and reduce mortality in many fatal diseases such as cancer. One of the main requirements is to find new ways to deliver therapeutics/drugs more efficiently and only to affected tissues/organs. An exciting new technology is nanomaterials which are being widely investigated as potential nanocarriers to achieve localized drug delivery that would improve therapy and reduce adverse drug side effects. Among all the nanocarriers, iron oxide nanoparticles (IONPs) are one of the most promising as, thanks to their paramagnetic/superparamagnetic properties, they can be easily modified with chemical and biological functions and can be visualized inside the body by magnetic resonance imaging (MRI), while delivering the targeted therapy. Therefore, iron oxide nanoparticles were produced here with a novel method and their properties for potential applications in both diagnostics and therapeutics were investigated. The novel method involves production of free standing IONPs by inert gas condensation via the Mantis NanoGen Trio physical vapor deposition system. The IONPs were first sputtered and deposited on plasma cleaned, polyethylene glycol (PEG) coated silicon wafers. Surface modification of the cleaned wafer with PEG enabled deposition of free-standing IONPs, as once produced, the soft-landed IONPs were suspended by dissolution of the PEG layer in water. Transmission electron microscopic (TEM) characterization revealed free standing, iron oxide nanoparticles with size < 20 nm within a polymer matrix. The nanoparticles were analyzed also by Atomic Force Microscope (AFM), Dynamic Light Scattering (DLS) and NanoSight Nanoparticle Tracking Analysis (NTA). Therefore, our work confirms that inert gas condensation by the Mantis NanoGen Trio physical vapor deposition sputtering at room temperature can be successfully used as a scalable, reproducible process to prepare free-standing IONPs. The PEG- IONPs produced in this work do not require further purification and thanks to their tunable narrow size distribution have potential to be a powerful tool for biomedical applications.

Keywords: iron oxide nanoparticles; PVD; Mantis NanoGen Trio; drug delivery



Citation: Hemben, A.; Chianella, I.; Leighton, G.J.T. Surface Engineered Iron Oxide Nanoparticles Generated by Inert Gas Condensation for Biomedical Applications.

Bioengineering **2021**, *8*, 36.

<https://doi.org/10.3390/bio802036>

<https://www.mdpi.com/2075-4436/8/2/36>

Academic Editors: Ashiqur Rahman, Md Symon Jaham Sajid and Si Amar Dasouzama

Received: 13 January 2021

Accepted: 13 February 2021

Published: 15 March 2021

Figure 4: Published Paper related to production of iron oxide nanoparticles by magnetron sputtering using argon gas via inert gas condensation (Chapter 2).

[Bioengineering | Free Full-Text | Surface Engineered Iron Oxide Nanoparticles Generated by Inert Gas Condensation for Biomedical Applications \(mdpi.com\)](https://www.mdpi.com/2075-4436/8/2/36)